




Universitat Autònoma de Barcelona

ADVERTIMENT. L'accés als continguts d'aquesta tesi queda condicionat a l'acceptació de les condicions d'ús establertes per la següent llicència Creative Commons:  http://cat.creativecommons.org/?page_id=184

ADVERTENCIA. El acceso a los contenidos de esta tesis queda condicionado a la aceptación de las condiciones de uso establecidas por la siguiente licencia Creative Commons:  <http://es.creativecommons.org/blog/licencias/>

WARNING. The access to the contents of this doctoral thesis it is limited to the acceptance of the use conditions set by the following Creative Commons license:  <https://creativecommons.org/licenses/?lang=en>

Exploration of the Higgs sector after its discovery

Marc Riembau

Institut de Física d'Altes Energies
Universitat Autònoma de Barcelona

Memòria de recerca presentada per a l'obtenció del títol de

Doctor en Física

Juliol 2018



Exploration of the Higgs sector
after its discovery

Marc Riembau

Director de tesi

Christophe Grojean

Co-Director de tesi

Giuliano Panico

Tutor de tesi

Oriol Pujolàs

Resum

El descobriment del bosó de Higgs és la culminació d'una recerca que ha durat 40 anys, i completa un marc teòric sota el qual gairebé totes del dades obtingudes de col·lisionadors de partícules poden ser explicades consistentment. Simultàniament, i paradoxalment, l'aparent confirmació d'una separació d'escala entre l'electrofeble i la que suposadament estableix la massa del bosó de Higgs posa el relleu el problema de la jerarquia. En la recerca d'una descripció del món que simplifiqui els patrons i simetries del Model Estàndard, l'exploració de l'escala dels TeVs i en particular l'estudi del bosó de Higgs tindran un paper central. En aquesta tesi presentem les possibilitats que el LHC i futurs col·lisionadors proveiran, amb énfasi en la determinació de l'auto-acoblament del bosó de Higgs. També considerarem l'estudi de la producció de bosons electrofebles com a eina per entendre les interaccions dels bosons de Goldstone que formen part del doblet de Higgs, mostrant la seva rellevància al combinar-ho amb les dades del pol de la Z i altres cerques al LHC. Finalment, ens centrem en com el moment dipolar elèctric de l'electró posa fortes restriccions en models on el bosó de Higgs és descrit com un estat compost.

Abstract

The discovery of the Higgs boson culminates a 40-year long hunt and completes a theoretical framework under which almost all collider data can be consistently explained. At the same time, paradoxically, the confirmation of an apparent mass gap above the electroweak scale exacerbates the problem of the electroweak hierarchy. In the search of a description of the world that simplifies the patterns and symmetries of the Standard Model, the exploration of the TeV scale and in particular the study of the Higgs boson will play a central role. In this thesis we explore the possibilities that the LHC and future colliders will bring, with particular emphasis on the determination of the Higgs self-coupling. We also consider the pair production of electroweak bosons as a probe of the Goldstone interactions in the Higgs doublet, and show its relevance as a way to improve the Z pole measurements and its interplay with other LHC searches. Finally, we focus on how the electron's electric dipole moment can set strong constraints on models where the Higgs arises as a composite state.

This thesis is based on the following publications

- S. Di Vita, C. Grojean, G. Panico, M. Riembau and T. Vantalon,
“A global view on the Higgs self-coupling,”
JHEP **1709** (2017) 069 [arXiv:1704.01953 [hep-ph]].
- S. Di Vita, G. Durieux, C. Grojean, J. Gu, Z. Liu, G. Panico, M. Riembau and
T. Vantalon,
“A global view on the Higgs self-coupling at lepton colliders,”
JHEP **1802** (2018) 178 [arXiv:1711.03978 [hep-ph]].
- G. Panico, M. Riembau and T. Vantalon,
“Probing light top partners with CP violation,”
arXiv:1712.06337 [hep-ph].
- M. Carena, Z. Liu and M. Riembau,
“Probing Electroweak Phase Transition via Enhanced Di-Higgs Production,”
arXiv:1801.00794 [hep-ph].

Further publications during the PhD

- J. Elias-Miro, M. Montull and M. Riembau,
“The renormalized Hamiltonian truncation method in the large E_T expansion,”
JHEP **1604** (2016) 144 [arXiv:1512.05746 [hep-th]].
- M. Chala, C. Grojean, M. Riembau and T. Vantalon,
“Deciphering the CP nature of the 750GeV resonance,”
Phys. Lett. B **760** (2016) 220 [arXiv:1604.02029 [hep-ph]].
- D. de Florian *et al.* [LHC Higgs Cross Section Working Group],
“Handbook of LHC Higgs Cross Sections: 4. Deciphering the Nature of the Higgs
Sector,”
arXiv:1610.07922 [hep-ph].

Acknowledgements

I am grateful to Christophe Grojean for his support. The environment he creates is very fruitful for research and his pursuit for the relevant question to be asked really shaped my scientific view. I am also very thankful to Giuliano Panico. His guidance over all these years has been crucial, and his dedication has been a great inspiration for me.

I am thankful to La Caixa-Severo Ochoa program for providing the economical support for this thesis.

It has been a fantastic pleasure to work with M. Carena, M. Chala, S. Di Vita, G. Durieux, J. Elias-Miró, C. Grojean, J. Gu, Z. Liu, M. Montull, G. Panico and T. Vantalon.

I have very good memories from my stay at IFAE and DESY, as well as from my visit at Fermilab and various schools and conferences. I would like to thank the many students and postdocs I met during this time. In particular, both Marc M. and Thibaud had to suffer my company both in Barcelona and Hamburg, and also to Joan, Mateo, Matteo, Sergi, Clara, Gauthier, Oleksii, Stefano, Jiayin and many others.

M'agradaria agrair a la meva família pel suport incondicional,

i a la Laura, per absolutament tot.

“Not entirely, dear Adso,” my master replied. “True, that kind of print expressed to me, if you like, the idea of ‘horse’, the verbum mentis, and would have expressed the same to me wherever I might have found it. But the print in that place and at that hour of the day told me that at least one of all possible horses had passed that way. So I found myself halfway between the perception of the concept ‘horse’ and the knowledge of an individual horse. And in any case, what I knew of the universal horse had been given me by those traces, which were singular. I could say I was caught at that moment between the singularity of the traces and my ignorance, which assumed the quite diaphanous form of a universal idea. If you see something from a distance, and you do not understand what it is, you will be content with defining it as a body of some dimension. When you come closer, you will then define it as an animal, even if you do not yet know whether it is a horse or an ass. And finally, when it is still closer, you will be able to say it is a horse even if you do not yet know whether it is Brunellus or Niger. And only when you are at the proper distance will you see that it is Brunellus (or, rather, that horse and not another, however you decide to call it). And that will be full knowledge, the learning of the singular. So an hour ago I could expect all horses, but not because of the vastness of my intellect, but because of the paucity of my deduction. And my intellect’s hunger was sated only when I saw the single horse that the monks were leading by the halter. Only then did I truly know that my previous reasoning, had brought me close to the truth. And so the ideas, which I was using earlier to imagine a horse I had not yet seen, were pure signs, as the hoofprints in the snow were signs of the idea of ‘horse’; and signs and the signs of signs are used only when we are lacking things.”

William of Baskerville, talking about Effective Field Theory,
in 'The Name of the Rose' by Umberto Eco

Contents

1	Introduction	2
2	Future colliders	12
3	A global view on the Higgs self-coupling	18
3.1	Introduction	18
3.2	The effective parametrization	20
3.2.1	Higgs primary couplings	20
3.2.2	Additional operators contributing to Higgs observables	23
3.2.3	Large Higgs self-interactions in a consistent EFT expansion	26
3.3	Fit from inclusive single-Higgs measurements	30
3.3.1	Single-Higgs rates and single-Higgs couplings	31
3.3.2	Global fit including Higgs self-coupling	38
3.3.3	Impact of the trilinear coupling on single-Higgs couplings	42
3.4	Double Higgs production	43
3.5	Differential observables	46
3.5.1	Impact of single-Higgs differential measurements	47
3.5.2	Robustness of the fits	49
4	The Higgs self-coupling at future lepton colliders	52
4.1	Introduction	52
4.2	Low-energy lepton machines	53
4.2.1	Higher-order corrections to single-Higgs processes	53
4.2.2	Global analysis	56
4.2.2.1	Analysis of Higgs data at lepton colliders alone	56
4.2.2.2	Synergy between measurements at the HL-LHC and lepton-colliders	60
4.3	High-energy lepton machines	61
4.3.1	Higgs pair production	62

4.3.2	Global analysis	67
4.4	Summary	69
5	Probing the Electroweak Phase Transition via Enhanced Di-Higgs Production	76
5.1	Introduction	76
5.2	Model framework	77
5.2.1	Stability, Unitarity and EWSB conditions	78
5.2.2	Properties of the singlet-like scalar	81
5.3	Enhancing the di-Higgs signal via interference effects	84
5.3.1	Anatomy of the interference effect	84
5.3.2	Parametric dependence of the on-shell interference effect	87
5.4	Phenomenological study	89
5.4.1	Differential distribution	90
5.4.2	Signal and background analysis for $pp \rightarrow HH \rightarrow b\bar{b}\gamma\gamma$	91
5.4.3	Discovery and exclusion reach of the HL- and HE-LHC	92
5.4.4	Implications for the first order electroweak phase transition	94
5.5	Summary	97
6	Diboson production at LHC	98
6.1	Introduction	98
6.2	Theoretical framework	100
6.3	Results with current LHC data	103
6.3.1	Data used and statistical analysis	103
6.3.2	Correlations among the Higgs basis parameters	105
6.3.3	LHC bounds on $\delta V_{\bar{q}q}$ vs LEP-1	106
6.3.4	LHC bounds on aTGC and interplay with $\delta V_{\bar{q}q}$	109
6.4	Projected bounds for the HL-LHC	110
6.4.1	Data used and assumptions for the HL-LHC	110
6.4.2	HL-LHC projections on $\delta V_{\bar{q}q}$ vs LEP-1	111
6.4.3	HL-LHC projections on aTGC and interplay with $\delta V_{\bar{q}q}$	112
6.5	Interpretation of the constraints	114
6.5.1	Quadratic BSM amplitudes and EFT validity	114
6.5.2	Power countings and BSM interpretation	116
6.5.3	A model with triplets: diboson reach vs other searches	117
6.6	Summary	121

7	Probing light top partners with CP violation	124
7.1	Introduction	124
7.2	CP violation from top partners	127
7.2.1	Electron EDM	129
7.2.1.1	Electron EDM as a running effect	131
7.2.1.2	The full result	134
7.2.2	CP-violating effects for the light quarks	134
7.2.2.1	Neutron and Mercury EDM	137
7.2.3	Experimental bounds	138
7.2.4	Comparison with direct top partner searches	144
7.3	Non-minimal models	147
7.3.1	The $14 + 1$ model with a light singlet	147
7.3.2	The $5 + 5$ 2-site model	149
7.4	Summary	154
A	Higgs production and decay rates in the EFT framework	156
A.1	EFT cross section for hadron colliders	156
A.2	Trilinear dependence for e^+e^- colliders	163
B	Indirect constraints on the singlet model	165
C	Summary of LEP-1 constraints on the light quark couplings	167
D	Summary of diboson constraints	169
	Bibliography	172

Chapter 1

Introduction

The discovery [1, 2] of a spin zero field with properties consistent with the Higgs boson predicted by the Standard Model (SM) culminates a theoretical framework where most of the collider data is consistently explained. At the same time, paradoxically, since on theoretical grounds the Higgs boson should be accompanied by other states with a mass around the weak scale, the discovery of an apparent mass gap above the electroweak scale puts into question our understanding of physics. The lack of any hint in the LHC data that might lead us to a more complete picture of Nature is not an unexpected blow, but rather the final piece of evidence that the electroweak scale is fine tuned to some degree.

The need for the existence of a deeper explanation of why the electroweak symmetry is broken is supported by an overwhelming circumstantial evidence pointing that the SM cannot be the end of the story. There is no candidate to play the role of the dark matter that the astrophysical and cosmological observations require, the asymmetry of matter and antimatter in the universe is unexplained, the CKM matrix has an obvious structure that begs for explanation, the neutrinos are massive, the strong CP problem of QCD is an unexplained fine tuning, a period of inflation is required and so on. And, ultimately, gravity must be embedded in a bigger framework like string theory. The central, pivotal, vital role of the electroweak naturalness problem is that it has to be addressed at the electroweak scale, where we have direct experimental access, and cannot be postponed to an arbitrarily large scale. In this way, understanding the origin of the electroweak scale is of paramount importance, and the rest of our picture of the world spins around it.

To appreciate where we are and what is at stake at the LHC, it is important to go back and appreciate where we were and what was at stake at LEP, or PETRA.

“*We present a series of hypothesis and speculations leading inescapably to the conclusion that $SU(5)$ is the gauge group of the world*”. This first sentence of the famous paper by H. Georgi and S. L. Glashow in '74 [3], where they present the idea behind Grand Unified Theories (GUT), shows the feelings of someone that realized that $SU(5)$ does not only contain the SM group $SU(3) \times SU(2)_L \times U(1)_Y$ as a maximal subgroup, but that the different SM quarks and leptons can be embedded into a $\bar{5} + 10$. In one stroke, they provided more progress in the search of a *final theory* than anyone before them in all their live. One consequence is that since the electromagnetic charge $U(1)_{em}$ belongs to a bigger group, it must be traceless, leading to e.g. $Q_d = Q_e/N_c$, explaining why the proton and electron have the same charge, multiples of the same unit. There is also a sharp prediction for the weak mixing angle, $\sin \theta_W = Tr(T_3^2)/Tr(Q_{em}^2) = 3/8$. From the GUT scale, this runs down to a value which was in perfect agreement with the observations at that time. This remarkable success is even more attractive if one extends the gauge group to $SO(10)$, which includes $SU(5) \times U(1)$ as a maximal subgroup. Here, the spinor representation **16** contains not only the full set of quarks and leptons, but also an extra fermion, singlet under the SM group, that can play the role of a right handed neutrino. This right handed neutrino can receive a mass from a term $M_{Pl}^{-1} \nu_R \nu_R v_{GUT}^2$, leading to $M_R \sim 10^{14}$ GeV for $v_{GUT} \sim 10^{16}$ GeV and $M_{Pl} \sim 10^{18}$ GeV. Then, the right handed neutrinos participate in the seesaw induced by the electroweak Higgs boson $v_{ew} = 246$ GeV, that gives the left handed neutrinos a tiny mass $v_{ew}^2/M_R \sim 0.1$ eV, in accordance with the experiment.

All this could have gone wrong very easily, it is hard to overstate how small the window of opportunity is. GUT theories predict proton decay, which is measured to be extremely stable, setting a constraint to the scale of grand unification of order $10^{15} - 10^{16}$ GeV. If the running of the couplings predicted the GUT scale to be even 10^{13} GeV, this idea of GUT would have died before being born. If the couplings unified above the Planck scale, nobody would have payed much attention. And since the running is a logarithmic running, it is easy to imagine any of this to happen if there is no deeper reason behind this structure. But the unification does not only take place at the allowed region, but it does at the good scale to generate neutrino masses and where most models of inflation take place, all at a *loop distance* from the Planck scale, connecting GUT physics with gravity and string theory, where an embedding of QFT into a bigger framework is expected. The window were all the clues lie in the same path is very narrow, and it is hard to take seriously the possibility that all these ideas are just plainly misguided, unless one accepts that Nature is trying to be maximally confusing.

There is, however, a puzzling fact, that sets the stage for the electroweak hierarchy problem. If the $SU(5)$ group is broken to the SM group by the vacuum expectation value (vev) of a scalar field Σ , $\langle \Sigma \rangle = v_{GUT} \text{diag}(2, 2, 2, -3, -3)$, and if the Higgs belongs to a $\mathbf{5}$, the terms $\lambda \mathbf{5}_H \Sigma \mathbf{5}_H + m_\Sigma^2 \Sigma^2$ will generate a mass $m_\Sigma^2 - 3\lambda v_{GUT}^2$ for the $SU(2)$ -charged part of the $\mathbf{5}$, identified with the electroweak Higgs, and $m_\Sigma^2 + 2\lambda v_{GUT}^2$ for the triplet partner inside the $\mathbf{5}$. Since the triplet will generate proton decay, that combination should be of order of the GUT scale. However, the $SU(2)$ charged Higgs is responsible for electroweak symmetry breaking, and therefore $m_\Sigma^2 - 3\lambda v_{GUT}^2 \sim (100\text{GeV})^2$. This is, the scales should balance each other, without any reason, in one part in 10^{36} . The hierarchy problem hits you in the face when the Higgs mass is calculable, and the *doublet-triplet splitting problem* of GUT theories is the prime example [4, 5].

In parallel to those developments, it was discovered that one could extend the Poincaré symmetry, using fermionic generators [6–9]. This new type of symmetry, called supersymmetry, relates bosons with fermions. If supersymmetry were exact, for each fermion there would be a scalar with the same quantum numbers and degenerate in mass. A remarkable consequence is that if the mass of a fermion is protected by chiral symmetry, supersymmetry transfers this protection to the scalar partner, so there is the possibility of having a light scalar with a large mass gap above him. However, these Fermi-Bose multiplets have not been observed, so supersymmetry has to be broken, and if it is a good symmetry of the world, it must spontaneously broken [10]. Since we do not know how supersymmetry is broken, a phenomenological way to parametrize the effects of the breaking is to break supersymmetry explicitly with dimensionful operators [11, 12], called soft terms, that from a UV perspective could be understood as the vev of the underlying dynamics. The effects of the SUSY breaking dynamics can generate masses M_i for the fermionic superpartners of the SM gauge fields, the gauginos λ_i , $i = 1, 2, 3$, and masses \tilde{m} for the scalar partners of the fermionic SM fields, the squarks and sleptons \tilde{q} and \tilde{e} . Only the so far unobserved states are precisely the ones that should receive a mass, while the others are protected by gauge and chiral symmetry and their masses are generated only through electroweak symmetry breaking.

The Higgs sector in a supersymmetric theory consists of two Higgs doublets H_u and H_d . This is because only one Higgs doublet cannot give mass simultaneously to up and down quarks. Incidentally, or not, this is very welcome since the fermionic partners of the Higgs boson, the higgsinos, would induce an anomaly and lead to an inconsistent theory. The two Higgs doublets give five physical scalar states, with a light a heavy CP-even states, a CP-odd state, and one electromagnetically charged Higgs boson. In

the Higgs sector there is, a priori, no reason for the SUSY breaking dynamics to generate masses only to a part of the multiplet, so both scalars and fermions get soft mass terms $\sim m_{soft}^2$ of the same order. Crucially, the Higgs sector contains a SUSY preserving mass scale μ , which gives a vectorlike mass term $\mu^2 H_u H_d$, so it also contributes to the mass of the Higgses and higgsinos. Since this mass term preserves supersymmetry, its size is expected to be $\sim M_{Pl}$. However, it contributes to electroweak symmetry breaking, so phenomenologically one expects $\mu \sim m_Z$. This tension is, again, another incarnation of the hierarchy problem. Fortunately, the supersymmetric case is more tractable, since it is enough to impose an R-symmetry so that this term is forbidden [13], and therefore can only be generated once one breaks supersymmetry, so its size is controlled by the SUSY breaking dynamics, $\mu \sim m_{soft}$, just like the other mass terms.

The SM possesses some accidental symmetries, like baryon or lepton number. They are there for the trivial reason that there are no terms in the SM that break them, and have no deeper origin. Therefore, by extending the SM, the new sector will break those accidental symmetries unless some structure is imposed. In the case of SUSY, the squarks and sleptons generate dimension 4 operators that mediate proton decay, with a lifetime of a fraction of a second [14, 15]. An attitude towards this phenomenological disaster is that it is not a failure, but an opportunity to learn about the symmetries of the UV theory. If one imposes an R parity that depends on the spin s of the particle as $(-1)^{3B-L+2s}$, all SM particles have R parity 1 while the superpartners have R parity -1. This forbids the terms that generate proton decay, but at the same time one makes the lightest supersymmetric partner (LSP) stable. Quite remarkably, if one computes the relic density of this LSP, and assuming it has electroweak interactions with the SM particles and a mass around the electroweak scale, it matches with the amount of dark matter (DM) observed. Also, extrapolating this description of Nature up to large scales is not only consistent, but it gives a precise unification of the gauge couplings at the GUT scale. It is hard to imagine a stronger evidence that one is in the right track, the amount of *human input* is minimal, and the whole construction has a feeling to it that it was there at plain sight, waiting for physicists to be discovered, very much in perfect analogy with Dirac and the doubling of the world in matter and antimatter.

In the most naive SUSY spectrum, the masses of the particles are dictated by RGEs, therefore, particles with large couplings like gluinos and squarks are at the top of the spectrum and the sleptons and neutralinos are at the bottom. The mass of the lightest Higgs, at tree level, is famously bounded to be below the Z boson mass,

$$m_H < m_Z |\cos 2\beta|, \tag{1.1}$$

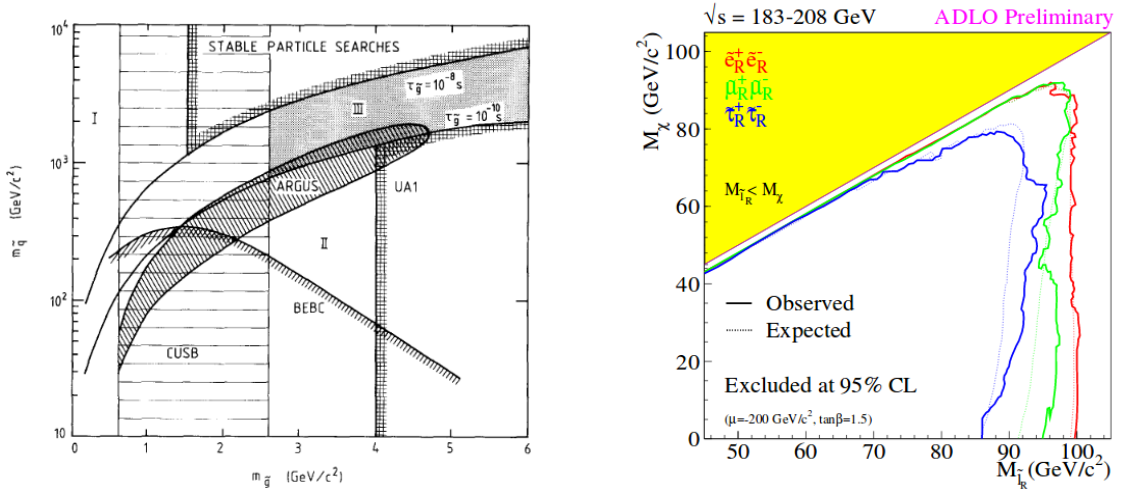


Figure 1.1: Left: Exclusion on gluino and squark masses at PETRA, [16] 1987, in a primitive split SUSY scenario. Right: Exclusion on neutralino and slepton at LEP [17]

with $\beta = \tan^{-1} v_u/v_d$ being the angle parametrizing the ratio of the vevs of the two Higgs doublets. This upper bound on the Higgs boson mass implies that in the naive picture the Z boson is at the top, with the gluinos and squarks, with the Higgs lying safely below the Z mass. This, even before LEP, already clashed with experiment. PETRA set constraints on superpartners at around $\sim 40\text{GeV}$ for the selectron and neutralino, and also on gluinos, see Figure 1.1. In the seminal paper by R. Barbieri and G.F. Giudice in '88 [18], they wrote “A seemingly embarrassing point when one starts to talk about supersymmetry is the fact that, among all known particles, not even one (broken) boson-fermion supermultiplet can as yet be reconstructed”.

Another piece of tension with the experiment came gradually from indirect probes. As we stressed, the squarks and sleptons tend to break some global symmetries of the SM, generating large contributions to the electron EDM or flavor violating processes. Like previously we did with proton decay and the introduction of R parity, we can take this as hints for an organizing principle that allows us to understand how SUSY is broken at high energies, and understanding why SUSY preserves flavor and CP might shed light to the CKM structure.

But the second strike came with LEP, finding the Z boson and nothing else below 114 GeV, neither Higgs boson nor neutralinos [19]. This put the first real question mark on the idea of naturalness, since in order to rise the tree level Higgs mass one must have large logs of the stop mass, so a fairly heavy stop is required, entering in the fine tuned regime.

SUSY was not the only LEP's victim. Precision measurements of the electroweak gauge bosons interactions set strong constraints on the so called S and T parameters, that describe in a model independent way the possible deviations in the two point function of the electroweak gauge bosons [20, 21]. The data revealed that those corrections should be smaller than one part per mille, which put into question the technicolor proposal for the generation of the electroweak scale, where a condensate of some heavy quark pair $\langle Q\bar{Q} \rangle$ induced by a new strong force is identified with the electroweak scale v [22, 23]. Those theories generically predict a large S and T parameters.

The T parameter is specially interesting, since it signals the discovery of another global symmetry of the SM, the custodial symmetry, which is tested at the per mille level. Like flavour in the quark sector, custodial symmetry is just an accidental symmetry in the electroweak sector relating the W mass and the Z mass via $m_W = \cos \theta_W m_Z$, where θ_W is the Weinberg angle, given by the ratio of the $U(1)_Y$ and $SU(2)$ couplings g'/g . Like before with baryon conservation and R parity, one can treat this accidental symmetry as a hint towards the structure of the UV theory. One can imagine that the strong sector has a global symmetry \mathcal{G} , broken down to \mathcal{H} via strong interactions. Then, if the custodial symmetry is identified with \mathcal{H} (or a subgroup of it), the Higgs doublet will be a goldstone boson of this new strong sector [24, 25]. The Higgs potential can be generated by explicitly breaking the global symmetry by weak and strong interactions. This idea introduces the goldstone scale f , which one would expect it to be $f \sim v$. However, electroweak precision measurements already indicated a mild tuning $v^2/f^2 \leq 0.1$, and forced the strong sector resonances to lie above ~ 3 TeV.

The third strike came with the LHC data. The apparent confirmation of a mass gap above the electroweak scale corroborates the indirect hints by LEP, and the fine tuning of the electroweak scale is an unavoidable fact. Our job now is to discover *how much* fine tuning. But, most importantly, *why*.

In '89 Weinberg [26] argued that, if the cosmological constant was larger than the constraints at that time, the universe would have entered in a period of acceleration that would not have allowed galaxies and complex structures to form. A few years after [27, 28], a nonvanishing cosmological constant was found where Weinberg's anthropic argument predicted it to be, 120 orders of magnitude smaller than what the naive expectation is [29]. A crucial ingredient for the anthropic argument to work is to have a set of universes and populate them all, and only then one can understand why the observers lie in the ones with a small cosmological constant. In an accurate analogy, one can explain anthropically the Earth-Sun distance not only by observing that it is the right distance

to form life, but that there are other solar systems with many planets. With only one solar system, the position of the Earth would appear extremely fine tuned. But, how do we get 10^{120} universes?

String theory provided the solution. Since the theory lives naturally in 10 or 11 spacetime dimensions, one has to compactify the rest to get down to four. The number of different compactifications is extremely large, each one determining a completely different low energy field theory. On top of it, each compactification has between 10 and 100 moduli fields that parametrize deformations of the compactification. After stabilizing those fields, one ends up with a scalar potential with a very large number of minima. It was estimated that string theory contains the order of $10^{\mathcal{O}(100)}$ vacua [30]. Therefore, it seems that our best candidate for a complete description of gravity automatically incorporates this large number of vacua.

The success of the anthropic argument for the cosmological constant might imply the ultimate Copernican twist, relegating our vacuum to be just one among many. So, it is the end of the reductionism attitude and a deeper explanation for the value of the cosmological constant cannot be obtained. Even if the value of the cosmological constant can be computed from first principles, we would need an extreme precision on the fundamental parameters to be able to check whether it is right or not. It is not a failure of physics, in the same way that it is not a failure not being able to compute the Earth-Sun distance from first principles. It is just the wrong question to ask.

What hunts particle physicists at night is the idea that the electroweak scale has a similar anthropic origin. There is some evidence that slight changes in the masses of the electron and light quarks, that ultimately depend on the Higgs vev, can have a drastic impact on the nucleosynthesis and chemistry [31,32]. However, there is a major difference between the cosmological constant and the electroweak scale, since while we know how to make the latter natural, we are clueless about the former. On top of this, while the cosmological constant is unique, the electroweak scale is just a feature of a particular model, and one might imagine ways to generate complex structures without it [33].

So, if we forget about a purely anthropic explanation of the electroweak scale, what is data telling us? It seems that a meso-tuned scenario might be the answer. The most famous example is split supersymmetry, where one embraces the fine tuning and pushes the scalar quarks to the hundreds of TeV, while keeping the neutralinos at the TeV scale. This spectrum, while fine tuned, reconciles the positive hints for SUSY (GUT, dark matter) with the experimental results (no violation of global symmetries of SM,

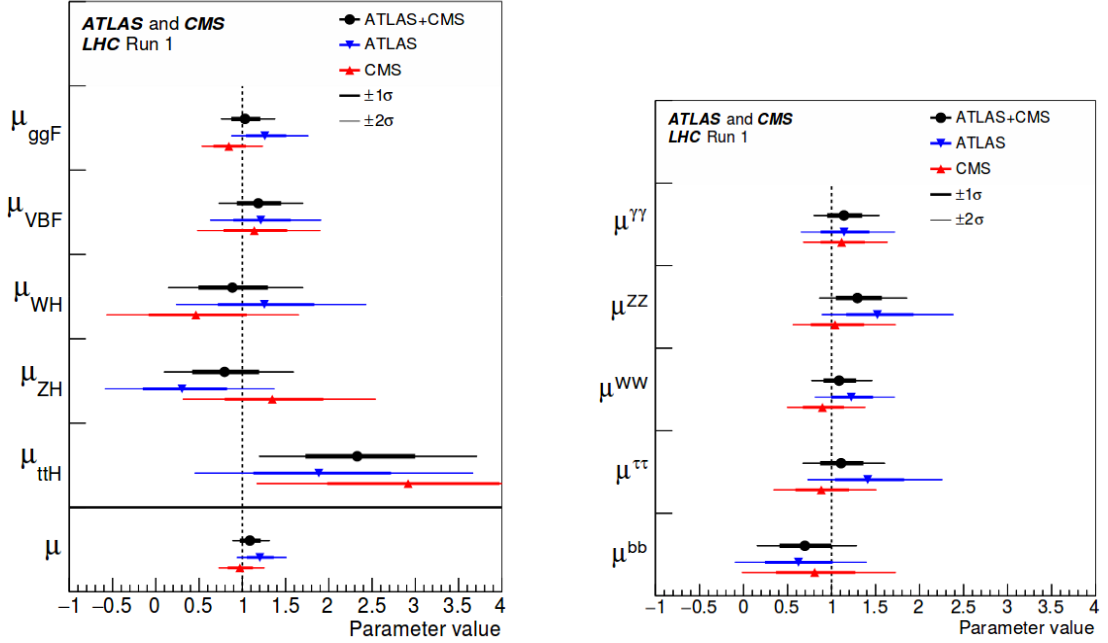


Figure 1.2: Global combination of the Run 1 data by the ATLAS and CMS collaborations [35] for the signal strengths of the Higgs production (left) and decay (right) modes.

direct constraints, large Higgs mass). Still, the question of *why* remains. An example of what might be going is found in [34], where a SUSY model with R parity violation is presented, that generates the baryon asymmetry via decays of a bino, which has to be sufficiently heavy to generate the necessary amount of asymmetry. Therefore, in this setup one can have an unnatural universe with matter in it, or a beautifully natural one with no one there to see.

In the search for answers the study of the Higgs boson will play a central role. Already its mass gives important constraints for UV completions. It tells us that superpartners must be heavy in order to lift it in supersymmetric theories, while it forces composite top partners to be light in order to generate a mass light enough in composite theories. It is amusing that the Higgs mass is precisely in the middle point where both descriptions are uncomfortably valid.

One of the most distinct characteristics of a SM Higgs is that its couplings are totally determined and are proportional to the masses of the particles it couples to. Therefore, any deviation from this behavior will signal a departure from the way the SM parametrizes the electroweak symmetry breaking dynamics. So far, ATLAS and CMS analyses [35] show an overall agreement with the SM expectations, see Figure 1.2. However, the Higgs boson couplings are currently only determined at the $\sim 20\%$ accuracy

at most, so large deviations are still allowed.

A particularly interesting property of the Higgs boson is that, unlike any other SM particle, it interacts with itself.¹ This self interaction is determined by the shape of the potential, so its measurement is a direct probe of the structure of our vacuum. However, its measurement is specially elusive experimentally, since it requires the observation of double Higgs production, which is quite challenging at the LHC due to the small cross section and the small branching ratios of the clean channels. In [chapter 3](#), based on [36], we will explore how single Higgs production might help on its determination.

The LHC will only be sensitive to deviation on the Higgs couplings of the order of a few per cent at most. To really push forward a precision program on its couplings, future lepton machines are required. Those colliders will be able to explore the Higgs properties up to an extreme accuracy. In [chapter 4](#), based on [37], we will present the synergy between the measurements of single and double Higgs production in future lepton machines.

An important consequence of a Higgs of 125 GeV is that the electroweak phase transition in the SM is a smooth crossover of second order. Therefore, it fails to generate a strong first order phase transition that would provide a context for electroweak baryogenesis to take place and explain the matter-antimatter asymmetry. The most simple way to address this is to extend the SM potential with a scalar singlet. Since it has to modify the SM potential sufficiently, the singlet cannot be arbitrarily heavy or arbitrarily decoupled, so it has to leave an imprint. However, it can be very challenging to hunt it down at the LHC, and in [chapter 5](#), based on [38], we will study whether the interference with the background when the heavy singlet decays into a Higgs pair can lift the discriminating power of the analysis.

Other key players in the description of electroweak symmetry breaking are obviously the Goldstone bosons that generate the longitudinal polarization of the massive gauge bosons. It is possible to test their interactions by studying diboson production at high energies. In [chapter 6](#), based on an unpublished work with C. Grojean and M. Montull, we discuss the different operators that can be probed in diboson, and their interplay among other experiments.

The success of the SM in describing flavour data is particularly remarkable. The global symmetries of the SM are uncontested so far, and testing them provides low energy probes of very high energy phenomena if those symmetries are broken in the

¹Both graviton and gluons change helicity.

UV. For example, the SM the electron to have a CP violating electric dipole moment (EDM) vanishingly small, and since any generic new physics scenario will generate a contribution, the electron EDM sets strong requirements to the new CP phases. In [chapter 7](#), based on [39], we will explore this in the context of composite Higgs scenarios, and show the interplay between the high precision probes and the direct searches of composite top partners.

In summary, there is an important conclusion to be made: the origin of the electroweak scale is the pillar of our understanding of the universe, and its exploration is now more crucial and challenging than ever. Hints towards the underlying structure will almost certainly come in tiny fragments, and gluing them will require a global effort across multiple fields.

The unreasonable success of the SM should remind everyone about the unreasonable success of Maxwell's electrodynamics at the end of the XIX century. The connections between the Higgs hierarchy problem and the electron's own hierarchy problem is certainly suited. It is worth to keep always in mind that the solution for the latter, which was the combination of special relativity and quantum mechanics to generate the electron-positron pairs that convert the linear $1/r$ UV divergence into a logarithmic one, went far beyond what human imagination was capable of.

"Physics thrives on crisis. We all recall the great progress made while finding a way out of various crises of the past: the failure to detect a motion of the Earth through the ether, the discovery of the continuous spectrum of the beta decay, the $\tau - \theta$ problem, the ultraviolet divergences in electromagnetic and then in weak interactions, and so on. Unfortunately, we have run out short of crises lately. The "standard model" of electroweak and strong interactions currently faces neither internal inconsistencies nor conflicts with experiment. It has plenty of loose ends; we know no reason why the quarks and leptons have the masses they have, but then we know no reason why they should not."

Steven Weinberg, [26]

Chapter 2

Future colliders

By the time of writing, the LHC has just restarted the collision period for 2018. It is expected to accumulate 60 fb^{-1} of data, slightly more than what the 50 fb^{-1} collected in 2017, which was already a fantastic year in this regard. After this, in 2019 the machine will enter in the second long shutdown for two years, and restart the collisions in 2021 at 14 TeV of center of mass energy and will collect data until end of 2023. The goal is that by the end of Run 3 a total of 300 fb^{-1} will be collected. Then the experiment will enter in the third long shutdown that will last until 2026. After the maintenance and upgrade period, the LHC will enter in the High Luminosity phase, where it is expected that an improvement of the quality of the beam will multiply the instantaneous luminosity by a factor of 5 to 7. This is achieved by increasing the number of protons per bunch from 1.15 at the LHC to 2.2 at the HL-LHC and by reducing the beam size by a factor 0.4. This improvement of the luminosity will come at the price of increasing the pileup, i.e. the number of collisions per bunch crossing, by a factor of 5-7 as well. This will lead to a total of 3 fb^{-1} of total integrated luminosity by the end of 2035.

There are many proposals on the table on how to keep exploring high energy particle physics. It is expected that in a short timescale the final decision on some of those projects will be taken. The reason is simple: if we want the field of particle physics to keep moving beyond the LHC reach without a large gap between the end of it and the start of the new machine, we need the new collider running by 2035. Since the construction and setup time for those machines can easily span 10-15 years at least, it is already an urgent matter to take a decision.

In the following we will shortly discuss the different options. The final goal would be to build a large circular proton proton collider with a perimeter of around 100km and with a center of mass energy of around 100TeV. There are two proposals to build it, in Europe and China, called Future Circular Collider (FCC) and Super Proton Proton

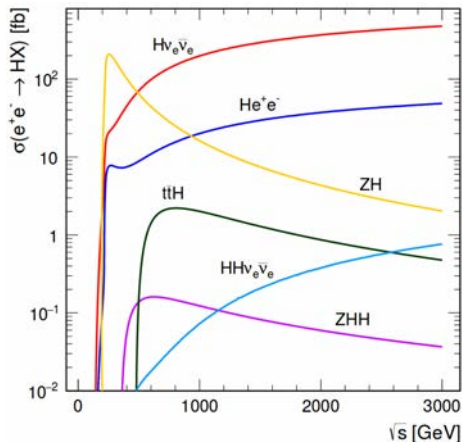


Figure 2.1: Single and double Higgs production cross sections in an e^+e^- collider as a function of the center of mass energy of the collider. Plot taken from [43]

Collider (SppC) respectively. This machine will have a mass reach roughly an order of magnitude larger than the LHC. As a benchmark, while the HL-LHC will be sensitive to gluinos up to 2.5TeV, a 100TeV collider will reach 14TeV of mass for gluinos (see e.g. [40, 41]). Regarding Higgs physics, there are many new interesting avenues opening up at such large energies. Dihiggs production could be measured precisely, reaching a precision of 5% on the determination of the Higgs self coupling [42]. Also, gluon fusion will produce Higgs bosons with a transverse momentum in the multi-TeV range, exploring the hgg coupling significantly away from the Higgs pole.

The construction in China might have an advantage with respect the FCC in Switzerland due to the lower cost of the civil construction. These high energy proton proton machines could easily cost 30B\$. A part of it is mainly due to the requirement of having 16T superconducting magnets, which might be one of the main challenges. 11-12T superconducting magnets are ready to be mass produced for the HL-LHC, but reaching mass production of 16T magnets might only be archived by 2035. The first 15T prototype is being currently constructed Fermilab and expected to be tested in this year (see the recent HL/HE LHC meeting held in Fermilab [44] and talks within). See Ref [45] for an overview on the challenges for the future hadron colliders.

A 100TeV machine is clearly the perfect option to continue the exploration of high energy physics, but they might only be constructed in a far future. Actually, in the same way that LEP preceded the LHC by using the same tunnel with electron positron collisions, the FCC and SppC are expected to be preceded by FCC-ee and CEPC (Circular Electron Positron Collider) respectively. Both machines are planned to collect about 5/ab at an energy of 240GeV [46, 47]. This center of mass energy maximizes the $e^+e^- \rightarrow Zh$

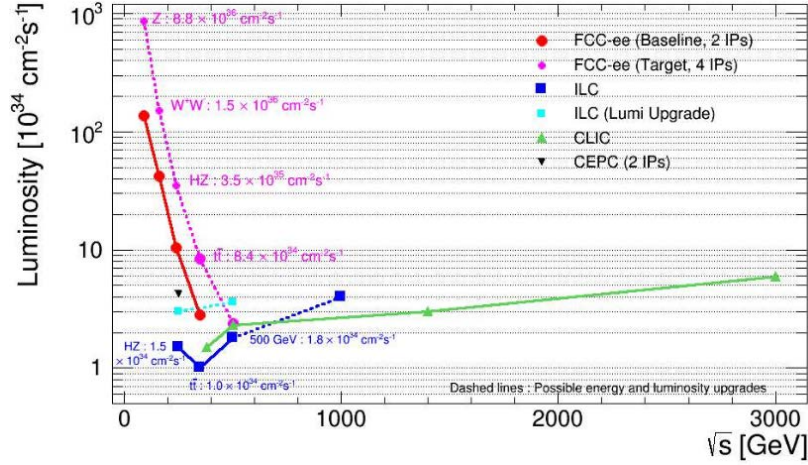


Figure 2.2: Comparison between different lepton colliders in terms of the center of mass energy and the luminosity. Figure taken from [49]

cross section, allowing for sub-% precision on the determination of Higgs couplings, see [48]. While CEPC does not officially contemplate another leptonic run, the FCC-ee program includes a run at 350-365 GeV to collect around 1.5/ab of data, used to improve the precision on top quark physics. Even if the cross section for $e^+e^- \rightarrow \nu\bar{\nu}h$ increases from 240 to 350 GeV while Zh decreases, the latter is still the dominant production mode. Even if the total Higgs production rate is reduced, probing the Higgs couplings at different energies helps to resolve degeneracies among EFT coefficients and provides an important discriminator for a model independent analysis, as we will show in Chapter 4, see also [48]. A possible additional run at 90 GeV with a very large integrated luminosity of $\sim 150/\text{ab}$ would be very relevant to improve the precision on the SM input parameters.

The most optimistic time scale for the FCC contemplates the start of its construction by 2025 and 10 years of construction, with FCC-ee running by 2035, nicely overlapping with the end of the HL-LHC. The time scales for the CEPC/SppC can be accelerated, with a construction stage lasting only 6 years, and possibly starting the lepton collisions before 2030. The cost of both CEPC and FCC-ee can be roughly estimated to be around 10B\$, similar to the LHC cost [50].

The circular lepton colliders provide a very large luminosity output and a relatively low center of mass energy. The large luminosity is archived by the recycling of the beam by going around the collider many times. The synchrotron radiation scales as $\propto \gamma^4/R^2$, where R is the radius of the collider and $\gamma = E/m$ is the Lorentz factor of the particle being accelerated, with E and m being its energy and its mass. Therefore, the scaling

with the fourth power makes exponentially costly to increase the energy of the electrons. While accelerating protons alleviates this effect by a $(m_e/m_p)^4 \sim 10^{-9}$ factor, another option is to build a linear lepton collider.

A linear lepton collider has the advantage over a circular one that the center of mass energy reached can be much larger. A proposal that is currently in advanced stages is the ILC (International Linear Collider), planned to be build in Japan. The program is to accumulate $2/\text{ab}$ at 250GeV for the Zh process, then make a short run of $200/\text{fb}$ at 350GeV to improve the top couplings, and then collect $4/\text{ab}$ at 500GeV , just at the $t\bar{t}h$ threshold.

The polarization of the electron and positron beams in a lepton collider plays a crucial role due to the chiral nature of the electroweak sector [51]. The polarization of the beam is defined as the relative abundance of left and right handed electrons

$$P = \frac{N_R - N_L}{N_R + N_L} \quad (2.1)$$

where $N_{L,R}$ is the number of left and right handed particles. A 100% purity in the beam is not achievable, and the standard numbers for the beam polarizations are ± 0.8 for the electrons and ± 0.3 for the positrons [52]. The luminosities discussed above are shared between left handed polarizations ($P(e^-, e^+) = (-0.8, +0.3)$), which maximizes the Zh cross section, and right handed polarizations ($P(e^-, e^+) = (+0.8, -0.3)$) [53, 54]. However, investing 5% of the luminosity into same sign polarizations might be useful for new physics searches.

The ILC 500GeV run will be able to measure the process $e^+e^- \rightarrow t\bar{t}h$ with a 8% precision, which translates into a 5% precision on the top yukawa coupling [48]. This is very important measurement since the top quark plays a special role in many BSM scenarios due to its large mass, and because the limited precision that can be reached at LHC.

The construction of the ILC might start in a few years timescale if the project is approved before 2018. This would mean that the ILC might start running before 2030, overlapping with the HL-LHC phase. This would certainly have a huge positive impact in the field, with two machines running simultaneously and exploring the physics landscape from a different but complementary perspectives. The ILC program is expected to last 20 years, being a perfect bridge that connects the LHC with the future hadron collider.

The ILC might receive an upgrade to reach the 1TeV center of mass energy. Its acceleration technology is based on superconducting radio frequency cavities, which is

well understood. The energy range of linear colliders might be extended to the multi-TeV regime, which is the objective for the Compact Linear Collider (CLIC), proposed to be build at CERN [55], that would reach energies of 3TeV. It is projected to be running by 2035, matching with the end of the HL-LHC phase. The timescale coincides with the possible construction of the FCC at CERN, so it is perhaps doubtful to expect both of them to be build.

At 3TeV of center of mass, the Higgs production is dominated by W boson fusion is the process $e^+e^- \rightarrow \nu\bar{\nu}h$, due to the t -channel momenta exchange of the W bosons, and the $1/s$ suppression for the Zh production. The double Higgs production via $e^+e^- \rightarrow \nu\bar{\nu}hh$ has a cross section of roughly 1fb, which will allow to determine the self coupling of the Higgs to high precision, as we will thoroughly explore in the following chapters.

Going back to hadron colliders, the option of the High Energy LHC (HE-LHC) is gaining more consideration. In this upgrade the LHC magnets would be replaced by the 16T superconducting magnets designed for the SppC/FCC, reaching 27TeV ($= 14 \text{ TeV} \times 16 \text{ T} / 8.33 \text{ T}$) of center of mass energy. This has the same challenges as obtaining the magnets for SppC/FCC, the main advantage being that it is expected to be rather affordable, costing around 5B\$, a factor 6 less than the SppC/FCC, and would extend the LHC's lifetime.

Some searches depend crucially on the luminosity accumulated, but the most basic BSM searches only rely on the mass reach, so the HL-LHC will not be able to improve substantially. The factor 2 in the mass reach for new phenomena in the HE-LHC with respect the HL-LHC will bring new clues for the understanding of the electroweak scale. This will be exemplified with a simple model in [chapter 5](#).

In the far future, there are some speculative ideas on how to continue the exploration of high energy physics. An old idea is to build a muon collider. Due to the larger mass, the energy reach can be much larger than an electron collider, but the finite lifetime poses important difficulties. On the other hand, recent rapid progress in advanced accelerator techniques give hope for a real breakthrough in linear electron colliders that might substantially rise the energy reached. The option of a 30TeV electron positron collider was recently discussed in [56], see the talks within. There are still many challenges to be overcome in such project. To give only one example, a useful particle physics collider requires large enough luminosity, which translates into a high energetic beam of electrons and it is not clear how the plasma in a weak field accelerator behaves under

	Region	type	\sqrt{s} [TeV]	\mathcal{L} [ab ⁻¹]	construction	running
HL-LHC	CERN	pp	13	3	-	2025-2030
ILC	Japan	e^+e^-	0.25/0.35/0.5	2/0.2/4	2019-2029	2030 - 2050
CEPC	China	e^+e^-	0.24	5	2022 - 2027	2027-2037
SppC	China	pp	100	10-20	2038 - 2045	2045 - 2060
CLIC	CERN	e^+e^-	0.35/1.4/3	0.5/1.5/2	2025-2035	2035-2055
FCC-ee	CERN	e^+e^-	0.24/0.36	5/1.5	2025-2035 (?)	2035-2055 (?)
FCC-hh	CERN	pp	100	10-20	2055-?	?
μ -collider	?	$\mu^+\mu^-$	10-30 (?)	?	203X-?	?
ALIC	?	e^+e^- ?	10-50 ?	??	203X-?	?

Table 2.1: Summary of the different colliders under development

such extreme conditions. A study on the viability of such program is currently under way, and a document is planned to be released by the end of this year.

The long term future of high energy particle physics is going to be decided in the forthcoming years. Pushing the high energy frontier has proven to be the most efficient way to explore how Nature works, it has inspired around 30% of physicists and physics research, and has contributed to a Nobel prize every 2.9 years [57]. It has been like this in the past, and we should push forward to continue like this in the future.

Chapter 3

A global view on the Higgs self-coupling

3.1 Introduction

It should not be forgotten that the LHC is more than a discovery machine. It can also be used for precision measurements giving an extra handle to reveal the existence of new physics. In this roadmap, the acclaimed Higgs boson plays a central role: with all its couplings uniquely predicted in the Standard Model (SM), it is the new metronome that can serve to quantify the accuracy of the SM description of our world. Major efforts have been devoted first to provide consistent theoretical frameworks to deform the SM Higgs couplings in a way as model independent as possible, and second to pin down or at least bound these deformations using the experimental data (see for instance refs. [58, 59]). A quantity of particular interest but notoriously intangible is the Higgs cubic self-interaction. It is even often said that the value of this coupling is a key to check the electroweak symmetry breaking. Indeed, the SM Higgs potential, is given after breaking by

$$\mathcal{L} \supset -\frac{m_h^2}{2}h^2 - \lambda_3^{SM}vh^3 - \lambda_4^{SM}h^4, \quad (3.1)$$

$$\lambda_3^{SM} = \frac{m_h^2}{2v^2}, \quad \lambda_4^{SM} = \frac{m_h^2}{8v^2}, \quad (3.2)$$

where the Higgs vacuum expectation value (VEV) $v \simeq 246$ GeV can be related to the Fermi constant and measured in muon decay, and m_h is precisely determined by fitting a bump in the di-photon and the four-lepton decay channels. And measuring λ_3 is a good way to check that electroweak symmetry breaking (EWSB) follows from a simple Ginzburg–Landau ϕ^4 potential. Moreover many different Beyond the Standard Model

(BSM) scenarios allow large deviations for the Higgs self-couplings (see for instance ref. [58]), and measuring λ_3 could be a way to probe the existence of new physics.

Until recently, the main approach to constrain the Higgs cubic self-coupling (the quartic is likely to remain impalpable before long) was relying on the measurement of the double Higgs production rate that directly depends, at leading order (LO), on the value of λ_3 . This measurement is, however, complicated by the low cross section as well as the small decay fractions in the channels that can compete against the ever annoying dominant QCD background. And the sensitivity remains frustrating low. A few years ago, ref. [60] proposed to measure/constrain the Higgs cubic self-coupling at e^+e^- colliders via the quantum corrections it induces in single Higgs channels. Recently this idea has been revisited at hadronic machines by refs. [61–63], which concluded that potentially this approach could be complementary if not competitive or even superior to the traditional strategy. This idea has also been further extended to bound the Higgs self-coupling deviations using EW precision measurements [64,65] with the conclusion again that competitive results can be derived. Such dramatically optimistic conclusions deserve to be scrutinized and disputed. First it should be noted that those analyses look at scenarios where only the Higgs self-coupling deviates from the SM. After understanding which particular UV dynamics would fulfill this assumption, one should question the robustness of their conclusions under less restrictive hypotheses. A corollary question is also to understand to which extend the traditional and simple fits of the single Higgs couplings, that were neglecting the effects of the Higgs trilinear, could get distorted. Truly model-independent bounds on the Higgs couplings cannot be obtained. It is of the uttermost importance to be alerted on the sometimes hidden dynamical assumptions sustaining the bounds derived from a particular fit. And be aware of the classes of models these bounds safely apply to.

Even in models where the Higgs self-coupling receives a correction parametrically enhanced compared to the deviations of the other Higgs couplings, a careful multi-dimensional analysis is in order. Indeed, even loop suppressed deviations to couplings to gauge bosons or fermions will affect at LO single Higgs processes, whereas the Higgs trilinear coupling enters at next-to-leading order (NLO). So both effect can typically be of the same order. And to set bounds on each coupling deviation, a complete and global fit is needed. This is the main question we address in this chapter. We first notice that a fit to the inclusive single Higgs observables alone suffers from a blind direction and that it is not possible to bound individually each of the coupling nor to extract any information on the Higgs trilinear interaction. We advocate that extra observables are needed to resolve this degeneracy. We first focus our attention to the benefit of

including information on the double Higgs production channels. We then explore the use of differential kinematic distributions in single Higgs processes and we conclude that it is a promising idea that however requires a realistic and detailed estimate of the systematic uncertainties. However, we caution that in scenarios that produce enhanced deviations in the Higgs self-couplings, one should also pay particular attention to the constraints imposed by electroweak precision measurements that could be, for Higgs physics, far less restrictive than in generic BSM models, requiring an even more global fit of Higgs and EW data together.

3.2 The effective parametrization

3.2.1 Higgs primary couplings

In a large class of scenarios, if a sizable gap is present between the SM states and the mass scale of the BSM dynamics, the new-physics effects can be conveniently encapsulated into an EFT framework. The EFT operators can be organized according to their canonical dimension, thus expanding the effective Lagrangian into a series

$$\mathcal{L} = \mathcal{L}_{\text{sm}} + \sum_i \frac{c_i^{(6)}}{\Lambda^2} \mathcal{O}_i^{(6)} + \sum_i \frac{c_i^{(8)}}{\Lambda^4} \mathcal{O}_i^{(8)} + \dots, \quad (3.3)$$

where \mathcal{L}_{sm} is the SM Lagrangian, $\mathcal{O}_i^{(D)}$ denote operators of dimension D and Λ is the SM cut-off, i.e. the scale at which the new dynamics is present.¹

The leading new-physics effects are usually associated with EFT operators with the lowest dimensionality, namely the dimension-6 ones. In the following we restrict our attention to these operators and neglect higher-order effects. To further simplify our analysis we also assume that the new physics is CP-preserving and flavor universal. With these restrictions we are left with 10 independent operators that affect Higgs physics at leading order and have not been tested below the % accuracy in existing precision measurements [66].²

Before discussing our operator basis, it is important to mention that a much larger set of dimension-6 operators could in principle be relevant for Higgs physics. A first class of these operators include deformations of the SM Lagrangian involving the light

¹In the above expansion we neglected operators with odd energy dimension since they violate lepton number conservation (for $D = 5$) and $B - L$ invariance (for all odd D). These effects are constrained to be extremely small and do not play any role in our analysis.

²The assumption of flavor universality is not crucial for our analysis. It is only introduced to restrict the EFT analysis to the operators that can only be tested in Higgs physics. The same can be done in several other flavor scenarios, as for instance minimal flavor violation and anarchic partial compositeness.

SM fermions. They correct at tree level the Higgs processes but also affect observables not involving the Higgs. Therefore most of them have already been tested with good precision in EW measurements. A second set of dimension-6 operators involve the top quark and are typically much less constrained. However they affect Higgs physics only at loop level, thus their effects are usually not very large. We postpone a more detailed discussion to [subsection 3.2.2](#).

A convenient choice for dimension-6 operators is provided by the ‘‘Higgs basis’’ [59, 67] in which the Higgs is assumed to be part of an $SU(2)_L$ doublet and operators connected to the LHC Higgs searches are separated from the others that can be tested in observables not involving the Higgs.³ The 10 effective operators we will focus on can be split into three classes: the first one contains deformations of the Higgs couplings to the SM gauge bosons, parametrized by

$$\delta c_z, c_{zz}, c_{z\Box}, \hat{c}_{z\gamma}, \hat{c}_{\gamma\gamma}, \hat{c}_{gg}, \quad (3.4)$$

the second class is related to deformations of the fermion Yukawa’s

$$\delta y_t, \delta y_b, \delta y_\tau, \quad (3.5)$$

and finally the last effect is a distortion of the Higgs trilinear self-coupling

$$\kappa_\lambda. \quad (3.6)$$

The corresponding corrections to the Higgs interactions in the unitary gauge are given by

$$\begin{aligned} \mathcal{L} \supset & \frac{h}{v} \left[\delta c_w \frac{g^2 v^2}{2} W_\mu^+ W^{-\mu} + \delta c_z \frac{(g^2 + g'^2) v^2}{4} Z_\mu Z^\mu \right. \\ & + c_{ww} \frac{g^2}{2} W_{\mu\nu}^+ W^{-\mu\nu} + c_{w\Box} g^2 (W_\mu^- \partial_\nu W^{+\mu\nu} + \text{h.c.}) + \hat{c}_{\gamma\gamma} \frac{e^2}{4\pi^2} A_{\mu\nu} A^{\mu\nu} \\ & \left. + c_{zz} \frac{g^2 + g'^2}{4} Z_{\mu\nu} Z^{\mu\nu} + \hat{c}_{z\gamma} \frac{e\sqrt{g^2 + g'^2}}{2\pi^2} Z_{\mu\nu} A^{\mu\nu} + c_{z\Box} g^2 Z_\mu \partial_\nu Z^{\mu\nu} + c_{\gamma\Box} g g' Z_\mu \partial_\nu A^{\mu\nu} \right] \\ & + \frac{g_s^2}{48\pi^2} \left(\hat{c}_{gg} \frac{h}{v} + \hat{c}_{gg}^{(2)} \frac{h^2}{2v^2} \right) G_{\mu\nu} G^{\mu\nu} - \sum_f \left[m_f \left(\delta y_f \frac{h}{v} + \delta y_f^{(2)} \frac{h^2}{2v^2} \right) \bar{f}_R f_L + \text{h.c.} \right] \\ & - (\kappa_\lambda - 1) \lambda_3^{SM} v h^3, \quad (3.7) \end{aligned}$$

³For the relation between the independent couplings in the Higgs basis and the Wilson coefficients of other operator bases, see [67].

where the parameters δc_w , c_{ww} , $c_{w\Box}$, $c_{\gamma\Box}$, $\hat{c}_{gg}^{(2)}$ and $\delta y_f^{(2)}$ are dependent quantities, defined as

$$\begin{aligned}
\delta c_w &= \delta c_z, \\
c_{ww} &= c_{zz} + 2 \frac{g'^2}{\pi^2(g^2 + g'^2)} \hat{c}_{z\gamma} + \frac{g'^4}{\pi^2(g^2 + g'^2)^2} \hat{c}_{\gamma\gamma}, \\
c_{w\Box} &= \frac{1}{g^2 - g'^2} \left[g^2 c_{z\Box} + g'^2 c_{zz} - e^2 \frac{g'^2}{\pi^2(g^2 + g'^2)} \hat{c}_{\gamma\gamma} - (g^2 - g'^2) \frac{g'^2}{\pi^2(g^2 + g'^2)} \hat{c}_{z\gamma} \right], \\
c_{\gamma\Box} &= \frac{1}{g^2 - g'^2} \left[2g^2 c_{z\Box} + (g^2 + g'^2) c_{zz} - \frac{e^2}{\pi^2} \hat{c}_{\gamma\gamma} - \frac{g^2 - g'^2}{\pi^2} \hat{c}_{z\gamma} \right], \\
\hat{c}_{gg}^{(2)} &= \hat{c}_{gg}, \\
\delta y_f^{(2)} &= 3\delta y_f - \delta c_z.
\end{aligned} \tag{3.8}$$

In the above expressions we denoted by g , g' , g_s the $SU(2)_L$, $U(1)_Y$ and $SU(3)_c$ gauge couplings respectively. The electric charge e is defined by the expression $e = gg' / \sqrt{g^2 + g'^2}$.

Notice that in the Higgs basis the distortion of the trilinear Higgs coupling is encoded in the parameter $\delta\lambda_3$ and denotes an additive shift in the coupling, $\mathcal{L}_{\text{self}} \supset -(\lambda_3^{SM} + \delta\lambda_3)vh^3$. In our notation κ_λ denotes instead a rescaling of the Higgs trilinear coupling, as specified in Equation 3.7. We use this modified notation in order to make contact with previous literature discussing the measurement of the Higgs self-coupling.

In Equation 3.7 and Equation 3.8 we also used a non-standard normalization for the \hat{c}_{gg} , $\hat{c}_{\gamma\gamma}$ and $\hat{c}_{z\gamma}$ parameters. The contact Higgs coupling to gluons has been normalized to the LO top loop prediction in the SM computed in the infinite m_t limit, whereas we included an additional factor $1/\pi^2$ in the couplings $\hat{c}_{\gamma\gamma}$ and $\hat{c}_{z\gamma}$. The relation with the standard normalization of ref. [59] is given by

$$c_{gg} = \frac{1}{12\pi^2} \hat{c}_{gg} \simeq 0.00844 \hat{c}_{gg}, \quad c_{\gamma\gamma} = \frac{1}{\pi^2} \hat{c}_{\gamma\gamma} \simeq 0.101 \hat{c}_{\gamma\gamma}, \quad c_{z\gamma} = \frac{1}{\pi^2} \hat{c}_{z\gamma} \simeq 0.101 \hat{c}_{z\gamma}. \tag{3.9}$$

With these normalizations values of order one for \hat{c}_{gg} , $\hat{c}_{\gamma\gamma}$ and $\hat{c}_{z\gamma}$ correspond to BSM contributions of the same order of the SM gluon fusion amplitude and of the $H \rightarrow \gamma\gamma$ and $H \rightarrow Z\gamma$ partial widths.

Since our analysis takes into account NLO corrections to the single-Higgs production and decay rates, it is important to discuss the issue of renormalizability in our EFT setup. In general, when we deform the SM Lagrangian with higher-dimensional operators, a careful renormalization procedure is needed when computing effects beyond the LO. However, as discussed in ref. [62], if we are only interested in NLO effects induced by

a modified Higgs trilinear self-coupling, no UV divergent contributions are generated. This is a consequence of the fact that the Higgs trilinear coupling does not enter at LO in single-Higgs observables but only starts to contribute at NLO. As far as the modified trilinear is concerned, our setup essentially coincides with that of ref. [62], so we can carry over to our framework their results. We report them in [Appendix A](#) for completeness.

Possible subtleties could instead arise considering the NLO contributions due to deformations of the single-Higgs couplings, since these interactions already enter in the LO contributions. The deviations in single-Higgs couplings, however, are already constrained to be relatively small, and will be tested in the future with a precision of the order of 10% or below. Their contributions at NLO can thus be safely neglected. For this reason we will include their effects only at LO, in which case no subtleties about renormalization arise.

3.2.2 Additional operators contributing to Higgs observables

As we already mentioned, a larger set of dimension-6 operators can in principle affect Higgs observables. We will list them in the following and discuss how they can be constrained through measurements not involving the Higgs.

- *Vertex corrections.* A first class of operators include the vertex corrections mediated by interactions of the form

$$\mathcal{O}_{vert} = (iH^\dagger \overleftrightarrow{D}_\mu H)(\bar{f}\gamma^\mu f), \quad \mathcal{O}_{vert}^{(3)} = (iH^\dagger \sigma^a \overleftrightarrow{D}_\mu H)(\bar{f}\gamma^\mu \sigma^a f). \quad (3.10)$$

They give rise at the same time to deformations of the couplings of the Z and W bosons with the fermions and to $hVff$ contact interactions. Both these effects can modify Higgs physics at tree level. The gauge couplings deformations, for instance, affect the production cross section in vector boson fusion. The $hVff$ vertices, instead, modify the cross section of ZH and WH production and the decay rates in the $h \rightarrow VV^* \rightarrow 4f$ channels.

Under the assumption of flavor universality, all the vertex-correction operators can be constrained at the $10^{-2} - 10^{-3}$ level [68–70]. Even in the high-luminosity LHC phase, Higgs observables will have at least *few* % errors. Vertex corrections in flavor universal theories are thus too small to be probed in Higgs physics and can be safely neglected.

If the assumption of flavor universality is relaxed, larger corrections to specific vertex operators are allowed [69].⁴ The gauge couplings involving leptons are still very well constrained and below detection in Higgs physics. Sizable corrections can instead modify the quark couplings. In particular the couplings involving the first generation quarks can deviate at the level of *few* % and Higgs measurements at the high-luminosity LHC could be sensitive to them. The gauge couplings involving second generation quarks or the bottom are still very well constrained. Finally the couplings involving the top quark are very poorly bounded. In particular the coupling $Z\bar{t}_R t_R$ at present is practically unconstrained, while in the future it could be tested with some accuracy in $t\bar{t}Z$ production.

- *Dipole operators.* A second class of operators that can correct Higgs observables are dipole-like contact interactions of the generic form

$$\mathcal{O}_{dip} = \bar{f} H \sigma_{\mu\nu} T^a f F^{a\mu\nu} . \quad (3.11)$$

These operators induce at the same time dipole interactions of the gauge bosons with the fermions and vertices of the form $h\partial V f f$. The $h\partial V f f$ operators can modify Higgs decays into four fermions. However in this case the dipole contributions do not interfere with the SM amplitudes since they have a different helicity structure. Moreover the experimental bounds on dipole moments put strong constraints on the coefficients of the dipole operators, in particular for the light generation fermions. For these reasons dipole operators can typically be neglected in Higgs physics [66]. A possible exception is the chromomagnetic operator involving the top quark, which can modify the $t\bar{t}H$ production channel. Although in many BSM scenarios this operator is expected to be safely small, the current direct bounds from the $t\bar{t}$ process are relatively weak [71], so that the top dipole operator could still play a role in Higgs physics [72].

- *Four-fermion operators.* A third set of operators that can affect Higgs physics is given by four-fermion interactions. Operators involving light generation fermions and the top quark can correct at tree-level the $t\bar{t}H$ production channel. These effects are suppressed in several BSM scenarios since they would be correlated to 4-fermion interactions involving only light quarks, which are tightly constrained by dijet searches. However the direct bounds on operators involving top quarks, which

⁴In this discussion we do not consider new-physics contributions to the W boson couplings with the right-handed fermions. Contributions induced by these couplings do not interfere with the SM amplitudes and are thus typically too small to play any significant role.

can be tested in $t\bar{t}$ production, are not strong enough yet to forbid non-negligible effects in Higgs physics.⁵

On the other hand, 4-fermion operators involving only third generation fermions do not modify Higgs observables at tree-level, but can induce loop corrections. Obviously the loop factor gives a strong suppression for these effects. Nevertheless four-fermion operators involving the top quark are poorly constrained at present, so that large coefficients are allowed, which could compensate the loop suppression. For instance four-top operators can correct the gluon-fusion cross section, while operators with top and bottom quarks can modify the Higgs branching ratio into a bottom pair.

Taking into account the possible chirality structures, 12 four-fermion operators involving only third generation quarks can be written. A few constraints on some combination of them are available at present. The strongest one comes from the measurement of the $Z\bar{b}_L b_L$ vertex, which receives loop corrections from four-fermion operators involving the left-handed quark chirality [73]. Additional constraints can be obtained from bounds on the $t\bar{t}$ and $t\bar{t}t\bar{t}$ cross sections. For instance the current LHC measurements put a bounds of order $1/(600 \text{ GeV})^2$ on the coefficient of the $(\bar{t}_R\gamma^\mu t_R)(\bar{t}_R\gamma_\mu t_R)$ operator [74]. A suppression of this size is enough to ensure that the loop corrections to Higgs physics are smaller than the achievable precision.

Of course a fully model-independent analysis of the four-fermion operators should be done by considering all operators simultaneously and not just one at a time (as done in the experimental analysis of ref. [74]). Such study is beyond the scope of this work, so we will neglect the effects of four-fermion operators in our analysis.

A final comment is in order. In the above discussion we assumed that the BSM effects are parametrized by dimension-6 operators in which the electroweak symmetry is linearly realized. This assumption allows to relate the $hVff$ and $h\partial Vff$ to the vertex and dipole operators, so that these operators can be tested in processes not involving the Higgs. If the electroweak symmetry is not linearly realized (or equivalently if the expansion in Higgs powers is not valid) the interactions involving the Higgs become independent and can not be constrained any more in non-Higgs physics. In such case a more complicated analysis, taking into account all the operators, must be performed. We will give more details about the non-linear Lagrangian in the following subsection.

⁵We thank E. Vryonidou for pointing this out to us.

3.2.3 Large Higgs self-interactions in a consistent EFT expansion

An important issue to take into account when using the effective framework is the range of validity of the EFT approximation. This is a delicate issue, crucially depending on the choice of power counting encoding the assumptions about the UV dynamics. Here we only include a concise discussion with a few examples and refer the reader to the literature [75] for possible subtleties.

As we will see in the following, the LHC measurements, especially in the high-luminosity phase, can probe inclusive single-Higgs observables with a precision of the order or slightly below 10%. In the absence of new physics, possible BSM effects will thus be constrained to be significantly smaller than the SM contributions. This translates into tight bounds on the coefficients of the operators that correct the Higgs interactions with the gauge bosons (Equation 3.4) and with the fermions (Equation 3.5). The leading effects due to these operators arise from the interference with the SM amplitude, while quadratic terms are subleading. Corrections arising from dimension-8 operators lead to effects that are generically of the same order of the square of the dimension-6 ones and are subleading as well.⁶ This justifies our approximation of keeping only the leading EFT operators.

The discussion about the trilinear Higgs self-coupling is instead more subtle. As we will see in the following, the constraints on κ_λ we can obtain from the LHC data are quite loose. The Higgs trilinear coupling can only be tested at order one, even at the end of the high-luminosity LHC program. Such large deviations in κ_λ , accompanied by small deviations in the Higgs couplings to gauge fields and fermions, can only be obtained in very special BSM scenarios. Indeed in generic new-physics models the deviations in all Higgs couplings are expected to be roughly of the same order. For instance in models that follow the SILH power counting [76–78] we expect

$$\delta c_z \sim v^2/f^2, \quad \delta \kappa_\lambda \equiv \kappa_\lambda - 1 \sim v^2/f^2, \quad (3.12)$$

where the f parameter is related to the typical coupling g_* and mass scale m_* of the new dynamics by $f \sim m_*/g_*$. In this class of models the deviations in the Higgs self-interactions are typically small, much below the LHC sensitivity. A fit of the single-Higgs couplings, neglecting the trilinear Higgs modifications is thus fully justified in these scenarios. At the same time the constraints achievable on κ_λ at the LHC will hardly have any impact in probing the parameter space of SILH theories. The situation

⁶There exist particular classes of theories in which the size of effects coming from the dimension-8 operators is enhanced with respect to the square of the dimension-6 ones. We will not consider these scenarios in our analysis. For a discussion of these effects see for instance refs. [75,76].

could however change at future high-energy machines, as for instance a 100 TeV hadron collider, which could test κ_λ with a precision below 10%, implying non-trivial constraints on models following the SILH power counting [42,76].

Enhanced deviations only in Higgs self-couplings are possible in other classes of models. Interesting possibilities are provided for instance (i) by scenarios in which the Higgs is a generic bound state of a strongly coupled dynamics (i.e. not a Goldstone boson) (see discussion in ref. [76]), (ii) by bosonic technicolor scenarios and (iii) by Higgs-portal models. In all these cases large deviations in the Higgs self-couplings can be present and accompanied by small corrections in single Higgs interactions. As an explicit example, we will analyze the Higgs portal scenarios later on.

It is important to stress that, in the presence of large corrections to Higgs self-interactions, the EFT expansion in Higgs field insertions may break down. In this case the expansion in derivatives can still be valid, since it is controlled by the expansion parameter E/Λ , but we can not neglect operators with arbitrary powers of the Higgs field. The effective parametrization can still be used in such situation provided that we interpret the effective operators as a “resummation” of the effects coming from operators with arbitrary Higgs insertions. This is equivalent to a “non-linear” effective parametrization in which the Higgs is not assumed to be part of an $SU(2)_L$ doublet, but is instead treated as a full singlet (see ref. [59] for a brief account on non-linear EFT and for a list of further references). The only caveat with this parametrization is the fact that interactions with multiple Higgs fields are not connected any more to the single-Higgs couplings. In this case a different global fit should be performed, in which $c_{gg}^{(2)}$ and $\delta y_f^{(2)}$ are treated as independent parameters. Notice also that the $hVff$ and $h\partial Vff$ operators should a priori be included in the analysis, as we discussed in subsection 3.2.2 and EW precision data and Higgs data cannot be analyzed separately any longer.

To clarify the issues discussed above, we now analyze an explicit class of models, the Higgs portal scenarios. As a concrete example, we assume that a new scalar singlet φ , neutral under the SM gauge group, is described by the Lagrangian⁷

$$\mathcal{L} \supset \theta g_* m_* H^\dagger H \varphi - \frac{m_*^4}{g_*^2} V(g_* \varphi / m_*) , \quad (3.13)$$

where the dimensionless parameter θ measures the mixing between the Higgs sector and the neutral sector, and V is a generic potential. In the EFT description obtained after

⁷The power counting we derive in the following applies also to more general Higgs portal models. In particular it is valid for scenarios characterized by a single coupling g_* and a single mass scale m_* in which the Higgs is coupled to the new dynamics through interactions of the type $\theta H^\dagger H \mathcal{O}$, where \mathcal{O} is a generic new-physics operator. Note that a different power counting can arise for portal scenarios in which the new-physics sector is charged under the SM (see ref. [79] for a classification of possible scenarios).

integrating out φ the derivative expansion is valid if $E/m_* \ll 1$, while the expansion in Higgs-field insertions is valid when

$$\varepsilon \equiv \frac{\theta g_*^2 v^2}{m_*^2} \ll 1. \quad (3.14)$$

Note that θ and ε are truly dimensionless quantities in mass and coupling dimensions. The corrections to the Higgs couplings with gauge fields come indirectly from operators of the type $\partial_\mu(H^\dagger H)\partial^\mu(H^\dagger H)$ and can be estimated as

$$\delta c_z \sim \theta^2 g_*^2 \frac{v^2}{m_*^2}. \quad (3.15)$$

The corrections to the Higgs trilinear coupling are instead given by

$$\delta \kappa_\lambda \sim \theta^3 g_*^4 \frac{1}{\lambda_3^{SM}} \frac{v^2}{m_*^2}. \quad (3.16)$$

First of all, we can notice that $\delta \kappa_\lambda \sim \theta g_*^2 / \lambda_3^{SM} \delta c_z$, thus a large hierarchy between the corrections to linear Higgs couplings and the deviation in the self-interactions requires sizable values of the Higgs portal coupling θ (and/or large values of the new-sector coupling g_*).

When the corrections to the Higgs potential become large, some amount of tuning is typically needed to fix the correct properties of the Higgs potential. Notice that Higgs-portal scenarios do not typically provide a solution to the hierarchy problem. Thus they will in general suffer from some amount of tuning in the Higgs mass term, exactly as generic extensions of the SM. On top of this some additional tuning in the Higgs quartic coupling can also be present. In the following we will refer only to this additional tuning, which we denote by Δ . We can estimate Δ by noticing that the quartic coupling needs to be fixed with a precision of the order of λ_3^{SM} . By comparing the new-physics corrections to the quartic coupling with the SM value we get

$$\Delta \sim \frac{\theta^2 g_*^2}{\lambda_3^{SM}}. \quad (3.17)$$

We can easily relate $\delta \kappa_\lambda$ given in [Equation 3.16](#) to the amount of tuning Δ as

$$\delta \kappa_\lambda \sim \varepsilon \Delta. \quad (3.18)$$

This relation has an interesting consequence. If we require the expansion in Higgs insertions to be valid ($\varepsilon \lesssim 1$) and the model not to suffer additional tuning ($\Delta \lesssim 1$), we get that the corrections to the Higgs trilinear coupling can be at most of order

one ($\delta\kappa_\lambda \lesssim 1$). Larger corrections can however be obtained if at least one of the two conditions $\varepsilon \lesssim 1$ and $\Delta \lesssim 1$ is violated.

As we already mentioned, if the expansion in Higgs insertions is not valid ($\varepsilon > 1$), large deviations in the Higgs couplings are possible. In particular single- and multiple-Higgs couplings are not related any more and a non-linear effective parametrization must be used. In this scenario, however, large corrections to the linear Higgs couplings to the SM fields are expected, so that significant tuning is required to pass the precision constraints from single-Higgs processes.

A second scenario, in which $\varepsilon \lesssim 1$ while some tuning is present in the Higgs potential ($\Delta > 1$), can instead naturally lead to small deviations in the linear Higgs couplings. For instance by taking $\theta \simeq 1$, $g_* \simeq 3$ and $m_* \simeq 2.5$ TeV we get

$$\varepsilon \simeq 0.1, \quad 1/\Delta \simeq 1.5\%, \quad \delta c_z \simeq 0.1, \quad \delta\kappa_\lambda \simeq 6. \quad (3.19)$$

Since we are going to consider sizable deviations in the trilinear Higgs coupling, it is important to understand whether such corrections are compatible with a high-enough cut-off of the effective description. If large corrections are present in the Higgs self-interactions, scattering processes involving longitudinally polarized vector bosons and Higgses, in particular $V_L V_L \rightarrow V_L V_L h^n$, lose perturbative unitarity at relatively low energy scales. The upper bound for the cut-off of the EFT description can be estimated as [67]

$$\Lambda \lesssim \frac{4\pi v}{\sqrt{|\kappa_\lambda - 1|}} \sqrt{\frac{32\pi}{15} \frac{v}{m_h}}. \quad (3.20)$$

This bound is not very stringent: for $|\kappa_\lambda| \lesssim 10$ one gets $\Lambda \lesssim 5$ TeV. For values of κ_λ within the expected high-luminosity LHC bounds, perturbativity loss is thus well above the energy range directly testable at the LHC.

As a last point, we comment on the issue of the stability of the Higgs vacuum. As pointed out in ref. [62], if the only deformation of the Higgs potential is due to the $(H^\dagger H)^3$ operator, the usual vacuum is not a global minimum for $\kappa_\lambda \gtrsim 3$. In this case the vacuum becomes metastable, although it could still have a long enough lifetime. Additional deformations from higher-dimensional operators can remove the metastability bound, even for large values of κ_λ . A lower bound $\kappa_\lambda > 1$ can also be extracted if we naively require the Higgs potential to be bounded from below for arbitrary values of the Higgs VEV $\langle h \rangle$, i.e. if we require the coefficient of the $(H^\dagger H)^3$ operator to be positive. This constraint, however, is typically too restrictive. Our estimate of the effective potential, in fact, is only valid for relatively small values of the Higgs VEV, which satisfy $\varepsilon = \theta g_*^2 \langle h \rangle^2 / m_*^2 \lesssim 1$. For large values of $\langle h \rangle$ the expansion in

the Higgs field breaks down and the estimate of the potential obtained by including only dimension-6 operators is not reliable any more and the whole tower of higher-dimensional operators should be considered. In this case large negative corrections to the Higgs trilinear coupling could be compatible with a stable vacuum. Examples of such scenarios are the composite Higgs models in which the Higgs field is identified with a Goldstone boson. In these models the Higgs potential is periodic and a negative coefficient for the effective $(H^\dagger H)^3$ operator does not generate a runaway behavior of the potential.

3.3 Fit from inclusive single-Higgs measurements

As we mentioned in the introduction, single-Higgs production measurements can be sensitive to large variations of the Higgs trilinear self-coupling. These effects arise at loop level and can be used to extract some constraints on the κ_λ parameter. Under the assumption that only the trilinear Higgs coupling is modified, κ_λ can be constrained to the range $\kappa_\lambda \in [-0.7, 4.2]$ at the 1σ level and $\kappa_\lambda \in [-2.0, 6.8]$ at 2σ [62] at the end of the high luminosity phase of the LHC. This result was obtained by assuming that the experimental uncertainties are given by the ‘Scenario 2’ estimates of CMS [80, 81], in which the theory uncertainties are halved with respect to the 8 TeV LHC run and the other systematic uncertainties are scaled as the statistical errors. The actual precision achievable in the high-luminosity LHC phase could be worse than this estimate, leading to a slightly smaller sensitivity on κ_λ . Nevertheless the result shows that single Higgs production could be competitive with other measurements, for instance double-Higgs production, in the determination of the Higgs self coupling.

A similar analysis, focusing only on the gluon fusion cross section and on the $H \rightarrow \gamma\gamma$ branching ratio, was presented in ref. [61]. With this procedure a bound $\kappa_\lambda \in [-7.0, 6.1]$ at the 2σ level was derived, whose overall size is in rough agreement with the result of ref. [62].

In subsection 3.2.3 we saw that large corrections to the Higgs self-couplings are seldom generated alone and are typically accompanied by deviations in the other Higgs interactions. In scenarios that predict $\mathcal{O}(1)$ corrections to κ_λ , single Higgs couplings, such as Yukawa interactions or couplings with the gauge bosons, usually receive corrections of the order of 5 – 10%. Since these corrections modify single-Higgs processes at tree level, their effects are comparable with the ones induced at loop level by a modification of the Higgs self-coupling. In these scenarios, a reliable determination of κ_λ

thus requires a global fit, in which also the single-Higgs coupling distortions are properly included.

In this section we will perform such a fit, taking into account deformations of the SM encoded by the 10 effective operators introduced in [section 3.2](#) (see [Equation 3.7](#)). As we will see, when all the effective operators are turned on simultaneously, some cancellations are possible, resulting in an unconstrained combination of the effective operators. This flat direction can not be resolved by taking into account only inclusive single-Higgs production measurements. Additional observables are thus needed to disentangle deviations in the Higgs self-coupling from distortions of single-Higgs interactions. We will discuss various possibilities along this line in [section 3.4](#) and [section 3.5](#).

Before performing the actual fit, it is also important to mention that large deviations in κ_λ could in principle also have an impact on the determination of single-Higgs couplings. We will discuss this point in [subsection 3.3.3](#).

3.3.1 Single-Higgs rates and single-Higgs couplings

As a preliminary step in our analysis, we focus on single Higgs couplings neglecting the effects of κ_λ and we perform a global fit exploiting single-Higgs processes.

Measurements of the production and decay rates of the Higgs boson are usually reported in terms of signal strengths, i.e. the ratio of the measured rates with respect to the SM predictions. The total signal strength, μ_i^f , for a given production mode i and decay channel $h \rightarrow f$, is thus given by

$$\mu_i^f = \mu_i \times \mu^f = \frac{\sigma_i}{(\sigma_i)_{\text{SM}}} \times \frac{\text{BR}[f]}{(\text{BR}[f])_{\text{SM}}}. \quad (3.21)$$

Obviously the production and decay signal strengths can not be separately measured and only their products are directly accessible.

Single Higgs production can be extracted with good accuracy at the LHC in five main modes: gluon fusion (ggF), vector boson fusion (VBF), associated production with a W or a Z (WH , ZH), and associated production with a top quark pair ($t\bar{t}H$). Moreover the main Higgs decay channels are into ZZ , WW , $\gamma\gamma$, $\tau^+\tau^-$ and $b\bar{b}$.⁸ A large subset of all the combinations of these production and decay modes can be extracted at the high-luminosity LHC with a precision better than 10–20%. It is thus possible to linearly expand the signal strengths as

$$\mu_i^f \simeq 1 + \delta\mu_i + \delta\mu^f, \quad (3.22)$$

⁸For simplicity we neglect the $\mu^+\mu^-$ and $c\bar{c}$ decay modes and assume that no invisible decay channels are present.

since quadratic terms are negligible.

As can be seen from [Equation 3.22](#), a rescaling of the production rates $\mu_i \rightarrow \mu_i + \delta$ can be exactly compensated by a rescaling of the branching ratios $\mu^f \rightarrow \mu^f - \delta$. For this reason, out of the 10 quantities describing the production and decay of an on-shell particle (5 productions and 5 decays), only 9 independent constraints can be derived experimentally, which are enough to determine the set of single-Higgs couplings $(\delta c_z, c_{zz}, c_{z\Box}, \hat{c}_{z\gamma}, \hat{c}_{\gamma\gamma}, \hat{c}_{gg}, \delta y_t, \delta y_b, \delta y_\tau)$.

In our numerical analysis we estimate the theory and experimental systematic uncertainties by following the ATLAS projections presented in ref. [\[82\]](#). The full list of uncertainties is given in [Table 3.1](#). Notice that, with respect to the ATLAS analysis we introduced a few updates. We reduced the theory uncertainty in the gluon fusion production cross section to take into account the recent improvement in the theory predictions [\[59, 83\]](#). In addition, we updated the entries corresponding to the VBF production mode with ZZ and WW final states using the more recent estimates presented in refs. [\[84\]](#) and [\[85\]](#). To estimate the separate uncertainties in the WH and the ZH production modes with ZZ final state, which are considered together in ref. [\[82\]](#), we divided the experimental uncertainty for VH by the square root of the corresponding event fractions.⁹

Our projections are also in fair agreement with the ‘Scenario 1’ in the CMS extrapolations [\[80\]](#), in which the systematic uncertainties are assumed to be the same as in the 8 TeV LHC run. Notice that our choice is more conservative than the one made in ref. [\[62\]](#), and should be interpreted as a ‘pessimistic’ scenario. We will comment in [subsection 3.5.2](#) on how the numerical results change as a function of the systematic uncertainties.

To extract the fit we assume that the central values of the measured signal strengths are equal to the SM predictions, i.e. $\mu_i^f = 1$, and we perform a simple statistical analysis by constructing the χ^2 function

$$\chi^2 = \sum_{i,f} \frac{(\mu_i^f - 1)^2}{(\sigma_i^f)^2}, \quad (3.23)$$

where σ_i^f are the errors associated to each channel.

If we consider only small deviations in the single-Higgs couplings, we can linearly expand the signal strengths in terms of the 9 fit parameters (the numerical expressions

⁹In this way, we get that the ratio of uncertainties between the WH and ZH channels with ZZ final state is in good agreement with a previous estimate by ATLAS [\[86\]](#).

Process		Combination	Theory	Experimental
$H \rightarrow \gamma\gamma$	ggF	0.07	0.05	0.05
	VBF	0.22	0.16	0.15
	$t\bar{t}H$	0.17	0.12	0.12
	WH	0.19	0.08	0.17
	ZH	0.28	0.07	0.27
$H \rightarrow ZZ$	ggF	0.06	0.05	0.04
	VBF	0.17	0.10	0.14
	$t\bar{t}H$	0.20	0.12	0.16
	WH	0.16	0.06	0.15
	ZH	0.21	0.08	0.20
$H \rightarrow WW$	ggF	0.07	0.05	0.05
	VBF	0.15	0.12	0.09
$H \rightarrow Z\gamma$	incl.	0.30	0.13	0.27
$H \rightarrow b\bar{b}$	WH	0.37	0.09	0.36
	ZH	0.14	0.05	0.13
$H \rightarrow \tau^+\tau^-$	VBF	0.19	0.12	0.15

Table 3.1: Estimated relative uncertainties on the determination of single-Higgs production channels at the high-luminosity LHC (14 TeV center of mass energy, 3/ab integrated luminosity and pile-up 140 events/bunch-crossing). The theory, experimental (systematic plus statistic) and combined uncertainties are listed in the ‘Theory’, ‘Experimental’ and ‘Combination’ columns respectively. All the estimates are derived from refs. [84, 85] and [59, 83].

are given in [Appendix A](#)). In this way the χ^2 function becomes quadratic in the parameters and we end up in a Gaussian limit. The 1σ intervals and the full correlation matrix (with large correlations enlightened in boldface) for the parameters are given by (by construction the best fit coincides with the SM point, where all the coefficients vanish)

$$\begin{pmatrix} \hat{c}_{gg} \\ \delta c_z \\ c_{zz} \\ c_{z\Box} \\ \hat{c}_{z\gamma} \\ \hat{c}_{\gamma\gamma} \\ \delta y_t \\ \delta y_b \\ \delta y_\tau \end{pmatrix} = \pm \begin{pmatrix} 0.07 & (0.02) \\ 0.07 & (0.01) \\ 0.64 & (0.02) \\ 0.24 & (0.01) \\ 4.94 & (0.65) \\ 0.08 & (0.02) \\ 0.09 & (0.02) \\ 0.14 & (0.03) \\ 0.17 & (0.09) \end{pmatrix} \begin{bmatrix} 1 & -0.01 & -0.02 & 0.03 & 0.08 & 0.01 & -\mathbf{0.71} & 0.03 & 0.01 \\ & 1 & -0.45 & 0.36 & -0.61 & -0.33 & 0.18 & \mathbf{0.89} & 0.53 \\ & & 1 & -\mathbf{0.99} & 0.69 & 0.11 & 0.38 & -0.47 & -\mathbf{0.74} \\ & & & 1 & -0.58 & -0.23 & -0.42 & 0.42 & \mathbf{0.71} \\ & & & & 1 & -0.58 & 0.09 & -0.46 & -0.63 \\ & & & & & 1 & 0.14 & 0.04 & 0.04 \\ & & & & & & 1 & 0.25 & -0.08 \\ & & & & & & & 1 & 0.57 \\ & & & & & & & & 1 \end{bmatrix}. \quad (3.24)$$

The numbers listed in parentheses correspond to the 1σ uncertainties obtained by considering only one parameter at a time, i.e. by setting to zero the coefficients of all the other effective operators.

The comparison between the global fit and the fit to individual operators shows that some bounds can significantly vary with the two procedures. The most striking case, as noticed already in ref. [66], involves the c_{zz} and $c_{z\Box}$ coefficients, whose fit shows a high degree of correlation. As a consequence, the constraints obtained in the global fit are more than one order of magnitude weaker than the individual fit ones. This high degeneracy can be lifted by including in the fit constraints coming from EW observables. Indeed, as we will discuss later on, a combination of the c_{zz} and $c_{z\Box}$ operators also modifies the triple gauge couplings, generating an interesting interplay between Higgs physics and vector boson pair production.

Another element of particular interest in the correlation matrix is the $\hat{c}_{gg} - \delta y_t$ entry. The cleanest observable constraining these couplings is the gluon fusion cross section, which however can only test a combination of the two parameters. In order to disentangle them one needs to consider the $t\bar{t}H$ production mode. This process, however, has a limited precision at the LHC, explaining the large correlation between \hat{c}_{gg} and δy_t and the weaker bounds in the global fit. Other ways to gain information about the top Yukawa coupling are to rely on an exclusive analysis of gluon fusion with an extra hard jet [87] or to consider the effects of off-shell Higgs production [88, 89]

High correlations are also present between the bottom Yukawa parameter δy_b and all the other parameters except \hat{c}_{gg} and δy_t . The origin of the correlations can be traced back to the fact that the main impact of a modified bottom Yukawa is a rescaling of the Higgs branching ratios. Since the $b\bar{b}$ decay channel can only be tested with limited

accuracy, the main constraints on δy_b come exploiting the gluon fusion channel with the Higgs decaying into $\gamma\gamma$, ZZ , WW and $\tau\tau$. A variation of the bottom Yukawa leaves the gluon fusion cross section nearly unchanged, thus to recover the SM predictions one needs to compensate the variations in the branching ratios induced by δy_b with contributions from the δc_z , c_{zz} , $c_{z\Box}$, $\hat{c}_{z\gamma}$, $\hat{c}_{\gamma\gamma}$ and δy_τ . This feature gives rise to the large correlations between δy_b and these parameters.

The presence of sizable correlations among various parameters significantly limits the robustness of the results shown in Equation 3.24. In particular the Gaussian approximation we used to derive the bounds is not fully justified. We checked that, by using the full expressions for the signal rates the 1σ limits are significantly modified. The largest effects are found in the c_{zz} and $c_{z\Box}$ bounds, which change at order one. Such large sensitivity to the quadratic (and higher-order) terms in the fit also signals that corrections coming from higher-dimensional effective operators could also affect the fit in a non-negligible way. To solve this problem we need to lift the approximate flat directions related to the large entries in the correlation matrix. One way to achieve this goal is to include in the fit additional observables that can provide independent constraints on the Higgs couplings. We will list in the following a few possibilities.

Di-boson data. A first set of observables that has an interplay with Higgs physics is given by the EW boson trilinear gauge couplings (TGC's). The deviations in the EW boson trilinear gauge couplings induced by CP-preserving dimension-6 operators can be encoded in the following effective Lagrangian

$$\begin{aligned} \mathcal{L} \supset & i g c_w \delta g_{1,z} (W_{\mu\nu}^+ W^{\mu-} - W_{\mu\nu}^- W^{\mu+}) Z^\nu \\ & + i e \delta \kappa_\gamma A^{\mu\nu} W_\nu^+ W_\nu^- + i g c_w \delta \kappa_z Z^{\mu\nu} W_\mu^+ W_\nu^- \\ & + i \frac{e \lambda_\gamma}{m_w^2} W_\nu^{\mu+} W_\rho^{\nu-} A_\mu^\rho + \frac{g c_w \lambda_Z}{m_w^2} W_\nu^{\mu+} W_\rho^{\nu-} Z_\mu^\rho, \end{aligned} \quad (3.25)$$

where s_w and c_w denote the sine and cosine of the weak mixing angle.

In the Higgs basis the above couplings depend only on one free parameter, λ_z , while the other coefficients are combinations of the Higgs coupling parameters $\hat{c}_{\gamma\gamma}$, $\hat{c}_{z\gamma}$, c_{zz}

and $c_{z\Box}$. The explicit expressions are given by

$$\delta g_{1,z} = \frac{g'^2}{2(g^2 - g'^2)} \left[\hat{c}_{\gamma\gamma} \frac{e^2}{\pi^2} + \hat{c}_{z\gamma} \frac{g^2 - g'^2}{\pi^2} - c_{zz} (g^2 + g'^2) - c_{z\Box} \frac{g^2}{g'^2} (g^2 + g'^2) \right], \quad (3.26)$$

$$\delta \kappa_\gamma = - \frac{g^2}{2(g^2 + g'^2)} \left[\hat{c}_{\gamma\gamma} \frac{e^2}{\pi^2} + \hat{c}_{z\gamma} \frac{g^2 - g'^2}{\pi^2} - c_{zz} (g^2 + g'^2) \right], \quad (3.27)$$

$$\delta \kappa_z = \delta g_{1,z} - \frac{g'^2}{g^2} \delta \kappa_\gamma, \quad (3.28)$$

$$\lambda_\gamma = \lambda_z. \quad (3.29)$$

Therefore, in the Higgs basis the deviations of two TGC's are correlated to the single-Higgs couplings modifications. Measurements of the WWZ and $WW\gamma$ interactions can be converted into constraints on two linear combinations of the $\hat{c}_{\gamma\gamma}$, $\hat{c}_{z\gamma}$, c_{zz} and $c_{z\Box}$ parameters which can be used to remove the correlation between c_{zz} and $c_{z\Box}$. At present the WWZ and $WW\gamma$ couplings are tested with an accuracy of order $\sim 5\%$ [90, 91]. For our numerical analyses we will assume a precision of order 1% at the end of the high-luminosity LHC phase.

Rare Higgs decays. Another set of observables related to the Higgs couplings is obtained by considering additional, more rare Higgs decays. The inclusion of the $h \rightarrow Z\gamma$ decay, which is expected to be measured with $\sim 30\%$ accuracy at the high-luminosity LHC [92], can be used to constrain the $\hat{c}_{z\gamma}$ parameter. The $h \rightarrow \mu^+\mu^-$ decay, on the other hand, has a limited impact on the fit, since it depends on an additional parameter, the deviation in the muon Yukawa δy_μ . In the flavor universal case, however, the muon and tau Yukawa receive equal new-physics contributions, $\delta y_\mu = \delta y_\tau$, and the determination of δy_μ can be used to improve the fit on δy_τ . The improvement is anyhow limited, since the precision achievable in the measurement of the $h \rightarrow \mu^+\mu^-$ decay is comparable with the one achievable directly on the τ Yukawa. Apart from the impact on δy_τ , the influence of the $h \rightarrow \mu^+\mu^-$ channel on the fit of the remaining single Higgs couplings is negligible.

The above constraints, in particular the ones coming from TGC's and $h \rightarrow Z\gamma$, significantly help in improving the fit on single Higgs couplings and lowering the correlations. The 1σ fit intervals on the EFT parameters and the correlation matrix are

modified as

$$\begin{pmatrix} \hat{c}_{gg} \\ \delta c_z \\ c_{zz} \\ c_{z\Box} \\ \hat{c}_{z\gamma} \\ \hat{c}_{\gamma\gamma} \\ \delta y_t \\ \delta y_b \\ \delta y_\tau \end{pmatrix} = \pm \begin{pmatrix} 0.07 & (0.02) \\ 0.05 & (0.01) \\ 0.05 & (0.02) \\ 0.02 & (0.01) \\ 0.09 & (0.09) \\ 0.03 & (0.02) \\ 0.08 & (0.02) \\ 0.12 & (0.03) \\ 0.11 & (0.09) \end{pmatrix} \begin{bmatrix} 1 & 0.04 & -0.01 & -0.01 & 0.04 & 0.31 & -\mathbf{0.76} & 0.05 & 0.02 \\ & 1 & -0.07 & -0.26 & 0.01 & 0.01 & 0.36 & \mathbf{0.88} & 0.27 \\ & & 1 & -\mathbf{0.87} & 0.13 & 0.20 & 0.03 & -0.07 & -0.06 \\ & & & 1 & -0.09 & -0.09 & -0.09 & -0.17 & 0.08 \\ & & & & 1 & 0.05 & -0.02 & -0.02 & -0.03 \\ & & & & & 1 & -0.32 & -0.19 & -0.12 \\ & & & & & & 1 & 0.50 & 0.28 \\ & & & & & & & 1 & 0.36 \\ & & & & & & & & 1 \end{bmatrix}. \quad (3.30)$$

These results have been obtained by linearizing the signal strengths. We however checked that, by using the full expressions for the μ_i^f , the results in Equation 3.30 remain basically unchanged. The additional constraints coming from the TGC's and $h \rightarrow Z\gamma$ measurements thus effectively resolve the approximate flat directions making our linearized EFT fit fully consistent and robust.

Higgs width. Finally one could also consider the constraint on the Higgs total width, which could be extracted by comparing off-shell and on-shell Higgs measurements [93–97].¹⁰ ATLAS estimated that a precision of 40% could be reached at the end of the high-luminosity LHC [100]. If we include this piece of information in the fit, we find that also this constraint has a negligible impact on the flat directions. To assess whether an improvement on such projections could have an effect on the global fit, we repeated our analysis varying the estimated precision on the width. As expected, the most sensitive coefficients are δy_b and δc_z . In order to affect their 1σ fit intervals, one needs a precision on the width of at least 20%. In particular, we find that if we assume a precision of 40%, 20%, and 10%, the 1σ bound on δy_b of Equation 3.30 shrinks to 0.11, 0.09, and 0.06, while the one on δc_z is reduced respectively to 0.05, 0.04 and 0.03.

To conclude the discussion about single-Higgs couplings, it is useful to report on what happens if we relax the assumption of small deviations in the Higgs interactions. In this case the linear expansion in the signal strengths is no longer appropriate and the full expressions must be retained. Additional minima are then present in the fit. Trivial ones are obtained by reversing the sign of the tau ($\delta y_\tau \simeq -2$) or bottom ($\delta y_b \simeq -2$) Yukawas, which leave the production cross sections and decay branching ratios unchanged.¹¹ Other minima are obtained by choosing \hat{c}_{gg} in such a way that its contribution to the gluon fusion amplitude is minus twice the SM one ($\hat{c}_{gg} \simeq -2$) or by choosing $\hat{c}_{\gamma\gamma}$ so that it

¹⁰See also refs. [88, 98, 99] for possible issues related to the EFT interpretation of these measurements.

¹¹In the case of a ‘wrong-sign’ bottom Yukawa with an unchanged top Yukawa a small contribution from \hat{c}_{gg} is needed to compensate for the small change in the gluon fusion cross section.

reverses the amplitude for Higgs decay into a photon pair ($\hat{c}_{\gamma\gamma} \simeq 1.6$). Less trivial minima are instead obtained by reversing the top Yukawa coupling ($\delta y_t \simeq -2$), with either $\hat{c}_{gg} \simeq 0$ or $\hat{c}_{gg} \simeq 2$. In this case the interference between the W and top contributions to the branching ratio $h \rightarrow \gamma\gamma$ changes sign and must be compensated by a contribution from $\hat{c}_{\gamma\gamma}$ ($\hat{c}_{\gamma\gamma} \simeq 2.1$ or $\hat{c}_{\gamma\gamma} \simeq 0.46$). An additional possibility is to reverse the sign of the associated production channels amplitude ($\delta c_z \simeq -2$), in which case the change in the $h \rightarrow \gamma\gamma$ amplitude can be compensated by $\hat{c}_{\gamma\gamma} \simeq -0.45$ or $\hat{c}_{\gamma\gamma} \simeq -2.1$. Finally by reversing both the sign of both the top Yukawa and of the associated production channels amplitude, one finds two additional minima with $\hat{c}_{\gamma\gamma} \simeq -1.6$ or $\hat{c}_{\gamma\gamma} \simeq 0.01$.

Some of these additional minima can be probed by considering other observables. The sign of the top Yukawa can be extracted from the measurement of $h + \text{top}$ production, as shown in refs. [101–103]. Large contributions to \hat{c}_{gg} can instead be probed in double-Higgs production, which can be used to exclude the $\hat{c}_{gg} \simeq -2$ minimum [76]. The sign of the bottom Yukawa can instead be tested by considering the transverse momentum distributions in Higgs production with an extra jet [104] (see also ref. [105]).¹² We are instead not aware of any process which could be sensitive to the sign of the tau Yukawa.

In our analysis we also assumed that the sign of the hWW and hZZ couplings are the same (fixing them to be positive for definiteness). Such assumption is well motivated theoretically, since a sign difference would imply large contributions to custodial breaking operators. From the experimental point of view, however, testing the sign of the hWW and hZZ couplings explicitly is very difficult at the LHC. It could be possible at future lepton colliders, which could be sensitive to the relative sign of the two couplings in ZH and ZHH production [107].

3.3.2 Global fit including Higgs self-coupling

We can now discuss how the above picture changes when we introduce in the fit the additional parameter κ_λ controlling the Higgs self-coupling deformations. As we saw in the previous subsection, the measurement of 5 production and 5 Higgs decay channels allows us to extract 9 independent constraints on the coefficients of the EFT Lagrangian. By introducing κ_λ in our fit, we reach a total of 10 independent parameters, thus we expect one linear combination to remain unconstrained in the fit. This is indeed what happens. The global fit has an exact flat direction along which the χ^2 vanishes.

¹²An additional Higgs associated production channel, namely $H\gamma$, could be used to test large deviations in $\hat{c}_{\gamma\gamma}$ [106].

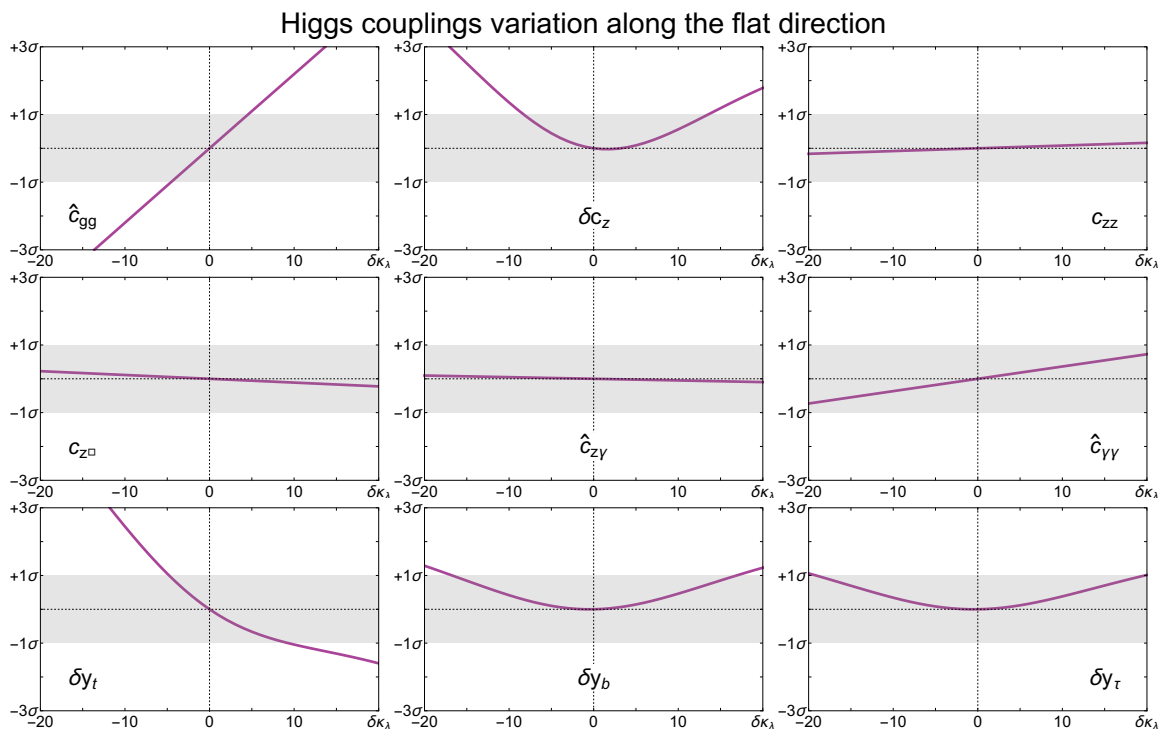


Figure 3.1: Variation of the Higgs basis parameters along the flat direction as a function of the Higgs trilinear coupling κ_λ . The gray bands correspond to the 1σ error bands at the high-luminosity LHC (see [Equation 3.24](#)).

In [Figure 3.1](#) we plot the values of the single-Higgs coupling parameters as a function of κ_λ along the flat direction. It is interesting to notice that a strong correlation is found between the Higgs trilinear coupling κ_λ , the Higgs contact interaction with gluons \hat{c}_{gg} and the top Yukawa δy_t . When we limit the κ_λ variation to the region $\kappa_\lambda \in [-1, 10]$, as indicated by the constraints coming from double Higgs production, \hat{c}_{gg} and δy_t vary by an amount comparable with the 1σ error at the high-luminosity LHC (obtained in a fit without κ_λ). On the other hand, along the flat direction, the remaining parameters vary by a much lower amount ($\hat{c}_{\gamma\gamma}$, δc_z , δy_b and δy_τ) or, in some cases, remain almost unchanged (c_{zz} , $c_{z\Box}$, $\hat{c}_{z\gamma}$).¹³

It must be stressed that the exact flat direction could in principle be lifted if we include in the signal strengths computation also terms quadratic in the EFT parameters. The additional terms, however, become relevant only for very large values of κ_λ , so that for all practical purposes we can treat the flat direction as exact. Notice moreover that, when the quadratic terms become important, one must a priori also worry about possible corrections from higher-dimensional operators, which could become comparable to the square of dimension-6 operators.

As we discussed in the previous section, additional observables can provide independent bounds on the Higgs couplings. In particular some of the strongest constraints come from the measurements of TGC's and of the $h \rightarrow Z\gamma$ branching ratio. In the fit of the single-Higgs couplings these constraints were enough to get rid of the large correlation between c_{zz} and $c_{z\Box}$ and to improve the bound on $\hat{c}_{z\gamma}$. The impact on the global fit including the Higgs trilinear coupling is instead limited. The reason is the fact that the combination of parameters tested in TGC's (see ??) and in $h \rightarrow Z\gamma$ are 'aligned' with the flat direction, i.e. they involve couplings whose values along the flat direction change very slowly (see [Figure 3.1](#)). Although the flat direction is no more exact, even assuming that the TGC's and $c_{z\gamma}$ can be tested with arbitrary precision, very large deviations in the Higgs self-coupling would still be allowed.

An additional way to probe the flat direction is to compare single-Higgs production rates at different collider energies. This possibility stems from the fact that the kinematic distributions in Higgs production channels with associated objects (VBF, ZH , WH and $t\bar{t}H$) change in a non-trivial way as a function of the collider energy [62, 63]. As a consequence the impact of the modification of the Higgs couplings on the production

¹³An interesting feature is the fact that along the flat direction not only $\delta\mu_i^f = 0$, but also the individual production and decay signal strengths are approximately equal to the SM ones, namely $|\delta\mu_i| < 0.005$, $|\delta\mu^f| < 0.005$ for $|\kappa_\lambda| < 20$.

rates shows some dependence on the energy as well. As one can see from the numerical results reported in appendix A, the dependence of the VBF, ZH and WH rates on the c_{zz} , $c_{z\Box}$, $\hat{c}_{z\gamma}$ and $\hat{c}_{\gamma\gamma}$ parameters changes as a function of the collider energy (Equation A.1.1), (Equation A.1.2) and (Equation A.1.3)). The corrections due to κ_λ also show a dependence on the energy. In particular the strongest effects are present in the $t\bar{t}H$ production rate, as can be seen from Equation A.1.14 and the list of coefficients in Table A.2.

The difference in the new physics effects at the different LHC energies are quite small, so that they do not really allow for an improvement in the fit, taking also into account the fact that accurate enough predictions will be obtained only for one center of mass energy. Future colliders (as for instance a 27 TeV hadron machine) could lead to more pronounced changes in the parameter dependence.¹⁴ However the improvement achievable with a combined fit is only marginal. A more efficient way of exploiting higher-energy machines is to look for double Higgs production which could probe κ_λ with enough accuracy to make its contributions to single Higgs processes negligible (assuming that no significant deviation with respect to the SM is found) [42].

To conclude the discussion on the extraction of the Higgs self-coupling, we show in Figure 3.2 the χ^2 obtained from the global fit on single-Higgs observables. The fit also includes the constraints from TGC's and the bound on the $h \rightarrow Z\gamma$ decay rate.¹⁵ The results have been derived by assuming a 14 TeV LHC energy with an integrated luminosity of 3/ab. The dashed curve shows the χ^2 obtained by setting all the single-Higgs couplings deviations to zero. One can see that the Higgs self-coupling can be restricted to the interval $\kappa_\lambda \in [-1.1, 4.7]$ at the 1σ level. To compare with the existing literature, we also show the exclusive fit obtained in the optimistic 'Scenario 2' of CMS (dashed curve), which is in very good agreement with the results of ref. [62].

On the other hand by profiling over the single Higgs couplings we find that the Higgs trilinear coupling remains basically unconstrained (see solid curve in Figure 3.2).¹⁶ As expected, even with the inclusion of the TGC's constraints and of the bounds on the $h \rightarrow Z\gamma$ decay rate, an almost flat direction is still present in the fit.

¹⁴We thank D. Pagani for providing us with the results for the κ_λ contribution to the inclusive observables at 33 and 100 TeV.

¹⁵A full computation of the corrections to the $h \rightarrow Z\gamma$ branching ratio due to the Higgs trilinear interaction is not available at present. For this reason we only took into account the effect of the Higgs wavefunction renormalization, which scales as κ_λ^2 (see Appendix A), and we neglected the additional corrections linear in κ_λ which are not known.

¹⁶Since in our linear approximation the χ^2 as a function of the single-Higgs couplings is quadratic the resulting distribution is Gaussian. In this case a profiling procedure gives the same result as a marginalization.

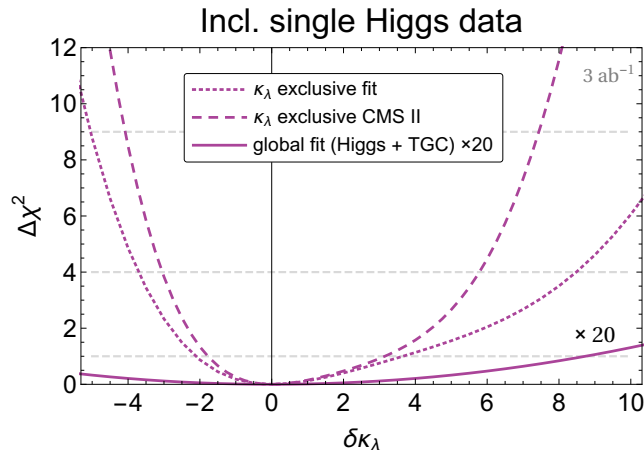


Figure 3.2: χ^2 as a function of the Higgs trilinear coupling κ_λ obtained by performing a global fit including the constraints coming from TGC’s measurements and the bound on the $h \rightarrow Z\gamma$ decay rate. The results are obtained by assuming an integrated luminosity of $3/\text{ab}$ at 14 TeV. The dotted curve corresponds to the result obtained by setting to zero all the other the Higgs-coupling parameters, while the solid curve is obtained by profiling and is multiplied by a factor 20 to improve its visibility. To compare with previous literature (ref. [62]), we also display the exclusive fit performed assuming the uncertainty projections from the more optimistic ‘Scenario 2’ of CMS [80] (dashed curve).

3.3.3 Impact of the trilinear coupling on single-Higgs couplings

The presence of a flat direction can also have an impact on the fit of the single-Higgs couplings. If we perform a global fit and we allow κ_λ to take arbitrary values we also lose predictivity on the single-Higgs EFT parameters. The effect is more pronounced on the couplings that show larger variations along the flat direction, namely \hat{c}_{gg} and δy_t . A milder impact is found for the δc_z , δy_b , δy_τ and $\hat{c}_{\gamma\gamma}$, whereas c_{zz} , $c_{z\Box}$ and $\hat{c}_{z\gamma}$ are almost unaffected, unless extremely large values of κ_λ are allowed.

In Figure 3.3 we compare the fit in the $(\delta y_t, \hat{c}_{gg})$ and $(\delta y_b, \hat{c}_{\gamma\gamma})$ planes obtained by setting the Higgs trilinear to the SM value ($\delta\kappa_\lambda = 0$), with the results obtained by allowing $\delta\kappa_\lambda$ to vary in the ranges $|\delta\kappa_\lambda| \leq 10$ and $|\delta\kappa_\lambda| \leq 20$.

In the $(\delta y_t, \hat{c}_{gg})$ case (left panel of Figure 3.3), there is a strong (anti-)correlation between the two parameters as we explained in subsection 3.3.1. When the Higgs self-coupling is included in the fit the strong correlation is still present. The constraint along the correlated direction becomes significantly weaker, even if we restrict $\delta\kappa_\lambda$ to the range $|\delta\kappa_\lambda| \leq 10$. The constraint in the orthogonal direction is instead only marginally affected.

In the case of the $(\delta y_b, \hat{c}_{\gamma\gamma})$ observables, we find that the 1σ uncertainty on the determination of the two parameters is roughly doubled if the Higgs trilinear coupling

Incl. single Higgs data

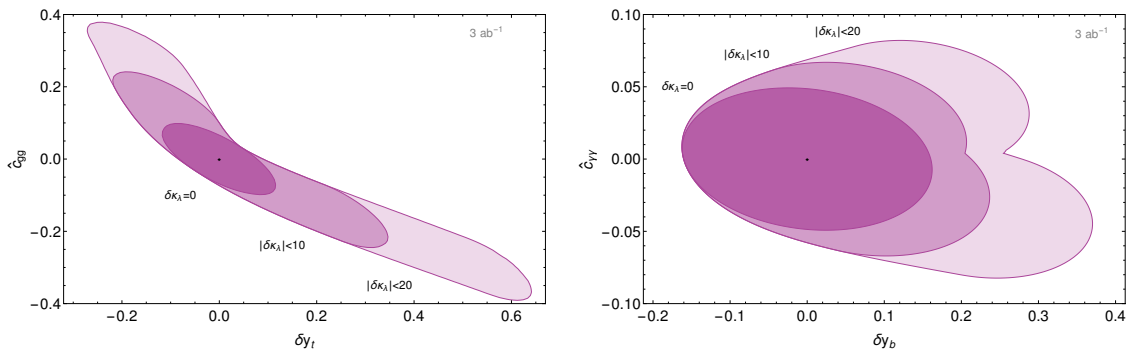


Figure 3.3: Constraints in the planes $(\delta y_t, \hat{c}_{gg})$ (left panel) and $(\delta y_b, \hat{c}_{\gamma\gamma})$ (right panel) obtained from a global fit on the single-Higgs processes. The darker regions are obtained by fixing the Higgs trilinear to the SM value $\kappa_\lambda = 1$, while the lighter ones are obtained through profiling by restricting $\delta\kappa_\lambda$ in the ranges $|\delta\kappa_\lambda| \leq 10$ and $|\delta\kappa_\lambda| \leq 20$ respectively. The regions correspond to 68% confidence level (defined in the Gaussian limit corresponding to $\Delta\chi^2 = 2.3$).

is allowed to take values up to $|\delta\kappa_\lambda| \sim 20$.

This above discussion makes clear that a global fit on the single-Higgs observables can not be properly done without including some assumption on the allowed values of the trilinear self-coupling of the Higgs (see subsection 3.2.3). If κ_λ can sizably deviate from the SM value ($\delta\kappa_\lambda \gtrsim 5$) including it into the fit is mandatory in order to obtain accurate predictions for the single-Higgs couplings. On the other hand, if we have some theoretical bias that constrains the Higgs self-coupling modifications to be small ($\delta\kappa_\lambda \lesssim$ few), a restricted fit in which only the corrections to single-Higgs couplings are included is reliable.

We will see in the following that the situation can drastically change if we include in the fit additional measurements that can lift the flat direction. In particular we will focus on the measurement of double Higgs production in the next section and of differential single Higgs distributions in section 3.5.

3.4 Double Higgs production

A natural way to extract information about the Higgs self-coupling is to consider Higgs pair production channels. Among this class of processes, the production mode with the largest cross section, which we can hope to test with better accuracy at the LHC, is

gluon fusion.¹⁷ Several analyses are available in the literature, focusing on the various Higgs decay modes. The channel believed to be measurable with the highest precision is $hh \rightarrow b\bar{b}\gamma\gamma$ [76, 111, 116–122]. In spite of the small branching ratio (BR $\simeq 0.264\%$), its clean final state allows for high reconstruction efficiency and low levels of backgrounds. In the following we will thus focus on this channel for our analysis.

Additional final states have also been considered in the literature, in particular $hh \rightarrow b\bar{b}b\bar{b}$ [123–126], $hh \rightarrow b\bar{b}WW^*$ [111, 124, 127] and $hh \rightarrow b\bar{b}\tau^+\tau^-$ [111, 123, 124, 128, 129]. All these channels are plagued by much larger backgrounds. In order to extract the signal, one must rely on configurations with boosted final states and more involved reconstruction techniques, which limit the achievable precision.

The dependence of the double Higgs production cross section on the EFT parameters has been studied in refs. [76, 129–131]. It has been shown that a differential analysis taking into account the Higgs pair invariant mass distribution can help in extracting better bounds on the relevant EFT parameters.

On top of the dependence on κ_λ , double Higgs production is sensitive at leading order to 4 additional EFT parameters, namely δy_t , $\delta y_t^{(2)}$, \hat{c}_{gg} and $\hat{c}_{gg}^{(2)}$. The explicit expression of the cross section is given in [Appendix A, Equation A.1.21](#). As we discussed in [section 3.2](#), in the linear EFT description only δy_t and \hat{c}_{gg} are independent parameters, while the other two correspond to the combinations given in [Equation 3.8](#). By a suitable cut-and-count analysis strategy, the total SM Higgs pair production cross section is expected to be measured with a precision $\sim 50\%$ at the high-luminosity LHC [76]. These estimates are in good agreement with the recent projections by ATLAS [122].

As a first point, we focus on the determination of the trilinear Higgs self-coupling. In the left panel of [Figure 3.4](#) we show the χ^2 as a function of κ_λ . The solid curve corresponds to the result of a global fit including single-Higgs and inclusive double-Higgs observables. All the single-Higgs EFT parameters have been eliminated by profiling. The dashed curve shows how the fit is modified if we neglect the dependence on κ_λ in single-Higgs processes. Finally, the dotted curve is obtained by performing an exclusive fit, in which all the deviations in single-Higgs couplings are set to zero.

As expected, the measurement of double-Higgs production removes the flat direction that was present in the fit coming only from single-Higgs observables. The global fit

¹⁷It has been pointed out in ref. [108] that the WHH and ZHH production modes could provide a good sensitivity to positive deviations in the Higgs self-coupling (see also refs. [109–111]). As we will see in the following, the gluon fusion channel is instead more sensitive to negative deviations. The associated double Higgs production channels could therefore provide useful complementary information for the determination of κ_λ . For simplicity we only focus on the gluon fusion channels in the present analysis. We leave the study of the VHH channels, as well as of the double Higgs production mode in VBF (see refs. [110, 112–115]), for future work.

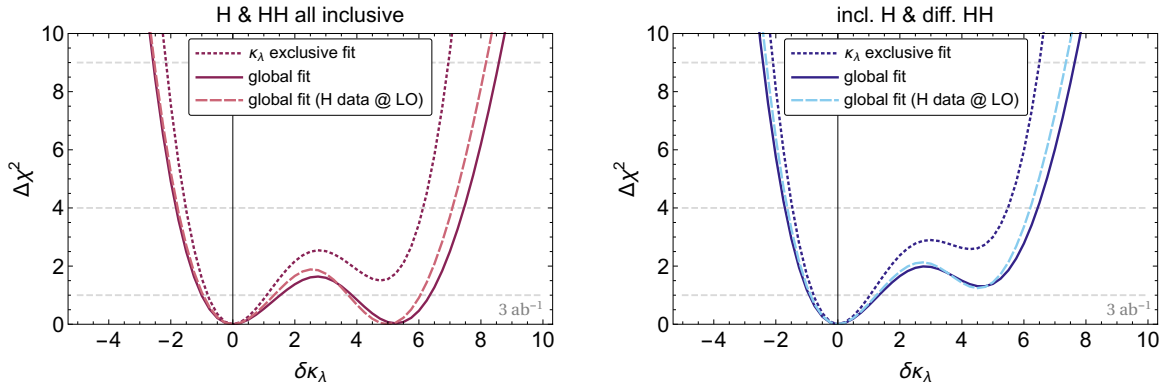


Figure 3.4: *Left*: The solid curve shows the global χ^2 as a function of the corrections to the Higgs trilinear self-coupling obtained from a fit exploiting inclusive single Higgs and inclusive double Higgs observables. The dashed line shows the fit obtained by neglecting the dependence on $\delta\kappa_\lambda$ in single-Higgs observables. The dotted line is obtained by exclusive fit in which all the EFT parameters, except for $\delta\kappa_\lambda$, are set to zero. *Right*: The same but using differential observables for double Higgs.

constrains the Higgs trilinear self-coupling to the intervals $\kappa_\lambda \in [0.0, 2.5] \cup [4.9, 7.4]$ at 68% confidence level and $\kappa_\lambda \in [-0.8, 8.5]$ at 95%. As we can see by comparing the solid and dashed lines in Figure 3.4, the fit of κ_λ is almost completely determined by Higgs pair production. This result is expected and is coherent with the fact that a flat direction involving κ_λ is present in the single-Higgs fit. On the other hand if we perform an exclusive fit in which we set to zero all the deviations in single-Higgs couplings, the determination of the Higgs trilinear self-coupling is significantly modified. In particular the exclusive fit disfavors large deviations in κ_λ , so that values $\delta\kappa_\lambda \sim 5$, which were allowed by the global fit, are now excluded at the 1σ level. The 95% fit region is also slightly reduced becoming $\kappa_\lambda \in [-0.5, 7.1]$.

It is also interesting to discuss what happens if we include in the fit a differential analysis of double Higgs production. As shown in ref. [76], each new physics effect deforms the Higgs-pair invariant mass distribution in a different way. Deviations in the Higgs self-coupling mostly affect the threshold distribution, while they have a limited impact in the high invariant-mass tail. On the contrary δy_t and \hat{c}_{gg} modify more strongly the peak and tail of the distribution. A differential analysis can exploit this different behavior to extract better constraints on the various EFT coefficients. The fits including the differential information on Higgs pair production are shown in the right panel of Figure 3.4. Sizable positive corrections to κ_λ are now disfavored even in a global fit. The 1σ interval is now reduced to $\kappa_\lambda \in [0.1, 2.3]$, while the 2σ interval is $\kappa_\lambda \in [-0.7, 7.5]$.

Another aspect worth discussing is the impact of double-Higgs production measure-

ment on the determination of the single-Higgs couplings. We find that the global fit determines the latter couplings with a precision comparable with the one obtained by neglecting the deviations in κ_λ (see [subsection 3.3.1](#), [Equation 3.24](#)). This result may look surprising at a first sight. Double-Higgs measurements at the LHC can only probe the order of magnitude of the Higgs trilinear self-coupling, so that large deviations from the SM value, $\kappa_\lambda \sim 6$, will be allowed at the 68% confidence level. Such big deviations could in turn compensate non-negligible corrections to the single-Higgs measurements (by moving along the flat direction of the single-Higgs observables fit). The reason why this does not happen is related to the fact that double-Higgs production is sensitive not only to κ_λ , but also to δy_t and \hat{c}_{gg} . Actually, the sensitivity on the latter two parameters is relatively strong, so that the bounds on δy_t and \hat{c}_{gg} coming from double-Higgs alone are not much weaker than the ones coming from single-Higgs processes [76]. These results hold with the assumption that EW symmetry is linearly realized. We will see in [subsection 3.5.2](#) how they are modified in the context of a non-linear EFT.

3.5 Differential observables

Up to now we focused on inclusive single Higgs observables, which allowed us to get robust predictions backed up by the estimates made by the ATLAS and CMS experimental collaborations. It is however clear that inclusive observables do not maximize the information attainable from the data. Important additional information can be extracted by exploiting differential single-Higgs distributions. This can be crucial in our analysis since flat directions are present in the inclusive fit.

The exploitation of differential distributions can help to break the degeneracy thanks to the fact that the various effective operators affect the kinematic distributions in different ways. Consider for instance associated production of a Higgs with a vector boson. EFT operators that modify the single-Higgs couplings give effects that grow with the centre of mass energy, hence they mostly affect the high-energy tail of the invariant mass or transverse momentum distributions. On the contrary, the effect of a modified Higgs trilinear self-coupling is larger near threshold. This different behavior is the key feature that can allow us to efficiently disentangle the two effects [62, 63].

The change in the differential single Higgs distributions, in particular in the WH , ZH , $t\bar{t}H$ and VBF channels, as a function of the distortion of the Higgs self-coupling has been studied in refs. [62, 63].¹⁸ In this section we will use these results as a building

¹⁸Recently, ref. [132] also computed the impact of the Higgs coupling deviations in the Higgs basis on angular distributions in the four-lepton decay channels of the Higgs boson. We have not included these effects in our analysis.

block to perform a first assessment of the impact of the differential single-Higgs measurements on the extraction of the Higgs self-interactions and on the global fit of the Higgs couplings.

3.5.1 Impact of single-Higgs differential measurements

In the following we focus our attention on the differential distributions in associated Higgs production channels, ZH , WH and $t\bar{t}H$. We instead neglect the VBF channel, which was found to have a negligible impact on the determination of the trilinear Higgs coupling in ref. [62, 63].

For our analysis we consider the differential distributions in the total invariant mass of the processes. As we discussed in section 3.2, considering high energetic bins in differential distributions might lead to issues with the validity of the EFT interpretation. For this reason we only include in our analysis bins with an invariant mass up to three times the threshold energy for the various channels, which corresponds to ~ 600 GeV for associated production with a gauge boson and to ~ 1.4 TeV for $t\bar{t}H$. The numerical LO predictions of the ZH and WH cross sections in each bin as a function of the single-Higgs EFT parameters are given in Appendix A, while the signal strength for $t\bar{t}H$ is instead modified at LO in an energy-independent way. Concerning the loop-induced effect of κ_λ on the invariant mass distributions of the ZH , WH , and $t\bar{t}H$ cross-sections, only the 13 TeV results are known [62]. Therefore we use this center of mass energy for our numerical study. We however expect that our results provide a fair assessment of the precision achievable at the 14 TeV high-luminosity LHC, since the differences with respect to the 13 TeV case should not be very large.

For our numerical analysis we estimate the statistical and systematic uncertainties from the high-luminosity-LHC ATLAS projections [82]. In order to evaluate the dependence of our results on the experimental accuracy we consider two different procedures to estimate the uncertainties. In the first, more optimistic procedure, the systematic uncertainty is assumed to be the same in all the invariant mass bins, whereas the statistical uncertainty is rescaled according to the expected number of events in each bin. In the second, more pessimistic estimate, we extract the uncertainty for each bin by rescaling the total experimental error according to the expected number of events in each bin. In this way we are effectively inflating the systematic errors assuming that they degrade as the statistical ones in bins with fewer events. The uncertainties for the two scenarios are reported in Table A.6 and Table A.7.

Notice that the invariant mass of some processes is not directly accessible experimentally, since the event kinematics can not be fully reconstructed. We nevertheless use it

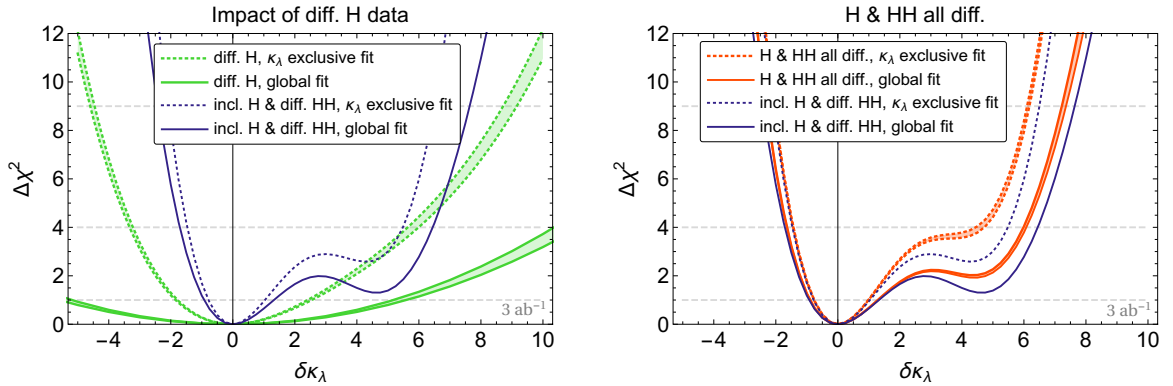


Figure 3.5: *Left*: χ^2 as a function of the Higgs trilinear self-coupling. The green bands are obtained from the differential analysis on single-Higgs observables and are delimited by the fits corresponding to the optimistic and pessimistic estimates of the experimental uncertainties. The dotted green curves correspond to a fit performed exclusively on $\delta\kappa_\lambda$ setting to zero all the other parameters, while the solid green lines are obtained by a global fit profiling over the single-Higgs coupling parameters. *Right*: The red lines show the fits obtained by a combination of single-Higgs and double-Higgs differential observables. In both panels the dark blue curves are obtained by considering only double-Higgs differential observables and coincide with the results shown in fig. 3.4.

for our analysis for simplicity. As a cross check, we verified that performing the analysis with transverse momentum binning does not significantly modify the results of the fit. Since our estimates of the experimental uncertainties and our analysis strategy are quite crude, we do not expect our numerical results to be fully accurate. They must instead be interpreted as rough estimates which can however give an idea of the discriminating power that we could expect by the exploitation of differential single-Higgs distributions.

As a first step we consider the impact on the determination of single-Higgs couplings. Including the differential information in the fit helps in reducing the correlation between c_{zz} and $c_{z\Box}$. The overall change in the fit is however small and the 1σ intervals are nearly unchanged with respect to the ones we obtained in the inclusive analysis (see Equation 3.30).

More interesting results are instead obtained when we focus on the extraction of the Higgs trilinear self-coupling. We find that differential distributions are able to lift the flat direction we found in the inclusive single-Higgs observables fit. The solid green lines in Figure 3.5 show the χ^2 obtained in a global fit on single-Higgs observables including the differential information from associated production modes. The two lines correspond to the ‘optimistic’ and ‘pessimistic’ assumptions on the experimental uncertainties. Through this procedure one could constrain the Higgs trilinear coupling to the interval $|\delta\kappa_\lambda| \lesssim 5$ at the 1σ level. An exclusive fit, in which all the single-Higgs cou-

plings deviations are set to zero, gives a range $\kappa_\lambda \in [-0.8, 3.5]$ at 1σ and $\kappa_\lambda \in [-2, 7]$ at 2σ (dotted green lines), which is significantly smaller than the one obtained through a global fit, as can be seen by comparing with the solid lines in [Figure 3.5](#).

The results in [Figure 3.5](#) show that in a global fit the impact of differential single-Higgs measurements on the extraction of κ_λ is weaker than the one of differential double-Higgs production. This can be clearly seen by comparing the solid green lines with the solid dark blue curve which represent the χ^2 coming from double Higgs measurements (this curve coincides with the results shown on the right panel of [Figure 3.4](#)). Nevertheless, combining the single-Higgs differential information with the double-Higgs fit helps in testing large positive deviations in κ_λ , increasing the χ^2 value for values $\delta\kappa_\lambda \sim 5$. This improvement can be seen on the right panel of [Figure 3.5](#) (solid curves).

Differential single-Higgs measurements have a significantly more relevant role in exclusive fits in which the single-Higgs parameters are set to zero. One can see in the left panel of [Figure 3.5](#) that the sensitivity of the single-Higgs differential fit (dotted blue line) is comparable with the one of double-Higgs measurements, especially for positive deviations in κ_λ . Combining single-Higgs and double-Higgs information provide a good improvement in the fit, in particular at the 2σ level, as can be seen in the right panel of [Figure 3.5](#) (dotted lines).

3.5.2 Robustness of the fits

As a final point we want to discuss how much the determination of the Higgs trilinear self-interaction and of the single-Higgs couplings depends on the experimental accuracy and on the theoretical assumptions underlying the EFT parametrization.

In the left panel of [Figure 3.6](#) we show how the fit on κ_λ changes if we rescale the errors on single-Higgs measurements by a factor in the range $[1/2, 2]$. One can see that the χ^2 function around the SM point $\delta\kappa_\lambda = 0$ is not strongly affected, so that the 1σ region is only mildly modified. Large positive deviations from the SM can instead be probed with significantly different accuracy. In particular the 2σ region is enlarged to $\kappa_\lambda \in [-0.8, 7.7]$ if we double the uncertainties, whereas it shrinks to $\kappa_\lambda \in [-0.5, 5.3]$ if we reduce the errors by a factor $1/2$.

A second point worth investigating is how the fit changes if we modify the assumptions on the EFT parametrization. As an illustrative example we analyze a scenario in which the EFT Lagrangian has a non-linear form, i.e. the expansion in Higgs powers breaks down. As we already discussed in [subsection 3.2.3](#), in this case operators containing Higgs fields can not be tested any more in precision measurements not involving the Higgs. A fully consistent fit should thus include all possible operators and not just the

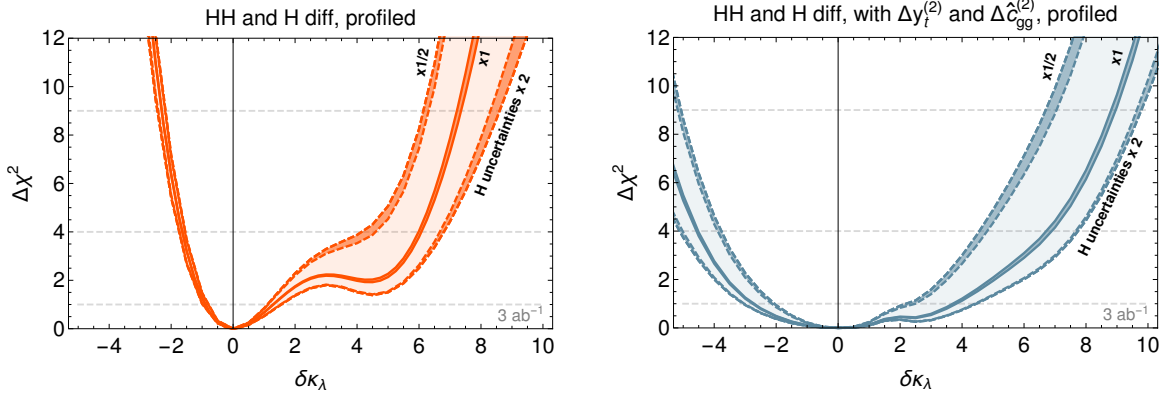


Figure 3.6: Band of variation of the global fit on the Higgs self-coupling obtained by rescaling the single-Higgs measurement uncertainties by a factor in the range $x \in [1/2, 2]$. The lighter shaded bands show the full variation of the fit due to the rescaling. The darker bands show how the fits corresponding to the ‘optimistic’ and ‘pessimistic’ assumptions on the systematic uncertainties (compare Figure 3.5) change for $x = 1/2, 1, 2$. The left panel shows the fit in the linear Lagrangian, while the right panel corresponds to the non-linear case in which $\Delta y_f^{(2)}$ and $\Delta \hat{c}_{gg}^{(2)}$ are treated as independent parameters.

restricted basis we defined in Equation 3.7 and Equation 3.8. Performing such analysis is beyond the scope of the present work. For illustration we restrict our attention only to two effective operators, $h^2 G_{\mu\nu} G^{\mu\nu}$ and $h^2 \bar{t}t$, whose impact on Higgs pair production via gluon fusion was studied in ref. [76].

In the linear EFT Lagrangian the $h^2 G_{\mu\nu} G^{\mu\nu}$ and $h^2 \bar{t}t$ operators are connected to single-Higgs couplings (see Equation 3.8). Treating them as independent operators amounts to include the $\delta y_f^{(2)}$ and $\delta \hat{c}_{gg}^{(2)}$ parameters as free quantities in our fits. For convenience we introduce two new parameters that encode the deviations of $\delta y_f^{(2)}$ and $\hat{c}_{gg}^{(2)}$ from the linear Lagrangian relations:

$$\Delta y_f^{(2)} \equiv \delta y_f^{(2)} - (3\delta y_u - \delta c_z), \quad \Delta \hat{c}_{gg}^{(2)} \equiv \hat{c}_{gg}^{(2)} - \hat{c}_{gg}. \quad (3.31)$$

To understand the impact of $\Delta y_f^{(2)}$ and $\Delta \hat{c}_{gg}^{(2)}$ on the global fit, we give in the following

equation the 1σ intervals for the Higgs couplings in the linear and non-linear scenarios

$$\begin{array}{c}
 \textit{Fit with } \Delta y_f^{(2)} = \Delta \hat{c}_{gg}^{(2)} = 0 \\
 \\
 \begin{pmatrix} \hat{c}_{gg} \\ \delta c_z \\ c_{zz} \\ c_{z\Box} \\ \hat{c}_{z\gamma} \\ \hat{c}_{\gamma\gamma} \\ \delta y_t \\ \delta y_b \\ \delta y_\tau \\ \delta \kappa_\lambda \end{pmatrix} = \pm \begin{pmatrix} 0.06 \\ 0.04 \\ 0.04 \\ 0.02 \\ 0.09 \\ 0.03 \\ 0.06 \\ 0.07 \\ 0.11 \\ 1.0 \end{pmatrix}, \\
 \\
 \textit{Global fit} \\
 \\
 \begin{pmatrix} \hat{c}_{gg} \\ \delta c_z \\ c_{zz} \\ c_{z\Box} \\ \hat{c}_{z\gamma} \\ \hat{c}_{\gamma\gamma} \\ \delta y_t \\ \delta y_b \\ \delta y_\tau \\ \delta \kappa_\lambda \\ \Delta y_f^{(2)} \\ \Delta \hat{c}_{gg}^{(2)} \end{pmatrix} = \pm \begin{pmatrix} 0.07 \\ 0.04 \\ 0.04 \\ 0.02 \\ 0.09 \\ 0.03 \\ 0.08 \\ 0.08 \\ 0.11 \\ 4.1 \\ 0.29 \\ 0.45 \end{pmatrix}. \tag{3.32}
 \end{array}$$

One can see that the non-linear fit mostly affects the determination of κ_λ , whose precision significantly degrades. The impact on the determination of single-Higgs couplings is instead quite limited and is due to the fact that a weaker constraint on the Higgs self-interaction allows to move along the flat direction in the single-Higgs global fit. Indeed we find that the 1σ intervals for \hat{c}_{gg} , δy_t and δy_b are slightly larger in the non-linear scenario. The differences are however only marginally relevant.

To better quantify how the determination of κ_λ changes in the non-linear case, we show the χ^2 obtained in the global fit in the right panel of [Figure 3.6](#). The 1σ band in this case becomes $\kappa_\lambda \in [-2, 5]$. We also show how the fit depends on the precision in the measurement of the single-Higgs observables. One can see that a reduction by a factor $1/2$ of the uncertainties on single-Higgs measurements could help significantly in improving the determination of κ_λ , reducing the 1σ band by $\sim 40\%$.

Chapter 4

The Higgs self-coupling at future lepton colliders

4.1 Introduction

In this chapter we consider a comprehensive set of benchmark scenarios including low-energy lepton machines (such as FCC-ee and CEPC) as well as machines that can also run at higher energies (ILC and CLIC). We will show that low-energy colliders, although not able to access directly the Higgs trilinear coupling in Higgs pair production processes, can still probe it by exploiting loop corrections to single Higgs channels that can be measured to a very high precision. This approach, pioneered in Ref. [60], allows for a good determination of the Higgs trilinear interaction, which can easily surpass the HL-LHC one. In performing this analysis, however, one must cope with the fact that different new-physics effects may affect simultaneously the single Higgs cross sections, see Ref. [48] as well as Refs. [133–141]. In such a situation, a robust determination of the Higgs self coupling can only be obtained through a global fit that takes into account possible deviations in other SM couplings. We will show that, within the SM effective field theory (EFT) framework with a mild set of assumptions, the relevant operators correcting single Higgs production can be constrained provided enough channels are taken into account. In this way, a consistent determination of the Higgs self-coupling is possible even without direct access to Higgs pair production.

High-energy machines, on the other hand, are able to directly probe the trilinear coupling via Higgs pair production, through Zhh associated production and WW -fusion. We will see that these two channels provide complementary information about the Higgs self interaction, being more sensitive to positive and negative deviations from the SM value respectively. We will also show, as anticipated in Ref. [142], that a differential analysis of the WW -fusion channel, taking into account the Higgs-pair invariant mass distribution, can be useful to constrain sizable positive deviations in the Higgs trilinear coupling that are hard to probe with an inclusive study.

4.2 Low-energy lepton machines

In this section we study the precision reach on the trilinear Higgs coupling through the exploitation of single Higgs production measurements. These are the dominant handles available at future circular lepton colliders, like the CEPC and FCC-ee, which cannot easily deliver high luminosities at center-of-mass energies where the Higgs pair production rate becomes sizable. These machines could run above the $e^+e^- \rightarrow Zh h$ threshold, at a 350 GeV center-of-mass energy in particular, but the small cross section (in the attobarn range) and the limited integrated luminosity lead to a negligible sensitivity to this channel. The analysis of single-Higgs production can also be relevant for the ILC. While this machine could eventually reach a center-of-mass energies of 500 GeV (or even of 1 TeV) in a staged development, its initial low-energy runs can have an impact on the determination of the trilinear Higgs coupling that is worth investigating.

We focus on the following benchmark scenarios:

- **Circular colliders (CC)** with 5 ab^{-1} at 240 GeV, $\{0, 200 \text{ fb}^{-1}, 1.5 \text{ ab}^{-1}\}$ at 350 GeV and unpolarized beams. The scenario with only a 240 GeV (5 ab^{-1}) run corresponds to the **CEPC** Higgs program, while the 240 GeV (5 ab^{-1}) + 350 GeV (1.5 ab^{-1}) scenario corresponds to the **FCC-ee** Higgs and top-quark programs.
- **Low-energy ILC** with 2 ab^{-1} at 250 GeV, $\{0, 200 \text{ fb}^{-1}, 1.5 \text{ ab}^{-1}\}$ at 350 GeV, and integrated luminosities equally shared between $P(e^-, e^+) = (\pm 0.8, \mp 0.3)$ beam polarizations.¹

Later in this section we also extend these scenarios to cover a continuous range of luminosities at 240 (250) and 350 GeV.

4.2.1 Higher-order corrections to single-Higgs processes

As a first step, we analyze how a modification of the trilinear Higgs coupling affects single-Higgs processes. We parametrize possible new physics effects through the quantity κ_λ defined as the ratio between the actual value of the trilinear Higgs coupling λ_3 and its SM expression λ_3^{SM} (the Higgs vacuum expectation value is normalized to $v = 1/(\sqrt{2}G_F)^{1/2} \approx 246 \text{ GeV}$),²

$$\kappa_\lambda \equiv \frac{\lambda_3}{\lambda_3^{\text{SM}}}, \quad \lambda_3^{\text{SM}} = \frac{m_h^2}{2v^2}. \quad (4.2.1)$$

¹The current run plan of CLIC anticipates a low-energy operation at 380 GeV as a Higgs factory. We did not consider this run alone as the lack of a separate run at a lower energy will constitute an hindrance to the indirect determination of the Higgs cubic self-interaction.

²This parametrization is equivalent to an EFT description in which deviations in the Higgs trilinear self-coupling arise from a dimension-6 operator $|H^\dagger H|^3$.

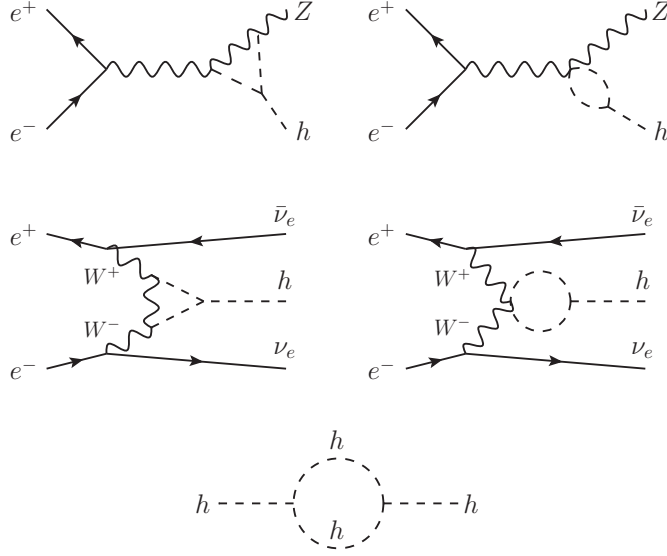


Figure 4.1: One-loop diagrams involving the trilinear Higgs coupling contributing to the main single Higgs production processes: $e^+e^- \rightarrow hZ$ (top row) and $e^+e^- \rightarrow \nu\bar{\nu}h$ (middle row). The Higgs self-energy diagram (bottom) gives a universal modification to all Higgs production processes via wave function renormalization.

While the trilinear coupling does not enter single-Higgs processes at leading order (LO), it affects both Higgs production and decay at next-to-leading order (NLO). The corresponding diagrams for Higgsstrahlung ($e^+e^- \rightarrow hZ$) and WW -fusion ($e^+e^- \rightarrow \nu\bar{\nu}h$) production processes are shown in Fig. 4.1. In addition to the vertex corrections, which are linear in κ_λ , the trilinear coupling also generates corrections quadratic in κ_λ through the wave function renormalization induced by the Higgs self-energy diagram. Such contributions have been computed for electroweak [64, 65, 143] and single-Higgs observables [60–63, 144, 145].

Following Ref. [62], we can parametrize the NLO corrections to an observable Σ in a process involving a single external Higgs field as

$$\Sigma_{\text{NLO}} = Z_H \Sigma_{\text{LO}} (1 + \kappa_\lambda C_1), \quad (4.2.2)$$

where Σ_{LO} denotes the LO value, C_1 is a process-dependent coefficient that encodes the interference between the NLO amplitudes involving κ_λ and the LO ones, while Z_H corresponds to the universal resummed wave-function renormalization and is explicitly given by

$$Z_H = \frac{1}{1 - \kappa_\lambda^2 \delta Z_H}, \quad \text{with} \quad \delta Z_H = -\frac{9}{16} \frac{G_\mu m_H^2}{\sqrt{2}\pi^2} \left(\frac{2\pi}{3\sqrt{3}} - 1 \right) \simeq -0.00154. \quad (4.2.3)$$

The impact of a deviation $\delta\kappa_\lambda \equiv \kappa_\lambda - 1$ from the SM value of the trilinear Higgs

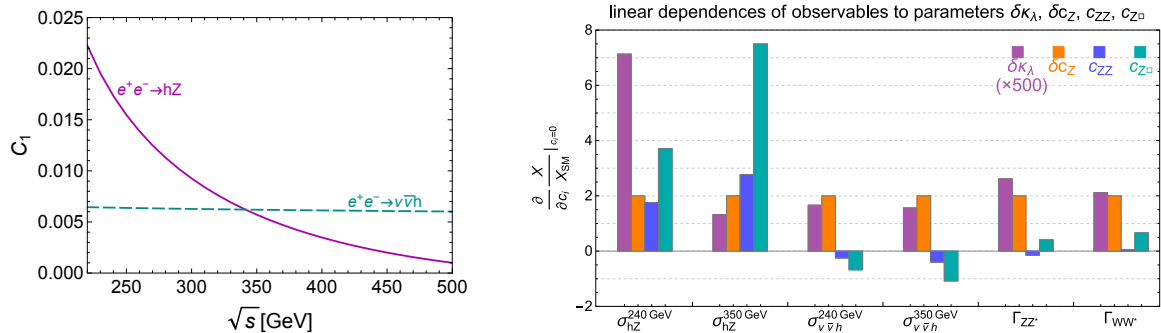


Figure 4.2: **Left:** Value of C_1 as a function of the center of mass energy \sqrt{s} for the $e^+e^- \rightarrow hZ$ and $e^+e^- \rightarrow \nu\bar{\nu}h$ single Higgs production processes. **Right:** The linear dependence of production and decay rates on the $\delta\kappa_\lambda$, δc_Z , c_{ZZ} and $c_{Z\Box}$ parameters (see Section 4.2.2 for details on the meaning of these parameters). For $e^+e^- \rightarrow \nu\bar{\nu}h$, only the WW -fusion contribution is included. The dependence on $\delta\kappa_\lambda$ is amplified by a factor of 500.

self-coupling is therefore

$$\delta\Sigma \equiv \frac{\Sigma_{\text{NLO}}}{\Sigma_{\text{NLO}}(\kappa_\lambda = 1)} - 1 \simeq (C_1 + 2\delta Z_H)\delta\kappa_\lambda + \delta Z_H\delta\kappa_\lambda^2, \quad (4.2.4)$$

up to subleading corrections of higher orders in δZ_H and C_1 .³ The linear approximation in $\delta\kappa_\lambda$ is usually accurate enough to describe the deviations in single Higgs processes inside the typical constraint range $|\delta\kappa_\lambda| \lesssim 5$. We will nevertheless use the unexpanded $\delta\Sigma$ expressions throughout this work to derive numerical results.

The value of C_1 in Higgsstrahlung ($e^+e^- \rightarrow hZ$) and WW -fusion ($e^+e^- \rightarrow \nu\bar{\nu}h$) processes are shown in the left panel of Fig. 4.2 as functions of the center-of-mass energy \sqrt{s} . Very different energy dependences are observed for the two processes. A quick decrease is seen in Higgsstrahlung, from $C_1 \simeq 0.022$ at threshold to about $C_1 \simeq 0.001$ at a center-of-mass energy of 500 GeV. On the other hand, a nearly constant value $C_1 \simeq 0.006$ is observed for the WW -fusion process over the same range of energy. Further numerical values are provided in Section A.2 for both production and decay processes. Beside the inclusive production and decay rates, we also checked the impact of a correction to $\delta\kappa_\lambda$ on the angular asymmetries that can be exploited in $e^+e^- \rightarrow hZ \rightarrow h\ell^+\ell^-$ measurements (see Refs. [146, 147]). We found that these effects are almost negligible and have no impact on the fits.

We show in the right panel of Fig. 4.2 the linear dependences of a set of production rates and Higgs partial widths on $\delta\kappa_\lambda$ and on three EFT parameters that encode deviations in the Z -boson couplings, δc_Z , c_{ZZ} and $c_{Z\Box}$. Only leading-order dependences are

³We checked explicitly that the one-loop squared term of order $\delta\kappa_\lambda^2$ is subdominant compared to the $\delta Z_H\delta\kappa_\lambda^2$ one.

accounted for, at one loop for $\delta\kappa_\lambda$ and at tree level for the other parameters. One can see that the various observables have very different dependences on the EFT parameters. For instance, δc_Z affects all the production processes in an energy-independent way.⁴ On the contrary, the effects of c_{ZZ} and $c_{Z\Box}$ grow in magnitude for higher center-of-mass energy in both Higgsstrahlung and WW -fusion cross sections. It is apparent that the combination of several measurements can allow us to efficiently disentangle the various BSM effects and obtain robust constraints on $\delta\kappa_\lambda$. From the sensitivities shown in Fig. 4.2, we can roughly estimate that a set of percent-level measurements in single-Higgs processes has the potential of constraining $\delta\kappa_\lambda$ with a precision better than $\mathcal{O}(1)$ and the other Higgs EFT parameters to the percent level. We will present a detailed quantitative assessment of the achievable precisions in the following.

4.2.2 Global analysis

4.2.2.1 Analysis of Higgs data at lepton colliders alone

Having obtained the one-loop contributions of $\delta\kappa_\lambda$ to single Higgs observables, we are now ready to determine the precision reach on the Higgs trilinear self-interaction. In order to obtain a robust estimate, we perform here a global fit, taking into account not only deviations in the Higgs self-coupling, but also corrections to the other SM interactions that can affect single-Higgs production processes.

For our analysis, we follow Ref. [48], in which the impact of single-Higgs measurements at lepton colliders on the determination of Higgs and electroweak parameters was investigated. We include in the fit the following processes

- Higgsstrahlung production: $e^+e^- \rightarrow hZ$ (rates and distributions),
- Higgs production through WW -fusion: $e^+e^- \rightarrow \nu\bar{\nu}h$,
- weak boson pair production: $e^+e^- \rightarrow WW$ (rates and distributions),

with Higgs decaying into a gauge boson pair ZZ^* , WW^* , $\gamma\gamma$, $Z\gamma$, gg or pairs of fermions $b\bar{b}$, $c\bar{c}$, $\tau^+\tau^-$, $\mu^+\mu^-$.

New physics effects are parametrized through dimension-six operators within an EFT framework. For definiteness, we express them in the Higgs basis and refer to Ref. [67] for a detailed discussion of the formalism. Since CP-violating effects are strongly constrained experimentally, we exclusively focus on CP-conserving operators. We also ignore dipole operators and work under the assumption of flavor universality. We relax this assumption only to consider independent deviations in the of top, bottom, charm, tau, and muon Yukawa couplings.

To estimate the precision in the measurement of the EFT parameters, we assume that the central value of the experimental results coincides with the SM predictions

⁴In the language of the dimension-six operators, δc_Z is generated by the operator $\mathcal{O}_H = \frac{1}{2}(\partial_\mu |H^2|)^2$, which modifies all Higgs couplings universally via the Higgs wave function renormalization.

and we neglect theory uncertainties. For simplicity we compute the SM cross sections at LO, neglecting NLO effects coming from SM interactions. These contributions can be important for the experimental analysis, since the modifications they induce in the SM cross sections can be non negligible compared to the experimental accuracy. For the purpose of estimating the bounds on BSM effects, however, they play a negligible role. We adopt a further simplification regarding electroweak precision observables, treating them as perfectly well measured. Such an assumption can significantly reduce the number of parameters to consider and is straightforward to implement in the Higgs basis which transparently separates the Higgs and electroweak parameters. The potential impact of this assumption will be discussed at the end of [Section 4.4](#).

Under the above assumptions, we are left with twelve independent dimension-six effective operators that can induce leading-order contributions to single-Higgs and diboson processes. To this set of operators, we add the correction to the Higgs self-coupling parametrized by $\delta\kappa_\lambda$.⁵ The full list of parameters included in our fit contains:

- corrections to the Higgs couplings to the gauge bosons: $\delta c_Z, c_{ZZ}, c_{Z\Box}, c_{\gamma\gamma}, c_{Z\gamma}, c_{gg}$,
- corrections to the Yukawa's: $\delta y_t, \delta y_c, \delta y_b, \delta y_\tau, \delta y_\mu$,
- corrections to trilinear gauge couplings only: λ_Z ,
- correction to the trilinear Higgs self-coupling: $\delta\kappa_\lambda$.

Since our focus is on the future sensitivity on the trilinear Higgs self-coupling, we present results in terms of $\delta\kappa_\lambda$ only, profiling over all other parameters. For a detailed analysis of the sensitivity on the other operators see Refs. [\[48, 141\]](#).

In our fit, we only include terms linear in the coefficients of the EFT operators, neglecting higher-order corrections. This approximation can be shown to provide very accurate results for all the parameters entering in our analysis [\[48\]](#). The only possible exception is $\delta\kappa_\lambda$, which can be tested experimentally with much lower precision than the other parameters. Although we checked that a linear approximation is reliable also for $\delta\kappa_\lambda$, we keep [Eq. \(4.2.4\)](#) unexpanded in our numerical analyses. For simplicity, cross terms involving $\delta\kappa_\lambda$ and other EFT coefficients are however neglected, since the strong constraints on the latter coefficients and the loop factor make these contributions irrelevant.

In order to estimate the precision on Higgs measurements at different luminosities, we use a naive scaling with an irreducible 0.1% systematic error. This systematic error has no impact for the benchmark scenarios we consider, but becomes non-negligible for the large-luminosity projections presented at the end of this section (see [Fig. 4.5](#)). Another important source of uncertainty in our fit comes from the precision on the determination of trilinear gauge couplings (TGCs). In our analysis, we consider a range

⁵In the notation of Ref. [\[67\]](#) the $\delta\kappa_\lambda$ parameter corresponds to $\delta\lambda_3/\lambda$.

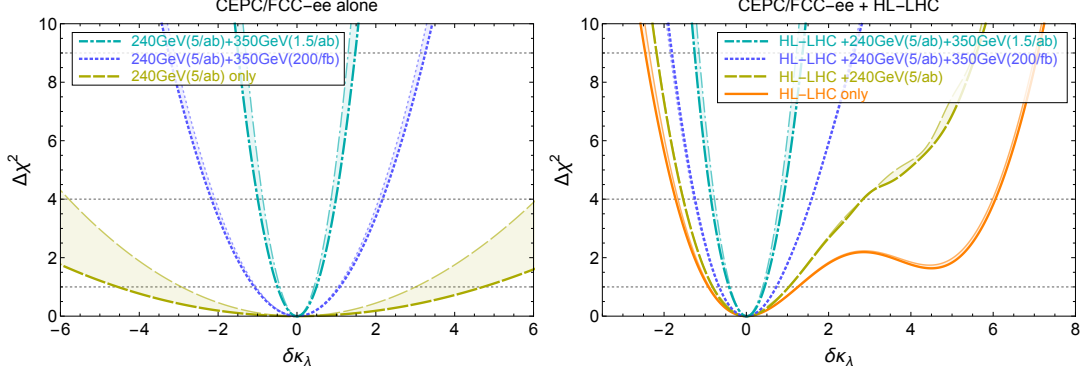


Figure 4.3: Chi-square as a function of $\delta\kappa_\lambda$ after profiling over all other EFT parameters. Three run scenarios are considered for circular colliders, with 5 ab^{-1} at 240 GeV and $\{0, 200 \text{ fb}^{-1}, 1.5 \text{ ab}^{-1}\}$ at 350 GeV, without beam polarization. The shaded areas cover different assumptions about the precision of TGC measurements. **Left:** circular lepton collider measurements only. **Right:** combination with differential single and double Higgs measurements at the HL-LHC.

of possibilities. In the most conservative case, we assume 1% systematic errors in each bin of the $e^+e^- \rightarrow WW$ angular distributions used to constrain anomalous TGCs (aTGCs) [48]. In the most optimistic case, we assume that aTGCs are constrained much better than all the other parameters, so that they do not affect our fit. This is equivalent to enforcing the following relations among the EFT parameters:

$$\begin{aligned}
\delta g_{1,Z} &= \frac{g^2 + g'^2}{2(g^2 - g'^2)} \left[-g^2 c_{Z\Box} - g'^2 c_{ZZ} + e^2 \frac{g'^2}{g^2 + g'^2} c_{\gamma\gamma} + g'^2 \frac{g^2 - g'^2}{g^2 + g'^2} c_{Z\gamma} \right] = 0, \\
\delta\kappa_\gamma &= -\frac{g^2}{2} \left(c_{\gamma\gamma} \frac{e^2}{g^2 + g'^2} + c_{Z\gamma} \frac{g^2 - g'^2}{g^2 + g'^2} - c_{ZZ} \right) = 0, \\
\lambda_Z &= 0.
\end{aligned} \tag{4.2.5}$$

We start our discussion of the fit results by considering the benchmark scenarios for circular colliders. The profiled $\Delta\chi^2$ fit as a function of $\delta\kappa_\lambda$ is shown in the left panel of Fig. 4.3. The 68% CL intervals are also reported in Table 4.1.

The numerical results show that a 240 GeV run alone has a very poor discriminating power on the Higgs trilinear coupling, so that only an $\mathcal{O}(\text{few})$ determination is possible (brown dashed lines in the plot). The constraint is also highly sensitive to the precision in the determination of TGCs, as can be inferred from the significantly different bounds in the conservative and optimistic aTGCs scenarios. The inclusion of measurements at 350 GeV drastically improve the results. An integrated luminosity of 200 fb^{-1} at 350 GeV, is already sufficient to reduce the uncertainty to the level $|\delta\kappa_\lambda| \lesssim 1$, whereas 1.5 ab^{-1} leads to a precision $|\delta\kappa_\lambda| \lesssim 0.5$.

It is interesting to compare the above results with the constraints coming from an exclusive fit in which only corrections to the trilinear Higgs coupling are considered

	lepton collider alone		lepton collider + HL-LHC	
	non-zero aTGCs	zero aTGCs	non-zero aTGCs	zero aTGCs
HL-LHC alone			$[-0.92, +1.26]$	$[-0.90, +1.24]$
CC 240 GeV (5 ab^{-1})	$[-4.55, +4.72]$	$[-2.93, +3.01]$	$[-0.81, +1.04]$	$[-0.82, +1.03]$
+350 GeV (200 fb^{-1})	$[-1.08, +1.09]$	$[-1.04, +1.04]$	$[-0.66, +0.76]$	$[-0.66, +0.74]$
+350 GeV (1.5 ab^{-1})	$[-0.50, +0.49]$	$[-0.43, +0.43]$	$[-0.43, +0.44]$	$[-0.39, +0.40]$
ILC 250 GeV (2 ab^{-1})	$[-5.72, +5.87]$	$[-5.39, +5.62]$	$[-0.85, +1.13]$	$[-0.85, +1.12]$
+350 GeV (200 fb^{-1})	$[-1.26, +1.26]$	$[-1.18, +1.18]$	$[-0.72, +0.83]$	$[-0.71, +0.80]$
+350 GeV (1.5 ab^{-1})	$[-0.64, +0.64]$	$[-0.56, +0.56]$	$[-0.52, +0.54]$	$[-0.48, +0.50]$

Table 4.1: One-sigma bounds on $\delta\kappa_\lambda$ from single-Higgs measurements at circular lepton colliders (denoted as CC) and the ILC. The first column shows the results for lepton colliders alone, while the second shows the combination with differential measurements of both single and double Higgs processes at the HL-LHC. For each scenario two benchmarks with conservative and optimistic assumptions on the precision on trilinear gauge couplings are listed. The integrated luminosity is assumed equally shared between $P(e^-, e^+) = (\pm 0.8, \mp 0.3)$ for the ILC.

and all the other parameters are set to zero. With 5 ab^{-1} collected at 240/250 GeV, and irrespectively of the presence of a run at 350 GeV, we find that such a fit gives a precision of approximately 14% in the determination of $\delta\kappa_\lambda$. The strongest constraints come from the measurement of the $e^+e^- \rightarrow Zh$ cross section at the 240 GeV run, which is the observable with the largest sensitivity to $\delta\kappa_\lambda$ (see discussion in Section 4.2.2 and left panel of Fig. 4.2). Other processes at the 240 GeV run and the higher-energy runs have only a marginal impact on the exclusive fit.

The exclusive fit provides a bound much stronger than the global analyses, signaling the presence of a nearly flat direction in the global fits. We found that $\delta\kappa_\lambda$ has a strong correlation with δc_Z and c_{gg} , while milder correlations are present with $c_{Z\Box}$ and λ_Z .⁶ This result sheds some light on the origin of the improvement in the global fit coming from the combination of the 240 GeV and 350 GeV runs. The latter runs, although probing processes with a smaller direct sensitivity to $\delta\kappa_\lambda$, are useful to reduce the uncertainty on the other EFT parameters. In particular, the 350 GeV run with 1.5 ab^{-1} of integrated luminosity allows for a reduction of the uncertainty on δc_Z , c_{gg} , $c_{Z\Box}$ and λ_Z by a factor of about 4. This in turn helps in lifting the flat direction in the global fit. This effect is clearly visible from the left panel of Fig. 4.4, which shows the fit on the $\delta\kappa_\lambda$ and δc_Z parameters obtained with a 240 GeV run only and with the inclusion

⁶Notice that a loosely constrained direction involving δc_Z is already present in the global fit not including $\delta\kappa_\lambda$ [48]. The addition of the trilinear Higgs coupling makes this feature even more prominent.

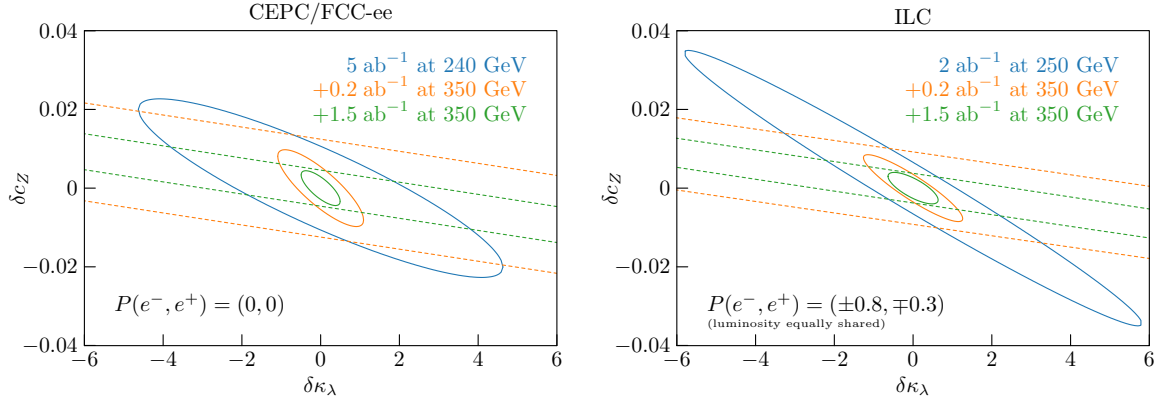


Figure 4.4: Global constraints on δc_Z and $\delta \kappa_\lambda$, obtained from single Higgs measurements at circular colliders (left panel) and ILC (right panel), illustrating the improvement brought by 350 GeV runs. Dashed lines are for the latter only, while solid lines combined them with the 240/250 GeV one.

of a 350 GeV run.

4.2.2.2 Synergy between measurements at the HL-LHC and lepton-colliders

So far, we only considered the precision reach of lepton colliders on the extraction of the trilinear Higgs self-coupling. Significant information on $\delta \kappa_\lambda$ can however also be obtained at the high-luminosity LHC. It is thus interesting to estimate the impact of combining the different sets of measurements.

We shortly summarize here the previous results for the HL-LHC constraints on the Higgs trilinear self-coupling. It can be accessed at the mainly through the exploitation of the Higgs pair production channel $pp \rightarrow hh$. An analysis of this channel within the EFT framework has been presented in Ref. [76], in which the most promising channel, namely $pp \rightarrow hh \rightarrow b\bar{b}\gamma\gamma$, has been investigated. A fully differential analysis (taking into account the Higgs pair invariant mass distribution) allows to constrain $\delta \kappa_\lambda$ to the interval $[-1.0, 1.8]$ at 68% CL. A second minimum is however present in the fit, which allows for sizable positive deviations in $\delta \kappa_\lambda$, namely an additional interval $\delta \kappa_\lambda \in [3.5, 5.1]$ can not be excluded at 68% CL. Some improvement can be obtained complementing the pair-production channel with information from single Higgs channels, which are affected at NLO by the Higgs self-coupling. In this way, the overall precision becomes $\delta \kappa_\lambda \in [-0.9, 1.2]$ at 68% CL (with the additional minimum at $\delta \kappa_\lambda \sim 5$ excluded) and $\delta \kappa_\lambda \in [-1.7, 6.1]$ at 95% CL [36]. To estimate the impact of HL-LHC, we will use here the results of the combined fit with differential single and pair production (corresponding to the orange solid curve in the right panel of Fig. 4.3).

The combinations of the HL-LHC fit with our benchmarks for circular lepton colliders are shown in the right panel of Fig. 4.3. One can see that a 240 GeV run is already sufficient to completely lift the second minimum at $\delta \kappa_\lambda \sim 5$, thus significantly reducing

the 2σ bounds. The precision near the SM point ($\delta\kappa_\lambda = 0$) is however dominated by the HL-LHC measurements, so that the lepton collider data can only marginally improve the 1σ bounds. The situation is reversed for the benchmarks including a 350 GeV run. In this case, the precision achievable at lepton colliders is significantly better than the HL-LHC one. The combination of the LHC and lepton collider data can still allow for a significant improvement in the constraints if limited integrated luminosity can be accumulated in the 350 GeV runs (see [Table 4.1](#)). With 1.5 ab^{-1} collected at 350 GeV, on the other hand, the lepton collider measurements completely dominate the bounds.

Similar results are obtained for the low-energy ILC benchmarks. In this case, the lower integrated luminosity forecast at 250 GeV (2 ab^{-1}) can be compensated through the exploitation of the two different beam polarizations $P(e^-, e^+) = (\pm 0.8, \mp 0.3)$. The only difference with respect to the circular collider case is the fact that the 250 GeV run fit is more stable under changes in the trilinear gauge couplings precision. This is due to the availability of runs with different polarizations, which provide better constraints on the EFT parameters. Analogously to the circular collider scenarios, the combination of the 250 GeV measurements with the HL-LHC data allows to completely lift the minimum at $\delta\kappa_\lambda \sim 5$, while a 350 GeV run would easily surpass the LHC precision. We report the results for the ILC benchmarks in ?? (see ??). For completeness, we mention that an exclusive fit on $\delta\kappa_\lambda$ at the ILC allows for a precision of approximately 32%, significantly better than the one expected through a global fit. Also in this case a nearly flat direction is present when deviations in all the EFT parameters are simultaneously allowed (see right panel of [Fig. 4.4](#)).

Having observed the significant impact of the combination of measurements at 240/250 GeV and 350 GeV center-of-mass energies, to conclude the discussion, we now explore a continuous range of integrated luminosities accumulated at the various colliders. The one-sigma limits as functions of the integrated luminosity are displayed in [Fig. 4.5](#) for the circular colliders and the ILC. Conservative and optimistic precisions for TGC measurements are respectively assumed to obtain the solid and dashed curves. The combination of runs at these two different energies always brings drastic improvements. The fastest improvements in precision on the $\delta\kappa_\lambda$ determination is obtained along the $L_{350 \text{ GeV}}/L_{240 \text{ GeV}} \simeq 0.7$ and $L_{350 \text{ GeV}}/L_{250 \text{ GeV}} \simeq 0.5$ lines for circular colliders and the ILC, respectively.

4.3 High-energy lepton machines

Having explored the reach of low-energy lepton colliders in the previous section, we now enlarge our scope to include machines with center-of-mass energies above 350 GeV. They offer the opportunity of probing directly the trilinear Higgs self-coupling through Higgs pair production processes, double Higgsstrahlung $e^+e^- \rightarrow Zh h$ and WW -fusion $e^+e^- \rightarrow \nu\bar{\nu} h h$ in particular. The precision reach in the determination of $\delta\kappa_\lambda$ at ILC

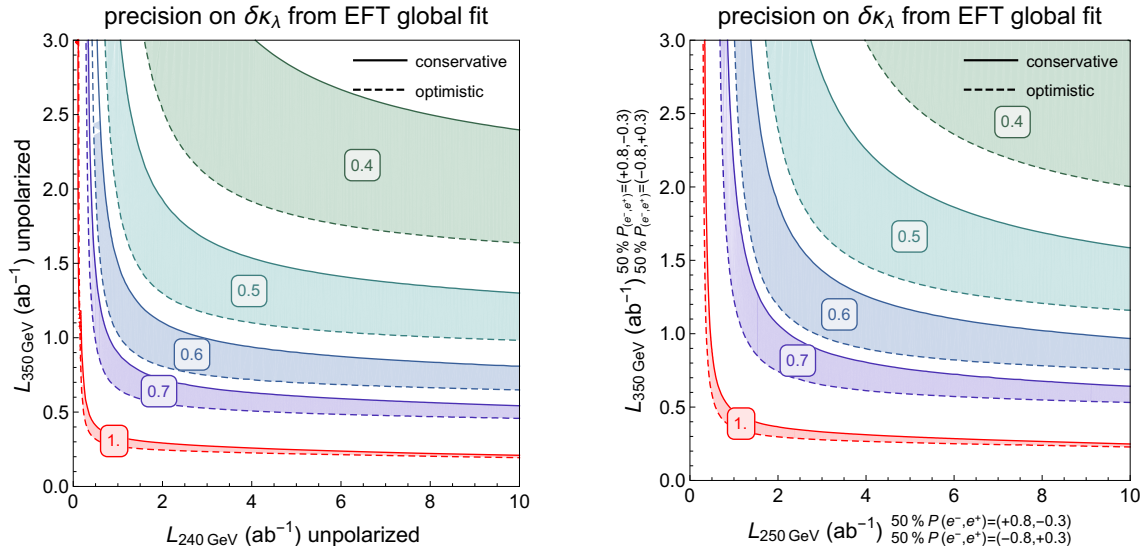


Figure 4.5: One-sigma bound on $\delta\kappa_\lambda$ deriving from single Higgs and diboson production measurements at lepton colliders as a function of the integrated luminosity collected at both 240/250 and 350 GeV. Conservative (solid) and optimistic (dashed) assumptions are used for the precision of diboson measurements.

and CLIC has already been studied by the experimental collaborations [43, 148]. These studies performed an exclusive fit, allowing for new-physics effects only in the trilinear Higgs self-coupling.

In this section, we first review the experimental projections on the extraction of the Higgs self-coupling from double Higgs channels. In this context, we also point out how differential distributions, in particular in the WW -fusion channel, can allow for an enhanced sensitivity to $\delta\kappa_\lambda$. Afterwards, we reconsider Higgs pair production measurements from a global EFT perspective, showing how the determination of $\delta\kappa_\lambda$ is modified by performing a simultaneous fit for all EFT parameters. We also evaluate how these results are modified by combining double-Higgs data with single-Higgs measurements from low-energy runs.

4.3.1 Higgs pair production

As already mentioned, Higgs pair production at high-energy lepton machines is accessible mainly through the double Higgsstrahlung $e^+e^- \rightarrow Zh h$ and WW -fusion $e^+e^- \rightarrow \nu\bar{\nu}h h$ channels. The cross sections for these two production modes as functions of the center-of-mass energy of the collider are shown in Fig. 4.6. It is interesting to notice their completely different behavior, so that the relevance of the two channels drastically changes at different machines. At energies below approximately 1 TeV, double Higgsstrahlung is dominant whereas, at higher energy, the channel with the larger cross section is WW -fusion. To be more specific, the cross section of double Hig-

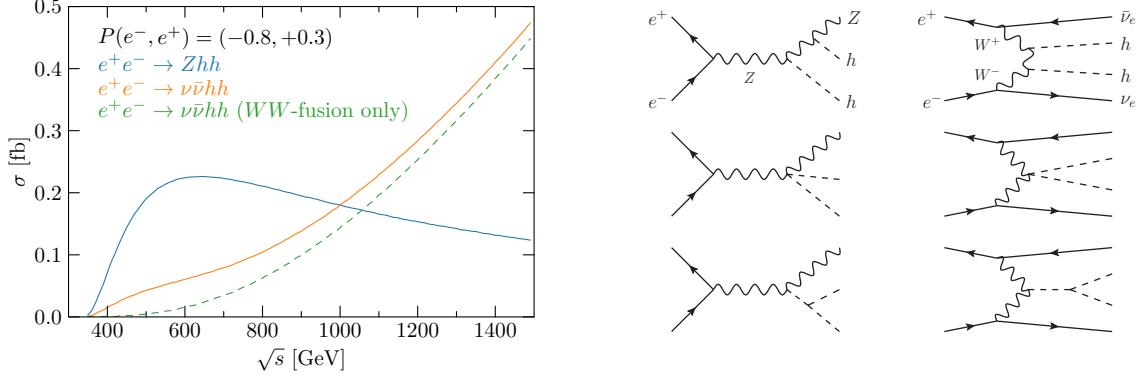


Figure 4.6: Higgs pair production cross sections at lepton colliders as functions of the center-of-mass energy (based on Fig.7 of Ref. [149]) and illustrative diagrams. The difference between the two $\nu\bar{\nu}hh$ curves is entirely due to double Higgsstrahlung followed by invisible Z decay.

gsstrahlung reaches a maximum at $\sqrt{s} \simeq 600$ GeV before starting to slowly decrease as the s -channel Z boson gets more and more offshell. On the contrary, the $e^+e^- \rightarrow \nu\bar{\nu}hh$ cross section initially grows steadily with the center-of-mass energy of the collider and adopts a logarithmic behavior above 10 TeV. Notice that the $e^+e^- \rightarrow \nu\bar{\nu}hh$ channel receives non-negligible contributions that are not of WW -fusion type. The largest of them arises from double Higgsstrahlung followed by a $Z \rightarrow \nu\bar{\nu}$ decay. These contributions can however be efficiently identified at sufficiently high center-of-mass energies since the kinematic of the process is significantly different from that of WW -fusion. Notice, moreover, that both double-Higgs production cross sections are significantly affected by the beam polarization (see ?? and ??).

The $e^+e^- \rightarrow Zhh$ process at the ILC with 500 GeV center-of-mass energy has been thoroughly studied in Ref. [148]. A total luminosity of 4 ab^{-1} , equally split into two beam polarization runs $P(e^-, e^+) = (\pm 0.8, \mp 0.3)$, allows for a precision of 21.1% on the cross section determination through the exploitation of the $hh \rightarrow b\bar{b}b\bar{b}$ final state. A further improvement can be obtained by also including the $hh \rightarrow b\bar{b}WW^*$ channel, in which case the precision reaches 16.8%.

The $e^+e^- \rightarrow \nu\bar{\nu}hh$ process has also been studied at a 1 TeV center-of-mass energy. A significance of 2.7σ (corresponding to a precision of 37%) could be achieved in the $hh \rightarrow b\bar{b}b\bar{b}$ channel, assuming an integrated luminosity $\mathcal{L} = 2 \text{ ab}^{-1}$ and $P(e^-, e^+) = (-0.8, +0.2)$ beam polarization [150].

Studies of the $e^+e^- \rightarrow \nu\bar{\nu}hh$ process at CLIC (both at 1.4 TeV and 3 TeV center-of-mass energy) are available in Ref. [43]. Assuming unpolarized beams and 1.5 ab^{-1} , the precision on the 1.4 TeV cross section could reach 44%. With 1.5 ab^{-1} , the 3 TeV cross section could be measured with a 20% precision. Both $b\bar{b}b\bar{b}$ and $b\bar{b}WW^*$ channels are included in these analyses, though the sensitivity is mainly driven by the former, as shown in Table 28 in Ref. [43].

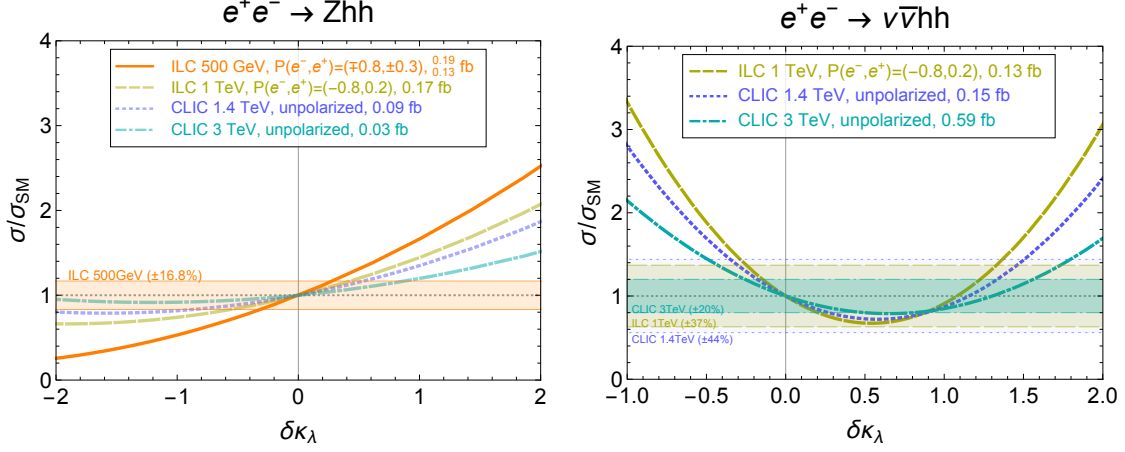


Figure 4.7: Dependence of the Higgs pair production rates on $\delta\kappa_\lambda$ at various center-of-mass energies. Shaded bands display the precision claimed by dedicated experimental studies on the standard-model cross sections. Absolute cross sections are provided in the legend.

	68 %CL	95%CL
ILC 500 GeV	$[-0.31, 0.28]$	$[-0.67, 0.54]$
ILC 1 TeV	$[-0.25, 1.33]$	$[-0.44, 1.52]$
ILC combined	$[-0.20, 0.23]$	$[-0.37, 0.49]$
CLIC 1.4 TeV	$[-0.35, 1.51]$	$[-0.60, 1.76]$
CLIC 3 TeV	$[-0.26, 0.50] \cup [0.81, 1.56]$	$[-0.46, 1.76]$
CLIC combined	$[-0.22, 0.36] \cup [0.90, 1.46]$	$[-0.39, 1.63]$
+Zhh	$[-0.22, 0.34] \cup [1.07, 1.28]$	$[-0.39, 1.56]$
2 bins in $\nu\bar{\nu}hh$	$[-0.19, 0.31]$	$[-0.33, 1.23]$
4 bins in $\nu\bar{\nu}hh$	$[-0.18, 0.30]$	$[-0.33, 1.11]$

Table 4.2: Constraints from an exclusive fit on $\delta\kappa_\lambda$ derived from the measurements of $\nu\bar{\nu}hh$ and $e^+e^- \rightarrow \nu\bar{\nu}hh$ cross sections at ILC and CLIC, with all other parameters fixed to their standard-model values.

The dependence of the Higgs pair production cross sections on $\delta\kappa_\lambda$ is shown in Fig. 4.7 for a set of benchmark scenarios. The SM cross section for each benchmark is provided in the legend.⁷ Shaded bands show the precisions on the determination of the SM rates discussed above. Note the experimental collaborations made no forecast for

⁷The ILC 1 TeV SM cross section is obtained from Fig. 7 of Ref. [149] and scaled from $P(e^-, e^+) = (-0.8, +0.3)$ to $P(e^-, e^+) = (-0.8, +0.2)$. The unpolarized CLIC SM cross sections are taken from Ref. [43].

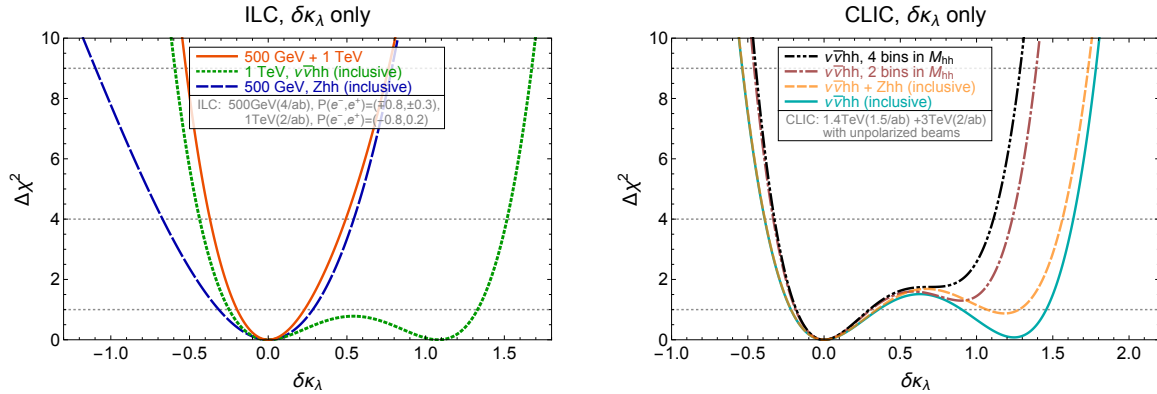


Figure 4.8: Chi-square for the exclusive fit of $\delta\kappa_\lambda$ for various combinations of Higgs pair production measurements at the ILC (left) and CLIC (right).

the precision on double Higgsstrahlung at 1 TeV and above.

It is interesting to notice that, around the SM point, the sensitivity of both Higgs pair production channels to $\delta\kappa_\lambda$ gets milder at higher center-of-mass energy. On the contrary, the sensitivity to the other EFT parameters tends to increase with energy. Another important feature is the significant impact of terms quadratic in $\delta\kappa_\lambda$ on the behavior of the cross section around the SM point, especially for the WW -fusion channel shown in the right panel of Fig. 4.7. For this reason, a linear approximation is in many cases not sufficient to extract reliable bounds. In Table 4.2, we list the 68% and 95% CL bounds obtained from the benchmarks ILC and CLIC runs retaining the full dependence of the cross section on $\delta\kappa_\lambda$.

From Fig. 4.7, one can see that the interference between diagrams with and without a trilinear Higgs vertex has opposite sign in double Higgsstrahlung and WW -fusion. These two processes are thus more sensitive to positive and negative values of $\delta\kappa_\lambda$ respectively. A combination of double Higgsstrahlung and WW -fusion measurements could hence be used to maximize the precision for both positive and negative values of $\delta\kappa_\lambda$. Such a scenario could be achieved at the ILC through the combination of a 500 GeV and a 1 TeV run. The impact of such combination can be clearly seen from the plot in the left panel of Fig. 4.8.

Being quadratic functions of $\delta\kappa_\lambda$, inclusive cross sections (for each process and collider energy) can match the SM ones not only for $\delta\kappa_\lambda = 0$, but also for an additional value of the trilinear Higgs self-coupling, resulting in a second minimum in the $\Delta\chi^2$. In WW -fusion, the SM cross section is also obtained for $\delta\kappa_\lambda \simeq 1.08$, 1.16 and 1.30 at center-of-mass energies of 1, 1.4 and 3 TeV, respectively. Whereas, for double Higgsstrahlung at 500 GeV, the SM cross section is recovered at $\delta\kappa_\lambda \simeq -5.8$. This latter solution poses no practical problem for ILC since it can be excluded by HL-LHC measurements. Alternatively, it can be constrained by Higgs pair production through WW -fusion at 1 TeV, as well as through the indirect sensitivity of single Higgs measurements.

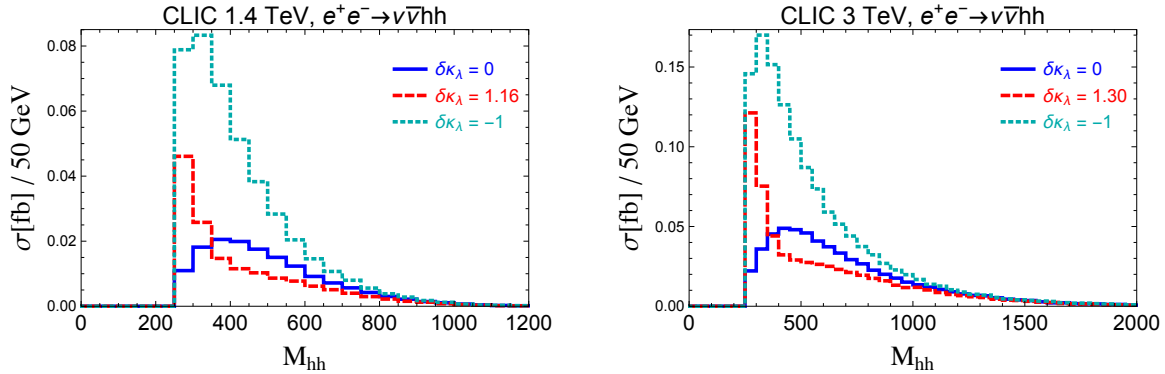


Figure 4.9: Invariant mass distribution of the Higgs pair in $e^+e^- \rightarrow \nu\bar{\nu}hh$ at 1.4 TeV (left) and 3 TeV (right). The solid blue curves are obtained in the SM ($\delta\kappa_\lambda = 0$). The red dashed curves are obtained with the other value of $\delta\kappa_\lambda$ which leads to a cross section equal to the SM one. The cyan dotted curves are obtained for vanishing Higgs self-coupling ($\delta\kappa_\lambda = -1$).

For CLIC, the secondary solutions at $\delta\kappa_\lambda \simeq 1$ are more problematic. They can be constrained neither by HL-LHC data, nor by single Higgs measurements which are mostly efficient close to the threshold of the single Higgsstrahlung production. A more promising possibility is to exploit double Higgsstrahlung rate measurements. At center-of-mass energies above 1 TeV, however, they only provide weak handles on $\delta\kappa_\lambda$. The $e^+e^- \rightarrow Zhh$ cross section becomes relatively small, being only 0.08 fb at 1.4 TeV with unpolarized beams. Moreover, the sensitivity to the trilinear Higgs self-coupling decreases with energy, as shown in Fig. 4.7. Since the experimental collaborations did not provide an estimate for the CLIC precision achievable on the SM $e^+e^- \rightarrow Zhh$ rate, we estimate it by naively rescaling the ILC 500 GeV projections by the total cross section at CLIC. We find that adding this information to inclusive $e^+e^- \rightarrow \nu\bar{\nu}hh$ rates measurements only excludes the second minimum to the 1σ level (dashed orange line in the right panel of Fig. 4.8).

In addition, we consider the possibility of performing a differential analysis of double Higgs production through WW -fusion, studying whether a fit of the Higgs pair invariant mass distribution M_{hh} can be sufficient to further exclude the $\delta\kappa_\lambda \simeq 1$ points. The M_{hh} distribution shows a good sensitivity to the Higgs trilinear, which mainly affects the shape of the distribution close to the kinematic threshold. This can be observed in Fig. 4.9, obtained at the parton level with MadGraph5 [151] (with FeynRules [152] and the BSMC Characterisation model [153]) for 1.4 and 3 TeV center-of-mass energies. The solid blue curves correspond to the SM point $\delta\kappa_\lambda = 0$. The dashed red curves are obtained for the other value of $\delta\kappa_\lambda$ at which the $\nu\bar{\nu}hh$ coincides with the SM value ($\delta\kappa_\lambda = 1.16$ for 1.4 TeV and $\delta\kappa_\lambda = 1.30$ for 3 TeV). The dotted cyan distributions are obtained for vanishing trilinear Higgs self-coupling ($\delta\kappa_\lambda = -1$).

We estimate the impact of a differential analysis of the $\nu\bar{\nu}hh$ channel by performing

	2 bin boundaries [GeV]		4 bin boundaries [GeV]			
1.4 TeV	250-400	400-1400	250-350	350-500	500-600	600-1400
3 TeV	250-500	500-3000	250-450	450-650	650-900	900-3000

Table 4.3: Definitions of the bins used in the Higgs-pair invariant mass distribution of $e^+e^- \rightarrow \nu\bar{\nu}hh$ at 1.4 TeV and 3 TeV.

a simple fit of the M_{hh} invariant mass distribution. We consider either two or four bins, whose ranges are listed in Table 4.3. For simplicity, we work at parton level and assume a universal signal over background ratio across all bins. The right panel of Fig. 4.8 summarizes the result of the fits. It shows that a differential analysis can be useful in enhancing the precision on $\delta\kappa_\lambda$. In particular, it allows us to exclude the second fit solution $\delta\kappa_\lambda \simeq 1.3$ at the 68% CL, and to reduce significantly the 95% CL bounds for positive deviations in the Higgs self-coupling. For instance, the 4-bin fit restricts $\delta\kappa_\lambda$ to the range $[-0.18, 0.30]$ at 68% CL and $[-0.33, 1.11]$ at 95% CL.

4.3.2 Global analysis

It is important to verify whether the results discussed in Section 4.3.1, obtained assuming new physics affects only the triple Higgs coupling, are robust in a global framework once all other EFT parameters are taken into consideration. We therefore perform a global analysis at ILC and CLIC including measurements of both double-Higgs (Higgsstrahlung and WW -fusion) and single-Higgs processes ($\nu\bar{\nu}h$, Zh , $t\bar{t}h$ and e^+e^-h) in addition to diboson production.

We adopt the following benchmark scenarios chosen by the experimental collaborations for Higgs measurement estimates:

- **ILC:** we follow the scenario in Ref. [54], assuming ILC can collect 2 ab^{-1} at 250 GeV, 200 fb^{-1} at 350 GeV and 4 ab^{-1} at 500 GeV, equally shared between the $P(e^-, e^+) = (\pm 0.8, \mp 0.3)$ beam polarizations. We also consider the possibility of an additional run at 1 TeV gathering 2 ab^{-1} with one single $P(e^-, e^+) = (-0.8, +0.2)$ beam polarization.
- **CLIC:** we follow Ref. [43] and assume 500 fb^{-1} at 350 GeV, 1.5 ab^{-1} at 1.4 TeV and 2 ab^{-1} at 3 TeV can be collected with unpolarized beams. It should be noted that a left-handed beam polarization could increase the $\nu\bar{\nu}hh$ cross section and somewhat improve the reach on $\delta\kappa_\lambda$.

For the global fit, we follow the procedure and assumptions adopted for the single Higgs processes fit at low-energy colliders. We also include the one-loop dependence on $\delta\kappa_\lambda$ in single Higgs production and decay processes, as done in Section 4.2. Such effects are also included in the top-Higgs associated production $e^+e^- \rightarrow t\bar{t}h$ and in ZZ -fusion

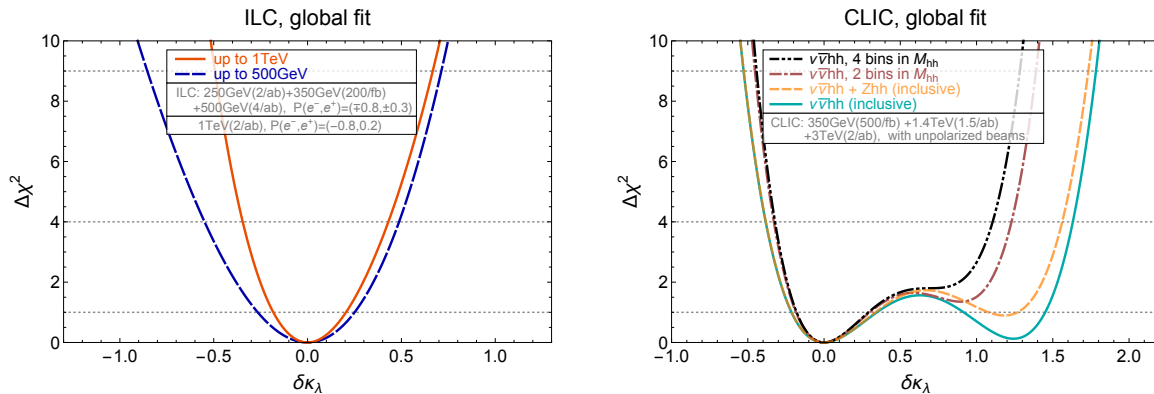


Figure 4.10: Chi-square as a function of $\delta\kappa_\lambda$ for the high-energy ILC (left) and CLIC (right) benchmarks. The results are obtained through a global analysis, profiling over all other EFT parameters.

$e^+e^- \rightarrow e^+e^-h$, although they have a negligible impact. On the other hand, only the tree-level Higgs self-coupling dependence is considered in Higgs pair production processes, since one-loop corrections are numerically insignificant. As already stressed, the quadratic dependence on $\delta\kappa_\lambda$ in Higgs pair production processes cannot be neglected. In this case, cross terms between $\delta\kappa_\lambda$ and other EFT parameters are also accounted for. The linear approximation is adopted elsewhere. The estimates for the precision of the SM Higgs pair production cross section are taken from Refs. [43, 148, 150] already discussed in the previous section.

The results of the global fit for the ILC and CLIC benchmark scenarios are shown in Fig. 4.10. The 68% and 95% CL intervals are also listed in Table 4.4. It is interesting to compare these results with the ones obtained through the exclusive fit on $\delta\kappa_\lambda$ discussed in Section 4.3.1 (see Fig. 4.8). The χ^2 curves for ILC (up to 500 GeV or 1 TeV) and CLIC (no binning, 2 bins and 4 bins in M_{hh}) show very mild differences in the global fit with respect to the exclusive one. This demonstrates that the additional EFT parameters are sufficiently well constrained by single Higgs measurements and therefore have a marginal impact on the global fit. We also analyzed the impact of combining ILC and CLIC measurements with HL-LHC ones. The precision achievable at the LHC is significantly poorer than the one expected at high-energy lepton colliders, so that the latter dominate the overall fit and only a mild improvement is obtained by combination.

We saw that allowing for other EFT deformations beside $\delta\kappa_\lambda$ does not worsen the global fit significantly. This result, however, was by no means guaranteed. To stress this point, we display in Fig. 4.11 the profiled χ^2 obtained by artificially rescaling the precision in single Higgs measurements. The ILC (up to 500 GeV, left panel) and CLIC (no binning in M_{hh} , right panel) benchmarks are used as examples. For each collider, we show the results of the exclusive $\delta\kappa_\lambda$ analysis of the Higgs pair production measurements (solid black curve) and of the global analysis (dashed blue/cyan). The additional dashed

	68 %CL	95%CL
ILC up to 500 GeV	$[-0.27, 0.25]$	$[-0.55, 0.49]$
ILC up to 1 TeV	$[-0.18, 0.20]$	$[-0.35, 0.43]$
CLIC	$[-0.22, 0.36] \cup [0.91, 1.45]$	$[-0.39, 1.63]$
+ Zhh	$[-0.22, 0.35] \cup [1.07, 1.27]$	$[-0.39, 1.56]$
2 bins in $\nu\bar{\nu}hh$	$[-0.19, 0.31]$	$[-0.33, 1.23]$
4 bins in $\nu\bar{\nu}hh$	$[-0.18, 0.30]$	$[-0.33, 1.11]$

Table 4.4: Precision on the determination of $\delta\kappa_\lambda$ obtained through a global fit including pair- and single-Higgs production channels for several benchmark scenarios at ILC and CLIC.

curves correspond to global fits in which the precision in single Higgs and diboson measurements is rescaled by factors ranging from 0.5 to 10. It can be seen that the global fit is sizably affected by such a rescaling, in particular the fit precision is significantly degraded if single Higgs measurements become worse. This result shows that a comprehensive global analysis of the single Higgs measurements is crucial for obtaining robust constraints on $\delta\kappa_\lambda$. Notice moreover that an improved precision on single Higgs measurements could have a positive impact on the determination of the Higgs self coupling at the ILC.

The impact of the uncertainty on the EFT parameters measurements on the extraction of the Higgs self-coupling from Higgs pair production was also recently investigated in Ref. [141]. It focused mainly on Higgs pair production through double Higgsstrahlung at ILC 500 GeV and on single-Higgs production in lower-energy runs, taking into account the uncertainties on SM parameters and electroweak precision observables. Loop-level contributions to single-Higgs processes coming from a modified Higgs self-coupling were not included in the fit, and the linear approximation was used to obtain the numerical results. The final fit takes into account runs at 250 and 500 GeV, with 2 and 4 ab^{-1} respectively equally shared between $P(e^-, e^+) = (\mp 0.8, \pm 0.3)$ beam polarizations. The estimated precision on the measurement of $\delta\kappa_\lambda$ is 30%, which is in good agreement with the constraints we obtained in our ILC benchmark scenario.

4.4 Summary

We summarize in this section the results of [chapter 3](#) and [chapter 4](#) for the global determination of the Higgs self-coupling at hadron and lepton colliders.

The possibility of exploiting single-Higgs production channels at hadron colliders to extract information about the Higgs trilinear self-coupling has been recently put forward in the literature [61–63]. The available results are quite encouraging. They show that the

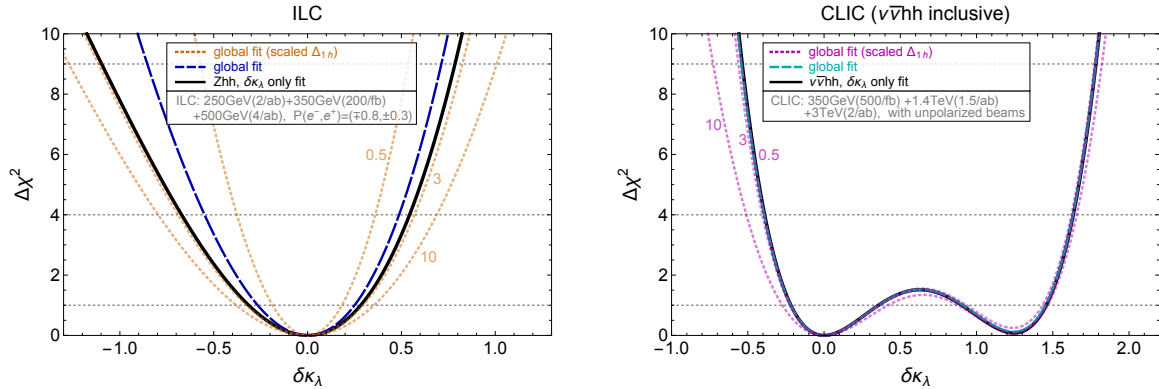


Figure 4.11: **Left:** Chi-square profiled over all EFT parameters but $\delta\kappa_\lambda$ for ILC (up to 500 GeV). **Right:** The same for CLIC (no binning in M_{hh}). Three scenarios are shown. The solid black curves correspond to the $\delta\kappa_\lambda$ only fit from the double-Higgs measurements. The dashed blue/cyan curves correspond to the global fits in Fig. 4.10. The additional dashed curves are obtained by rescaling the uncertainties of single Higgs measurements (including $e^+e^- \rightarrow WW$) by an overall factor. For example, $\Delta_{1h} \times 10$ denotes that the uncertainties of the single Higgs and diboson measurements are multiplied (worsened) by a factor 10.

new analysis strategy could be competitive with the study of double-Higgs production, which is usually considered the best way to probe the Higgs self-interactions.

The analyses performed so far, however, limited their focus to scenarios in which the only deformation of the SM Lagrangian is a modification of the Higgs potential. This assumption significantly restricts the realm of theories for which the new results are valid. Indeed, in a vast class of new-physics models, corrections to the Higgs trilinear coupling are not generated alone and additional deviations in the other Higgs interactions are simultaneously present. Since the Higgs self-coupling only affects at next-to-leading order the single-Higgs rates, its effects can be easily overwhelmed by even small modifications of the single-Higgs couplings. In this more generic situation a global analysis, taking into account deviations in all the Higgs couplings simultaneously, is essential to fully assess the achievable accuracy. The computations of refs. [61–63] are an essential building block that can be directly implemented in a global fit with all the parameters affecting the Higgs couplings turned on simultaneously.

For definiteness we studied deformations of the SM Lagrangian given by dimension-6 effective operators in the SMEFT framework. In particular, in addition to deviations in the Higgs self-coupling, we considered distortions of the single-Higgs couplings due to a set of 9 operators that can not be tested with $\%$ precision in measurements not involving the Higgs. In the Higgs basis these deformations are encoded in the coefficients δc_z , c_{zz} , $c_{z\Box}$, $\hat{c}_{z\gamma}$, $\hat{c}_{\gamma\gamma}$ and \hat{c}_{gg} which correspond to deformations of the Higgs couplings to gauge bosons, and δy_t , δy_b and δy_τ controlling deformations of the Yukawa’s.

To derive our numerical results we considered the high-luminosity LHC upgrade (14 TeV center of mass energy and 3/ab integrated luminosity) and we estimated the precision on single-Higgs measurements through a benchmark derived from the ATLAS and CMS projections [80, 82] (see table 3.1). Moreover we assumed that the central values of the future experimental measurements will coincide with the SM predictions.

We found that, if only single-Higgs observables are considered, a global fit involving the 10 free parameters has an (almost) exact flat direction. The flat direction is mostly aligned along the Higgs self-coupling κ_λ , the top Yukawa δy_t and the contact interaction with gluons \hat{c}_{gg} , with minor components along δc_z , δy_b and δy_τ (see fig. 3.1). The inclusion of trilinear gauge couplings measurements can only partially lift the flat direction. Very large deviations in κ_λ are however still allowed, so that the Higgs self-interaction remains practically unbounded (see fig. 3.2). This result clearly shows that the bounds obtained by an exclusive fit including only κ_λ ($\kappa_\lambda \in [-1.1, 4.7]$ at the 1σ level) must be interpreted with great care and are fully valid only in very specific BSM scenarios.

Large deviations in the Higgs self-coupling can also have a back-reaction on the extraction of single-Higgs couplings. As can be seen from Fig. 3.3, if large corrections, $|\delta\kappa_\lambda| \sim 10$, are allowed, the precision in the determination of the single-Higgs couplings is significantly degraded. This results shows the necessity of including in the global fit additional observables which could resolve the flat direction.

We explored two possible extensions of the fitting procedure, namely the inclusion of double-Higgs production via gluon fusion and the use of differential measurements in the associated single-Higgs production channels WH , ZH and $t\bar{t}H$.

As expected, an inclusive double Higgs production measurement can efficiently remove the flat direction, constraining the Higgs trilinear coupling to the range $\kappa_\lambda \in [0.0, 2.5] \cup [4.9, 7.4]$ at the 1σ confidence level (see fig. 3.4). Furthermore, differential double-Higgs distributions can provide additional help to probe large positive deviations in the Higgs trilinear. In particular they can be used to test the additional best fit point at $\kappa_\lambda \sim 6$ and to reduce the 2σ fit range (see right panel of Fig. 3.4). When double-Higgs measurements are included, the constraint on the Higgs trilinear coupling becomes $\kappa_\lambda \in [0.1, 2.3]$ at the 1σ confidence level, which is strong enough to ensure that the back-reaction on the single-Higgs couplings fit is almost negligible at the high-luminosity LHC. This result proves that neglecting the contributions from κ_λ when performing a fit on single Higgs couplings is a sensible procedure, even in BSM scenarios that can lead to $\mathcal{O}(1)$ deviations in the Higgs self-interactions.

The measurement of the differential distributions in the associated Higgs production channels can also help in determining the Higgs self-coupling. We performed a preliminary analysis with a simplified treatment of the experimental and theory uncertainties. We found that an exclusive fit on κ_λ can provide order one sensitivity ($\kappa_\lambda \in [-1, 3]$ at 1σ), roughly comparable with the one achievable through double-Higgs measurements (see fig. 3.5). On the other hand, in a global analysis, including deviations in single-Higgs

couplings, the sensitivity on κ_λ is strongly reduced and only large deviations $|\delta\kappa_\lambda| \gtrsim 5$ can be probed. Nevertheless, also in this case single-Higgs differential observables can be useful. Combining them with double-Higgs measurements can significantly help to constrain large positive corrections to the Higgs trilinear. To fully evaluate the impact of the differential observables a more careful analysis strategy, together with a detailed assessment of the experimental uncertainties, would be needed. We leave this subject for future work.

Another important aspect we investigated is the dependence of our results on the experimental uncertainties and on the assumptions underlying the EFT parametrization. As shown in the left panel of Fig. 3.6, a naive rescaling of all the experimental uncertainties in single-Higgs production affects only mildly the bounds on negative contributions to κ_λ , but has a major impact on the constraints on positive corrections (in particular at the 2σ confidence level).

The assumptions on the EFT description can also strongly modify the determination of κ_λ . As an illustrative example we considered a non-linear EFT Lagrangian in which the double-Higgs couplings to gluons and to tops are treated as independent parameters. This change affects almost exclusively the precision on the Higgs self-coupling, which is reduced by roughly a factor 3 (right panel of Fig. 3.6). On the contrary, the global fit on the single-Higgs couplings is much more stable and only the determination of \hat{c}_{gg} and δy_t becomes marginally worse.

We also analyzed the precision reach on the determination of the Higgs trilinear self-coupling at future lepton colliders. We covered a comprehensive set of scenarios including low-energy and high-energy machines. The former can only access the Higgs self-interaction indirectly through NLO corrections to single Higgs processes. High-energy colliders can instead test deviations in the Higgs trilinear coupling directly, through the measurement of Higgs pair production, in particular double Higgsstrahlung and WW -fusion.

The results of the analysis are summarized in Fig. 4.12 for the various benchmark scenarios considered. For each scenario, three sets of bounds are shown. Thin lines with vertical ends show the precision expected from measurements at lepton colliders only. The superimposed thick bars combine them with HL-LHC measurements. Finally, the thin solid and dotted lines are obtained by combining single Higgs measurements only at lepton colliders ($1h$) with the HL-LHC bounds. As discussed in the main text, unpolarized beams are assumed for the CEPC, FCC-ee and CLIC. For the ILC runs up to 500 GeV, an equal share of the luminosity at the two $P(e^-, e^+) = (\pm 0.8, \mp 0.3)$ beam polarizations is assumed, whereas a single polarization $P(e^-, e^+) = (-0.8, +0.2)$ is adopted at 1 TeV.

We found that a global analysis is essential to derive robust bounds on $\delta\kappa_\lambda$. This is the case, in particular, if only low-energy lepton machines, such as CEPC or FCC-ee, are available. In this scenario, the Higgs self-coupling can be determined with good

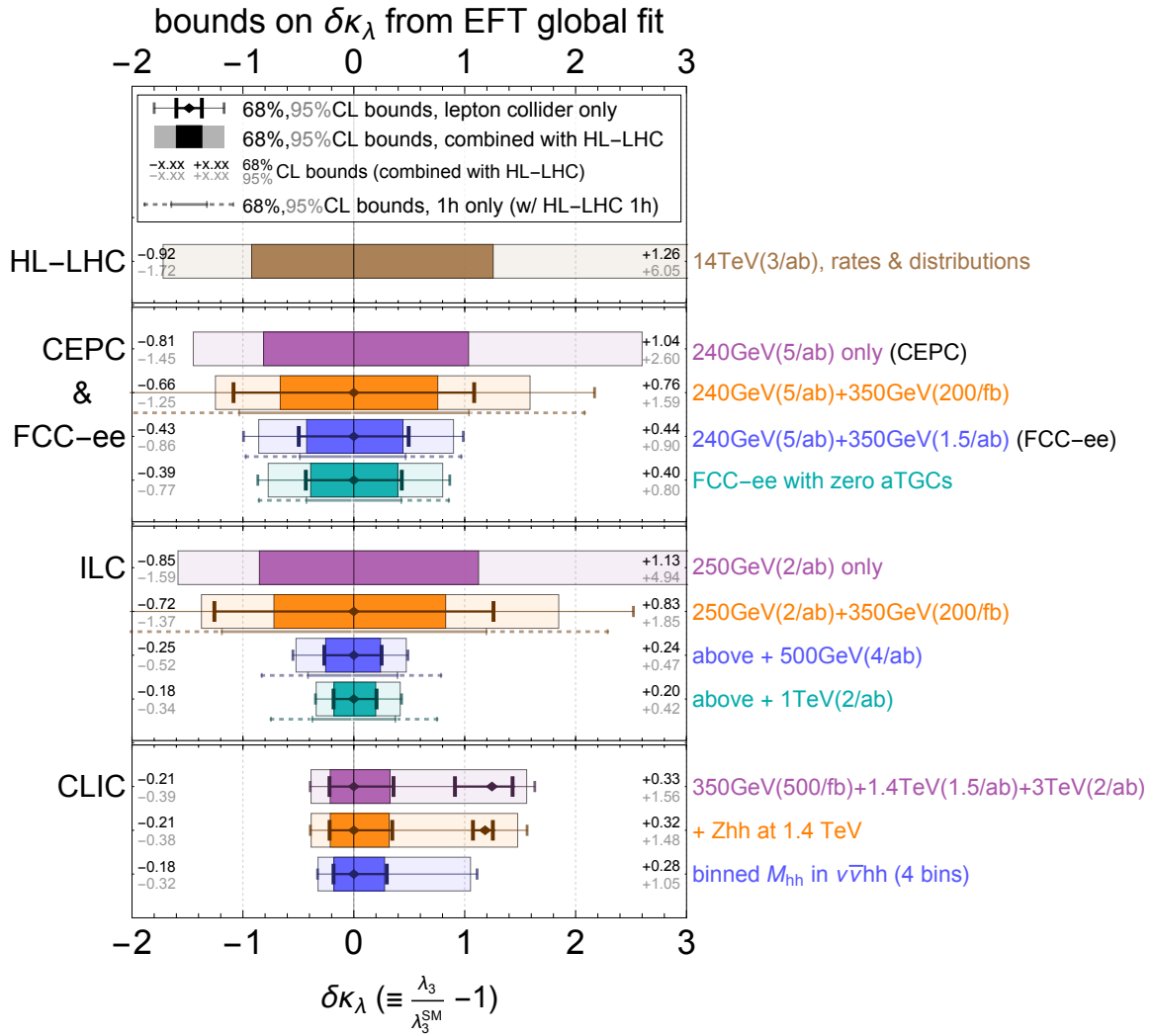


Figure 4.12: A summary of the bounds on $\delta\kappa_\lambda$ from global fits for various future collider scenarios. For the “1h only” scenario, only single Higgs measurements at lepton colliders are included.

accuracy, around 40% at the 68% CL, by exploiting single Higgs measurements in the $\nu\bar{\nu}h$ and Zh channels as well as diboson production. In order to achieve this accuracy, it is essential to combine runs at different center-of-mass energy, for instance at 240 GeV and at 350 GeV, both with luminosities in the few attobarns range. Measurements at a single energy, in fact, leave a nearly flat direction unresolved in the global fit and lead to a very poor determination of $\delta\kappa_\lambda$. Runs at two different energies can instead significantly reduce the flat direction by constraining with better accuracy on the other EFT parameters.

The high-energy linear colliders making direct measurements of the triple Higgs self-coupling through pair production still provide the best constraints. Double Higgsstrahlung and WW -fusion yield complementary information, being more sensitive to

positive and negative deviations in the Higgs self-coupling respectively. It is interesting to notice that the dependence of these two processes on $\delta\kappa_\lambda$ is stronger at lower center-of-mass energy, as shown in Fig. 4.7, so that ILC runs at 500 GeV and 1 TeV energy maximize the overall precision allowing for a determination of the trilinear Higgs self-coupling with a 20% uncertainty approximately, at the 68% CL.

High-energy measurements alone, such as the ones available with the 1.4 and 3 TeV CLIC runs, can only rely on $\nu\bar{\nu}hh$ production and have limited sensitivity to positive deviations in $\delta\kappa_\lambda$. In this case, a second minimum in the global fit is present for $\delta\kappa_\lambda \sim 1$. The additional minimum can be excluded by performing a differential analysis exploiting the Higgs pair invariant mass distribution, whose threshold behavior is strongly sensitive to deviations in the Higgs self-coupling. A differential analysis can provide an order-20% determination of $\delta\kappa_\lambda$ at 68% CL, however at 95% CL values $\delta\kappa_\lambda \simeq 1$ would still be allowed.

It is interesting to compare the above results with the ones achievable at the HL-LHC and at possible future hadron colliders. The HL-LHC is expected to be sensitive only to deviations of $\mathcal{O}(1)$ in the Higgs self-coupling. As one can see from Fig. 4.12, this precision is comparable to (or better than) the one achievable at low-energy lepton colliders with low integrated luminosity at 350 GeV runs. This is the case for our circular collider benchmarks with 200 fb^{-1} integrated luminosity at 350 GeV, as well as for the low-energy runs of the ILC. In these scenarios the HL-LHC data will still play a major role in the determination of $\delta\kappa_\lambda$, while lepton colliders always help constraining large positive $\delta\kappa_\lambda$ that the HL-LHC fails to exclude beyond the one-sigma level. On the other hand, with 1 ab^{-1} of luminosity collected at 350 GeV, the lepton collider data starts dominating the combination.

The situation is instead different at high-energy hadron colliders which can benefit from a sizable cross section in double Higgs production through gluon fusion. A pp collider with 100 TeV center-of-mass energy is expected to determine $\delta\kappa_\lambda$ with a precision of order 5% [42], thus providing a better accuracy than lepton machines. Intermediate-energy hadron machines, such as a high-energy LHC at 27 – 33 TeV could instead provide a precision comparable to that of high-energy lepton colliders. A rough estimate of the $\delta\kappa_\lambda$ determination at a 27 TeV pp collider gives a $\sim 30\%$ precision at 68% CL for an integrated luminosity of 10 ab^{-1} .

To conclude the discussion, let us come back to our assumption of perfectly well measured electroweak precision observables. It seems fully justified if low-energy runs at the Z -pole are performed. This could for instance be the case at the ILC, CEPC, and FCC-ee which could respectively produce 10^9 , 10^{10} , and 10^{12} Z bosons. A Z -pole run for these machines can provide significant improvements with respect to LEP measurements ($2 \cdot 10^7$ Z bosons), making electroweak precision observables basically irrelevant for the extraction of the Higgs trilinear self-coupling.

Without a new Z -pole run, evaluating the impact of a limited accuracy on elec-

electroweak precision observables might be less straightforward. An analysis of such scenario for the ILC collider has been recently presented in Ref. [141]. This work explicitly includes present constraints on m_Z , the A_ℓ asymmetry at the Z -pole, $\Gamma_{Z\rightarrow ll}$, Γ_Z , Γ_W and forecasts for improved m_W , m_H , and Γ_W measurements, assuming no new run at the Z -pole. In that scenario, it is argued that Higgs measurements can be used to improve the constraints on the electroweak parameters. The achievable precision is sufficient to ensure that electroweak precision observables do not significantly affect the determination of $\delta\kappa_\lambda$.

The precision necessary to decouple electroweak and Higgs parameters determinations in other benchmark scenarios might deserve further exploration. We think that electroweak precision measurements will have a negligible impact on trilinear Higgs self-coupling determination at high-energy machines where Higgs pair production is accessible. This conclusion is supported by the results of Section 4.3 showing that the determination of $\delta\kappa_\lambda$ is only mildly affected by the other EFT parameters, once a wide-enough set of single Higgs measurements is considered. The situation for low-energy colliders, in which the Higgs self-coupling can be accessed only indirectly through single Higgs processes, is instead less clear. As we saw in Section 4.2, the precision on $\delta\kappa_\lambda$ obtained through a global fit is significantly lower than the one estimated through an exclusive analysis. Consequently, the precision of the single-Higgs and triple-gauge coupling extractions has a relevant impact on the fit. In principle, electroweak precision parameters could affect the bounds on single Higgs couplings and thus indirectly degrade the $\delta\kappa_\lambda$ constraint. This aspect might be worth a more careful investigation, which is however beyond the scope of the present work.

Chapter 5

Probing the Electroweak Phase Transition via Enhanced Di-Higgs Production

5.1 Introduction

Probing the intriguing possibility of electroweak baryogenesis [154–158] becomes of higher relevance after the SM Higgs boson discovery at the LHC [1, 2]. In such mechanism, a strongly first-order electroweak phase transition (EWPT) is a crucial ingredient to maintain the matter-antimatter asymmetry generated at the electroweak scale [159]. The SM Higgs potential is insufficient to provide such condition and many extensions of the SM have hence been proposed [129, 160–192]. Generically, including additional bosonic degrees of freedom with sizable coupling strength to the SM Higgs boson can increase the barrier between the broken and unbroken electroweak vacua at the critical temperature of the phase transition, see e.g., Ref. [193]. Amongst many of the possibilities, the singlet scalar extension of the SM is of particular interest [177–180]. Due to its singlet nature, the scalar is hard to be probed at the LHC. Therefore the singlet SM extension serves as the simplest, yet elusive benchmark to test a sufficiently strong first order phase transition compatible with the Higgs boson mass measurements at the LHC [176, 177].

The scalar potential of a real singlet scalar extension of the SM can be further categorized into three types, depending on the behavior of the real singlet s under the Z_2 parity operation $s \rightarrow -s$, namely: the Z_2 symmetric, the spontaneous Z_2 breaking, and the general potential. The Z_2 symmetric potential leads to a stable singlet scalar, resulting in the singlet being a possible dark matter candidate and yielding missing energy signals at colliders [177]. Without Z_2 protection, the singlet would mix with the SM Higgs and (in most cases) a promptly decaying scalar particle would provide a rich phenomenology at colliders. The singlet scalar could be produced resonantly and decay

back to pairs of SM particles, dominantly into WW , ZZ , HH and $t\bar{t}$. The signal of a singlet scalar resonance decaying into HH is a smoking-gun for singlet enhanced EWPT [59, 179, 180, 194–199].

Searches for resonant di-Higgs production have received much attention by both the ATLAS and CMS collaborations [200–205]. In the case of a singlet resonance, constraints from SM precision measurements render these searches more challenging. From one side precision measurements imply that the singlet-doublet mixing parameter is constrained to be small over a large region of parameter space. From the other side, the singlet only couples to SM particles through mixing with the SM Higgs doublet. This results in a reduced di-Higgs production via singlet resonance decays. In particular, the singlet resonance amplitude becomes of the same order as the SM triangle and box diagram amplitudes. Most important, in this work we shall show that a large relative phase between the SM box diagram and the singlet triangle diagram becomes important. This special on-shell interference effect has been commonly overlooked in the literature and turns out to have important phenomenological implications. We shall choose the spontaneous Z_2 breaking scenario of the SM plus singlet to demonstrate the importance of the novel on-shell interference effect for the resonant singlet scalar searches in the di-Higgs production mode.

5.2 Model framework

We will consider the simplest extension of the SM that can assist the scalar potential to induce a strongly first order electroweak phase transition, consisting of an additional real scalar singlet with a Z_2 symmetry. The scalar potential of the model can be written as

$$V(s, \phi) = -\mu^2 \phi^\dagger \phi - \frac{1}{2} \mu_s^2 s^2 + \lambda (\phi^\dagger \phi)^2 + \frac{\lambda_s}{4} s^4 + \frac{\lambda_{s\phi}}{2} s^2 \phi^\dagger \phi, \quad (5.2.1)$$

where ϕ is the SM doublet¹ and s represents the new real singlet field. In the above, we adopt the conventional normalization for the couplings of the SM doublets and match the other couplings with the singlet with identical normalization. We allow for spontaneous Z_2 breaking with the singlet s acquiring a vacuum expectation value (vev) v_s , since this case allows for interesting collider phenomenology of interference effects. As we shall show later, the (on-shell) interference effects commonly exist for loop-induced processes in BSM phenomenology and it is the focus of this work. The CP even neutral component h of the Higgs doublet field ϕ mixes with the real singlet scalar s , defining the new mass eigenstates H and S

$$\begin{pmatrix} h \\ s \end{pmatrix} = \begin{pmatrix} \cos \theta & \sin \theta \\ -\sin \theta & \cos \theta \end{pmatrix} \begin{pmatrix} H \\ S \end{pmatrix}, \quad (5.2.2)$$

¹ $\phi^T = (G^+, \frac{1}{\sqrt{2}}(h + iG^0 + v))$, where $G^{\pm,0}$ are the Goldstone modes.

where θ is the mixing angle between these fields. The five free parameters in Eq.(5.2.1) can be traded by the two boundary conditions

$$m_H = 125 \text{ GeV}, \quad v = 246 \text{ GeV} \quad (5.2.3)$$

and the three ‘‘physical’’ parameters,

$$m_S, \quad \tan \beta (\equiv \frac{v_s}{v}), \quad \text{and} \quad \sin \theta, \quad (5.2.4)$$

where $\tan \beta$ characterizes the ratio between the vevs of the doublet and the singlet scalar fields, respectively.

As a result, the parameters in the scalar potential in Eq.(5.2.1) can be expressed as functions of these new parameters,

$$\mu^2 = \frac{1}{4} (2m_H^2 \cos^2 \theta + 2m_S^2 \sin^2 \theta + (m_S^2 - m_H^2) \tan \beta \sin 2\theta) \quad (5.2.5)$$

$$\mu_s^2 = \frac{1}{4} (2m_H^2 \sin^2 \theta + 2m_S^2 \cos^2 \theta + (m_S^2 - m_H^2) \cot \beta \sin 2\theta) \quad (5.2.6)$$

$$\lambda = \frac{m_H^2 \cos^2 \theta + m_S^2 \sin^2 \theta}{2v^2} \quad (5.2.7)$$

$$\lambda_s = \frac{m_H^2 \sin^2 \theta + m_S^2 \cos^2 \theta}{2 \tan^2 \beta v^2} \quad (5.2.8)$$

$$\lambda_{s\phi} = \frac{(m_S^2 - m_H^2) \sin 2\theta}{2 \tan \beta v^2}. \quad (5.2.9)$$

Observe that the condition of spontaneous symmetry breaking implies that dimensionful quantities μ^2 and μ_s^2 can be directly expressed in terms of the original quartic couplings and the vevs,

$$\mu^2 = v^2 \left(\lambda + \frac{1}{2} \tan^2 \beta \lambda_{s\phi} \right), \quad \mu_s^2 = v^2 \left(\tan^2 \beta \lambda_s + \frac{1}{2} \lambda_{s\phi} \right). \quad (5.2.10)$$

5.2.1 Stability, Unitarity and EWSB conditions

It is useful to understand the quartic couplings in the potential in Eq.(5.2.1) in terms of the physical parameters defined in Eq.(5.2.4), since the physical parameters make a straightforward connection with collider physics. In Fig. 5.1 we show the three independent quartic couplings in the Z_2 -symmetric potential λ , λ_s and $\lambda_{s\phi}$ in blue, red, and black contours, respectively, as a function of the heavy singlet-like scalar mass m_S and the singlet-doublet mixing angle $\sin \theta$ for $\tan \beta = 1$ (left panel) and $\tan \beta = 10$ (right panel). As shown in the red contours, for low values of $\tan \beta$, a large quartic λ_s is needed to obtain a heavy singlet, due to the fact that the singlet mass and its vev are related via its quartic coupling, see Eq.(5.2.8). However, the correlation between the singlet quartic, its mass and its vev is only mildly dependent on the mixing angle $\sin \theta$. A

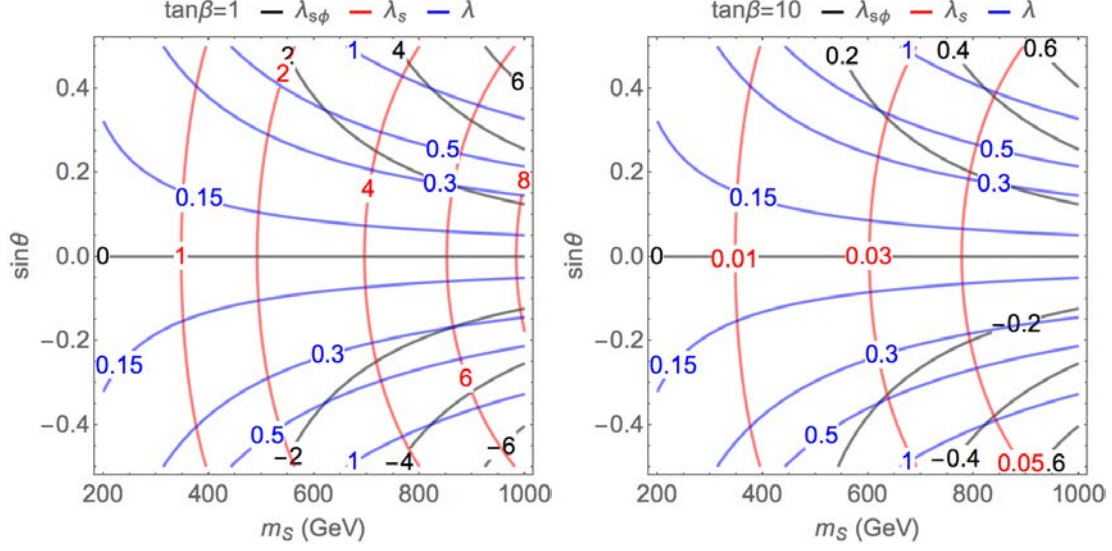


Figure 5.1: The values of the quartic couplings λ , λ_s and $\lambda_{s\phi}$ as a function of the singlet-like scalar mass m_S and the mixing angle $\sin\theta$ shown in blue, red and black contours, respectively. The left and right panels correspond to $\tan\beta$ values of 1 and 10, respectively.

different behavior occurs for the Higgs quartic, in blue, being independent of the singlet vev but sensitive to the mixing angle.

The stability of the potential and the perturbative unitarity arguments set constraints on the allowed sizes and signs of the quartic couplings that we will discuss now. The requirement of the potential being bounded from below leads to the conditions to the quartic couplings

$$\lambda, \lambda_s > 0 \text{ and } \lambda_{s\phi} > -2\sqrt{\lambda\lambda_s}. \quad (5.2.11)$$

The positivity of the Higgs and singlet quartic couplings is understood by considering large field values in the directions $\{h, 0\}$ and $\{0, s\}$. The extra condition arises from considering large field values in an arbitrary direction. We see that negative values for the mixing quartic coupling $\lambda_{s\phi}$ are allowed if the other two quartics are large enough.

Furthermore, the spontaneous Z_2 and electroweak symmetry breaking vacuum $\langle \phi, s \rangle = \{v/\sqrt{2}, v_s\}$ is a global minimum if the following is satisfied

$$\lambda_{s\phi} < +2\sqrt{\lambda\lambda_s}. \quad (5.2.12)$$

For larger values of $\lambda_{s\phi}$, the electroweak and Z_2 breaking vacuum becomes a saddle point and the minima are located at $\langle \phi, s \rangle = \{v/\sqrt{2}, 0\}$ and $\langle \phi, s \rangle = \{0, v_s\}$ ².

²Note that the expressions for the vevs in terms of model parameters differ for the different extrema under discussion. We denote them using the same symbols, $v/\sqrt{2}$ and v_s , since the discussion in this section does not rely on their precise values.

Observe that for positive values of μ^2 and μ_s^2 the origin $\langle \phi, s \rangle = \{0, 0\}$ is always a maximum.

The conditions Eq. (5.2.11) and Eq. (5.2.12) have the following physical interpretation. The determinant of the mass matrix at the electroweak and Z_2 breaking minimum is proportional to $4\lambda\lambda_s - \lambda_{s\phi}^2$, which is equivalent to the previous requirements. When the determinant of the mass matrix becomes negative, and therefore one of the conditions fails, a tachyonic direction will be generated, destabilizing the system and evolving it to other minima. From this perspective it is also clear that if we choose to work with $(v, m_H, m_S, \sin \theta, \tan \beta)$ as a set of parameters, the determinant of the mass matrix is just $m_H^2 m_S^2$ and the requirements in this basis are automatically satisfied with physical masses.

The potential might be destabilized due to loop corrections, and the quantity $4\lambda\lambda_s - \lambda_{s\phi}^2$ might become negative at high scales. We study this effect taking into account the renormalization group evolution (RGE) of the quartic couplings given by the RGE equations for the quartic couplings of the real singlet model are [206].

$$\begin{aligned} 16\pi^2 \frac{d}{d \ln \mu} \lambda &= 24\lambda^2 + \frac{1}{2}\lambda_{s\phi}^2 + 3\lambda(4y_t^2 - 3g^2 - g'^2) - 6y_t^4 + \frac{3}{8}(2g^4 + (2g'^2 + g^2)^2) \\ 16\pi^2 \frac{d}{d \ln \mu} \lambda_s &= 18\lambda_s^2 + 2\lambda_{s\phi}^2 \\ 16\pi^2 \frac{d}{d \ln \mu} \lambda_{s\phi} &= 4\lambda_{s\phi}^2 + 6\lambda_{s\phi}\lambda_s + 12\lambda_{s\phi}\lambda + \frac{3}{2}\lambda_{s\phi}(4y_t^2 - 3g^2 - g'^2). \end{aligned} \quad (5.2.13)$$

For the analysis we also take into account the running of the top Yukawa y_t and the QCD coupling g_s ,

$$16\pi^2 \frac{d}{d \ln \mu} y_t = \frac{3}{2}y_t^3 - 8g_s^2 y_t - \frac{9}{4}g^2 y_t - \frac{17}{12}g'^2 y_t, \quad 16\pi^2 \frac{d}{d \ln \mu} g_s = -7g_s^3. \quad (5.2.14)$$

Notice that the RGE of $\lambda_{s\phi}$ is proportional to itself, showing the fact that setting it to zero decouples the two sectors. In deriving the limits in Fig. 5.2, we start the RGE at 1 TeV. In Fig. 5.2 we show, shaded in red, the region where the vacuum becomes unstable at a given energy scale.

For small singlet masses and mixing angles the instability scale is not modified with respect to the SM (which is around $\sim 10^8$ GeV at one loop and relaxes to about 10^{11} GeV once two-loop RGE is included [207]), but for larger mixings the singlet shifts the values of the couplings, pushing the scale of instability to larger values. For larger $\tan \beta$, as shown in the right panel of Fig. 5.2, the singlet quartic couplings are smaller and the instability condition extends to a larger region since the effect of the singlet is insufficient to compensate the effect of the destabilizing top Yukawa coupling.

There is also a constraint on the size of the quartic couplings given by the perturbative unitarity arguments. The $2 \rightarrow 2$ amplitudes \mathcal{A} should satisfy

$$\frac{1}{16\pi s} \int_s^0 dt |\mathcal{A}| < \frac{1}{2}. \quad (5.2.15)$$

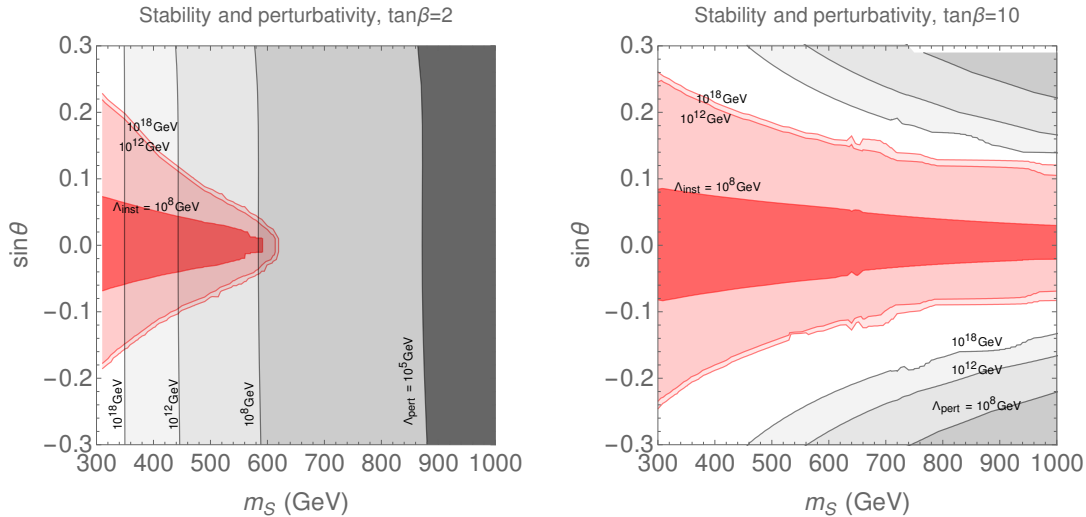


Figure 5.2: Regions of parameter space in the m_S - $\sin \theta$ plane disfavored by perturbativity and EW vacuum stability requirement at various scales. The gray shaded regions are disfavored by perturbative unitarity requirement at a given scale Λ_{pert} . The red shaded regions correspond to regions disfavored by stability requirement at a given scale Λ_{inst} .

This comes from decomposing the amplitude in partial waves and requiring it being consistent with the optical theorem. We consider the different scattering amplitudes among the components of the Higgs doublet and the singlet, and look for the combination of states giving the largest contribution to Eq. (5.2.15). This is done by building a matrix that contains all the $2 \rightarrow 2$ amplitudes among those states and taking the largest eigenvalue.

In Fig. 5.2, the gray shaded regions show the constraints from the perturbative unitarity arguments after including the RGE effects, labeled by the scale at which unitarity is broken. We observe that smaller values of $\tan \beta$ and larger singlet masses have a lower unitarity breaking scale. This is due to the fact that larger singlet masses require larger singlet quartic couplings. In addition, larger $\tan \beta$ corresponds to larger vevs of the singlet and yields larger masses for smaller values of the quartic couplings. Hence perturbative unitarity arguments are relaxed as $\tan \beta$ increases as well as for smaller values of m_S .

5.2.2 Properties of the singlet-like scalar

In addition to the effect of singlet-doublet mixing governed by $\sin \theta$, the relevant phenomenology of the production of di-Higgs final states is further characterized by two trilinear coupling parameters

$$\mathcal{L} \supset \lambda_{HHH} H^3 + \lambda_{SHH} S H^2. \quad (5.2.16)$$

The dimensionful parameter λ_{HHH} is the modified trilinear Higgs coupling and λ_{SHH} is the heavy Scalar-Higgs-Higgs coupling that drives the heavy scalar S decay into the di-Higgs final state. Both couplings can be written in terms of the physical parameters m_s , $\sin \theta$ and $\tan \beta$ as

$$\lambda_{HHH} = -\frac{m_H^2}{2 \tan \beta v} (\tan \beta \cos^3 \theta - \sin^3 \theta), \quad (5.2.17)$$

$$\lambda_{SHH} = -\frac{m_H^2}{2 \tan \beta v} \sin 2\theta (\tan \beta \cos \theta + \sin \theta) \left(1 + \frac{m_S^2}{2m_H^2}\right). \quad (5.2.18)$$

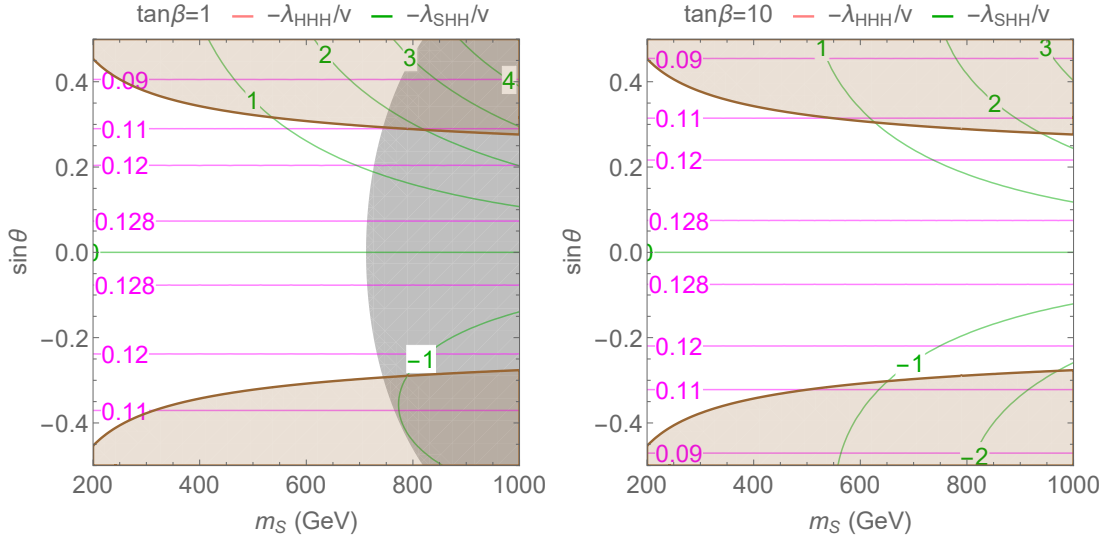


Figure 5.3: The phenomenologically interesting trilinear scalar couplings, normalized by the SM doublet vev v , $-\lambda_{HHH}/v$ and $-\lambda_{SHH}/v$ as a function of the singlet-like scalar mass m_S and the mixing angle $\sin \theta$ shown in magenta and dark green contours, respectively. The left and right panels correspond to $\tan \beta = 1$ and 10 , respectively. The gray shaded region is disallowed by vacuum stability and perturbative unitarity arguments, while the brown shaded regions are disallowed by EWPO.

In Fig. 5.3, we show the values of trilinear couplings between mass eigenstates, $-\lambda_{HHH}/v$ and $-\lambda_{SHH}/v$ in green and magenta curves, as a function of the heavy singlet-like scalar mass m_S and the singlet-doublet mixing angle $\sin \theta$ for $\tan \beta = 1$ (left panel) and $\tan \beta = 10$ (right panel). We can observe that the trilinear coupling of the SM-like Higgs remains insensitive to the singlet mass and receives moderate modifications with respect to its SM value. On the other hand, the trilinear λ_{SHH} that determines the rate of the heavy scalar decay into Higgs pairs is quite sensitive to the precise value of the singlet-like scalar mass and the mixing angle $\sin \theta$.

The heavy singlet mixing with the SM Higgs will induce a global shift on all the SM-like Higgs couplings. While this mixing does not change the SM branching ratios,

the production rates of the Higgs boson will be reduced by a factor $\cos^2 \theta$. The Higgs boson data from LHC at 7 and 8 TeV sets a constraint of $|\sin \theta| < 0.36$ at 95% C.L., independently of the singlet mass. The HL-LHC projection increases this limit very mildly due to the dominant effect from systematic and theory uncertainties. In addition, the current limit is driven by a measured $\sim 1\text{-}\sigma$ excess of signal strength over the SM Higgs expectation. Moreover, the singlet mixing affects the electroweak precision observables (EWPO) measured at LEP, setting slightly stronger limits than those coming from Higgs physics. Hence, in Fig. 5.3 we only show as brown shaded regions those excluded by EWPO, and refer to Appendix B for a detailed discussion. We also show in gray the region disallowed by vacuum stability and perturbative unitarity arguments at the scale m_S where the physical parameters are defined, as discussed in the previous section.

Let's now discuss the decay properties of the singlet like scalar. Its decay to Higgs pairs is governed by the trilinear coupling λ_{SHH}

$$\Gamma_S(S \rightarrow HH) = \frac{\lambda_{SHH}^2}{32\pi m_S} \sqrt{1 - \frac{4m_H^2}{m_S^2}} \quad (5.2.19)$$

and to other SM particles via its mixing with the SM Higgs. The total singlet like scalar width can be written as,

$$\Gamma_S^{\text{tot}} = \Gamma_S(S \rightarrow HH) + \sin^2 \theta \Gamma_H^{\text{tot}}|_{m_H \rightarrow m_S}, \quad (5.2.20)$$

where $\Gamma_H^{\text{tot}}|_{m_H \rightarrow m_S}$ is the total width of a SM Higgs with mass m_S .

In the left panel of Fig. 5.4, we show the total width of the heavy scalar state as a function of its mass and the mixing angle for $\tan \beta$ values of 1 and 10. We can see that its total width is not particularly sensitive to $\tan \beta$. On the right panel of Fig. 5.4, we show the singlet decay branching ratio to Higgs pairs in the plane of the singlet scalar mass and the singlet-doublet mixing angle for $\tan \beta$ of 1 (red, dashed lines) and 10 (blue, solid lines), respectively. The branching fraction features a rapid decrease of roughly 5% near the $t\bar{t}$ threshold due to the opening of this new decay channel. In addition, due to the possible cancellation from contributions to the λ_{SHH} trilinear coupling in parameter space, as depicted in Eq. (5.2.18), one can see strong variations in contour shapes for each value of $\tan \beta$.

The partial width of the singlet to Higgs bosons $\Gamma_S(S \rightarrow HH)$ scales as the third power of the scalar mass for a heavy scalar. This can be easily understood from Eq. (5.2.18) and Eq. (5.2.19). The partial width to WW and ZZ through the mixing with the SM Higgs also grows as the third power of the scalar mass due to the longitudinal enhancement for the massive vector gauge bosons. Consequently, the singlet branching fraction to HH remains in the 20%-40% range over a large span of the parameter space.

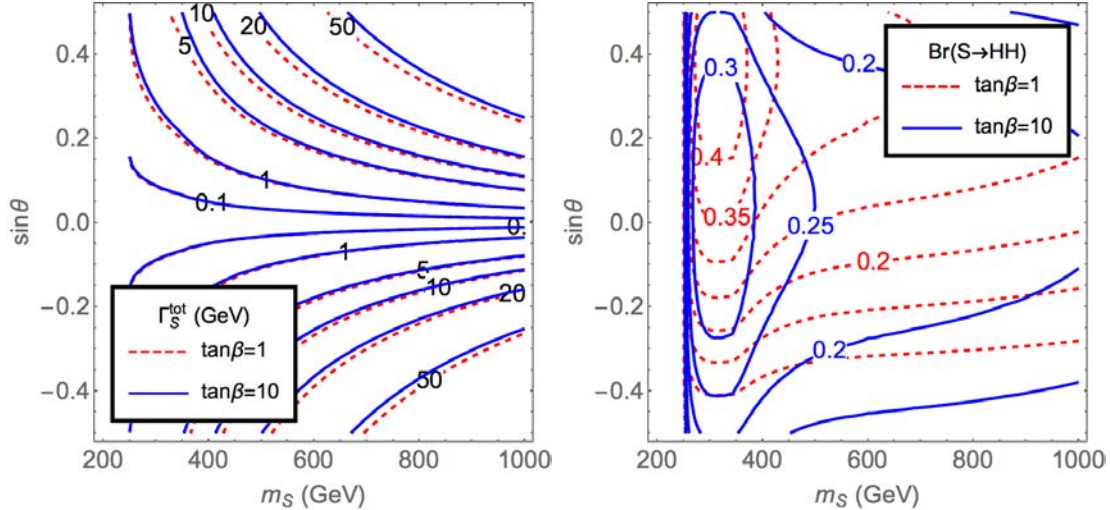


Figure 5.4: The total width (left panel) and branching fraction to Higgs pairs $\text{Br}(S \rightarrow \text{HH})$ (right panel) of the singlet-like scalar S as a function of the singlet-like scalar mass m_S and the mixing angle $\sin\theta$. The red (dashed) contours and blue (solid) contours correspond to $\tan\beta = 1$ and 10, respectively.

5.3 Enhancing the di-Higgs signal via interference effects

The on-shell interference effect may enhance or suppress the conventional Breit-Wigner resonance production. Examples in Higgs physics known in the literature, such as $gg \rightarrow h \rightarrow \gamma\gamma$ [208] and $gg \rightarrow H \rightarrow t\bar{t}$ [209], are both destructive. We discuss in detail in this section the on-shell interference effect between the resonant singlet amplitude and the SM di-Higgs box diagram. We shall show that in the singlet extension of the SM considered in this work, the on-shell interference effect is generically constructive and could be large in magnitude, thus enhances the signal production rate.

5.3.1 Anatomy of the interference effect

The interference effect between two generic amplitudes can be denoted as non-resonant amplitude A_{nr} and resonant amplitude A_{res} . The resonant amplitude A_{res} , defined as

$$A_{res} = a_{res} \frac{\hat{s}}{\hat{s} - m^2 + i\Gamma m}, \quad (5.3.21)$$

has a pole in the region of interest and we parametrize it as the product of a fast varying piece containing its propagator and a slowly varying piece a_{res} that generically is a product of couplings and loop-functions. The general interference effect can then be

parameterized as [208, 209],

$$\begin{aligned}
|\mathcal{M}|_{int}^2 &= 2 \operatorname{Re}(A_{res} \times A_{nr}^*) = 2 (\mathcal{I}_{int} + \mathcal{R}_{int}), \\
\mathcal{R}_{int} &\equiv |A_{nr}| |a_{res}| \frac{\hat{s}(\hat{s} - m^2)}{(\hat{s} - m^2)^2 + \Gamma^2 m^2} \cos(\delta_{res} - \delta_{nr}) \\
\mathcal{I}_{int} &\equiv |A_{nr}| |a_{res}| \frac{\hat{s}\Gamma m}{(\hat{s} - m^2)^2 + \Gamma^2 m^2} \sin(\delta_{res} - \delta_{nr}), \tag{5.3.22}
\end{aligned}$$

where δ_{res} and δ_{nr} denote the complex phases of a_{res} and A_{nr} , respectively.

Schematically, the three amplitudes that enter the di-Higgs production can be parametrized as the following,

$$A_{\triangleright}^H(\hat{s}) \propto f_{\triangleright}(\hat{s}) \cos \theta \frac{\lambda_{HHH}}{v} \frac{\hat{s}}{\hat{s} - m_H^2} \tag{5.3.23}$$

$$A_{\square}^H(\hat{s}) \propto f_{\square}(\hat{s}) \cos^2 \theta \tag{5.3.24}$$

$$A_{\triangleright}^S(\hat{s}) \propto f_{\triangleright}(\hat{s}) \sin \theta \frac{\lambda_{SHH}}{v} \frac{\hat{s}}{\hat{s} - m_S^2 + i\Gamma_S m_S}, \tag{5.3.25}$$

where $f_{\triangleright}(\hat{s})$ and $f_{\square}(\hat{s})$ are the corresponding loop functions. In Eq.(5.3.23) we have dropped the non-important factors for the SM Higgs total width as the pair production is far above the SM Higgs on-shell condition. For a CP-conserving theory that we are considering, all of the above parameters are real, except for the loop-functions $f_{\triangleright}(\hat{s})$ and $f_{\square}(\hat{s})$. The relevant phase between these loop functions³ induces non-trivial interference effect between these diagrams.

The detailed expressions for these three amplitudes can be found in Ref. [210]. The SM box contribution contains two pieces f_{\square} and g_{\square} . The g_{\square} piece corresponds to different helicity combinations of the gluons that does not interfere with the resonant term. In Fig. 5.5, we show as a function of the partonic center of mass energy $\sqrt{\hat{s}}$, the phases of the triangle and box loop functions and their relative phase in blue, magenta and yellow curves, respectively. We observe that the phases of both diagrams start to increase after the $t\bar{t}$ threshold, as expected from the optical theorem. In particular, the relative phase between the interfering box and triangle diagrams, shown as the yellow curves, grows quickly after the threshold and remains large for the entire region under consideration. This relative strong phase drives the physics discussed in this work as it allows for a non-vanishing \mathcal{I}_{int} interference effect between the singlet resonance diagram and the SM box diagram.

In Table 5.1, we summarize the different behaviours of all the interference terms allowed in this theory. We decompose the interference effects into the \mathcal{R}_{int} and \mathcal{I}_{int} , as defined in Eq.(5.3.22), and further highlight their dependence on the relative phase, model parameters and the resulting signs of the interference effects.

³These loop functions can also be understood as form factors of the effective gluon-gluon-Higgs(-Higgs) couplings.

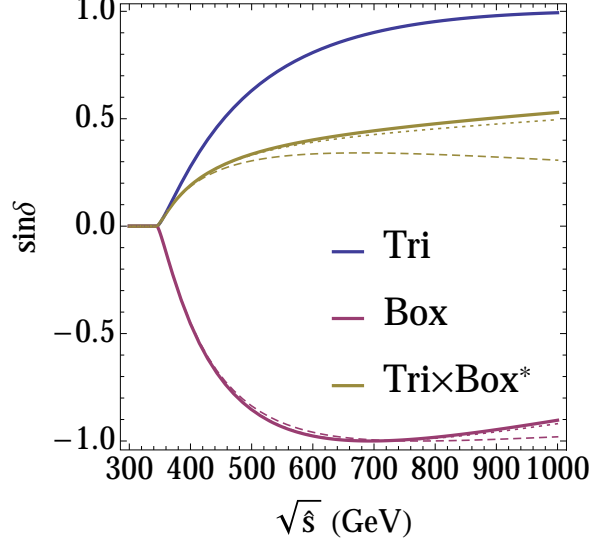


Figure 5.5: The phase of the interfering triangle and box amplitudes as a function of the partonic center of mass energy $\sqrt{\hat{s}}$. The solid, dotted, and dashed curves correspond to scattering angles of 0, 0.5 and 1 respectively.

The special \mathcal{I}_{int} terms vanish both for the interference between the SM diagrams $A_{\triangleright}^H - A_{\square}^H$ and the interference between the resonant singlet and the SM triangle diagrams $A_{\triangleright}^S - A_{\triangleright}^H$ for different reasons. For the latter, the singlet resonant amplitude and the SM triangle amplitude share a common source of the strong phase δ_{\triangleright} from the triangle fermionic loop of the induced gluon-gluon-scalar coupling. Hence, $\sin(\delta_{\triangleright} - \delta_{\triangleright}) = 0$ and this makes Eq. (5.3.22) vanish. For the interference between the SM box and triangle diagrams $A_{\triangleright}^H - A_{\square}^H$, denoted 0^* in the proportionality column of the table, the \mathcal{I}_{int} vanishes because we are always in the off-shell regime for the intermediate SM Higgs in the triangle diagram. Viewing the SM triangle diagram as A_{res} , then the \mathcal{I}_{int} part in Eq. (5.3.22) is strictly non-zero. However, due to the fact that we can never hit the SM Higgs pole in the relevant regime $\hat{s} > (2m_H)^2$, such contribution is

$$\frac{\hat{s}\Gamma_H m_H}{(\hat{s} - m_H^2)^2 + \Gamma_H^2 m_H^2} < \frac{4m_H^3 \Gamma_H}{9m_H^4} \approx 1.5 \times 10^{-5}, \quad (5.3.26)$$

and hence can be neglected.

In contrast, the special interference effect \mathcal{I}_{int} only appears between the singlet resonant diagram and the SM box diagram $A_{\triangleright}^S - A_{\square}^H$. This interference effect is proportional to the relative phase between the loop functions $\sin(\delta_{\triangleright} - \delta_{\square})$ and the imaginary part of the scalar propagator which is sizable near the scalar mass pole. In this work, we pay special attention to this effect whose importance has been overlooked in the past literature.

The signs of the interference effects are determined by a product of relative phases, model parameters and kinematics. The relative phases are always positive for the mass range considered here, as show in Fig. 5.5. The kinematics straightforwardly relies on the

Table 5.1: Decomposition of all the allowed interference terms and their characteristics in the CP-conserving theory under consideration. The fourth column picks up the model-parameter dependence. The last column represents the sign of the interference term below/above the heavy scalar mass pole. The proportionality for \mathcal{I}_{int} of the SM piece denoted 0^* contains more factors than the model parameter, see details in the text.

Inter. Term.		rel. phase	proportionality	Inter. Sign
$A_{\triangleright}^H - A_{\square}^H$	\mathcal{R}_{int}	$\cos(\delta_{\triangleright} - \delta_{\square})$	$\cos^3 \theta \lambda_{HHH}$	–
	\mathcal{I}_{int}	$\sin(\delta_{\triangleright} - \delta_{\square})$	0^*	0
$A_{\triangleright}^S - A_{\triangleright}^H$	\mathcal{R}_{int}	1	$\lambda_{SHH} \lambda_{HHH} \cos \theta \sin \theta$	–/+
	\mathcal{I}_{int}	0	$\lambda_{SHH} \lambda_{HHH} \cos \theta \sin \theta$	0
$A_{\triangleright}^S - A_{\square}^H$	\mathcal{R}_{int}	$\cos(\delta_{\triangleright} - \delta_{\square})$	$\lambda_{SHH} \cos^2 \theta \sin \theta$	+/-
	\mathcal{I}_{int}	$\sin(\delta_{\triangleright} - \delta_{\square})$	$\lambda_{SHH} \cos^2 \theta \sin \theta$	+

Higgs pair invariant mass with respect to the heavy scalar mass pole. In addition due to spontaneously Z_2 breaking model construction and consistency requirement, λ_{SHH} and $\sin \theta$ has opposite signs, in accordance to the sign of $\lambda_{s\phi}$ in the original potential. The overall signs of the interference effects end up being fixed as shown in Table 5.1.

5.3.2 Parametric dependence of the on-shell interference effect

After understanding the sources of various interference effects, especially the on-shell interference effect I_{int} , we study its parametric dependence in this section.⁴

We first show the lineshape decomposition into components discussed in Table 5.1 for two benchmark points in Fig. 5.6. We display the Breit-Wigner, non-resonant lineshape from SM triangle and box diagrams, and the total lineshape in red, brown and black curves, respectively. The interference terms \mathcal{R}_{int} proportional to the real part of the heavy scalar propagator are shown in blue and magenta curves. Observe that these interference terms flip their signs when crossing the scalar mass pole and this is shown by switching the solid curve for constructive interference to dashed curves for destructive interference. Finally, for the interference term proportional to the imaginary component of the scalar propagator, we show the special term I_{int} in (thick) dark blue curve. We can observe that the I_{int} piece has very similar lineshape to the Breit-Wigner resonance piece near the scalar mass pole. We shall denote this term \mathcal{I}_{int} as on-shell interference effect, since \mathcal{I}_{int} acquires its maximal value precisely on-shell. This is in contrast to the term \mathcal{R}_{int} that vanishes when the invariant mass of the final state is precisely at the scalar mass pole.

In the left panel of Fig. 5.6, we choose as a benchmark $m_S = 400$ GeV, $\tan \beta = 2$

⁴Throughout this work we use the finite m_t result at leading order [210]. We adopt the K-factor between the next-to-leading-order and the leading order result in the m_{hh} distribution provided by Ref. [195].

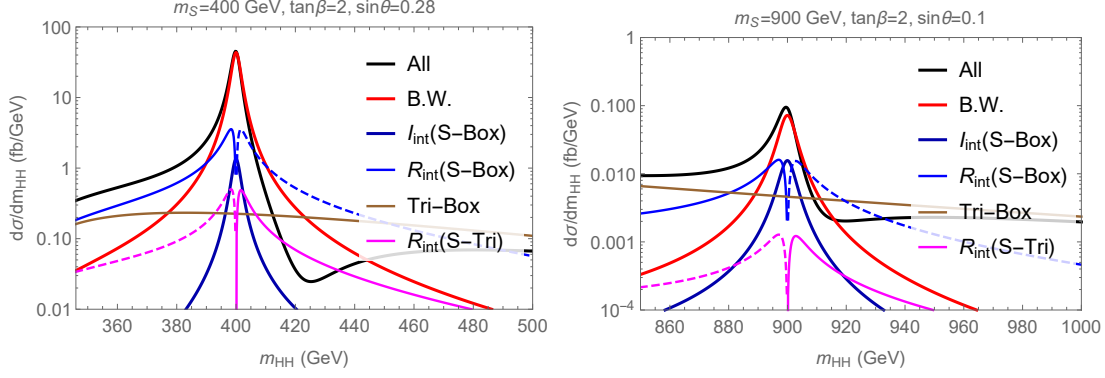


Figure 5.6: Decomposition of the differential distribution of the Higgs pair production in presence of a singlet resonance at 13 TeV LHC. The black curve represents the overall lineshape after coherent sum of all amplitudes squared. The red curve represent the Breit-Wigner resonance piece from the singlet resonant production. The dark blue (thick) curve represents the novel interference term between the singlet resonant amplitude and the SM box amplitude that enhances the signal resonant production, noting the identical lineshape of this contribution to that of the Breit-Wigner piece in red curves. The blue, brown and magenta lines represent the conventional interference terms \mathcal{R}_{int} between the three amplitudes. We show the corresponding destructive interference effects in dashed curves.

and mixing angle $\sin\theta = 0.28$ to match one of the benchmarks in Ref. [195].⁵ For this benchmark, we reproduce their result on the overall lineshape and some of the specific lineshape contributions shown in Ref. [195]. For this benchmark, the on-shell interference term \mathcal{I}_{int} , shown in the (thick) dark blue curve, is smaller than the Breit-Wigner contribution by almost two orders of magnitude and thus can be neglected. Instead, in the right panel of Fig. 5.6, we show the lineshape decomposition for a different benchmark point of heavy scalar mass $m_S = 900$ GeV, $\tan\beta = 2$ and mixing angle $\sin\theta = 0.1$. For this benchmark, we can clearly observe the contribution from the on-shell interference term \mathcal{I}_{int} , as its magnitude is more than 15% of the Breit-Wigner resonance shown by the red curve. This leads to an enhancement when comparing the overall lineshape (black curve) to the Breit-Wigner resonance alone near the resonance peak.

With the comprehensive understanding of the interference effect, we can quantify the relative size of the on-shell interference effect by normalizing it to the the Breit-Wigner contribution, $\sigma_{Int}/\sigma_{B.W.}$. This ratio is well-defined due to the similar lineshapes of these two contributions near the mass pole. We integrate over the scattering angle in the center of mass frame in the -0.5 to $+0.5$ range for central scattering and average over the ratio. We show in Fig. 5.7 the parametric dependence of this interference effect

⁵Our definition of $\tan\beta$ is the inverse of the $\tan\beta$ definition used in Ref. [195].

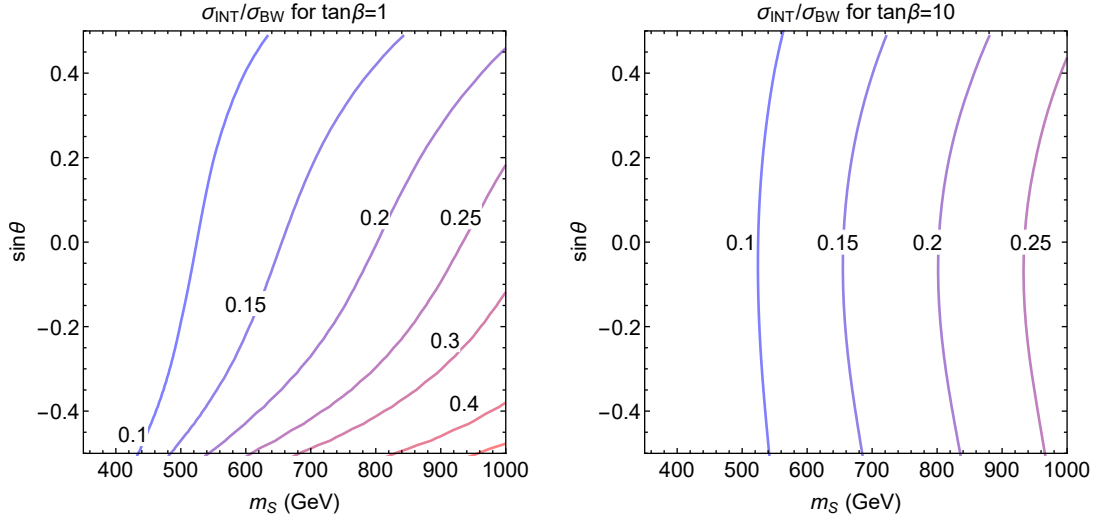


Figure 5.7: The relative size of the on-shell interference effect with respect to the Breit-Wigner contribution for the scalar singlet resonant production after averaging over the scattering angle $\cos\theta^*$ from -0.5 to $+0.5$ for central scattering.

as a function of the heavy scalar mass m_S and singlet-doublet mixing angle $\sin\theta$ for $\tan\beta = 1$ (left panel) and $\tan\beta = 10$ (right panel). We obtain that the size of this on-shell interference effect I_{int} varies between a few percent to up to 40% of the size of the Breit-Wigner resonance for the parameter region considered in this study. The effect is further enhanced for heavier scalar masses and larger widths. The quantitative differences of the iso-curvatures between the two panels in Fig. 5.7 are caused by the parametric dependence of λ_{SHH} and the singlet total decay width shown in Fig. 5.3 and Fig. 5.4, respectively. Clearly, the interference effect could play an important role in the phenomenology and further determination of model parameters if the heavy scalar is discovered.

5.4 Phenomenological study

We present in this section our analysis of the differential distribution of the Higgs pair invariant mass to estimate the relevance of the interference effects discussed in the previous section. We choose one of the best channels, $pp \rightarrow HH \rightarrow b\bar{b}\gamma\gamma$, as the benchmark channel to present the details of our analysis. Furthermore, we discuss another phenomenologically relevant piece of interference in the far off-shell region of the singlet scalar. We display the discovery and exclusion reach for both HL-LHC and HE-LHC for various values of $\tan\beta$ in the m_S - $\sin\theta$ plane. Finally in the last part of this section, we discuss the relevance of the di-Higgs channel in probing the strength of the first order electroweak phase transition in a simplified effective field theory (EFT) approach

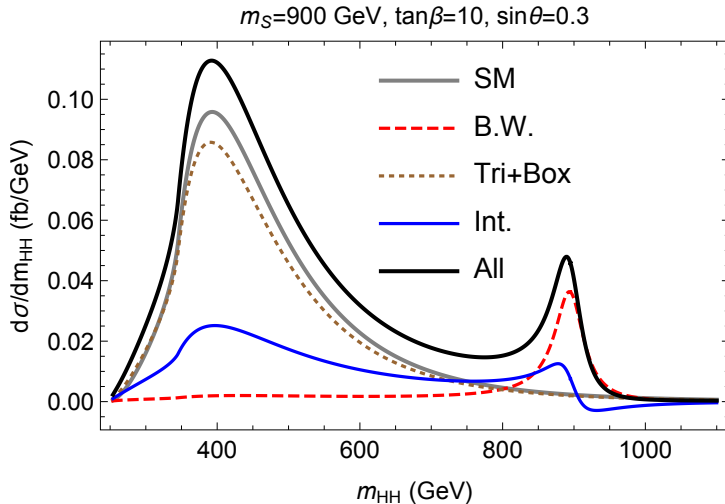


Figure 5.8: The differential di-Higgs distribution for a benchmark point of the singlet extension of the SM shown in linear scale and over a broad range of the di-Higgs invariant mass. The full results for the SM and the singlet SM extension are shown by the gray and black curves, respectively. In the singlet extension of the SM, the contributions from the resonant singlet diagram, the non-resonant diagram and the interference between them are shown in red (dashed), brown (dotted) and blue curves, respectively.

for both the spontaneous Z_2 breaking scenario and an explicit Z_2 breaking scenario.

5.4.1 Differential distribution

In Fig. 5.8 we display the differential cross section as a function of the Higgs pair invariant mass for a benchmark point with a heavy scalar mass of 900 GeV, mixing angle $\sin\theta = 0.3$ and $\tan\beta = 10$. The differential cross section is shown in linear scale for a broad range of di-Higgs invariant masses, including the low invariant mass regime favored by parton distribution functions at hadron colliders.

We choose this benchmark to show well the separation of the scalar resonance peak and the threshold enhancement peak above the $t\bar{t}$ -threshold. The SM Higgs pair invariant mass distribution is given by the gray curve while the black curve depicts the di-Higgs invariant mass distribution from the singlet extension of the SM. It is informative to present all three pieces that contribute to the full result of the di-Higgs production, namely, the resonance contribution (red, dashed curve), the SM non-resonance contribution (box and triangle diagrams given by the brown, dotted curve), and the interference between them (blue curve). Note that the small difference between the “Tri+Box” and the “SM” lineshapes is caused by the doublet-singlet scalar mixing, which leads to a $\cos\theta$ suppression of the SM-like Higgs coupling to top quarks as well as a modified SM-like Higgs trilinear coupling λ_{HHH} , as depicted Eq. (5.2.17). We observe that the full

Table 5.2: Summary of expected number of events for the SM Higgs pair production and the SM backgrounds for the $b\bar{b}\gamma\gamma$ di-Higgs search after selection cuts, obtained from Ref. [76] for the HL-LHC and further extrapolated for the HE-LHC.

# of events expected	HL-LHC 13 TeV @ 3 ab ⁻¹		HE-LHC 27 TeV @ 10 ab ⁻¹	
	SM HH	SM BKG	SM HH	SM BKG
bins (GeV)				
250-400	2.1	12.0	33.2	186.4
400-550	6.3	15.9	110.9	278.8
550-700	2.9	5.2	58.4	105.6
700-850	1.0	2.0	23.4	46.7
850-1000	0.3	1.4	8.9	38.8
1000-1200	0.2	0.7	4.7	20.4
1200-1400	-	-	1.9	8.0
1400-1600	-	-	0.8	3.5
1600-1800	-	-	0.4	1.7
1800-2000	-	-	0.2	0.9

results show an important enhancement in the di-Higgs production across a large range of invariant masses. This behavior is anticipated from the decomposition analysis in the previous section. There is a clear net effect from the interference curve shown in blue. Close to the the scalar mass pole at 900 GeV, the on-shell interference effect enhances the Breit-Wigner resonances peak (red, dashed curve) by about 25%. Off-the resonance peak, and especially at the threshold peak, the interference term (blue curve) enhances the cross section quite sizably as well. Hence, a combined differential analysis in the Higgs pair invariant mass is crucial in probing the singlet extension of the SM.

5.4.2 Signal and background analysis for $pp \rightarrow HH \rightarrow b\bar{b}\gamma\gamma$

In the following, we consider the di-Higgs decaying into $b\bar{b}\gamma\gamma$ in the singlet extension of the SM, and perform a consistent treatment of the interference effect and a differential analysis of the lineshapes. Although this channel is one of the most sensitive ones due to its balance between the cleanness of the final state and the signal statistics, the detailed analysis is nevertheless quite involved. For both the SM signal and background expected number of events at HL-LHC, we use the simulated and validated results listed in Table V of Ref. [76]. To extrapolate the signal expected from our singlet extension of the SM, we assume the same acceptance as the SM Higgs pair. For HE-LHC with a center of mass energy of 27 TeV, we assume the same acceptance as the HL-LHC that varies between 10% to 30% for the di-Higgs signal. For the SM background at the HE-LHC, we assume the same signal to background ratio as the HL-LHC in the low invariant mass bins, while

for the high invariant mass bins we consider a fixed signal to background ratio of 23%. In Table 5.2, we tabulate the expected number of events for the SM Higgs pair and SM background.⁶

We calculate and combine the significance of each bin using the following approximation [211],

$$\Delta\chi^2 = \sum_i^{\text{bins}} 2 \left((n_{s,i} + n_{b,i}) \log\left(1 + \frac{n_{s,i}}{n_{b,i}}\right) - n_{s,i} \right), \quad (5.4.27)$$

assuming all the bins are independent. As shown in Table 5.2, the bins are typically with low statistics, therefore it is reasonable to ignore systematics at this stage. We assume that the observed number of events in this channel follows the SM expectation values. $n_{b,i}$ represents the sum of the SM di-Higgs event rate and its background for each mass window listed in Table 5.2; $n_{s,i}$ represents the difference generated from the singlet model in the di-Higgs production channel with respect to the SM Higgs pair production in each bin. As shown in Ref. [211], this formulae provides a good approximation for the median discovery significance for a large range of underlying statistics, including relatively low statistical bins where Gaussian approximation fails.⁷

5.4.3 Discovery and exclusion reach of the HL- and HE-LHC

Using the analysis detailed above, we obtain the discovery and exclusion projections for the HL-LHC and HE-LHC. In Fig. 5.9 we show the projected $2\text{-}\sigma$ exclusion and $5\text{-}\sigma$ discovery reach for the HL-LHC in the $m_S\text{-}\sin\theta$ plane for $\tan\beta = 1$ (left panel) and $\tan\beta = 10$ (right panel) in solid and dashed curves, respectively. The shaded regions are within the reach of the HL-LHC for discovery and exclusion projections. To demonstrate the relevance of the interference effects discussed in the previous sections, we show both the results obtained with and without the inclusion of the interference effects in black and red contours, respectively.

We observe in Fig. 5.9 that the inclusion of the interference effects extend the projections in a relevant way. For example, considering the $\tan\beta = 10$ case in the right panel for $\sin\theta \simeq 0.35$ the interference effect increase the exclusion limit on m_S from 850 GeV to 1000 GeV. Note that the on-shell interference effect is larger for heavier scalar mass m_S .

In Fig. 5.10 we show the projections for the HE-LHC in a analogous fashion as in Fig. 5.9. The discovery and exclusion reach for heavy scalars can be significantly ex-

⁶Although this analysis includes different signal efficiencies depending on different Higgs pair invariant mass windows, a future analysis focusing in high invariant mass bins could lead to improved results, especially when combined with different decay final states.

⁷Although still facing sizable differences for the true significance with statistical simulations [211], the above treatment is sufficient for our current study as our purpose is to demonstrate the impact of the interference effect.

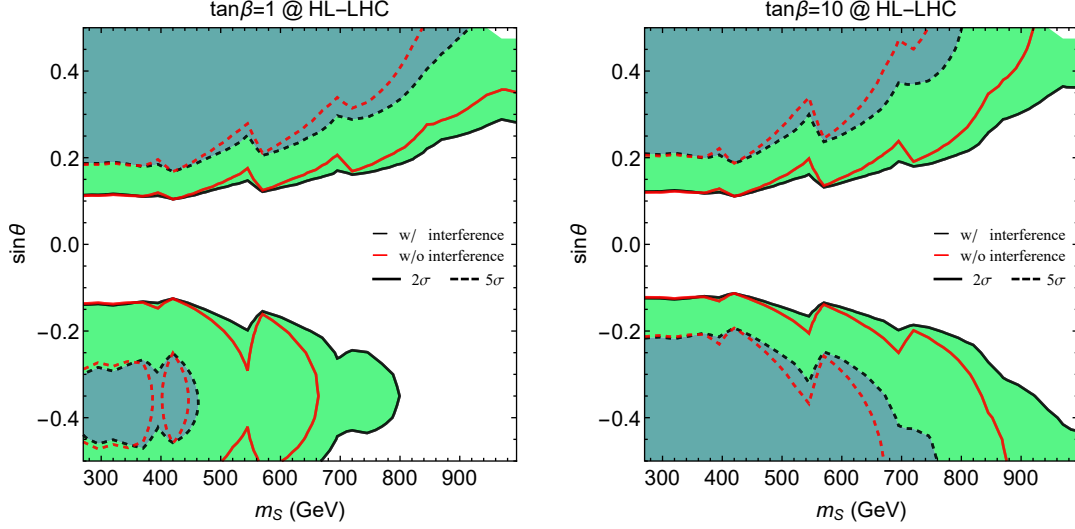


Figure 5.9: Projected exclusion and discovery limits at HL-LHC in the m_S - $\sin\theta$ plane with the line-shape analysis detailed in the text for $\tan\beta = 1$ (left panel) and $\tan\beta = 10$ (right panel). The shaded regions bounded by dashed/solid curves are within the discovery/exclusion reach of the HL-LHC. The black and red lines represent the projection with and without the inclusion of the interference effects between the singlet resonance diagram and the SM Higgs pair diagram, respectively.

tended by the HE-LHC operating at 27 TeV center of mass energy with 10 ab^{-1} of integrated luminosity. We show the results for $\tan\beta = 2$ (left panel) and $\tan\beta = 10$ (right panel). For example, considering the $\tan\beta = 2$ case in the right panel of Fig. 5.10, for $\sin\theta \simeq 0.35$ the exclusion reach increases from 1200 GeV to 1800 GeV, once more showing the importance of including the on-shell interference effects.

In Section 5.2.1, we have shown that in the spontaneous Z_2 breaking model, the perturbative unitarity requirement can place stringent upper bounds on the singlet scalar mass, depending on the value of $\tan\beta$. Such bounds are driven by the large singlet quartic λ_S needed to obtain heavy mass values from a relatively small vev $v_s = v \tan\beta$. In an explicit Z_2 breaking model, instead, larger values of the singlet mass are perfectly compatible with perturbative unitarity requirement even for small value of $\tan\beta$. Therefore, in Fig. 5.9 and Fig. 5.10 we perform a general analysis for the LHC reach without imposing the perturbative unitarity restrictions.

It is worth mentioning that when the heavy scalar resonance is divided evenly between two bins, its significance is reduced. This, together with a very coarse binning we choose in Table 5.2, leads to the wiggles in the discovery and exclusion projection contours in this section. A more refined analysis that leads to smoother projections would be desirable. In addition, due to the mixing with the SM Higgs, the heavy scalar also has sizable branching fractions into WW and ZZ , as implied in Fig. 5.4. New channels

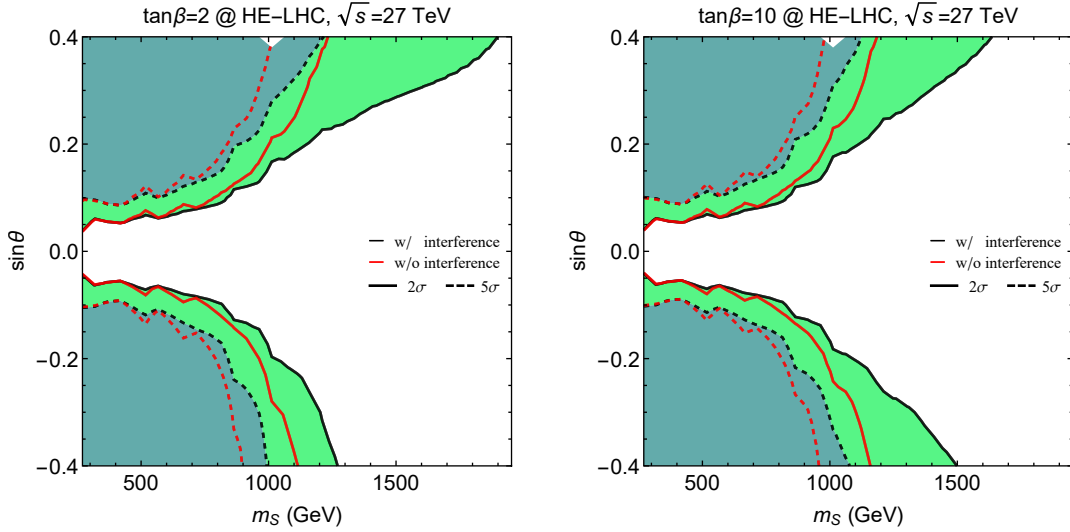


Figure 5.10: Similar to Fig. 5.9, projected exclusion and discovery limits at HE-LHC with 27 TeV center of mass energy and an integrated luminosity of 10 ab^{-1} for $\tan \beta = 2$ (left panel) and $\tan \beta = 10$ (right panel).

such as $gg \rightarrow S \rightarrow WW, ZZ$ could provide complementary and even competitive information and discovery potential for the heavy scalar. Note that similar on-shell and off-shell interference effects will take place in these channels as well. Hence, it would be interesting to consider a comprehensive treatment and comparison between different search channels, such as other decays of the Higgs pair, as well as other decay modes of the heavy scalar. We reserve these for future study.

5.4.4 Implications for the first order electroweak phase transition

In this section, we investigate the implications of the interference effects for the parameter regions enabling a first order electroweak phase transition. There are several phenomenological studies in the literature that investigate different realizations of first order electroweak phase transitions in singlet extensions of the SM. For the case of the Z_2 symmetric singlet extension, there are detailed studies in Ref. [177, 183, 212], including the possibilities of both 1-step and 2-step phase transitions. For a general singlet extend SM, several numerical and semi-analytical studies have been carried out [178, 180, 213]. Here we perform a simplified EFT analysis on the spontaneous Z_2 breaking scenario and a particular explicit Z_2 breaking scenario to *illustrate* the relevance of the interference effect. A detailed finite-temperature thermal history study for the full theory will be presented elsewhere.

A deformation of the Higgs thermal potential is the key to change the electroweak phase transition from second order to first order. The simplest way in EFT is to intro-

duce the dimension-six operator $O_6 \equiv (\phi^\dagger \phi)^3$. The authors in Ref. [214] provide the preferred region of the scale Λ_6 of this operator, to facilitate a first order electroweak phase transition. For a (negative) unity Wilson coefficient of the operator O_6 , Ref. [214] constraints the scale of this operator Λ_6 to be,

$$\frac{v^4}{m_H^2} < \Lambda_6^2 < \frac{3v^4}{m_H^2}, \quad (5.4.28)$$

and the detailed analysis in Ref. [215] improves the upper limit by about 25%. The upper bound can be understood from the requirement of the operator O_6 being sufficiently sizable to change the Higgs potential to provide a first order phase transition.

By integrating out the singlet field, one can map the general Lagrangian of the singlet extension of the SM to the corresponding SM EFT. The matching is detailed in Ref. [79, 216], where the EFT operators generated by integrating out the singlet field are explicitly shown for both tree-level and one loop-level. For tree-level generation of the O_6 operator, the Z_2 breaking vertex $s(\phi^\dagger \phi)$ is required. One may anticipate the spontaneous Z_2 breaking theory to generate the O_6 operator at tree-level as well. However, the two contributing tree-level diagrams involving $s^2(\phi^\dagger \phi)$ and s^3 cancel each other due to the simple form of the solution to the equation of motion for the singlet field.⁸ The Higgs potential is then modified by the singlet field at loop level. Consequently, the scale of the operator is further suppressed by a loop factor of $1/(16\pi^2)$. This results in insufficient modifications to the Higgs potential to trigger a first order electroweak phase transition. While the EFT is a good description for a one-step phase transition in the electroweak direction, where the singlet field is heavy enough to be treated as a classical field, the thermal history could be more complex. A detailed study to truly understand the relevant parameter space for sufficiently strong first order electroweak phase transition is required and we postpone it for future work.

To demonstrate the relevance of this interference effect on the first order electroweak phase transition, we consider, as an example, an explicit Z_2 breaking scenario. Without modifying any properties of the phenomenology discussed in this work (except for the RG running part), we choose the same potential as in Eq.(5.2.1), after the spontaneous symmetry breaking, and flip the sign of the coefficient of the s^3 term,⁹

$$- \lambda_s v \tan \beta s^3 \rightarrow + \lambda_s v \tan \beta s^3. \quad (5.4.29)$$

⁸The numerical factors for the two contributions to the O_6 operator from tree level diagrams are important. The EFT matching results from the earlier work in Ref. [134] without these factors lead to non-vanishing tree-level O_6 operators in the spontaneous Z_2 breaking singlet extension of the SM.

⁹In the generic, explicit Z_2 -breaking scenario, $\tan \beta$ is effectively absorbed into the definitions of individual coefficients in the potential. Here, for simplicity, we use the spontaneous Z_2 breaking parameterization, and hence keep $\tan \beta$, to avoid a cumbersome redefinition of many of the parameters in the model.

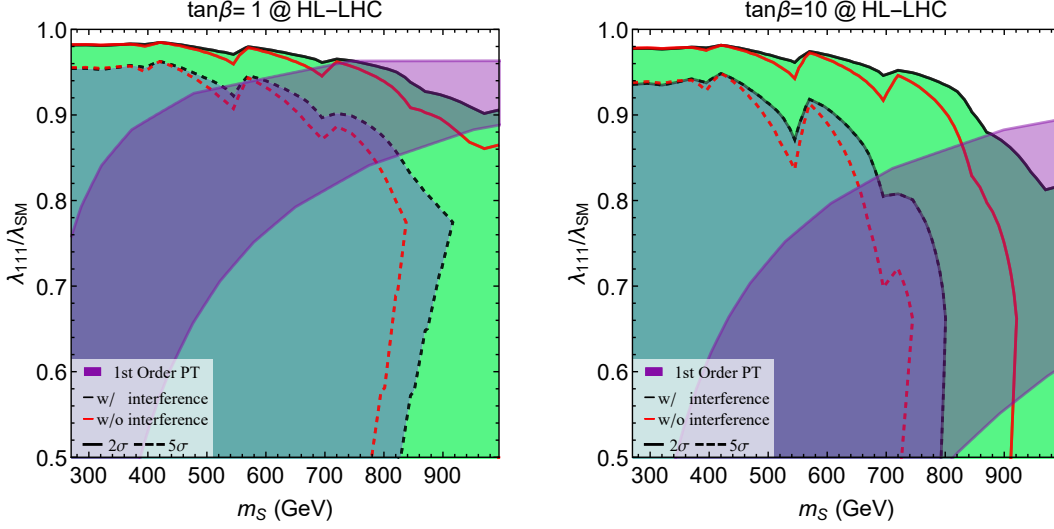


Figure 5.11: Projected exclusion (solid lines) and discovery (dashed lines) limits at HL-LHC as a function of the heavy singlet scalar mass m_S and the SM-like Higgs trilinear coupling λ_{111} , normalized to its SM value, for $\tan\beta = 1$ (left panel) and $\tan\beta = 10$ (right panel), for the explicit Z_2 -breaking SM plus singlet model scenario. The shaded region within the curves are at the HL-LHC reach. The black and red lines represent the projections with and without the interference effects between the singlet resonance diagram and the SM Higgs pair diagram. The purple shaded areas correspond to parameter regions with a first order electroweak phase transition from the EFT analysis detailed in the text.

Hence, one would generate the O_6 operator at tree-level with

$$\mathcal{L}_{EFT} \supset -\frac{\lambda_{s\phi}^3}{2\lambda_s m_s^2} (\phi^\dagger \phi)^3, \quad (5.4.30)$$

where $m_s^2 = 2\lambda_s \tan^2 \beta v^2$. The region preferred by the EFT analysis in this particular explicit Z_2 breaking theory requires $\lambda_{s\phi}$ being positive and such condition is also consistent with the EFT potential being bounded from below. This requirement corresponds to positive mixing angle between the singlet and the doublet, $\sin\theta > 0$.

Within the above setup, in Fig. 5.11 we show the exclusion and discovery projections at the HL-LHC in the singlet mass m_S and Higgs trilinear coupling plane, normalized to the SM Higgs trilinear coupling, $\lambda_{111}/\lambda_{111}^{\text{SM}}$. As shown in Section 5.2, the Higgs trilinear coupling is modified modestly and the trilinear coupling ratio varies between 0.5 to 1. In the purple band, we show the parameter region consistent with a first order electroweak phase transition in the EFT analysis.¹⁰ Similar to Fig. 5.9, we can see that the consistent

¹⁰The EFT analysis aims to provide a general picture of the relevance of electroweak phase transition. A detailed thermal history analysis is desirable, especially for singlet masses below 300 GeV.

inclusion of the interference effect improves the reach notably. Most importantly, we observe that the improved discovery and exclusion reach overlaps significantly with the parameter region preferred by the first order electroweak phase transition.

5.5 Summary

In this chapter, we analyze the interference effects in the $gg \rightarrow HH$ process in the presence of a heavy scalar resonance. We focus on the novel effect of the on-shell interference contribution and discuss it in detail considering the framework of the singlet extension of the SM with spontaneous Z_2 breaking. Such singlet extension of the SM is well-motivated as the simplest example compatible with a strong first order phase transition and consistent with the Higgs boson mass measurements at the LHC.

We outline the model setup and relate the model parameters, including quartic and trilinear scalar couplings, to physical parameters such as m_H , v , m_S , $\sin\theta$ and $\tan\beta$. We find that perturbative unitarity requirements set an upper bound on the mass of the singlet scalar only for low $\tan\beta$, and do not impose significant constraints for moderate values of the mixing angle $\sin\theta$. The heavy scalar total width grows as the third power of its mass, and the decay branching fraction into Higgs pairs varies moderately in the 20%-40% range for different regions of the model parameter space.

The interference pattern between the resonant heavy scalar contribution and the SM non-resonant triangle and box contributions show interesting features. We highlight the constructive on-shell interference effect that uniquely arises between the heavy scalar resonance diagram and the SM box diagram, due to a large relative phase between the loop functions involved. We observe that the on-shell interference effect can be as large as 40% of the Breit-Wigner resonance contribution and enhances notably the total signal strength, making it necessary taking into account in heavy singlet searches.

To better evaluate the phenomenological implications of the interference effects in the di-Higgs searches, we carried out a lineshape analysis in the $gg \rightarrow HH \rightarrow \gamma\gamma b\bar{b}$ channel, taking into account both the on-shell and off-shell interference contributions. We find that both for the HL-LHC and HE-LHC, the proper inclusion of the interference effects increases the discovery and exclusion reach significantly. Furthermore, using a simplified EFT analysis, we show that the parameter regions where the interference effects are important largely overlap with the regions where a first order electroweak phase transition is enabled in the singlet extension of the SM.

Moreover, our analysis is applicable for a general potential of the singlet extension of the SM as well as for more general resonance searches. A comprehensive analysis of the interference effects in different decay modes of the Higgs boson and the heavy scalar would provide complementarity information, adding to the LHC potential in the search for heavy scalars.

Chapter 6

Diboson production at LHC

6.1 Introduction

The study of WW and WZ production at the LHC provides a probe of the electroweak gauge boson interactions at very high energies, and therefore a test of the goldstone interactions of the Higgs doublet.

Deviations from the SM behaviour are parametrized in terms of the anomalous triple gauge couplings (aTGC), that were already constrained at LEP-2 at the level of a few per cent. However, deviations away from the SM induce a deformation to the amplitude that grows with the center of mass energy. Thanks to this behavior, the LHC can already surpass LEP-2 in precision [90, 91].

In those studies, one assumes that the couplings among the electroweak bosons and the light quarks do not deviate away from the SM values. This is because LEP-1 data set constraints on those deviations that were stringent than the constraints on the aTGC. However, these anomalous couplings also induce an energy growing behavior as mentioned in Refs. [217–219], and it is the goal of this chapter to focus the attention to the constraining power of diboson on the anomalous couplings between the W and Z gauge bosons and the light quarks. We find that due to the enhanced sensitivity at high energies, $pp \rightarrow WW, WZ$ can already be competitive or even surpass LEP-1 on setting bounds to $\delta V \bar{q}q$. We set the current bounds recasting the present data and also estimate the sensitivity by the end of the HL-LHC.

While the LHC is sensitive only to the first generation quarks, LEP-1 constraints strongly depend on the flavour assumptions, since an extra structure correlates the constraints of different families of quarks. We take two general flavour assumptions for the EFT: Flavour Universality (FU), where the EFT operators satisfy a $U(3)^5$ family symmetry, which in the Higgs basis corresponds to $[\delta g_{L,R}^{Zu,d}]_{ij} = A_{L,R}^{u,d} \delta_{ij}$, and Minimal Flavour Violation (MFV), see Ref. [220], where this symmetry is broken only by spurions of Yukawa couplings, which yields $[\delta g_{L,R}^{Zu,d}]_{ij} \simeq \left(A_{L,R}^{u,d} + B_{L,R}^{u,d} \frac{m_i}{m_3} \right) \delta_{ij}$. Diboson production

is insensitive to these assumptions, while the constraints from LEP-1 can change by an order of magnitude, see Ref. [69] or [Appendix C](#) where we summarize their results.

Due to the larger systematics at the LHC, the fact that it can surpass LEP-1 and LEP-2 in setting bounds to the EFT operators (for $M_{BSM} > \sqrt{s}$, i.e., when the EFT description is valid) may come as a surprise, but it can naively be understood by the fact that the amplitudes grow with the center of mass energy. For a particular process one has that $E_{LHC}^2/E_{LEP}^2 \sim \mathcal{O}(10^2)$, therefore if the BSM amplitudes grow with E^2 with respect to the SM ones, one can naively gain a factor $\mathcal{O}(10^2)$ on the BSM cross section coming from the BSM and SM interference, or what is the same, one can get the same bounds having a hundred times less precision. On the other hand, it is important to note that as explained in Refs. [75, 221–224] the larger systematics also imply in many cases that the new LHC bounds only exclude EFT coefficients for which the BSM contribution is larger than the SM one, limiting in some cases the generality of these bounds to only subsets of possible UV theories. For example, diboson production at the LHC can already extend the bounds set by LEP-2 on the operator \mathcal{O}_{3W} . However, it can only do so in regions where the BSM amplitude is larger than the SM one; this means that it is not providing any new constraints to most of the existing UV models where \mathcal{O}_{3W} is generated at loop level. We comment more on the EFT interpretation in [Section 6.5.1](#). Nonetheless, given that the LHC is running and we don't know what new physics may lay ahead, it is still important to make sure that all the regions of the EFT parameter space are explored in the most model independent way as possible.

The EFT study of diboson production at the LHC has received attention recently, see e.g. Refs. [218, 219, 224–226] and references therein. This is so due to the following: first of all, together with $h \rightarrow Vh$, $pp \rightarrow WV$ probes via the longitudinal polarizations of the gauge bosons, the interactions of the goldstone bosons making it one of first places where one would expect to find signs of new physics related to the electroweak symmetry breaking. Secondly,

We refer the reader to Refs. [224–226] where new experimental distributions and searches are proposed in order to increase the sensitivity to the EFT parameters. If these are implemented by the experiments, the increase of sensitivity could allow diboson production at the HL-LHC to set much stringent bounds on the BSM amplitudes reaching the point where they are smaller than the SM, and therefore can start constraining “more standard” BSM scenarios.

We briefly comment on the possible interpretation of the EFT bounds that we get. Also, to get a sense of the usefulness of diboson production we study a simplified model of heavy vector triplets and compare the diboson bounds to other searches like dijets or Higgs, finding that diboson can be complementary with other searches, and in the future may be the leading search in certain regions of the parameter space.

6.2 Theoretical framework

We work in the so called Higgs basis [59, 227] which parametrizes the $d = 6$ EFT operators as modifications to the SM vertices, and where the fields are in the mass eigenstates and in the unitary gauge. In this basis and considering only operators with $d \leq 6$, the relevant terms for $pp \rightarrow WV$ production are:

$$\mathcal{L}_{\text{diboson}} \supset \mathcal{L}_{\text{TGC}} + \mathcal{L}_{V\bar{q}q} \quad (6.2.1)$$

where the first term contains the SM interactions between the electroweak gauge bosons together with the aTGC deformations,

$$\begin{aligned} \mathcal{L}_{\text{TGC}} = & ie (W_{\mu\nu}^+ W_\mu^- - W_{\mu\nu}^- W_\mu^+) A_\nu + ie [(1 + \delta\kappa_\gamma) A_{\mu\nu} W_\mu^+ W_\nu^-] \\ & + ig c_W [(1 + \delta g_{1,z}) (W_{\mu\nu}^+ W_\mu^- - W_{\mu\nu}^- W_\mu^+) Z_\nu + (1 + \delta\kappa_z) Z_{\mu\nu} W_\mu^+ W_\nu^-] \\ & + i \frac{e}{m_W^2} \lambda_\gamma W_{\mu\nu}^+ W_{\nu\rho}^- A_{\rho\mu} + i \frac{g c_W}{m_W^2} \lambda_z W_{\mu\nu}^+ W_{\nu\rho}^- Z_{\rho\mu}, \end{aligned} \quad (6.2.2)$$

and the second one contains the SM contribution and deviations to the couplings between the up and down quarks to the $V = W, Z$, gauge bosons,

$$\begin{aligned} \mathcal{L}_{V\bar{q}q} = & \sqrt{g^2 + g'^2} Z_\mu \left[\sum_{f \in u,d} \bar{f}_L \gamma_\mu (T_f^3 - s_W^2 Q_f + \delta g_L^{Zf}) f_L + \sum_{f \in u,d} \bar{f}_R \gamma_\mu (-s_W^2 Q_f + \delta g_R^{Zf}) f_R \right] \\ & + \frac{g}{\sqrt{2}} (W_\mu^+ \bar{u}_L \gamma_\mu (I_3 + \delta g_L^{Wq}) d_L + \text{h.c.}) . \end{aligned} \quad (6.2.3)$$

Since at dimension six the following relations are satisfied,

$$\delta\kappa_z = \delta g_1^z - \tan^2 \theta \delta\kappa_\gamma, \quad \lambda_z = \lambda_\gamma, \quad \delta g_L^{Wq} = \delta g_L^{Zu} - \delta g_L^{Zd}, \quad (6.2.4)$$

the deviations of the form $\sim g_{SM} (1 + \delta)$ can be parametrized by two independent aTGC (which we choose to be $\delta\kappa_\gamma, \delta g_{1z}$), and four independent corrections to $Z\bar{q}q$ vertices (which we choose to be $\delta g_L^{Zu}, \delta g_R^{Zu}, \delta g_L^{Zd}, \delta g_R^{Zd}$). Notice that the aTGC parametrized by $\lambda_\gamma = \lambda_z$ introduces a new type of coupling non-existent in the SM. With this, we have that in total there are seven parameters in the Higgs basis contributing to the leading deformations to diboson production (three aTGC and four $\delta V\bar{q}q$).

In the Lagrangian of Eq.(6.2.3) we haven't included the term δg_R^{Wq} nor the dipole contributions since these terms are either zero, or are suppressed by the Yukawas of the light quarks, and therefore negligible for FU and MFV. We also ignore the deviations on the lepton sector since their bounds from LEP-1 data are an order of magnitude better than those on the quark sector [69].

High energy behaviour and correlations

In the Higgs basis, the energy growth of the amplitudes that interfere with the SM in the high energy limit can be understood as follows. At tree level in the SM, the leading

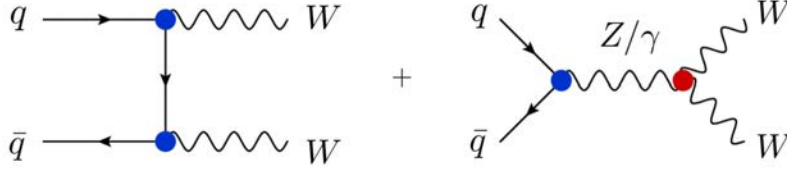


Figure 6.1: **Left:** Interaction of operators of the form $(HD_\mu H)(f\gamma^\mu f)$ appearing in e.g. the Warsaw basis that induce an amplitude that grows with s . **Right:** Tree level amplitude for $\bar{q}q \rightarrow WW$ with fields in the mass eigenstate and unitary gauge.

amplitude for $q\bar{q}' \rightarrow WW (WZ)$ is given by the sum of three diagrams, consisting of an s-channel exchange of the γ , Z bosons (W boson), and a t-channel contribution. Taking as an example the case of $\bar{q}q \rightarrow WW$, where $\bar{q}q = \bar{u}u, \bar{d}d$, one finds that the tree level SM amplitude is given by the Feynman diagrams of Fig. 6.1. One can check that at large center of mass energy, $s \gg m_W^2$, the total amplitude for $u\bar{u} \rightarrow W_L^+ W_L^-$ is given by

$$\mathcal{M}_\gamma + \mathcal{M}_Z + \mathcal{M}_t = i s \left[-\frac{e^2 \sin \theta}{2m_W^2} Q_f - \frac{e^2 \sin \theta}{2m_W^2} \frac{1}{s_W^2} (T_f^3 - s_W^2 Q_f) + \frac{e^2 \sin \theta}{2m_W^2} \frac{T_f^3}{s_W^2} \right] + \dots \quad (6.2.5)$$

where W_L^\pm stand for the longitudinal polarizations of the W^\pm gauge bosons, $s = E_{CM}^2$ stands for the squared center of mass energy, the dots stand for sub-leading contributions at high energy and θ is the angle between W^+ and the beam axis.¹

The key point of Eq. (6.2.5) is to notice that while each of the individual sub-amplitudes grows with s , the sum does not. Therefore, any modification to the SM couplings, shown in blue and red in Fig. 6.1, will spoil the cancellation of the different pieces in Eq. (6.2.5), and therefore the resulting amplitude will be proportional to s and the deformation of the SM coupling. In the Higgs basis it is specially clear to see that all the coefficients modifying diboson production will generically induce an amplitude that grows with s .

Regarding the effect of \mathcal{O}_{3W} = which generates the term $\lambda_\gamma W_{\mu\nu}^+ W_{\nu\rho}^- (s_W A_{\rho\mu} + c_W Z_{\rho\mu})$ in Eq. (6.2.2), one can see that this term is not generated in the SM. In this case one can't use the spoiling of the SM amplitude of Eq. (6.2.5) to see whether this term grows with the center of mass energy in the high energy limit. This is so because it only contributes to the amplitude $q\bar{q} \rightarrow W_\pm W_\pm, W_\pm Z_\pm$ which is not present in the SM model in the asymptotic high energy limit, and therefore it doesn't interfere with it when $m_W^2/s, m_q^2/s \rightarrow 0$. Nonetheless, one can see by direct calculation that the amplitude induced by these terms also grows with the E^2 due to having extra derivatives.

¹There is another term that grows with energy but we neglected since it is proportional to the quark masses. Its energy growth is canceled with the diagram including the Higgs, however, in our energy range it is negligible, and one can as a first approximation think of the quarks to be massless.

Helicity amplitudes at high energy and Correlations between aTGC and $\delta V \bar{q}q$

To estimate which operators or combinations of operators will be the most constrained, one can study each helicity amplitude appearing in diboson production as done in Refs. [91, 224]. In the limit where $s \gg m_W^2$ one finds that the leading helicity amplitudes for $pp \rightarrow WW$ are given by:

$$\begin{aligned}
\mathcal{M}(LL; 00) &= i \frac{s}{m_W^2} \frac{e^2 \sin \theta}{2s_W^2} \left[(2T_f^3) \delta g_L^{Wq} - \delta g_L^{Zq} - \delta g_{1z}(T_f^3 - s_W^2 Q_f) + \delta \kappa_\gamma t_W^2 (T_f^3 - Q_f) \right] + \dots \\
\mathcal{M}(RR; 00) &= i \frac{s}{m_W^2} \frac{e^2 \sin \theta}{2s_W^2} \left[\delta g_R^{Zq} - \delta g_{1z} Q_f s_W^2 + \delta \kappa_\gamma Q_f s_W^2 \right] + \dots \\
\mathcal{M}(LL; \pm\pm) &= i \frac{s}{m_W^2} \frac{e^2 \sin \theta}{2s_W^2} T_f^3 \lambda_\gamma + \dots,
\end{aligned} \tag{6.2.6}$$

while for $pp \rightarrow WZ$ they are

$$\begin{aligned}
\mathcal{M}(LL; 00) &= -i \frac{s}{m_W^2} \frac{e^2 \sin \theta}{2\sqrt{2}s_W^2 c_W} \left[\delta g_L^{Zu} - \delta g_L^{Zd} - \delta g_{1z} c_W^2 \right] + \mathcal{O}(s^0) \\
\mathcal{M}(LL; \pm\pm) &= -i \frac{s}{m_W^2} \frac{e^2 \sin \theta}{2\sqrt{2}s_W^2 c_W} \lambda_z + \mathcal{O}(s^0).
\end{aligned} \tag{6.2.7}$$

The L, R stand for the initial helicities of the quarks, while \pm and 0 stand for the transverse and longitudinal polarizations of the final electroweak bosons respectively.²

We can see, as pointed out in Refs. [91, 224], that in the asymptotic high energy regime there are only five independent combinations of parameters entering in $pp \rightarrow WW, WZ$ since

$$\mathcal{M}(u_L \bar{d}_L \rightarrow W_0 Z_0) \propto \mathcal{M}(\bar{u}_L u_L \rightarrow W_0 W_0) - \mathcal{M}(\bar{d}_L d_L \rightarrow W_0 W_0) + \mathcal{O}(s^0). \tag{6.2.8}$$

and therefore, there are only four relevant independent combinations for the longitudinal polarizations and one for the transverse ones in the high energy limit.³

From Eq. (6.2.6), Eq. (6.2.7), we find that in the Higgs basis there are seven coefficients parameterizing the five directions that grow with s for the processes $pp \rightarrow WW, WZ$. Hence, in the asymptotic high energy limit one has two completely flat directions among the Higgs basis coefficients even if each of the five high energy amplitudes are dominated by the d=6 BSM quadratic pieces. A simple way to see explicitly that these directions

²We computed these amplitudes using FeynCalc [228] using the BSMC package [229] for FeynRules [152], finding agreement with the expressions presented in Ref. [91], which also was a cross check for the .ufo file used in the Madgraph5 simulations.

³This counting may change for other flavour assumptions, since for example if FU or MFV are not imposed one has that for $pp \rightarrow WZ$ also the amplitude $\mathcal{M}(RR; 00) = -i \frac{e^2 s \sin \theta}{2\sqrt{2}m_W^2 s_W^2 c_W} \delta g_R^{Wq} + \mathcal{O}(s^0)$ is enhanced.

are there is by noting that any deviation of δg_{1z} and $\delta \kappa_\gamma$ in Eq. (6.2.6), Eq. (6.2.7) can be compensated by a modification of the vertex corrections $\delta V \bar{q}q$. Given that naively the characteristic energy of a process in diboson production is $\sqrt{s} \sim \text{TeV}$, one expects that the subleading amplitudes, which grow with \sqrt{s}/m_W instead of s/m_W^2 , can set bounds that are worse by a factor $\sqrt{s}/m_W \sim 10$ (as long as the BSM squared amplitudes dominate the cross section, as we will see that it is our case). These subleading amplitudes involve a longitudinal and a transverse vector boson in the final states. For $pp \rightarrow WW$ these are given by

$$\begin{aligned}\mathcal{M}(LL; 0\pm) &= -\frac{e^2\sqrt{s}\cos^2\frac{\theta}{2}}{\sqrt{2}m_W s_W^2} \left[(2T_f^3)\delta g_L^{Wq} - \delta g_L^{Zq} - \frac{1}{c_W^2}\delta g_{1z}(T_f^3 - s_W^2 Q_f) - T_f^3(\delta \kappa_\gamma + \lambda_\gamma) \right] \\ \mathcal{M}(RR; 0\pm) &= -\frac{e^2\sqrt{s}\sin^2\frac{\theta}{2}}{\sqrt{2}m_W s_W^2} \left[t_W^2 Q_f \delta g_{1z} - 2\delta g_R^{Zq} \right],\end{aligned}\tag{6.2.9}$$

while for $pp \rightarrow WZ$ one has

$$\mathcal{M}(LL; \pm 0) = -\frac{e^2\sqrt{s}}{2m_W s_W^2 c_W} \left[\delta g_L^{Zu} + \delta g_L^{Zd} + (\delta g_L^{Zu} - \delta g_L^{Zd}) \cos\theta - c_W^2(2\delta g_{1z} + \lambda_z) \sin^2\frac{\theta}{2} \right],\tag{6.2.10}$$

with the subleading terms are suppressed by $\sim 1/\sqrt{s}$. One can check that the combination of coefficients entering in the subleading terms cannot be obtained as a linear combination of the directions appearing in the leading s/m_W^2 amplitudes. Hence, one naively expects to find some directions in the EFT space that are $\mathcal{O}(10)$ times less well constrained than the five directions given by the amplitudes leading at high energy. We confirm this naive estimate later in Section 6.3.2 where we study the correlations among the different coefficients appearing in the Higgs basis.

6.3 Results with current LHC data

6.3.1 Data used and statistical analysis

To get the bounds on the different BSM coefficients we have used all the leptonic channels for $pp \rightarrow WW, WZ$ provided by CMS and ATLAS, which we show in Table 6.1. We indicate in each case the differential distribution used to perform the combined fit. We limited our analysis to purely leptonic decays due to their high sensitivity and the ease with which one can reproduce the experimental analyses. See [230] for a summary of the ATLAS and CMS constraints. There are nonetheless other channels that would be interesting to add, e.g. two quarks and two leptons in the final state [231], since they can set even tighter constraints than the purely leptonic ones.=

To perform the fit we calculate the BSM cross sections at tree level with MadGraph5 [151], while using FeynRules 2.0 [152] to generate the .ufo file for the BSMC model [229].

Experiment	$\mathcal{L}[\text{fb}^{-1}]$	\sqrt{s}	Process	Obs.	Ref.
ATLAS	4.6	7 TeV	$WW \rightarrow \nu\ell\nu$	$p_{T\ell}^{(1)}$	[232], Fig. 7
ATLAS	20.3	8 TeV	$WW \rightarrow \nu\ell\nu$	$p_{T\ell}^{(1)}$	[233], Fig. 11
CMS	19.4	8 TeV	$WW \rightarrow \nu\ell\nu$	$m_{\ell\ell}$	[234], Fig. 4
ATLAS	20.3	8 TeV	$WZ \rightarrow \ell\nu\ell\ell$	p_{TZ}	[235], Fig. 5
CMS	19.6	8 TeV	$WZ \rightarrow \ell\nu\ell\ell$	p_{TZ}	[236], Fig. 7
ATLAS	13.3	13 TeV	$WZ \rightarrow \ell\nu\ell\ell$	m_{WZ}	[237], Fig. 3

Table 6.1: Data used to extract the current LHC bounds.

This allows us to get the cross section in terms of the seven Higgs parameters $\delta g_{L,R}^{Zu,d}$ and $\delta g_{1z}, \delta\kappa_\gamma, \lambda_\gamma$. We perform a simulation to get the cross section for each bin for every differential distribution shown in Table 6.1, and then perform the cuts as described by the experimental collaborations in each case.⁴ To get the BSM cross section, we have generated for each bin several simulations corresponding to different values of the BSM coefficients and then we have fitted them to a general quadratic polynomial of the seven BSM coefficients $\delta g_{L,R}^{Zu,d}$ and $\delta g_{1z}, \delta\kappa_\gamma, \lambda_\gamma$ which we schematically call δ_i . With this we find that:⁵

$$\sigma_{SM+BSM}(\delta_1, \dots, \delta_n) = \sigma_{SM} + a_i \delta_i + b_{ij} \delta_i \delta_j, \quad (6.3.11)$$

where $i, j = 1, \dots, 7$, σ_{SM} corresponds to the SM contribution, which is found by setting all $\delta_i, \delta_j = 0$, and a_i and b_{ij} are the numerical coefficients to fit from all the runs done at different δ_i, δ_j which determine σ_{SM+BSM} as a function of δ_i, δ_j for each bin in each experimental search found in Table 6.1. We build the ratio $\delta\mu$ defined as

$$\mu(\boldsymbol{\delta}) = \frac{\sigma_{SM+BSM}(\boldsymbol{\delta})}{\sigma_{SM}} = 1 + \frac{\sigma_{BSM}(\boldsymbol{\delta})}{\sigma_{SM}} = 1 + \delta\mu(\boldsymbol{\delta}). \quad (6.3.12)$$

This is expected to largely cancel the systematic uncertainties since they are expected to be comparable for the SM and BSM contributions. If in the fiducial phase space into consideration the effects of taking into account the NLO corrections can be encapsulated by considering a k -factor, the $\delta\mu$ will also be stable under those corrections. Notice that

⁴In some cases, like $WW \rightarrow \nu\ell\nu\ell$, the cuts performed by the experiments for some sub-channels are performed using a Boosted Decision Tree and not just a cut and count approach. In this case we only generate the subchannel for which we can easily reproduce the cuts, i.e. $WW \rightarrow \nu_e e \nu_\mu \mu$ and then fit to the total combination assuming that it doesn't depend on the lepton flavor.

⁵When simulating the BSM cross sections, we modify the four $Z\bar{q}q$ couplings $\delta g_L^{Zu}, \delta g_L^{Zd}, \delta g_R^{Zu}, \delta g_R^{Zd}$, for all the quark generations at the same time, as one would do in the FU case, see Eq. (C.0.4). Nonetheless, due to the proton's PDF, the contribution of the light quarks u, d is more than a factor ten greater than the one of c, s , so one can safely assume that the modifications of $Z\bar{q}q$ for second and third generation give negligible contributions to diboson production. We expect that the results we get for the diboson fit on the $Z\bar{q}q$ couplings for the FU case also apply for the $Z\bar{q}q$ couplings for the first two generations of the MFV case, since in the MFV case $[\delta g_{L,R}^{Zu,d}]_{11} \simeq [\delta g_{L,R}^{Zu,d}]_{22}$.

this might not hold for transverse polarizations, due to the non-interfering effects, see Ref. [226]. With this we build a χ^2

$$\chi^2 = \sum_{I \in \text{channels}} \sum_{i \in \text{bins}} \frac{(\tilde{\sigma}_{SM}^{bkg} + \mu \tilde{\sigma}_{SM}^{signal} - \sigma_{measured})_{I,i}^2}{(\Delta_{sys})_{I,i}^2 + (\Delta_{stat})_{I,i}^2}, \quad (6.3.13)$$

where the first sum runs through all the channels under study, and the second sum runs over each bin for the chosen differential distribution. σ_{exp} is the measured cross section including signal and background, $\tilde{\sigma}_{SM}^{bkg}$ and $\tilde{\sigma}_{SM}^{signal}$ correspond to the simulated cross sections for the signal and background done by the experimental collaborations, Δ_{sys} is the theoretical uncertainty given by the experimental collaborations on the predicted SM cross sections, i.e. $\tilde{\sigma}_{SM}^{bkg}$ and $\tilde{\sigma}_{SM}^{signal}$, and Δ_{stat} is the statistical error which is given by $\Delta_{stat} = \sqrt{\mathcal{L} \sigma_{exp}}$ where \mathcal{L} stands for the integrated luminosity. In practice we multiply everything by the integrated luminosity and compute the χ^2 using the number of events shown in the figures referred to in Table 6.1. One can massage a bit the χ^2 in Eq. (6.3.13) to make it more intuitive, getting:

$$\chi^2 = \sum_{I \in \text{channels}} \sum_{i \in \text{bins}} \frac{(1 + \xi \delta\mu(\boldsymbol{\delta}) - \mu_{measured})^2}{(\delta_{sys})_{I,i}^2 + (\delta_{stat})_{I,i}^2}, \quad (6.3.14)$$

where $\xi = s/(s+b)$, with $s = \tilde{\sigma}_{SM}^{signal}$ and $b = \tilde{\sigma}_{SM}^{bkg}$, $\mu_{measured} = \sigma_{measured}/(s+b)$, $\delta_{sys} = \Delta_{sys}/(s+b)$ and $\delta_{stat} = \Delta_{stat}/(s+b)$. In Eq. (6.3.14), the $\boldsymbol{\delta}$ in $\delta\mu(\boldsymbol{\delta})$ stand for the seven BSM coefficients in the Higgs basis that we want to fit.

Regarding the χ^2 for LEP-1, we build it from the correlation matrices, central values and errors given in Ref. [69].⁶

6.3.2 Correlations among the Higgs basis parameters

When performing a χ^2 fit, if the χ^2 is Gaussian in terms of the parameters to be fit, one can easily find the correlation by looking at the entries of the correlation matrix. In our case, given that the χ^2 is not Gaussian due to the large size of the $d = 6$ BSM quadratic amplitudes, we can not extract a correlation matrix. Therefore, to see the correlations among the different BSM coefficients we perform a global fit and look at the two dimensional plots for each pair of coefficients profiling over all others.

As an example of the correlations among the different parameters that one finds in diboson processes, in the center of Fig. 6.2 we show the two dimensional slice for $(\delta\kappa_\gamma, \delta g_R^{Zu})$, a pair of parameters with a large correlation. The least constrained direction in the central plot follows the slope given by the combination appearing in the amplitude $\mathcal{M}(RR; 00)$ of Eq. (6.2.6). We find that in this case the flat direction is about

⁶We thank the authors of [69] for providing the Mathematica code with all the aforementioned quantities that had more precision than in the paper, and allowed to get a more reliable χ^2 for LEP-1.

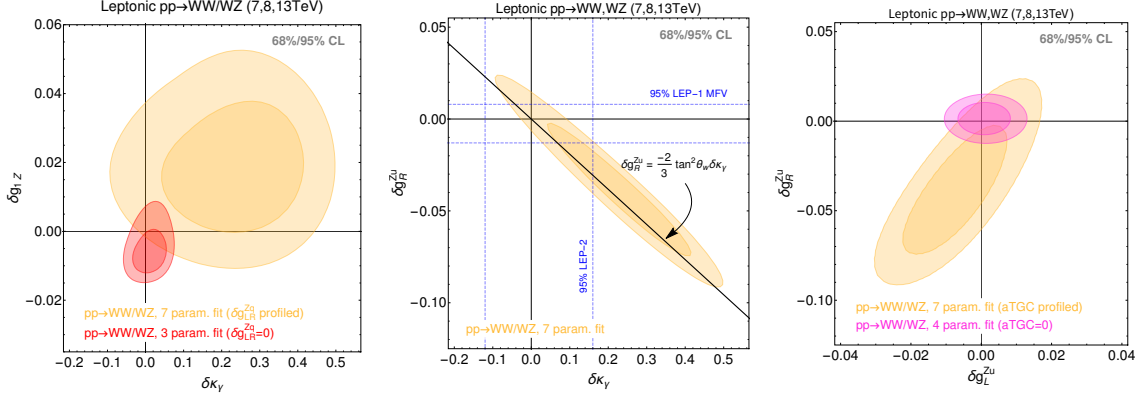


Figure 6.2: 68%, 95% CL fits to the LHC diboson data from Table 6.1. **Center:** fit to $\delta\kappa_\gamma$ and δg_R^{Zu} marginalizing over all other five parameters. The line shows the expected flat direction in the $s \rightarrow \infty$ limit that can be deduced from Eq. (??). **Left (Right):** in yellow the fit to aTGC (vertex corrections) marginalizing over all other parameters, and in red (pink) the fit when the four $\delta Z \bar{q}q$ (three aTGC) are set to zero.

ten times less constrained than orthogonal direction, in agreement with the naive estimate made in section Section 6.2.

The large correlation shown in the center of Fig. 6.2 makes δg_R^{Zu} and $\delta\kappa_\gamma$ very sensitive to each other. We show in horizontal blue dashed lines the allowed 95% CL bounds set by LEP-1 on δg_R^{Zu} and in vertical the 95% CL bounds set by LEP-2 on $\delta\kappa_\gamma$.

From this plot one can intuitively see that by allowing δg_R^{Zu} on may modify the bounds on $\delta\kappa_\gamma$ in a non-negligible way. This indicates that if the $\delta V \bar{q}q$ are to be included in the aTGC fit, it is important to use a global fit with LEP constraints. We see that the sensitivity of diboson to the different parameters is ultimately limited by the correlations, making a global combination crucial.

Fortunately, in a broad class of models the parameter $\delta\kappa_\gamma$ is expected to be generated only via loops, so it is expected to be parametrically smaller and therefore negligible when setting constraints. The same holds true for λ_γ , which is also typically loop suppressed. This is because both $\delta\kappa_\gamma$ and λ_γ modify the magnetic moment and electric quadrupole of the W , which are only generated at one loop by minimally coupled theories [77]. Due to the large correlations, setting them to zero can greatly increase the accuracy of the fit to the various $\delta V \bar{q}q$.

6.3.3 LHC bounds on $\delta V \bar{q}q$ vs LEP-1

In Fig. 6.3 we show the allowed 95% CL regions for the BSM coefficients δg_L^{Zu} , δg_R^{Zu} , δg_L^{Zd} , δg_R^{Zd} defined in Eq. (6.2.2), Eq. (6.2.3), assuming that the aTGC are not negligible (yellow), that $\lambda_\gamma = \delta\kappa_\gamma = 0$ (blue) and that $\lambda_\gamma = \delta\kappa_\gamma = \delta g_{1z} = 0$ (pink). In gray we show the bounds extracted from the LEP-1 fit in in [69], assuming that the EFT

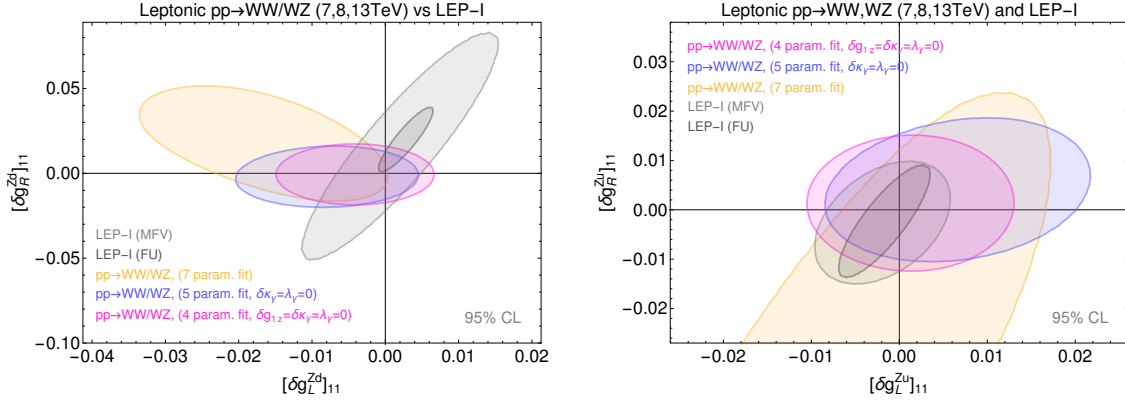


Figure 6.3: 95% CL regions for the anomalous couplings between the light quarks and the electroweak bosons. In light (dark) gray, the LEP-1 constraints assuming MFV (FU). In yellow, the diboson bounds after profiling over the remaining five parameters. In blue (pink) the same but setting $\delta\kappa_\gamma = \lambda_\gamma = 0$ ($\delta\kappa_\gamma = \lambda_\gamma = \delta g_{1z} = 0$).

satisfies either MFV (light gray) or FU (dark gray). To avoid confusion, let us remind that when extracting the diboson bounds, we do not differentiate the cases of MFV and FU since diboson production is mostly insensitive to possible differences between the light generations and the third generation that appear in the MFV case; the only difference is a matter of interpretation, i.e. if one assumes FU the diboson bounds on the $Z\bar{q}q$ anomalous couplings apply to all the three quark generations, while if one assumes MFV they only apply only to u, d, c and s quarks.

We find that even for the most general case where we include all the seven BSM parameters in the fit (yellow), the diboson bounds for the down-type couplings are already competitive with those from LEP-1 under the MFV scheme. Even more, for δg_R^{Zd} they are better than the MFV and competitive with LEP-1 under the FU assumption. On the other hand, for the up type quarks, we find that the bounds are still significantly worse than those from LEP-1 even under the MFV assumption.

Assuming that $\lambda_\gamma = \delta\kappa_\gamma = 0$ (blue), we find a big improvement on the diboson fit with respect to the seven parameter fit in yellow. The most striking difference being that for the up type couplings, δg_L^{Zu} and δg_R^{Zu} in the right plot, the diboson bounds become of the same order of magnitude as those from LEP-1; from these two, it is δg_R^{Zu} the one that benefits the most from setting $\lambda_\gamma = \delta\kappa_\gamma = 0$. For the down type couplings, we also find an improvement of about a factor two when setting the other two aTGC to zero. This is enough to allow the current diboson data to set constraints on δg_R^{Zd} to be of the same order of those from LEP-1 assuming FU and much better than the LEP-1 ones assuming MFV.

In pink we have the case where the three aTGC are negligible compared to $\delta Z\bar{q}q$, i.e. $\lambda_\gamma = \delta\kappa_\gamma = \delta g_{1z} = 0$. In this case we find a very similar situation than for the blue

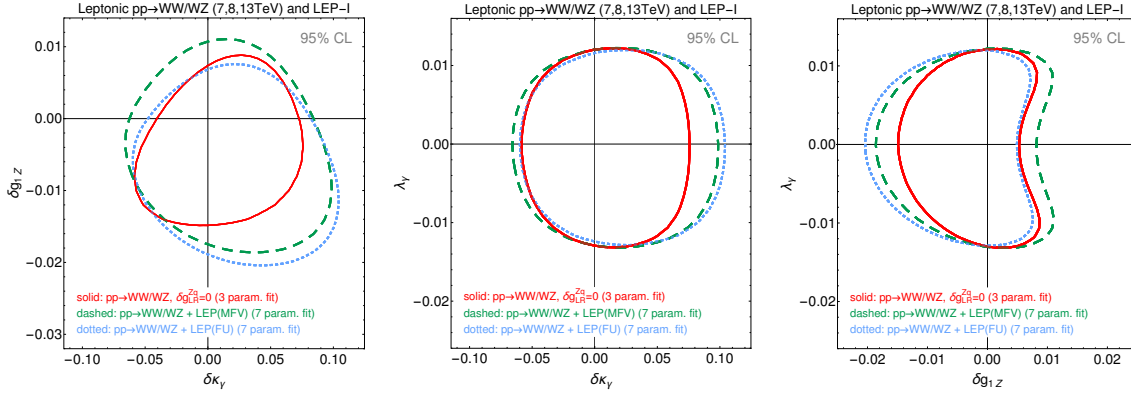


Figure 6.4: 95% CL regions for the aTGCs. In red we impose $\delta V \bar{q} q = 0$ and only use diboson data to perform a three parameter fit to the aTGC profiling over the remaining one. In green and blue we perform a seven parameter global fit using the diboson data and LEP-1 data assuming the MFV and FU assumptions respectively; we profile over all remaining parameters. **Top:** Bounds using the leptonic $pp \rightarrow WW, WZ$ LHC data.

case when δg_{1z} is not neglected. We see that the left handed couplings get a significant improvement with respect to the blue region, while the right handed ones are almost insensitive this extra assumption on δg_{1z} .

Notice that the correlations among the left and right couplings in LEP-1 are not aligned with the correlation appearing in $pp \rightarrow WV$, making the combination of the two experiments much more constraining than what one would naively expect. This can be seen in Table D.2 for example, where we show the individual constrains from diboson and LEP-1 and their combination in the case where $\delta \kappa_\gamma = \lambda_\gamma = 0$. Notice also that while the Flavour Universal LEP-1 data for down quarks has a two sigma excess (driven by the $Zb\bar{b}$ asymmetry), the LHC diboson data presents a two sigma excess as well, but in the opposite direction so the combination alleviates the tension with the SM. As an example we show in Table D.2 the individual and combined bounds for LEP-1 and $pp \rightarrow WW, WZ$ for the case where $\delta \kappa_\gamma = \lambda_\gamma = 0$, which appear in blue in Fig. 6.3.

One should remember that the bounds from $pp \rightarrow WV$ in Fig. 6.3 only constrain BSM theories where the new particles are above few TeV so the EFT expansion is valid, while those from LEP-1 apply to theories where the new particles can be as light as ~ 100 GeV. This can be schematically seen in Fig. 6.9 of ???. To finalize this section, we note that when performing the fits to $pp \rightarrow WV$ we find that the BSM quadratic amplitudes contributing to the diboson cross section are not negligible. We comment on what this means for the EFT interpretation and possible BSM models in Section 6.5.1.

6.3.4 LHC bounds on aTGC and interplay with $\delta V\bar{q}q$

In Fig. 6.4 we present the 95% CL regions for the three aTGC parametrized by δg_{1z} , $\delta\kappa_\gamma$, λ_γ . In red, we show a fit to the three aTGC setting $\delta g_L^{Zu} = \delta g_R^{Zu} = \delta g_L^{Zd} = \delta g_R^{Zd} = 0$ and profiling over the one aTGC not appearing in the plot. In this case we only use the LHC data from Table 6.1. In dashed green and dotted blue we make a fit to the seven BSM parameters, the three aTGC δg_{1z} , $\delta\kappa_\gamma$, λ_γ and the four $\delta g_{L,R}^{Zu,d}$ and profile over those not appearing in the plot; in this case we use $\chi^2 = \chi_{diboson}^2 + \chi_{LEP-1}^2$, assuming FU (dashed green) and MFV (dotted blue).

From Fig. 6.4 we see that the effect of not neglecting the $\delta Z\bar{q}q$ is the largest in the $(\delta\kappa_\lambda, \delta g_{1z})$ plane, where the constrained area in parameter space varies around 50% from one assumption to the other. This points to a large correlation between $\delta\kappa_\gamma$ and δg_{1z} on the $\delta V\bar{q}q$ parameters, which is to be expected since they appear in the same high energy amplitudes as seen in Eq. (6.2.6), Eq. (6.2.7). Regarding λ_γ we find that it is insensitive to the different assumptions, as expected from the fact that it is the only parameter appearing in the amplitudes that grow with s and have final polarizations $\pm\pm$.

Given that in many BSM models $\delta\kappa_\gamma$ and λ_γ are assumed to be loop induced and therefore parametrically smaller than δg_{1z} , we also study the effect of including $\delta Z\bar{q}q$ for the case where diboson data is used to set bounds on δg_{1z} alone. We do this since our fit is non-gaussian. In Fig. 6.5 we show in solid black the one parameter fit to δg_{1z} , setting all the other parameters to zero (i.e. aTGC and $\delta V\bar{q}q$ to zero). In dashed green and dotted blue, we allow δg_L^{Zu} , δg_R^{Zu} , δg_L^{Zd} , δg_R^{Zd} to be different than zero and perform a global fit.

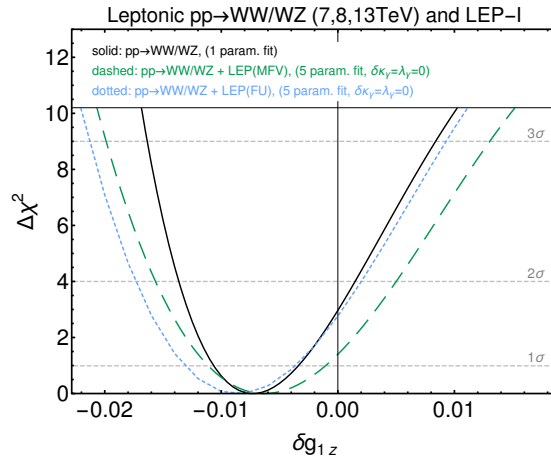


Figure 6.5: Constraints on δg_{1z} assuming $\delta\kappa_\gamma$ and λ_γ to be loop suppressed. In black, an exclusive fit where only δg_{1z} is taken into account. In dashed green and dotted blue, profiling over the fermion-electroweak boson vertices under different flavor assumptions.

Similarly to Fig. 6.4, in Fig. 6.5 we also find that including the effects of $\delta V\bar{q}q$ changes

the current constraints on δg_{1z} by a factor of about 25%. Also, we find that once the $\delta V_{\bar{q}q}$ are introduced, the FU and MFV assumptions which modify χ_{LEP-1}^2 yield qualitatively similar size effects to δg_{1z} but still with at least 10% differences between the two.

As mentioned in the introduction, Ref. [219] performed a similar analysis using the ATLAS 8 TeV $pp \rightarrow W^+W^- \rightarrow \ell\nu q\bar{q}$ data from Ref. [233] at NLO. We checked that we get very similar results for that case. In this section the aim was to study the same effect using all the current leptonic data to see if the effect was enhanced or decreased, and also to see the differences between assuming FU and MFV. Looking at the LEP-1 bounds for $\delta V_{\bar{q}q}$ in Fig. 6.3 could make one think that for the MFV case one could have even larger deviations in the aTGC fits. This seems not to be the case because the largest correlation in the fit appears to be between $\delta\kappa_\gamma$ and δg_R^{Zu} as we show in Section 6.3.2. Regarding the differences between fitting one channel or all of them, we find that by including more channels in the combined fit, the relative effect of including the $\delta V_{\bar{q}q}$ on the aTGC fit doesn't change qualitatively.

6.4 Projected bounds for the HL-LHC

6.4.1 Data used and assumptions for the HL-LHC

To estimate the bounds at the HL-LHC, as a first step and for simplicity, we have simulated the signal channels for $pp \rightarrow WW \rightarrow \nu\ell\nu\ell$ and $pp \rightarrow WZ \rightarrow \ell\nu\ell\ell$. We use a χ^2 with the same form as in Eq. (6.3.14), but in this case we assume that the measured number of events will be the same as in the SM prediction, so that $\mu_{measured} = 1$. To determine the systematic uncertainties and the background projections, there is a very limited literature from the experimental or theory groups on $pp \rightarrow WV$, specially for high energy bins. Instead of trying to do such an analysis, we opted for a very simple rule of thumb to get a sense of the possibilities of diboson production at the HL-LHC. For the systematics, based on the current uncertainties we take two benchmark scenarios, a more pessimistic one, where the systematics will be $\delta_{syst} = 30\%$ on all bins, and a more optimistic one, where they will be 5% in all bins. As we will see, since the constraining power comes from the last bins the limits are dominated by the statistical uncertainties. We study the results by the end of the HL-LHC. For the the WW channel, we consider the $m_{\ell\ell}$ distribution and for the WZ we consider the p_T^Z distribution. In both cases we have chosen the binning in such a way that the overflow bin contains ten events, to maximize the sensitivity while also having at least 10 events in the last bins.

We compare our estimated bounds on the aTGC for the HL-LHC with 3 ab^{-1} (shown in red in Fig. 6.4), with those in Fig. 3 of Ref. [238], which get the aTGC bounds from $W\gamma \rightarrow \ell\nu\gamma$ and $WZ \rightarrow \ell\nu\ell\ell$ assuming 100 fb^{-1} and 1 ab^{-1} at 14 TeV; we find that our bounds assuming $\delta_{sys} = 5\%$ (and no reducible background) for leptonic WW and WZ

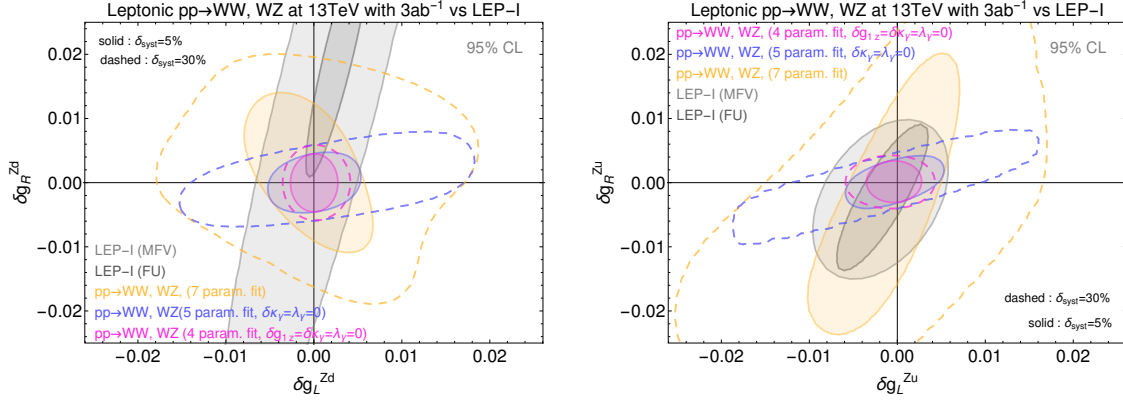


Figure 6.6: 95% CL regions for the anomalous couplings between the light quarks and the electroweak bosons. In light (dark) gray, the LEP-1 constraints assuming MFV (FU). In yellow, the diboson bounds after profiling over the remaining five parameters. In blue (pink) the same but setting $\delta\kappa_\gamma = \lambda_\gamma = 0$ ($\delta\kappa_\gamma = \lambda_\gamma = \delta g_{1z} = 0$).

are more conservative but very similar to those appearing in Fig. 3 of Ref. [238]. So our simple assumptions are in line with other literature. Also, both us and Ref. [238] are only focusing on the leptonic channels, it would be interesting to study the impact of including the semileptonic channels. Also, the inclusion of more refined observables like those presented in Refs. [224–226] may greatly increase the diboson reach, making our estimates on the diboson reach at the HL-LHC to be on the conservative side. See Section 6.5.3 where we compare the reach of leptonic WZ estimated in Ref. [224] with our combination of the leptonic WW and WZ .

6.4.2 HL-LHC projections on $\delta V \bar{q}q$ vs LEP-1

In Fig. 6.6 we show the allowed 95% CL regions for δg_L^{Zu} , δg_R^{Zu} , δg_L^{Zd} , δg_R^{Zd} assuming that the aTGC are not negligible (yellow), that $\lambda_\gamma = \delta\kappa_\gamma = 0$ (blue) and that $\lambda_\gamma = \delta\kappa_\gamma = \delta g_{1z} = 0$ (pink) using the estimates for the HL-LHC with 3 ab^{-1} . In gray we show the bounds extracted from the LEP-1 assuming that the EFT satisfies either MFV (light gray) or FU (dark gray). We find that by the end of the HL-LHC it may be possible, for low enough systematics, to surpass the LEP-1 bounds under the MFV assumption for all the $\delta V \bar{q}q$ in the case where $\delta\kappa_\gamma = \lambda_\gamma = 0$ (blue), and also when all three aTGC are set to zero (pink). Even more, these two cases will vastly surpass the LEP-1 bounds on the right handed couplings under the FU assumption, while for the left handed ones the HL-LHC will only be slightly better for $\delta\kappa_\gamma = \lambda_\gamma = 0$ and about a factor two better for the case when $\delta\kappa_\gamma = \lambda_\gamma = \delta g_{1z} = 0$. We see that the blue and pink bounds go from being at the percent level in the current bounds, see Fig. 6.3, to being at the few permille. Also, assuming $\delta_{sys} = 5\%$, we find that the seven parameter fit will also improve by about a factor three the bounds for all the $\delta V \bar{q}q$ with respect to today's bounds shown

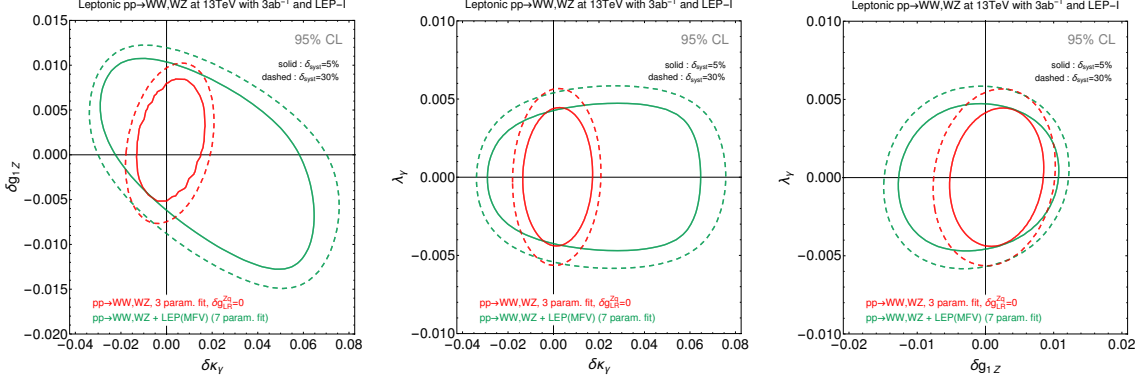


Figure 6.7: Estimate of the bounds for the HL-LHC. Solid and dashed stand for an assumed systematical error of 5% and 30% respectively.

in Fig. 6.3. We find that even for the seven parameter fit diboson production could equal or surpass LEP-1 under MFV for δg_L^{Zd} , δg_L^{Zu} and δg_R^{Zd} . On the other hand, if $\delta_{sys} = 30\%$, the improvement for seven parameter fit and $\delta\kappa_\gamma = \lambda_\gamma = 0$ with respect to today constraints, will be limited and mostly improve the right handed couplings, and only the HL-LHC bounds on δg_R^{Zd} will surpass the LEP-1 bounds (both for MFV and FU).

To summarize, using a simple analysis and only the leptonic channels $pp \rightarrow WW, WZ$ with the differential distributions being used today by CMS and ATLAS, the HL-LHC should be able greatly improve or equal the bounds on all the anomalous couplings between the Z gauge boson and the light quarks, reaching a few permille precision for theories with negligible $\delta\kappa_\gamma$. Given that we didn't include more sophisticated differential distributions, nor all the non leptonic channels, nor the $W\gamma$ ones, we expect that by the end of the HL-LHC diboson production can vastly improve the LEP-1 bounds on δg_L^{Zd} , δg_L^{Zu} , δg_R^{Zu} and δg_R^{Zd} in quite a model independent way for BSM theories with new particles above a few TeV.

6.4.3 HL-LHC projections on aTGC and interplay with $\delta V \bar{q}q$

In Fig. 6.7 we present the 95% CL regions for the three aTGC parametrized by δg_{1z} , $\delta\kappa_\gamma$, λ_γ . In red, we show a fit to the three aTGC setting $\delta g_L^{Zu} = \delta g_R^{Zu} = \delta g_L^{Zd} = \delta g_R^{Zd} = 0$ and profiling over the one aTGC not appearing in the plot. In green we make a fit to the seven BSM parameters, the three aTGC δg_{1z} , $\delta\kappa_\gamma$, λ_γ and the four $\delta g_{L,R}^{Zu,d}$ and profile over those not appearing in the plot. We use the HL-LHC projections to build $\chi_{diboson}^2$ while the χ_{LEP-1}^2 is built from the global fits performed in Ref. [69]. We find that for the HL-LHC the differences between assuming MFV or FU for χ_{LEP-1}^2 are negligible when performing a global fit $\chi^2 = \chi_{diboson}^2 + \chi_{LEP-1}^2$. For this reason in this section we only assume FU for the LEP-1 fit, which give almost identical results to the MFV case.

We find that the HL-LHC on the aTGC bounds shown in Fig. 6.7 are qualitatively

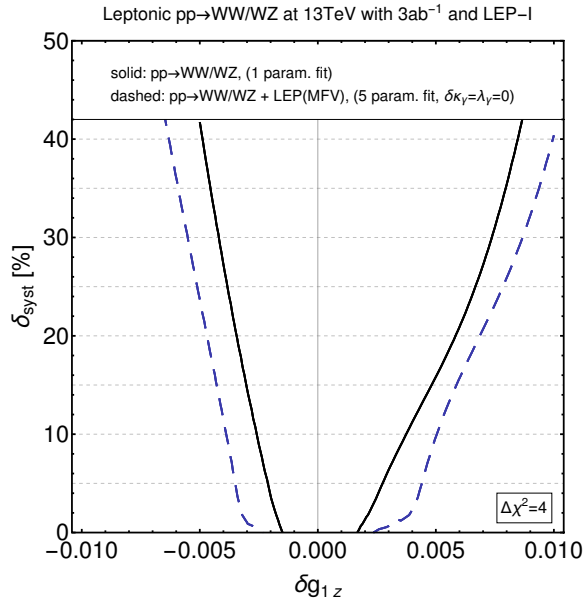


Figure 6.8: 95%CL constraints on δg_{1z} as a function of the systematic uncertainty assumed for the case where the light quark vertices are neglected (solid black) and for the case where we take them into account and combine the fit with LEP-1 data (dashed blue).

similar to those for the current data shown in Fig. 6.4 of Section 6.3.4. The main difference between the two is that the features found with the current data regarding the impact of $\delta V \bar{q} q$ are accentuated at the HL-LHC, i.e. we find that the $\delta V \bar{q} q$ will have a larger effect at the HL-LHC with respect to the current data. In particular, as seen from Fig. 6.7 the impact of introducing $\delta Z \bar{q} q$ won't be negligible for $\delta \kappa_\lambda$ and δg_{1z} . We see that the bounds on $\delta \kappa_\gamma$ and δg_{1z} vary more than a 100% if one assumes MFV or FU as the flavour assumptions. On the other hand λ_γ will be mostly unaffected as expected from Eq. (6.2.6), Eq. (6.2.7).

In Fig. 6.8 we show the 95%CL constraints on δg_{1z} as a function of the systematic uncertainty assumed. We compare the case where the light quark vertices are neglected with the case where we take them into account and combine the fit with LEP-1 data. We see that the fit is rather stable under modification of the systematic uncertainties, changing a factor two between neglecting the systematics (and therefore assuming all uncertainty coming from the statistical uncertainty) or setting them to 50%. The constraints are around the few per mille, an order of magnitude better than current constraints. However, there might be more promising analyses to push the constraints further [224].

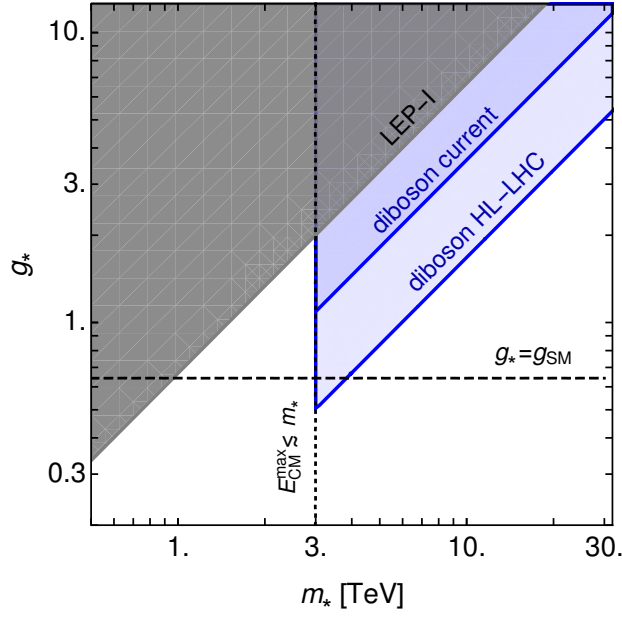


Figure 6.9: Excluded regions at the 95% CL consistent with the EFT expansion.

6.5 Interpretation of the constraints

6.5.1 Quadratic BSM amplitudes and EFT validity

Should be kept in mind that the constraints on the parameters presented so far apply only when the EFT expansion is valid, i.e. when the cutoff of the EFT is higher than the energies probed. This is schematically shown in Fig. 6.9, where blue regions show the excluded parameter space by diboson observables. If we characterize the high energy theory with a coupling g_* and a mass m_* , a simple counting gives $\delta g \sim g_* v^2 / m_*^2$ (this will be exemplified with more detail with a particular model). Diboson processes set constraints on g_* / m_*^2 . The fact that we should ensure that the maximum energy reach in the process E_{max} has to be smaller than m_* , this sets a lower limit on the size of the coupling we are probing, which translates to the fact that in most cases the EFT is sensitive only to strongly coupled theories.

Given that the center of mass energy of the interacting partons is not known at the LHC, it may be impossible to know the center of mass energy of a given process if the energy and momentum of the final states is not completely reconstructed. This is the case of the leptonic processes for $pp \rightarrow WV$, where one has one or two neutrinos in the final states, making it impossible to know the center of mass energy of any given process. One could extend the EFT reach below the 3 TeV mark in Fig. 6.9 without changing the experimental analysis by following the procedure explained in [75, 239]. The procedure is based on considering all the events, but simulating the BSM signal only for energies below some cutoff E_{cut} , so that one ensures the EFT validity. The constraints obtained

this way are, although pessimistic since one is throwing away the events above the cutoff, totally consistent with the EFT expansion. Note that in Ref. [224] a search strategy is proposed that allows to extend the EFT for a lower cutoff and therefore with much weaker coupling.

We find in our analysis that the quadratic pieces of the BSM amplitude are not negligible, neither with the current data nor for the HL-LHC. As already noted and extensively discussed in Refs. [75, 89–91, 218, 219, 221–226, 240, 241], when setting bounds to the EFT coefficients, it may happen that these bounds only constrain BSM amplitudes that are larger than the SM one. This makes the quadratic dimension six BSM amplitudes to be non negligible, which at the same time makes the dimension eight interference with the SM be naively non-negligible as well given that they have the same suppression of $1/\Lambda^4$.

It is useful to schematically write the ratio of amplitudes between the EFT and the SM. These estimates have already been discussed in [75, 226, 242], here we only give a small review for convenience. For the case in which we are most interested, where both final states WW (WZ) are longitudinally polarized one has that the ratio of amplitudes is given by

$$\left| \frac{\mathcal{M}_{\text{EFT}}}{\mathcal{M}_{\text{SM}}} \right|^2 \sim 1 + \frac{c_6}{g_{SM}^2} \frac{E^2}{\Lambda^2} + \left(\frac{c_6^2}{g_{SM}^4} + \frac{c_8}{g_{SM}^2} \right) \frac{E^4}{\Lambda^4} + \dots, \quad (6.5.15)$$

where c_6, c_8 represent the coefficients in front of the $d = 6, 8$ operators. The longitudinal helicity amplitude is particularly interesting since at high energy is the leading piece which sets constraints on all the EFT parameters entering diboson production except λ_γ . If the quadratic term in Eq. (6.5.15) dominates, it means that to be completely general one should perform a fit including the dimension eight operators as well. Since in this work we are not including them, our bounds only apply to theories where

$$c_6^2 \gtrsim g_{SM}^2 c_8, \quad (6.5.16)$$

which in general imposes that c_6 must be of order one or, equivalently, the operator should be generated at tree level. If one has that $c_6 \sim c_8 \sim g_\star^2$, then the requirement imposes that the BSM coupling must be larger than the SM one, i.e. $g_\star^2 \gtrsim g_{SM}^2$. Nonetheless, this constraint is automatically fulfilled for this power counting if the quadratic BSM pieces in Eq. (6.5.15) dominate. Comparing the linear and quadratic BSM contributions to the amplitude in Eq. (6.5.15), one finds that if the quadratic BSM pieces dominate, then

$$c_6 > g_{SM}^2 \frac{\Lambda^2}{E^2}. \quad (6.5.17)$$

For $\Lambda > E$, one finds that $c_6 \sim g_\star^2 \gtrsim g_{SM}^2$, making g_\star to be automatically larger than g_{SM} , which is the requirement to neglect the dimension eight operators. On the other hand, if one finds bounds where $g_\star^2 < g_{SM}^2$, then it is likely that the quadratic BSM amplitude is smaller than BSM interference with the SM.

For the case of amplitudes with mixed longitudinal and transverse polarizations, which have amplitudes that grow with \sqrt{s} and are therefore subleading, the requirements for the EFT to be valid are the same as for the longitudinal case.

For the case of transverse polarizations with $W_{\pm}V_{\pm}$, the ratio of amplitudes is given by

$$\left| \frac{\mathcal{M}_{\text{EFT}}}{\mathcal{M}_{\text{SM}}} \right|^2 \sim 1 + \frac{c_6}{g_{SM}^2} \frac{m_W^2}{E^2} \frac{E^2}{\Lambda^2} + \left(\frac{c_6^2}{g_{SM}^4} + \frac{c_8}{g_{SM}^2} \right) \frac{E^4}{\Lambda^4} + \dots \quad (6.5.18)$$

In this case, the naive requirement for one to be able to neglect the $d = 8$ operators is the same as before, since double insertion of dimension 6 operators dominates in the same regime. However, the suppression of the linear interference with dimension 6 means that for small coupling the leading contributions to the process come from dimension 8 insertions, limiting the validity of the EFT approach. See [242] for a detailed discussion of the interference effects.

We see that in Eq. (6.5.18), the interference between the SM amplitude and the EFT contributions has a suppression of m_W^2/E^2 due to the requirement of having helicity flips. One might enhance those terms after taking into account NLO effects as explained in Ref. [226, 242]. Since in our fits we find for λ_{γ} the quadratic BSM pieces always dominate by orders of magnitude, we don't expect that including NLO in the computation of the observables could have a significant effect on our conclusions.

The message of this section can be summarized as follows: If one finds when performing the fit that the quadratic $d = 6$ amplitudes are not negligible, this implies that the bounds only apply to theories that can generate operators satisfying the inequalities in Eq. (6.5.16), Eq. (6.5.18) and Eq. (6.5.17). Notice that this implies that they must be of tree level size. If one assumes power countings where $c_6 \sim c_8 \sim g_{\star}^2$ the bound won't in general be able to exclude values below g_{SM} . On the other hand, if one performs a fit to g_{\star} and finds that it is smaller than g_{SM} , it is likely that the quadratic BSM amplitude is subleading and the EFT is consistent as long as $\sqrt{s} \ll M \sim \Lambda/g_{\star}$.

6.5.2 Power countings and BSM interpretation

In the following, we present various power countings to exemplify the various assumptions made on the values of the three aTGC and four vertex corrections when presenting the results in Section 6.3. As a first step we differentiate between theories where the aTGC given by λ_{γ} and $\delta\kappa_{\gamma}$ are either tree level size or loop suppressed. For example, in many renormalizable UV models or SILH like models [77], λ_{γ} and $\delta\kappa_{\gamma}$ are in general loop suppressed while δg_{1z} is generated at tree level giving the following power counting for the aTGC:

$$\delta g_{1z} \sim \frac{m_W^2}{m_{\star}^2}, \quad \delta\kappa_{\gamma} \sim \frac{g_{\star}^2}{16\pi^2} \frac{m_W^2}{m_{\star}^2}, \quad \lambda_{\gamma} \sim \frac{g_{SM}^2}{16\pi^2} \frac{m_W^2}{m_{\star}^2}. \quad (6.5.19)$$

For this broad class of scenarios, $\delta\kappa_\gamma$ and λ_γ can be safely neglected since they are parametrically suppressed with respect δg_{1z} . Notice also that since δg_{1z} is only suppressed by $1/m_\star^2$, it means that if the experimental fit is driven by the quadratic terms of the cross section, one might be parametrically sensitive to insertions of dimension 8 operators.

If the light quarks mix with fermionic resonances Ψ (belonging to some strong sector) via $\epsilon_q m_\star \bar{q} \Psi$, the coupling of the light quarks to the strong sector is proportional to the strong coupling g_\star and the mixing parameter ϵ_q ,

$$\delta g_{L,R}^{Zu,d} \sim \epsilon_q \frac{g_\star^2}{g_{SM}^2} \frac{m_W^2}{m_\star^2}. \quad (6.5.20)$$

For these types of scenarios with composite light quarks, there is a hierarchy of parameters

$$\delta g_{L,R}^{Zu,d} : \delta g_{1z} : \delta\kappa_\gamma : \lambda_\gamma = \epsilon_q \frac{g_\star^2}{g_{SM}^2} : 1 : \frac{g_\star^2}{16\pi^2} : \frac{g^2}{16\pi^2} \quad (6.5.21)$$

However, in models where the SM only couples to the BSM sector via the mixing of the electroweak bosons, which is the standard definition of Universal Theories, one finds that in many cases, like in Composite Higgs (CH) models, the interaction with the physical states scales as g^2/g_\star^2 . In these cases, after canonically normalising the electroweak bosons one has that the vertex corrections are

$$\delta g_{L,R}^{Zu,d} \sim \frac{m_W^2}{m_\star^2}. \quad (6.5.22)$$

This is the same as δg_{1z} in Eq. (6.5.19). To motivate the inclusion of $\delta\kappa_\gamma$ and λ_γ in the fits, one can look at the exotic scenarios proposed in Ref. [243] with the *Remedios + ISO(4)* case, where the transverse gauge bosons belong to the composite sector. In these case, it could be possible that λ_γ , $\delta\kappa_\gamma$ and δg_{1z} are tree level size and have the following power counting

$$\delta g_{1z} \sim \frac{g_\star}{g_{SM}} \frac{m_W^2}{m_\star^2}, \quad \delta\kappa_\gamma \sim \frac{g_\star}{g_{SM}} \frac{m_W^2}{m_\star^2}, \quad \lambda_\gamma \sim \frac{g_\star}{g_{SM}} \frac{m_W^2}{m_\star^2}. \quad (6.5.23)$$

with $g_\star > g_{SM}$. Therefore, one may probe these types of theories effectively using diboson production at the LHC.

6.5.3 A model with triplets: diboson reach vs other searches

In this section we put the previous results in a global perspective, assessing the usefulness of diboson observables in a motivated UV toy model where other types of searches are also constraining the parameter space. Our motivation stems from the fact that from an EFT point of view, non-Universal corrections to the light quark vertices come from operators of the type $(\bar{f}\gamma_\mu f)(H^\dagger \overleftrightarrow{D}_\mu H)$; therefore, one expects to also generate the operators $(\bar{f}\gamma_\mu f)(\bar{f}\gamma_\mu f)$ and $(H^\dagger D_\mu H)(H^\dagger D_\mu H)$, which affect dijet processes and

Higgs physics respectively. Considering a particular model allows to see how the different searches constrain the parameter space.

We focus our attention to the general vector triplet models presented in Refs. [221, 244, 245], which appear in various BSM scenarios, and can produce sizable and non-Universal deviations to $\delta V \bar{q}q$ for the light quarks. We look at these models in different limits of the parameter space and study how diboson interacts with the other searches.

From Refs. [221, 244, 245] we consider the particular case where one has two vectorial resonances, L_μ and R_μ , with charges under $SU(2)_L \otimes SU(2)_R$ given by (3, 1) and (1, 3) respectively and singlets under the other SM groups. In the most general case, these resonances couple to the SM currents as follows:

$$\begin{aligned} \mathcal{L}_{int} = & L_\mu^a \left[\gamma_H J_\mu^{Ha} + \gamma_V J_\mu^a + \sum_f \gamma_f J_\mu^{fa} \right] \\ & + R_\mu^0 \left[\delta_H J_\mu^H + \delta_V J_\mu + \sum_f \delta_f J_\mu^f \right] + \frac{1}{\sqrt{2}} (\delta_H R_\mu^+ J_\mu^{-H} + h.c.) \end{aligned} \quad (6.5.24)$$

where the SM currents are given by

$$\begin{aligned} J_\mu^{Ha} &= \frac{i}{2} H^\dagger \sigma^a \overleftrightarrow{D}_\mu H, & J_\mu^a &= D^\nu W_{\nu\mu}^a, & J_\mu^{fa} &= \bar{f} \gamma_\mu \sigma^a f \\ J_\mu^H &= \frac{i}{2} H^\dagger \overleftrightarrow{D}_\mu H, & J_\mu &= \partial^\nu B_{\nu\mu}, & J_\mu^f &= \bar{f} \gamma_\mu f, & J_\mu^{H-} &= \frac{i}{2} H^T \overleftrightarrow{D}_\mu H. \end{aligned} \quad (6.5.25)$$

We assume that both resonances have a mass m_* and that they are large enough so that their effects are well captured by its EFT where L_μ, R_μ are integrated out at tree level, see [221]. At order $1/m_*^2$ this yields

$$\begin{aligned} \mathcal{L}_{tree}^{(6)} \supset & c_W \mathcal{O}_W + c_B \mathcal{O}_B + c_{2W} \mathcal{O}_{2W} + c_{2B} \mathcal{O}_{2B} + c_H \mathcal{O}_H \\ & + \sum_f (c_{Hf} \mathcal{O}_{Hf} + c_{Hf}^{(3)} \mathcal{O}_{Hf}^{(3)}) + \sum_{f,f'} (c_{ff'} \mathcal{O}_{ff'} + c_{ff'}^{(3)} \mathcal{O}_{ff'}^{(3)}), \end{aligned} \quad (6.5.26)$$

where the operators are defined as

$$\begin{aligned} \mathcal{O}_B &= \frac{ig'}{2m_W^2} (H^\dagger D_\mu H) \partial_\nu B_{\mu\nu}, & \mathcal{O}_W &= \frac{ig}{2m_W^2} (H^\dagger \sigma^i D_\mu H) \partial_\nu W_{\mu\nu}^i, & \mathcal{O}_H &= \frac{1}{2v^2} (\partial_\mu |H|^2)^2, \\ \mathcal{O}_{2B} &= \frac{1}{m_W^2} (\partial^\mu B_{\mu\nu})^2, & \mathcal{O}_{2W} &= \frac{1}{m_W^2} (\partial^\mu W_{\mu\nu}^i)^2, & \mathcal{O}_{Hf} &= \frac{i}{v^2} \bar{f} \gamma_\mu f H^\dagger D_\mu H, \\ \mathcal{O}_{Hf}^{(3)} &= \frac{i}{v^2} \bar{f} \sigma^i \gamma_\mu f H^\dagger \sigma^i D_\mu H, & \mathcal{O}_{ff'} &= \frac{1}{v^2} (\bar{f} \gamma_\mu f)^2, & \mathcal{O}_{ff'}^{(3)} &= \frac{1}{v^2} (\bar{f} \sigma^i \gamma_\mu f)^2. \end{aligned} \quad (6.5.27)$$

and their coefficients written in terms of the model's parameters are given by:

$$\begin{aligned}
c_W &= \frac{m_W^2}{m_\star^2} \frac{\gamma_H \gamma_V}{g^2}, & c_B &= \frac{m_W^2}{m_\star^2} \frac{\delta_H \delta_V}{g'^2}, & c_{2W} &= \frac{m_W^2}{4m_\star^2} \frac{\gamma_V^2}{g^2}, & c_{2B} &= \frac{m_W^2}{4m_\star^2} \frac{\delta_V^2}{g'^2}, \\
c_H &= 3 \frac{m_W^2}{m_\star^2} \frac{\delta_H^2 + \gamma_H^2}{g^2}, \\
c_{Hf} &= \frac{m_W^2}{m_\star^2} \frac{2}{g^2} (-\delta_H \delta_f + \delta_V \delta_f), & c_{Hf}^{(3)} &= \frac{m_W^2}{m_\star^2} \frac{2}{g^2} (-\gamma_H \gamma_f + \gamma_V \gamma_f) \\
c_{ff'} &= -\frac{m_W^2}{2m_\star^2} \frac{1}{g^2} \delta_f \delta_{f'}, & c_{ff'}^{(3)} &= -\frac{m_W^2}{2m_\star^2} \frac{1}{g^2} \gamma_f \gamma_{f'}.
\end{aligned} \tag{6.5.28}$$

In Eq.(6.5.26) the sums for f, f' can run over $\{Q_L^i, u_R^i, d_R^i, \ell_L^i, e_R^i\}$ for the operators $\mathcal{O}_{Hf}, \mathcal{O}_{ff'}$, and over $\{Q_L^i, \ell_L^i\}$ for $\mathcal{O}_{Hf}^{(3)}, \mathcal{O}_{ff'}^{(3)}$ where the couplings to each fermion depend on the specific assumptions on the UV model. Notice that we have used the equations of motion to change $\mathcal{O}_r = H^2(\partial_\mu H)^2$ for \mathcal{O}_H .

Only δg_{1z} and the four vertex corrections $\delta g_{L,R}^{Zu,d}$ are generated at tree level. The parameters $\delta \kappa_\gamma$ and λ_γ are generated at one loop by the operators $\mathcal{O}_{HB}, \mathcal{O}_{HW}$ and \mathcal{O}_{3W} defined in Table 97 of Ref. [59]. Therefore, this model is a particular example where the only non-negligible aTGC is δg_{1z} while the others are parametrically suppressed. Using the relations between the SILH and the Higgs basis, we can write the aTGC as

$$\delta g_{1z} = -\frac{g^2 + g'^2}{g^2 - g'^2} \left[(c_W + c_{2W}) + \frac{g'^2}{g^2} (c_B + c_{2B}) \right], \tag{6.5.29}$$

and the four $\delta Z \bar{q} q$ vertex corrections

$$\begin{aligned}
\delta g_L^{Zu} &= \frac{1}{2} \left[-c_{HQ} + c_{HQ}^{(3)} + c_{2W} + c_{2B} \frac{g'^2}{g^2} - \frac{2}{3} \frac{2g'^2}{g^2 - g'^2} \left(c_{2B} \frac{2g^2 - g'^2}{g^2} + c_{2W} + c_B + c_W \right) \right], \\
\delta g_L^{Zd} &= \frac{1}{2} \left[-c_{HQ} - c_{HQ}^{(3)} - c_{2W} - c_{2B} \frac{g'^2}{g^2} + \frac{1}{3} \frac{2g'^2}{g^2 - g'^2} \left(c_{2B} \frac{2g^2 - g'^2}{g^2} + c_{2W} + c_B + c_W \right) \right], \\
\delta g_R^{Zu} &= \frac{1}{2} \left[-c_{Hu} - \frac{2}{3} \frac{2g'^2}{g^2 - g'^2} \left(c_{2B} \frac{2g^2 - g'^2}{g^2} + c_{2W} + c_B + c_W \right) \right], \\
\delta g_R^{Zd} &= \frac{1}{2} \left[-c_{Hd} + \frac{1}{3} \frac{2g'^2}{g^2 - g'^2} \left(c_{2B} \frac{2g^2 - g'^2}{g^2} + c_{2W} + c_B + c_W \right) \right].
\end{aligned} \tag{6.5.30}$$

The operators $\mathcal{O}_{ff'}, \mathcal{O}_{ff'}^{(3)}$ and \mathcal{O}_H do not contribute to diboson production but they modify dijet and Higgs production and therefore can probe the parameters γ_f, δ_f and γ_H, δ_H with different observables.

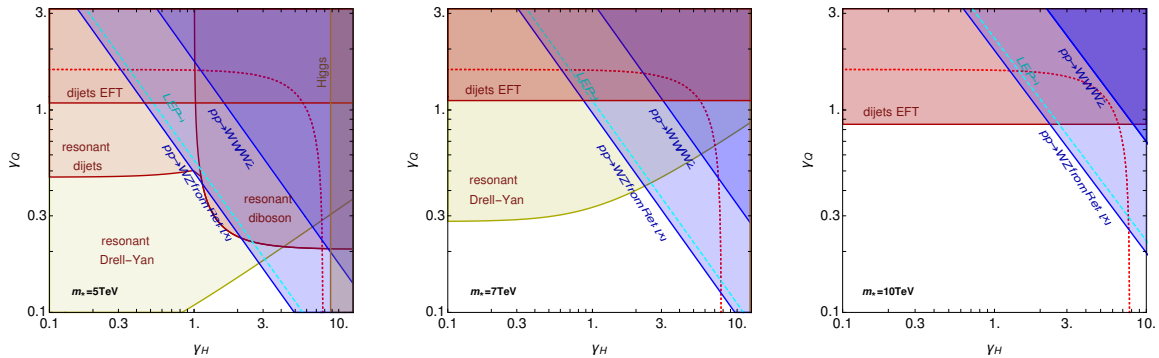


Figure 6.10: Excluded regions at the 95% CL, in the (γ_H, γ_Q) plane for the HL-LHC with 3 ab^{-1} . In blue our projected bounds for the leptonic $pp \rightarrow WW$ at the HL-LHC for systematics of 5, 10 and 30%. Higgs physics bounds are shown in brown and other searches in red.

General models with only L_μ

In this scenario we consider only the resonance L_μ and assume that the couplings γ_Q and γ_H can have any value. For simplicity we assume that γ_V is negligible. This case is interesting because it interpolates between strongly and weakly coupled Higgs and the fermionic sectors, and allows to have a global picture of which searches cover each region of this parameter space.

To do this, we fix the scale m_* and show in Fig. 6.10 the constraints in the (γ_H, γ_Q) plane from various experiments. In blue we show our projected constraints from the leptonic $pp \rightarrow WW$ at the HL-LHC for 3 ab^{-1} for different assumptions on the systematics. We show as a reference a black dotted line where $\gamma_H \gamma_Q = g^2$; naively one expects that in this region for the longitudinal case, the SM interference with the $d = 6$ one dominates as found in Section 6.5.1. Nonetheless if one would find that in this region the quadratic BSM pieces dominate, this would make the bound inconsistent. In our case, we find that the linear pieces dominate.

On the left plot (where L_μ has a mass of $m_* = 5 \text{ TeV}$), we show in red the excluded regions coming from direct resonance searches. In particular we look at the bounds coming from resonant dijet, diboson and Drell-Yan searches which we have taken or recasted from Refs. [246, 247]. We note that the excluded region coming from resonant Drell-Yan, shown in lighter red, is only valid if we make the couplings between L_μ and the leptons different than zero; to draw this exclusion region we assume that $\gamma_{\text{leptons}} = \gamma_Q$. We show in a bright red dotted line the boundary between the regions in which L_μ has a width smaller or larger than 20%; this separates the regions where the direct searches may stop being sensitive to these resonances (at large γ_Q and γ_H). In brown we show the excluded regions from Higgs searches which we take from Ref. [246]. In light blue we show the LEP-1 bounds taken from Ref. [69] under the assumption of MFV.

The projections from the Higgs bounds at the HL-LHC are taken from Ref. [86, 246, 248] where they find that $\xi = v^2 g_*^2 / m_*^2 < 0.08$ so that $g_* / m_* \lesssim 1 \text{ TeV}^{-1}$.

On the center and right plots, we show the same bounds as in the left plot, now for masses of $m_* = 7$ and 10 TeV . In the center plot we recasted the resonant dijet bounds and found them to be over the red line where $\Gamma / m_* > 20\%$, while for the right plot there are no bounds for resonant dijets. Also, the Higgs and resonant diboson bounds are too weak to set any constrain for these masses, and therefore we also don't include them. On the right plot, $m_* = 10 \text{ TeV}$ we find that there are no bounds coming from resonant Drell-Yan searches either. We see that in all three plots, the LEP-1 bounds are of the same order as the diboson ones for $\delta_{\text{sys}} \sim 10\%$.

The projections on dijet observables are taken from Ref. [223]. These are derived from the estimated bound on the coefficient Z at the HL-LHC. This coefficient appears in the $d = 6$ operators modifying the gluon two point function, which is given by:

$$\mathcal{L} \supset -\frac{Z}{2m_W^2} D_\mu G_{\mu\nu}^A D_\rho G_{\rho\nu}^A. \quad (6.5.31)$$

In Ref. [223] there are different possible estimates for the bounds on Z all of them around 10^{-4} . We take this as the order of magnitude of the bound. From Eq. (6.5.31) we rewrite Z in terms of the four fermion operators in Eq. (6.5.27) obtaining $Z = 3 \frac{m_W^2}{m_*^2} \frac{\epsilon_q^2 g_*^2}{g_s^2}$ which sets a bound on $\epsilon_q g_* / m_* \lesssim 1/11.5 \text{ TeV}^{-1}$.

The indirect diboson data is useful for regions where γ_Q is rather small, and γ_H is large for $\delta_{\text{sys}} \sim 10\%$. This region is of interest for CH models where the Higgs couples strongly to the resonances while instead the light quarks couple weakly it. We note that for $m_* = 5 \text{ TeV}$, the reach of the $pp \rightarrow WW$ EFT constrain for $\delta_{\text{sys}} \sim 10\%$ is similar to those coming from resonant diboson searches.

6.6 Summary

The high energies accessible at the LHC not only open the possibility to directly produce new states, but also enhance the sensitivity to physics out of reach but whose effects are encoded in higher dimension operators. We offered a detailed analysis of diboson processes at LHC, which provides an interesting probe of some of these operators.

Due to the increase in sensitivity, in the analysis we took into account not only the aTGCs but also the effect of including anomalous couplings among the light quarks and the electroweak bosons. On one hand, in our global fit to the current available LHC data, we find that diboson sets stronger constraints than LEP-1 data (assuming MFV) for the anomalous couplings $\delta Z \bar{q}q$ for the down quark. On the other, the aTGC fit is only marginally stable under profiling over the vertex corrections even when the LEP-1 (assuming MFV or FU) is included in the fit.

We did a simple estimate for the HL-LHC reach, finding an order of magnitude improvement in the constraints. The different flavour assumptions on the vertices will have a sizeable impact on the TGC constraints. The precision on light quark couplings will significantly surpass the LEP constraints for both MFV and FU assumptions.

There is an interplay between the operators probed in diboson and the ones probed in other searches, as dijets or Higgs physics. This is particularly clear taking into account that the operators affecting diboson take the form $(\bar{f}\gamma_\mu f)(H^\dagger D_\mu H)$, so one will generally expect to generate $(\bar{f}\gamma_\mu f)^2$ and $(H^\dagger D_\mu H)^2$ as well. As a concrete example, we presented a model where those deviations are induced, showing that indirect measurements in diboson offer a complementarity exploration of the parameter space.

There are several interesting future directions. First and foremost, from the experimental side it would be important to have access to a more reliable HL-LHC projections, both in WW and WZ leptonic channels. Semileptonic decays might benefit from fat jet techniques [231] that are worth of further exploration, perhaps allowing to reach higher invariant masses than the leptonic ones. Perhaps more importantly, the WZ channel allows to carry on the analysis performed in [224], where they claim an increase on the sensitivity, so the search for better observables might quantitatively improve the constraints. For instance, the use of machine learning techniques to disentangle the transverse and longitudinal modes of the gauge bosons might open a new approach to diboson data.

As a summary of the results presented in this chapter, in Fig. 6.11 we show the 95% CL constraints on the electroweak couplings of the light quarks. In gray, we show the LEP-1 constraints. In yellow, a global fit using diboson data only. In blue, the combination with LEP. We see that in the future, diboson alone will set stronger constraints than LEP-1. The combination closes the flat directions reaching the few per mille precision.

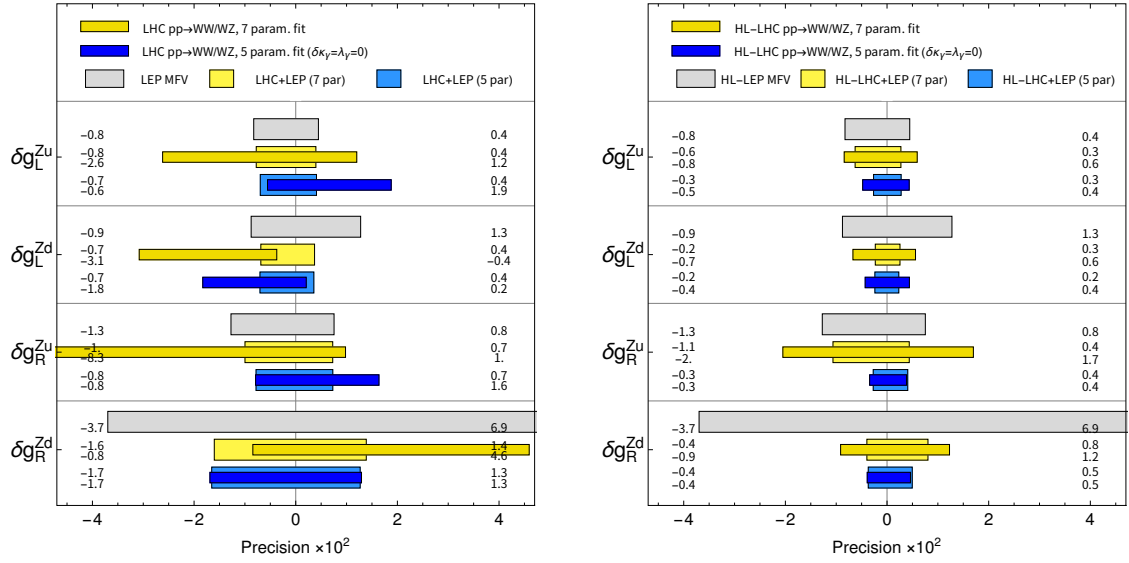


Figure 6.11: 95% CL constraints on the anomalous vertices among light quarks and electroweak bosons. In gray, we show LEP-1 results assuming MFV. In yellow we use LHC diboson data and perform a global fit including the aTGCs. In blue, we only profile over δg_{1z} and the vertex corrections. The thicker boxes combine LHC and LEP-1 data. Left and right correspond to the fit using the present data and the future estimate respectively.

Chapter 7

Probing light top partners with CP violation

7.1 Introduction

An appealing solution to the naturalness problem is based on the idea that the Higgs boson is not an elementary state, but rather a composite object coming from some new strongly-coupled dynamics at the TeV scale. This idea reached nowadays a quite compelling embodiment, which is denoted as “composite Higgs” (CH) scenario.¹ Its main assumption is the identification of the Higgs with a pseudo-Nambu-Goldstone boson [24], which, in minimal realizations, is associated to an $SO(5) \rightarrow SO(4)$ symmetry-breaking pattern [251]. An additional, fundamental ingredient is the generation of fermion masses through the partial-compositeness mechanism [252]. The latter hypothesis is necessary to keep under control dangerously large flavor-breaking effects and is strictly needed at least for the top quark sector.

An important consequence of partial compositeness is the presence of composite partners of the Standard Model (SM) fermions. Among them, the partners of the top play the most important role: besides controlling the generation of the top mass, they also govern the leading contributions to the radiatively-induced Higgs potential [253–255]. For this reason the top partners are directly connected with the amount of fine tuning and must be relatively light (around the TeV scale) to ensure that naturalness is preserved [256].

The presence of light top partners has deep consequences for the phenomenology of CH models. First of all, being charged under QCD, they have sizable production cross sections at hadron colliders, hence constituting one of the privileged ways to directly test the CH paradigm at the LHC. The bounds are nowadays surpassing 1 TeV (see for instance the constraints from pair production of charge- $5/3$ partners [257, 258]), thus

¹See refs. [78, 249, 250] for extensive reviews.

starting to put some pressure on the natural parameter space of the models.

Light top partners give also rise to sizable corrections to precision observables, which can be used as powerful indirect probes of the composite dynamics. For instance, large effects are expected in electroweak precision measurements, such as the S and T parameters and the Z coupling to the bottom quark. In this case the tight experimental constraints translate into exclusions on the top partner masses around the TeV scale [259–261], which are competitive with the ones from direct searches.

In this paper we will focus on another interesting effect due to light top partners, namely the generation of sizable contributions to flavor physics, in particular to CP-violating observables. These effects are due to the presence of additional complex phases in the top partners interactions. Such phases are expected in generic composite Higgs scenarios. Complex parameters can in fact be present in the composite sector interactions if CP-violation is allowed. Furthermore, even if the strongly-coupled dynamics is assumed to be CP preserving, complex mixings of the elementary SM fermions with the composite sector are still needed in many models to generate the non-trivial phase of the CKM matrix. For instance this is the case in scenarios in which the left-handed top field is mixed with multiple composite operators. Examples of such models are the minimal MCHM₅ constructions [251].

Among the possible CP-violating effects, some of the most relevant ones are the generation of dipole moments for the light leptons and quarks. Light top partners generically induce contributions to dipole operators at two-loop level through Barr-Zee-type diagrams [262].² Additional two-loop contributions are also generated for the gluonic Weinberg operator [264]. All these effects arise from the presence of CP-violating Higgs interactions involving the top and its partners. As we will see, in a large class of models, the main contributions come from derivative Higgs interactions induced by the non-linear Goldstone structure.³

The Barr-Zee effects and the Weinberg operator, in turn, give rise to sizable corrections to the electron [267, 268], neutron [269] and diamagnetic atoms [270] electric dipole moments (EDM's). All these effects are tightly constrained by the present data, moreover the experimental sensitivity is expected to increase by more than one order of magnitude in the near future [268, 271, 272]. As we will see, the present bounds allow to probe top partners masses of order *few* TeV and can be competitive with the direct LHC searches. The future improvements in the EDM experiments will push the exclusions beyond the 10 TeV scale, arguably making these indirect searches the most sensitive probes of top partners.

²Additional contributions can arise at the one-loop level in specific flavor set-ups, such as the “anarchic” scenario [263]. They are however absent in other flavor constructions. We will discuss these aspects later on.

³Analogous effects due to effective CP-violating Higgs interactions, including anomalous top and bottom Yukawa couplings, have been studied in the context of the SM effective field theory [265, 266].

For our analysis we adopt the effective parametrizations developed in ref. [273] and already used in the investigation of the bounds coming from electroweak precision measurements [260]. This framework allows for a model-independent description of the Higgs dynamics (including the whole non-linear Goldstone structure) and of the relevant composite resonances. As we will see, top partners contributions to the dipole operators are saturated by infrared (IR) effects. The leading corrections come from the lightest composite states and can be fully captured by the effective framework. IR saturation is instead not present for the contributions to the Weinberg operator, therefore, we expect non-negligible ultraviolet (UV) corrections to be present. The UV contributions, however, are expected to be independent of the IR effects and therefore should not lead to cancellations. The light top partners contributions can thus be interpreted as a lower estimate of the full CP-violating contributions and can be safely used to derive robust constraints.

It must be stressed that, depending on the specific flavor structure, additional contributions to flavor-violating and CP-violating observables can be present. Typical effects can arise from partners of the light-generation SM fermions as well as from heavy vector resonances with electroweak or QCD quantum numbers. All these effects are generically expected in “anarchic partial compositeness” scenarios and lead to additional constraints on the composite dynamics [78, 274]. Focussing first of all on the quark sector, strong bounds on the resonance masses, of order 5 – 10 TeV, come from $\Delta F = 2$ observables, in particular $s \rightarrow d$ transitions that can be tested in Kaon physics. One-loop contributions to $\Delta F = 1$ and CP-violating observables, for instance the neutron EDM, are also induced by partners of the light SM quarks. Contributions of comparable size can also be induced by the top partners due to the presence of relatively large mixing angles with the light SM fermions. The current constraints on $\Delta F = 1$ transitions and on the neutron EDM translate into bounds on the resonance masses of order *few* TeV. If the “anarchic” construction is naively extended to the lepton sector, more dangerous flavor effects arise [274]. In this case large one-loop contributions to the electron EDM and to $\mu \rightarrow e\gamma$ transitions are generated, which can be compatible with the present experimental bounds only if the scale of new physics is of order 50 – 100 TeV. In this scenario the two-loop contributions from top partners are clearly subdominant. Due to the extremely strong bounds, however, we find the naive “anarchic partial compositeness” scenario too fine-tuned to be considered as a fully satisfactory set-up.

Models featuring flavor symmetries can significantly help in reducing the experimental constraints. Several scenarios based on U(3) [275] or U(2) [276] symmetries in the quark sector have been proposed. In these cases leading contributions to flavor-violating and CP-violating observables are reduced and a compositeness scale around *few* TeV is still allowed. The flavor symmetry structure can also be extended to the lepton sector [277], thus keeping under control the one-loop contributions to the electron EDM and $\mu \rightarrow e\gamma$ transitions. In these scenarios the two-loop CP-violating effects we consider in this paper can still be present and can give significant bounds on the mass of the top

partners. Notice that additional phenomenological handles are typically present in these models due to the sizable amount of compositeness of the light generation fermions [278].

Another appealing flavor scenario, which has been recently proposed in the literature, is based on a departure from the classical partial compositeness paradigm for the light SM fermions [279, 280]. In these models only the top quark (or at most the third generation fermions) are assumed to be partially composite objects at the TeV scale, while the Yukawa couplings of the light SM fermions are generated by a dynamical mechanism at much higher energy scales. This construction leads to an effective minimal flavor violation structure and efficiently reduces all flavor-violating and CP-violating effects, most noticeably in the lepton sector [280]. The bounds on the masses of the composite states are lowered to the *few* TeV range, thus allowing for natural models with a small amount of fine-tuning. In these scenarios CP-violating effects from top partners are expected to play a major role and can lead to the strongest bounds on the compositeness scale.

7.2 CP violation from top partners

To discuss the general features of CP violation in composite models, and in particular the generation of electron and neutron EDM's, in this section we focus on a simplified model containing only one multiplet of top partners. As we will see, this set-up retains all the main features of more complex models, but allows us to obtain a simpler qualitative and quantitative understanding of CP-violating effects. Non-minimal scenarios with multiple top partners will be discussed in sec. 7.3.

For definiteness, we restrict our attention to the class of minimal composite Higgs models based on the global symmetry breaking pattern $SO(5) \rightarrow SO(4)$ [251].⁴ This pattern gives rise to only one Goldstone Higgs doublet and preserves an $SO(3)_c$ custodial symmetry, which helps in keeping under control corrections to the electroweak precision parameters. Motivated by fine-tuning considerations (see refs. [256, 281]), we assume that the $SU(2)_L$ doublet $q_L = (t_L, b_L)$ is linearly mixed with composite operators in the 14 representation of $SO(5)$. The right-handed top component is instead identified with a fully composite chiral singlet coming from the strongly-coupled dynamics. This scenario is usually dubbed 14 + 1 model [256, 273].

The possible quantum numbers of the top partners are determined by the unbroken $SO(4)$ symmetry. From the decomposition $14 = 9 \oplus 4 \oplus 1$, one infers that the partners can fill the nineplet, fourplet or singlet representations of $SO(4)$. As we will see, the main CP-violating effects typically arise from the lightest top partner multiplet. Restricting the analysis to a limited set of partners is thus usually a good approximation. For simplicity in this section we will consider a scenario in which the lightest partners transform in the fourplet representation.

⁴In order to accommodate the correct fermion hypercharges an additional $U(1)_X$ global Abelian subgroup is needed (see for instance ref. [78]).

The most general leading-order effective action for the SM quarks and a light composite fourplet ψ_4 can be written in the CCWZ framework [282, 283] (see ref. [78] for an in-depth review of the formalism) as

$$\begin{aligned} \mathcal{L} = & \ i\bar{q}_L \not{D} q_L + i\bar{t}_R \not{D} t_R + i\bar{\psi}_4 (\not{D} - i\phi)\psi_4 - (m_4 \bar{\psi}_{4L} \psi_{4R} + \text{h.c.}) \\ & + \left(-i c_t \bar{\psi}_{4R}^i \gamma^\mu d_\mu^i t_R + \frac{y_{Lt}}{2} f (U^t \bar{q}_L^{14} U)_{55} t_R + y_{L4} f (U^t \bar{q}_L^{14} U)_{i5} \psi_{4R}^i + \text{h.c.} \right) \end{aligned} \quad (7.2.1)$$

In the above formula q_L^{14} denotes the embedding of the q_L doublet into the representation 14, explicitly given by

$$q_L^{14} = \begin{pmatrix} 0 & 0 & 0 & 0 & -ib_L \\ 0 & 0 & 0 & 0 & -b_L \\ 0 & 0 & 0 & 0 & -it_L \\ 0 & 0 & 0 & 0 & t_L \\ -ib_L & -b_L & -it_L & t_L & 0 \end{pmatrix}. \quad (7.2.2)$$

The Goldstone Higgs components Π_i , in the real fourplet notation, are encoded in the matrix

$$U = \exp \left[i \frac{\sqrt{2}}{f} \Pi_i \widehat{T}^i \right], \quad (7.2.3)$$

where f is the Goldstone decay constant and \widehat{T}^i ($i = 1, \dots, 4$) are the generators of the $\text{SO}(5)/\text{SO}(4)$ coset. In the first line of Eq.(7.2.1), D_μ denotes the usual covariant derivative containing the SM gauge fields. The d_μ and e_μ symbols denote the CCWZ operators, defined as

$$U^t [A_\mu + i\partial_\mu] U = e_\mu^a T^a + d_\mu^i \widehat{T}^i, \quad (7.2.4)$$

with T^a ($a = 1, \dots, 6$) the $\text{SO}(4)$ generators and A_μ the SM gauge fields rewritten in an $\text{SO}(5)$ notation.

We can now easily identify possible sources of CP violation. The effective Lagrangian in Eq.(7.2.1) contains four free parameters, namely m_4 , y_{Lt} , y_{L4} and c_t . In general all of them are complex. By using chiral rotations, however, three parameters can be made real, so that only one physical complex phase is present in the model. It can be easily seen that m_4 can be always made real by a phase redefinition of ψ_{4L} . This redefinition does not affect the other parameters. The complex phases of the remaining three parameters are instead connected. The elementary-composite mixing parameters y_{Lt} and y_{L4} can be made real through phase rotations of t_R and ψ_{4R} , shifting all the complex phases into c_t . CP-violating effects are thus controlled by the complex phase of the combination $c_t y_{Lt}^* y_{L4}$.

Complex values of the elementary-composite mixing parameters can in general be present even if CP invariance is imposed in the composite sector (so that m_4 and c_t are real). This is the case, for instance if the q_L doublet is coupled with two composite operators in the UV, eg. with an operator \mathcal{O}_L corresponding to the fourplet partners and

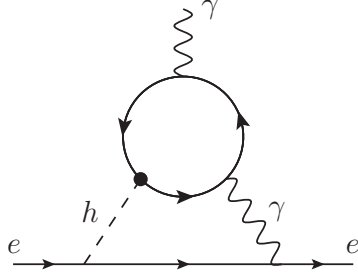


Figure 7.1: Barr-Zee type diagram giving rise to the contribution to the electron EDM.

with another \mathcal{O}_R corresponding to the composite t_R . It is however also possible that a single dominant mixing with \mathcal{O}_L is present. In this case one expects y_{Lt} and y_{LA} to have the same complex phase, thus avoiding CP-violation from top partners if the composite sector preserves CP.

It is also interesting to notice that, in the set-up we are considering, CP-violation is unavoidably linked to the presence of d_μ -interaction operators. If the term $-i c_t \bar{\psi}_{4R}^i \gamma^\mu d_\mu^i t_R$ is not present in the effective Lagrangian, CP is preserved. We will see in [Section 7.3.2](#), that a similar result is also valid in more generic models with additional top partners and multiple physical complex phases.

7.2.1 Electron EDM

The presence of CP-violating interactions of the top and its partners can give rise to sizable contributions to EDM's. In particular an EDM for the electron,

$$\mathcal{L}_{eff} = -d_e \frac{i}{2} \bar{e} \sigma^{\mu\nu} \gamma^5 e F_{\mu\nu}, \quad (7.2.5)$$

arises at two-loop level through Barr-Zee diagrams involving CP-violating Higgs interactions [262] (see [Fig. 7.1](#)). In this subsection we will investigate in detail how this effect arises and derive explicit expressions to compute it.

To discuss the CP-violating effects it is convenient to choose a field basis in which the physical complex phase is put into c_t , while the remaining parameters are real. In this basis, CP-violating Higgs couplings to the top quark and its partners arise only from the $-i c_t \bar{\psi}_{4R}^i \gamma^\mu d_\mu^i t_R$ operator. At leading order in the v/f expansion, where $v \simeq 246$ GeV denotes the Higgs vacuum expectation value, we obtain

$$-i c_t \bar{\psi}_{4R}^i \gamma^\mu d_\mu^i t_R + \text{h.c.} \supset i \frac{c_t}{f} \partial_\mu h \left(\overline{\widehat{X}}_{2/3R} \gamma^\mu t_R - \overline{\widehat{T}}_R \gamma^\mu t_R \right) + \text{h.c.}, \quad (7.2.6)$$

where we used the decomposition of the ψ_4 fourplet into components with definite quan-

tum numbers under the SM group

$$\psi_4 = \frac{1}{\sqrt{2}} \begin{pmatrix} -iB + iX_{5/3} \\ -B - X_{5/3} \\ -i\hat{T} - i\hat{X}_{2/3} \\ \hat{T} - \hat{X}_{2/3} \end{pmatrix}. \quad (7.2.7)$$

The components of ψ_4 correspond to two $SU(2)_L$ doublets, namely (\hat{T}, B) and $(X_{5/3}, \hat{X}_{2/3})$, with hypercharges $1/6$ and $7/6$ respectively.

The main contributions to the electron EDM arise from Barr-Zee diagrams involving a virtual photon. Additional corrections come from diagrams involving a virtual Z boson. These contributions, however, are proportional to the vector coupling of the Z to the charged leptons, which is accidentally small in the SM [262, 265]. They are thus strongly suppressed and can be safely neglected.

Since the photon couplings are flavor-blind and diagonal, the most convenient way to evaluate the Barr-Zee diagrams is to perform the computation in the mass eigenstate basis. In this way each fermionic state gives an independent contribution to the electron EDM. From the explicit form of the couplings in Eq. (7.2.6) it can be seen that only the charge- $2/3$ fields have CP-violating interactions involving the Higgs, thus these states are the only ones relevant for our computation.

The spectrum of the charge- $2/3$ states is quite simple. One combination of the \hat{T} and $\hat{X}_{2/3}$ fields (which we denote by $X_{2/3}$) does not mix with the elementary fields and has a mass $m_{X_{2/3}} = |m_4|$. The orthogonal combination

$$T = \frac{1}{\sqrt{2 + \cos(2v/f) + \cos(4v/f)}} \left[(\cos(v/f) + \cos(2v/f)) \hat{T} + ((\cos(v/f) - \cos(2v/f)) \hat{X}_{2/3} \right], \quad (7.2.8)$$

is mixed with the elementary top field and its mass acquires a shift controlled by the y_{L4} parameter, plus an additional subleading correction due to electroweak symmetry breaking,

$$m_T \simeq \sqrt{m_4^2 + y_{L4}^2 f^2} \left[1 - \frac{5 y_{L4}^2 f^2 v^2}{4 m_4^2 f^2} + \dots \right]. \quad (7.2.9)$$

The top mass is mostly determined by the y_{Lt} parameter and, at leading order in the v/f expansion, reads

$$m_{top}^2 \simeq \frac{1}{2} \frac{m_4^2}{m_4^2 + y_{L4}^2 f^2} y_{Lt}^2 v^2. \quad (7.2.10)$$

The full spectrum of the model also includes the $X_{5/3}$ field with electric charge $5/3$ and mass $m_{X_{5/3}} = |m_4|$ and the B field with electric charge $-1/3$ and mass $m_B = \sqrt{m_4^2 + y_{L4}^2 f^2}$. Notice that the $X_{5/3}$ and $X_{2/3}$ states are always the lightest top partners in the present set-up.

In order to compute the electron EDM, we need to determine the flavor-diagonal CP-violating couplings of the Higgs to the fermion mass eigenstates, in particular the

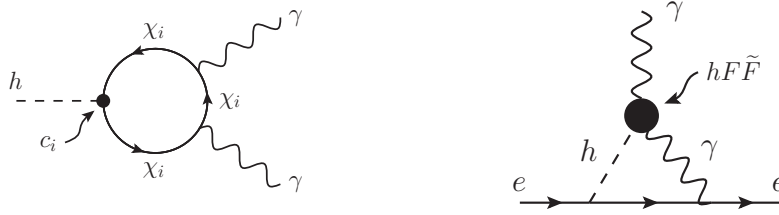


Figure 7.2: Contribution to the electron EDM from running.

top, the T and the $X_{2/3}$. It turns out that the $X_{2/3}$ field does not have such coupling, as a consequence of the fact that it has no mass mixing with the elementary states. The relevant couplings are thus given by

$$\frac{1}{f} \partial_\mu h [c_{top} \bar{t}_R \gamma^\mu t_R + c_T \bar{T}_R \gamma^\mu T_R] , \quad (7.2.11)$$

where, at leading order in v/f ,

$$c_T = -c_{top} = \text{Im } c_t \sin 2\varphi_R = \sqrt{2}v \frac{y_{L4} y_{L4} f}{m_4^2 + y_{L4}^2 f^2} \text{Im } c_t = 2 \text{Im } c_t \frac{y_{L4} f}{\sqrt{m_4^2 + y_{L4}^2 f^2}} \frac{m_{top}}{m_4} . \quad (7.2.12)$$

In the above expression φ_R denotes the rotation angle that diagonalizes the mass matrix of the t_R and T_R fields. Notice that the operators in Eq.(7.2.11) are necessarily CP-odd and their coefficients are real.

The result in Eq.(7.2.12) shows that the CP-violating couplings for the top quark and the T field have opposite coefficients. This relation is exact at all orders and is a consequence of the fact that the interactions coming from the d_μ -operator in the Lagrangian (Eq.(7.2.1)) are strictly off-diagonal. The trace of the coupling matrix must therefore vanish, so that the sum of the coefficients of the diagonal interactions in the mass eigenstate basis is always zero. This result can be easily generalized to scenarios with multiple top partners and with d_μ interactions that involve both fermion chiralities. In this case the sum of the coefficients of the CP-violating Higgs interactions over all fermions vanishes independently for each coupling chirality, namely $\sum_i c_{iL} = \sum_i c_{iR} = 0$.

7.2.1.1 Electron EDM as a running effect

Instead of presenting straight away the full result of the computation of the Barr-Zee diagrams, we find more instructive to follow a simplified approach that allows us to highlight a deeper physical origin of the EDM's. The full result will be presented in [subsubsection 7.2.1.2](#).

As a first step we focus on a single fermion mass eigenstate with CP-violating interactions analogous to the ones in Eq.(7.2.11). It is straightforward to see that such couplings give rise at one loop to CP-violating effective interactions among the Higgs and two photons, originating from diagrams analogous to the one shown in the left panel of Fig.7.2.

Parametrizing the CP-violating Higgs interactions as

$$\mathcal{L} \supset \frac{c_{iL,R}}{f} \partial_\mu h \bar{\chi}_i \gamma^\mu P_{L,R} \chi_i, \quad (7.2.13)$$

where $P_{L,R} = (1 \mp \gamma^5)/2$ are the left and right chirality projectors, we find that the one-loop matrix element is given by

$$\mathcal{M} = \pm i \frac{N_c}{2\pi^2 s} e^2 Q_{f_i}^2 \varepsilon_{\mu\nu\rho\sigma} \varepsilon^\nu(\lambda_1, k_1) \varepsilon^\mu(\lambda_2, k_2) k_1^\rho k_2^\sigma \frac{c_{iL,R}}{f} m_i^2 F(4m_i^2/s). \quad (7.2.14)$$

where the F function is defined as

$$F(\tau) = \begin{cases} \frac{1}{2} \left[\log \frac{1 + \sqrt{1-\tau}}{1 - \sqrt{1-\tau}} - i\pi \right]^2 & \text{for } \tau < 1 \\ -2 \arcsin^2(1/\sqrt{\tau}) & \text{for } \tau \geq 1 \end{cases}. \quad (7.2.15)$$

In Eq. (7.2.14), Q_{f_i} denotes the fermion electric charge (in the present set-up $Q_{f_i} = 2/3$), $k_{1,2}$ and $\varepsilon^{\mu,\nu}(\lambda_{1,2}, k_{1,2})$ are the momenta and the polarization vectors of the photons, while $s = (k_1 + k_2)^2$ coincides with m_h^2 for an on-shell Higgs.

The above result can be matched onto a series of CP-violating effective operators analogous to $(\square^n H^2) F_{\mu\nu} \tilde{F}^{\mu\nu}$, where F is the photon field strength and $\tilde{F}_{\mu\nu} = 1/2 \varepsilon_{\mu\nu\rho\sigma} F^{\rho\sigma}$ is the dual field-strength tensor. For this purpose it is convenient to expand $|\mathcal{M}|^2$ as a series in s/m_i^2 . In particular, for $4m_i^2 > s$ we find that the first terms in the expansion are

$$f(4m_i^2/s) \simeq -\frac{s}{2m_i^2} - \frac{s^2}{24m_i^4} + \dots. \quad (7.2.16)$$

The leading term matches onto the effective operator

$$\mp \frac{e^2 N_c Q_{f_i}^2 c_{iL,R}}{16v\pi^2 f} H^2 F_{\mu\nu} \tilde{F}^{\mu\nu}, \quad (7.2.17)$$

while the second term in the series corresponds to an effective operator involving two additional derivatives.

At the one-loop level, the $H^2 F_{\mu\nu} \tilde{F}^{\mu\nu}$ effective operator gives rise to a logarithmically divergent diagram (see right panel of Fig. 7.2) that induces a running for the electron EDM operator. The divergence, and thus the running, is eventually regulated by the Higgs mass m_h . The effective operator in Eq. (7.2.17) leads to the contribution

$$\frac{d_e}{e} = \mp \frac{N_c}{64\pi^4} e^2 Q_{f_i}^2 \frac{y_e}{\sqrt{2}} \frac{c_{iL,R}}{f} \log \frac{m_i^2}{m_h^2}, \quad (7.2.18)$$

where y_e denotes the electron Yukawa coupling.

To find the full contribution to d_e in our simplified $14 + 1$ model, we need to sum over the contributions of the T resonance and of the top. In this way we find the leading logarithmically-enhanced contribution to the electron EDM

$$\frac{d_e}{e} = -\frac{e^2}{48\pi^4} \frac{y_e}{\sqrt{2}} \frac{c_T}{f} \log \frac{m_T^2}{m_{top}^2}. \quad (7.2.19)$$

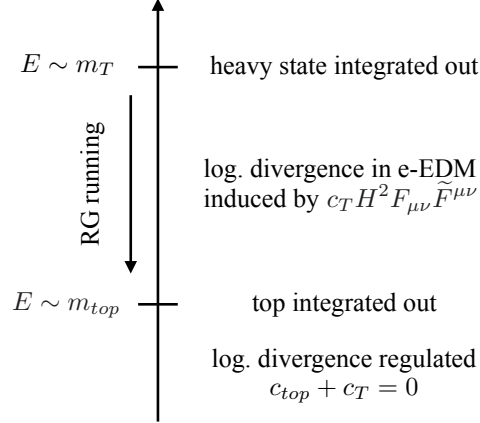


Figure 7.3: Schematic cartoon explaining the generation of an electron EDM as a two-loop running effect due to the top partners.

We will see later that this is the dominant contribution to the electron EDM, and additional threshold effects are subleading.

A few comments are in order. Although the result in Eq. (7.2.19) is logarithmically enhanced for large m_T , its overall coefficient c_T is inversely proportional to the top partner mass (see Eq. (7.2.12)). The overall effect is thus dominated by the contributions coming from the lightest top partners and is largely insensitive to the UV details of the theory.

It is also interesting to notice that the argument of the logarithm is given by the ratio of the T resonance mass and the top mass, whereas the Higgs mass that appeared in Eq. (7.2.18) is not present in the final result. This can be understood by comparing the contributions of the T and top loops to the electron EDM running. As schematically shown in Fig. 7.3, at the m_T scale a contribution to the $H^2 F_{\mu\nu} \tilde{F}^{\mu\nu}$ effective operator is generated, giving rise to a running for the electron EDM. A second contribution, exactly opposite to the first one, is then generated at the top mass scale, stopping the running. The exact compensation of the T and top contributions is a consequence of the relation $c_T = -c_{top}$.

This feature is not a peculiarity of our simple set-up, but is quite generic. Since the sum of all the CP violating coefficients $c_{i,l,r}$ vanishes, the total contributions to the effective operator $H^2 F_{\mu\nu} \tilde{F}^{\mu\nu}$ sum up to zero and the running effects in the electron EDM are always regulated at the top mass scale. This result has an interesting consequence for Higgs physics, since it forbids sizable CP-violating contributions to the Higgs decay into a photon pair. Effects of this type can only come from higher-dimension operators like $(\square^n H^2) F_{\mu\nu} \tilde{F}^{\mu\nu}$, and are necessarily suppressed by additional factors $(m_h^2/m_i^2)^n$. The contributions from heavy top partners are thus typically negligible, while relevant corrections can only come from the top quark.

7.2.1.2 The full result

We can now present the full computation of the top partners contribution to the electron EDM. For this purpose it is convenient to rewrite the CP-violating Higgs interactions in an equivalent form. Integrating by parts and using the equations of motion for the fermions (or equivalently by a suitable field redefinition), we can rewrite the interactions arising from the d_μ operators as CP-odd Yukawa couplings

$$\frac{c_{iL,R}}{f} \partial_\mu h \bar{\chi}_i \gamma^\mu P_{L,R} \chi_i \rightarrow \pm i \frac{c_{iL,R}}{f} m_i h \bar{\chi}_i \gamma^5 \chi_i. \quad (7.2.20)$$

The full two-loop Barr-Zee diagram involving CP-odd top Yukawa's has been computed in refs. [262, 265, 284]. Using these results we find that the full two-loop contribution to the electron EDM for a generic set of fermionic resonances is given by

$$\frac{d_e}{e} = 4 \frac{N_c}{f} \frac{\alpha}{(4\pi)^3} \frac{y_e}{\sqrt{2}} \sum_i Q_{f_i}^2 (c_{iR} - c_{iL}) f_1(x_i), \quad (7.2.21)$$

where $x_i = m_i^2/m_h^2$ and the f_1 function is given by

$$f_1(x) = \frac{2x}{\sqrt{1-4x}} \left[\text{Li}_2 \left(1 - \frac{1 - \sqrt{1-4x}}{2x} \right) - \text{Li}_2 \left(1 - \frac{1 + \sqrt{1-4x}}{2x} \right) \right], \quad (7.2.22)$$

with Li_2 denoting the usual dilogarithm $\text{Li}_2(x) = -\int_0^x du \frac{1}{u} \log(1-u)$.

To make contact with the result obtained in the previous section, we can expand the $f_1(x)$ function for large x (i.e. large fermion masses $m_i \gg m_h$), obtaining

$$\sum_i (c_{iR} - c_{iL}) f_1(x_i) = \sum_i (c_{iR} - c_{iL}) \left[\log x_i + \frac{1}{x_i} \left(\frac{5}{18} + \frac{1}{6} \log x_i \right) + \dots \right], \quad (7.2.23)$$

where we used $\sum_i c_{iR} = \sum_i c_{iL} = 0$. We can see that the leading logarithmic term exactly matches the result in Eq. (7.2.18). As expected, the subleading terms are suppressed by powers of m_h^2/m_i^2 and would match the contributions from higher-derivatives effective operators. It is interesting to notice that the subleading terms are also further suppressed by accidentally small numerical coefficients, and are almost negligible already for the top contributions.

7.2.2 CP-violating effects for the light quarks

The anomalous top and top partner couplings with the Higgs give also rise to additional CP-violating effects. The main ones are electric and chromoelectric dipole moments for the light quarks and a contribution to the gluonic Weinberg operator [264]. The light quark EDM's arise through two-loop diagrams similar to the one giving rise to the electron EDM (see Fig. 7.1), but with the electron line replaced by a quark line. The chromoelectric dipole moments (CEDM's) arise instead from Barr-Zee-type diagrams

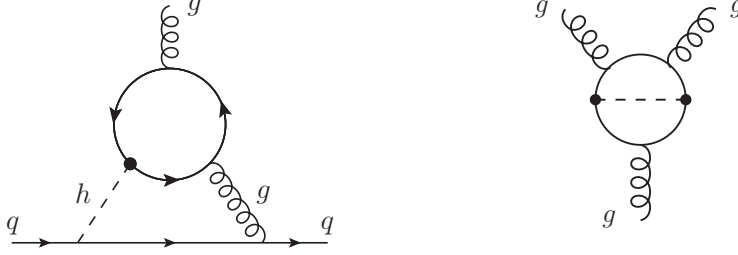


Figure 7.4: Two-loop diagrams giving rise to a chromoelectric dipole moment for the light quarks (left) and to the Weinberg operator (right).

involving gluons, as shown in the left panel of Fig. 7.4. Finally the Weinberg operator is generated by two-loop diagrams of the type shown in the right panel of Fig. 7.4. Notice that the Weinberg operator arises from diagrams that involve only the couplings of the Higgs to the top and top partners, hence it is independent of the light quark Yukawa's.

The dipole moments of the light quarks and the Weinberg operator can be parametrized through the following effective Lagrangian

$$\mathcal{L}_{eff} = -d_q \frac{i}{2} \bar{q} \sigma^{\mu\nu} \gamma^5 q F_{\mu\nu} - \tilde{d}_q \frac{i g_s}{2} \bar{q} \sigma^{\mu\nu} T^a \gamma^5 q G_{\mu\nu}^a - w \frac{1}{3} f^{abc} G_{\mu\sigma}^a G_\nu^{b,\sigma} \tilde{G}^{c,\mu\nu}, \quad (7.2.24)$$

where $q = u, d$ denote the first generation quarks, $\tilde{G}^{a,\mu\nu} = \frac{1}{2} \varepsilon^{\mu\nu\rho\sigma} G_{\rho\sigma}^a$ is the dual QCD field-strength tensor and T^a are the color generators, normalized as $\text{Tr}[T^a, T^b] = \delta_{ab}/2$.

The quark EDM's and CEDM's can be straightforwardly computed as we did in the previous subsection for the electron EDM. The full results are given by

$$d_q = -4Q_q \frac{N_c}{f} e \frac{\alpha}{(4\pi)^3} \frac{y_q}{\sqrt{2}} \sum_i Q_{f_i}^2 (c_{ir} - c_{il}) f_1(x_i), \quad (7.2.25)$$

$$\tilde{d}_q = -\frac{2}{f} \frac{\alpha_s}{(4\pi)^3} \frac{y_q}{\sqrt{2}} \sum_i (c_{ir} - c_{il}) f_1(x_i), \quad (7.2.26)$$

where y_q denote the light quark Yukawa couplings.

Let us now consider the Weinberg operator. The structure of the two-loop diagram contributing to this operator makes it sensitive to a larger set of CP-violating sources. Differently from the Barr-Zee-type contributions, the diagrams giving rise to the Weinberg operator involve a fermion loop with two insertions of Higgs couplings. As a consequence they receive contributions not only from the diagonal Higgs interactions, but also from the off-diagonal couplings involving two different fermion mass eigenstates [285].

Three sets of diagrams give rise to contributions to the Weinberg operator. The first set includes diagrams involving a CP-even Yukawa coupling and a CP-odd derivative Higgs interaction coming from the d_μ operator. As we already mentioned, these contributions can also come from fermion loops involving two different fermionic mass eigenstates. In fact, in generic composite Higgs theories, including the simplified set-up

considered in this section, the Higgs couplings to the top and top partners also have off-diagonal terms. This is true both for the Yukawa couplings and for the interactions coming from the d_μ operator.

The second class of contributions comes from diagrams involving two Yukawa couplings. In a large class of models the diagonal Yukawa couplings are always CP-even, in such case the contributions to the Weinberg operator can only come from diagrams involving two off-diagonal Higgs interactions.

Diagrams in the third class involve two d_μ derivative Higgs interactions. Since diagonal couplings of this type are necessarily CP-odd, the only contributions of this kind to the Weinberg operator come from the off-diagonal Higgs interactions. Such interactions can have both a CP-even and a CP-odd component.

Notice that, in the model we are considering in this section, only the first class of contributions is present, while diagrams involving two Yukawa couplings or two d_μ interactions do not give rise to CP-violating effects. The absence of contributions induced only by the Yukawa couplings is a consequence of the fact that, through a field redefinition, all complex phases can be removed from the mass parameters and from the mixings between the composite resonances and the elementary states. In this basis the only CP-violating vertices come from the d_μ interactions. Diagrams involving only d_μ couplings are instead absent since in our simplified set-up with only one light multiplet all these interactions have the same complex phase, which cancels out in the final result. We will discuss this in detail in the following.

The contribution to the Weinberg operator coming from a set of fermions with Yukawa couplings of the form

$$\mathcal{L} = -\frac{1}{\sqrt{2}} \sum_{i,j} \bar{\psi}_i [y_{ij} + i\tilde{y}_{ij}\gamma^5] \psi_j h, \quad (7.2.27)$$

is given by [285]

$$w = \frac{g_s^3}{4(4\pi)^4} \sum_{i,j} \frac{\text{Re}[y_{ij}\tilde{y}_{ij}^*]}{m_i m_j} f_3(x_i, x_j), \quad (7.2.28)$$

where the function f_3 is defined as

$$f_3(x_i, x_j) = 2x_i x_j \int_0^1 dv \int_0^1 du \frac{u^3 v^3 (1-v)}{[x_i u v (1-v) + x_j v (1-u) + (1-v)(1-u)]^2} + (x_i \leftrightarrow x_j). \quad (7.2.29)$$

This result can be straightforwardly adapted to our set-up by rewriting the d_μ interactions as Yukawa couplings (see eq. (7.2.20))

$$\frac{1}{f} \partial_\mu h \sum_{i,j} c_{ijl,r} \bar{\chi}_i \gamma^\mu P_{L,R} \chi_j \rightarrow \frac{1}{f} h \sum_{i,j} i c_{ijl,r} m_j \bar{\chi}_{iL,R} \chi_{jR,L} + \text{h.c.}, \quad (7.2.30)$$

corresponding to the following contributions to y_{ij} and \tilde{y}_{ij}

$$\Delta y_{ij} = i \frac{m_i - m_j}{\sqrt{2}f} c_{ijl,r}, \quad \Delta \tilde{y}_{ij} = \mp \frac{m_i + m_j}{\sqrt{2}f} c_{ijl,r}. \quad (7.2.31)$$

This formula shows that, if d_μ operators involving only left- or right-handed fermions are present, Δy_{ij} and $\Delta \tilde{y}_{ij}$ always have the same complex phase. In this case, the product of two d_μ -symbol vertices $\Delta y_{ij} \Delta \tilde{y}_{ij}^*$ appearing in Eq. (7.2.28) is real and does not lead to CP-violating effects. This explicitly proves that diagrams with two d_μ interactions do not contribute to the Weinberg operator in the $14 + 1$ set-up we are considering in this section.

The contribution to the Weinberg operator in Eq. (7.2.28) can be conveniently rewritten by using a simple approximation for the f_3 function. If $x_{i,j} \gg 1$ the $f_3(x_i, x_j)$ function is well approximated by $f_3 \simeq 1 - 1/3\bar{x}$, where \bar{x} is the largest between x_i and x_j . For practical purposes, if one of the resonances in the loop has a mass $m \gtrsim 500$ GeV, one can safely use the approximation $f_3 = 1$. The only case in which this estimate is not fully accurate is for loops involving only the top quark, in which case $f_3(x_t, x_t) \simeq 0.88$. Also in this case, however, the approximation $f_3 = 1$ is valid up to $\sim 10\%$ deviations.

By using straightforward algebraic manipulations, it can be shown that

$$\begin{aligned} w &\simeq \frac{g_s^3}{4(4\pi)^4} \sum_{i,j} \frac{\text{Re}[y_{ij} \tilde{y}_{ij}^*]}{m_i m_j} \\ &= -\frac{g_s^3}{4(4\pi)^4} \text{Re Tr} \left[\frac{2}{f} \Upsilon (c_r M^{-1} - M^{-1} c_l) - \frac{2}{f^2} i c_r M^{-1} c_l M + i \Upsilon M^{-1} \Upsilon M \right] \end{aligned} \quad (7.2.32)$$

where Υ_{ij} denotes the matrix of Yukawa couplings, defined as

$$\sum_{i,j} h \Upsilon_{ij} \bar{\chi}_{iL} \chi_{jR} + \text{h.c.}, \quad (7.2.33)$$

and M is the fermion mass matrix, defined as $\sum_{i,j} M_{ij} \bar{\chi}_{iL} \chi_{jR} + \text{h.c.}$.

7.2.2.1 Neutron and Mercury EDM

The quark electric and chromoelectric dipole operators and the Weinberg operator generate contributions to the neutron EDM d_n .⁵ The explicit expression is given by [265]

$$\frac{d_n}{e} \simeq (1.0 \pm 0.5) \left[0.63 \left(\frac{d_d}{e} - 0.25 \frac{d_u}{e} \right) + 1.1 \left(\tilde{d}_d + 0.5 \tilde{d}_u \right) + 10^{-2} \text{GeV} w \right], \quad (7.2.34)$$

where we took into account running effects from the top mass scale to the typical hadronic scale $\mu_H \simeq 1$ GeV.⁶

The CEDM's of the light quarks give also rise to EDM's for the diamagnetic atoms. At present the most stringent experimental constraints come from the limits on the EDM

⁵Additional contributions to the neutron EDM can be generated by a top dipole moment through running effects. If the top dipole is generated at loop level, as expected in many CH scenarios, these corrections are however quite small and well below the current experimental bounds [78].

⁶For simplicity we neglected additional running between the resonances masses and the top mass.

of mercury (Hg). The latter can be estimated as [265]

$$\frac{d_{\text{Hg}}}{e} \simeq -0.9 \cdot 10^{-4} \left(4_{-2}^{+8}\right) \left(\tilde{d}_u - \tilde{d}_d - 0.76 \cdot 10^{-3} \text{ GeV } w\right). \quad (7.2.35)$$

It is interesting to compare the size of the various contributions to the neutron and mercury EDM's. From Eq.(7.2.25) and Eq.(7.2.26) we can see that

$$d_q = \frac{8}{3} e Q_q \frac{\alpha}{\alpha_s} \tilde{d}_q \simeq 0.06 Q_q \tilde{d}_q, \quad (7.2.36)$$

where we set $Q_{f_i} = 2/3$, as in the model we consider in this section. The contributions to d_n coming from light quark EDM's is therefore suppressed by almost one order of magnitude with respect to the one from the quark CEDM's.

Let us now consider the contributions from the Weinberg operator. Due to the different structure of the top partner contributions, the effects due to the Weinberg operator and the ones from the Barr-Zee diagrams can not be exactly compared as we did for the electric and chromoelectric moments. To get an idea of the relative importance we can however use a rough approximation, namely

$$w \sim \frac{g_s^3}{(4\pi^4)} \frac{1}{f^2} \text{Im } c_t \sim \frac{g_s}{4m_q} \left(\frac{m_T}{f}\right)^2 \frac{1}{\log m_T/m_t} \tilde{d}_q \sim 40 \text{ GeV}^{-1} \left(\frac{m_T}{f}\right)^2 \frac{1}{\log m_T/m_t} \tilde{d}_q. \quad (7.2.37)$$

This estimate is quite close to the exact result (Eq.(7.2.47)), as we will see in Section 7.2.3. An interesting feature of the contributions to the Weinberg operator is the fact that they are controlled by the compositeness scale f , and are nearly independent of the top partner masses. As a consequence their relative importance with respect to the quark dipole contributions grows for large m_T/f .

Using the estimate in Eq.(7.2.37) we find that, for $m_T \sim f$, the w contributions to the mercury EDM are suppressed by almost two orders of magnitude with respect to the quark CEDM's ones. We thus expect the Weinberg operator to play a role for d_{Hg} only for sizable values of the ratio m_T/f , namely $m_T/f \gtrsim 10$. On general ground one expects $m_T \sim g_* f$, with g_* the typical composite sector coupling. The contributions from the Weinberg operator to d_{Hg} are thus relevant only for new dynamics that are close to be fully strongly-coupled.

The situation is significantly different for the neutron EDM. In this case the contributions from the Weinberg operator are suppressed by a factor $\sim 1/4$ if the top partners are light ($m_T/f = 1$). For heavier partner masses, $m_T/f \gtrsim 3$, the bounds coming from the Weinberg operator can thus become competitive with the ones from the quark CEDM's. We will discuss this point more quantitatively in the following.

7.2.3 Experimental bounds

We can now discuss the constraints coming from the experimental data. The present searches for electron [267], neutron [269] and mercury [270] EDM's give null results and

can thus be used to extract the following constraints

$$|d_e| < 9.4 \cdot 10^{-29} e \text{ cm} \quad \text{at } 90\% \text{ CL}, \quad (7.2.38)$$

$$|d_n| < 2.9 \cdot 10^{-26} e \text{ cm} \quad \text{at } 95\% \text{ CL}, \quad (7.2.39)$$

$$|d_{\text{Hg}}| < 7.4 \cdot 10^{-30} e \text{ cm} \quad \text{at } 95\% \text{ CL}. \quad (7.2.40)$$

Near-future experiments are expected to significantly improve the bounds on the neutron and electron EDM's. The neutron EDM bounds could be improved up to $|d_n| < 10^{-27} e \text{ cm}$ [271]. On the other hand, the ACME collaboration estimates the future sensitivity on the electron EDM to be [272]

$$|d_e| \lesssim 0.5 \cdot 10^{-29} e \text{ cm} \quad (\text{ACME II}) \quad (7.2.41)$$

and

$$|d_e| \lesssim 0.3 \cdot 10^{-30} e \text{ cm} \quad (\text{ACME III}) \quad (7.2.42)$$

that correspond to an improvement of the current constraints by more than two orders of magnitude.⁷

It is interesting to compare the impact of the different bounds on the parameter space of composite Higgs models. An easy way to perform the comparison is to focus on the constraints on the EDM of the electron and on the EDM's and CEDM's of the light quarks. As can be seen from Eq.(7.2.21), Eq.(7.2.25) and Eq.(7.2.26) in the $14 + 1$ model with a light fourplet all these effects depend on the quantity⁸

$$\tilde{\gamma} \equiv \frac{v}{f} \sum_i (c_{ir} - c_{il}) f_1(x_i). \quad (7.2.43)$$

The bounds on $\tilde{\gamma}$ can thus be used to compare the strength of the various experimental searches. For simplicity we will neglect corrections coming from the Weinberg operator, and we will assume that the electron and light quark Yukawa's coincide with the SM ones.

The constraints from the electron EDM measurements read

$$\begin{aligned} |\tilde{\gamma}| &< 0.029 && \text{current bound}, \\ |\tilde{\gamma}| &\lesssim 1.5 \times 10^{-3} && \text{ACME II}, \\ |\tilde{\gamma}| &\lesssim 1.0 \times 10^{-4} && \text{ACME III}. \end{aligned} \quad (7.2.44)$$

The bounds from the neutron EDM measurement are

$$\begin{aligned} |\tilde{\gamma}| &< [0.08, 0.23] && \text{current bound}, \\ |\tilde{\gamma}| &\lesssim [0.003, 0.01] && \text{improved bound}. \end{aligned} \quad (7.2.45)$$

⁷An additional bound on the electron EDM has been reported in ref. [268], $|d_e| < 1.3 \cdot 10^{-28} e \text{ cm}$ at 90% CL, which is slightly weaker than the current ACME constraint. This experiment is currently limited by statistics and in the future is expected to allow for a precision $\sim 10^{-30} e \text{ cm}$.

⁸As we discussed before, in the $14 + 1$ with a light fourplet only charge-2/3 partners contribute to Barr-Zee diagrams, thus $Q_{f_i} = 2/3$ in Eq.(7.2.21) and Eq.(7.2.25).

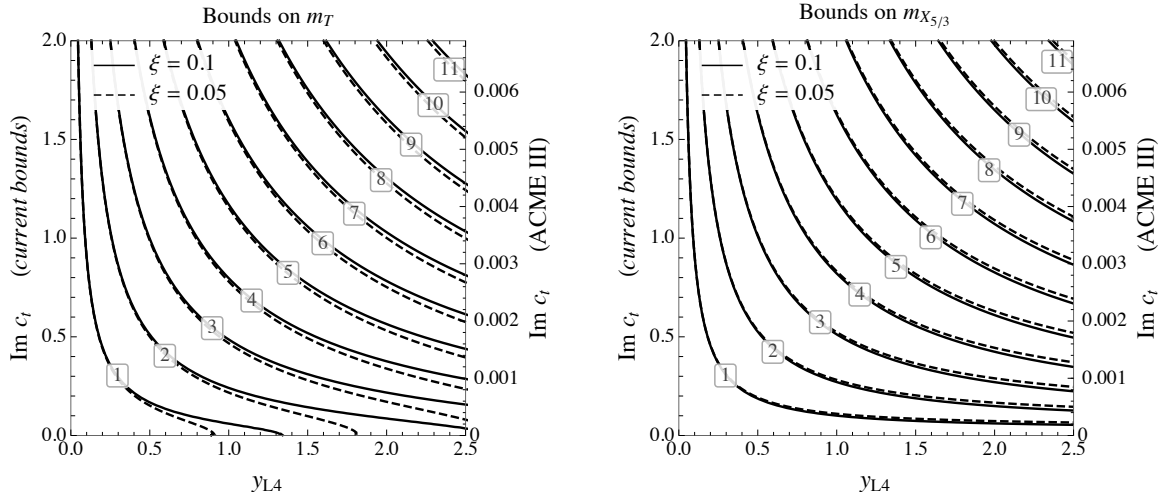


Figure 7.5: Bounds on the mass of the T (left panel) and $X_{5/3}$ (right panel) states derived from the constraints on the electron EDM. The bounds are expressed in TeV and are presented as a function of the elementary–composite mixing y_{L4} and of the imaginary part of c_t . The labels on the left vertical axis corresponds to the present bounds, while the ones on the right axis correspond to the ACME III projections. The solid and dashed lines correspond to the choice $\xi = 0.1$ and $\xi = 0.05$ respectively.

Finally the bounds from the mercury EDM are

$$|\tilde{\gamma}| < [0.06, 0.4]. \quad (7.2.46)$$

Notice that for the neutron and mercury EDM bounds we took into account the error range in the estimates in eqs. (7.2.34) and (7.2.35).

From the above results we find that, at present, the electron EDM measurements give the strongest constraints. The future improvements on the neutron EDM constraints could strengthen the present electron EDM bounds by a factor of order 3. These constraints, however, will be easily surpassed by the new electron EDM experiments, which can improve the current bounds by a factor of ~ 20 in the near future (ACME II) and by more than two orders of magnitude afterwards (ACME III).

The constraints on the top partner masses in the $14 + 1$ scenario are shown in Fig. 7.5 as a function of the y_{L4} mixing parameter and of the imaginary part of the c_t coupling. The value of the y_{Lt} mixing has been fixed by requiring that the correct top mass is reproduced. In the left panel we show the bounds on the mass of the T partner, while in the right panel we show the bounds on the mass of the lightest top partner in the multiplet, namely the $X_{5/3}$ state. The solid and dashed lines show the bounds for $\xi \equiv v^2/f^2 = 0.1$ and $\xi = 0.05$ respectively, which roughly correspond to the present constraints on ξ coming from Higgs couplings measurements [286] and to the projected bounds for high-luminosity LHC [86, 248, 287]. The impact of ξ on the bounds is however quite mild. Notice that the T mass, even without any constraint from

the electron EDM (i.e. for $\text{Im}c_t = 0$) is still bounded from below. This is due to the fact that, even setting $m_4 = m_{X_{5/3}} = 0$, m_T still gets a contribution from the mixing with the elementary states, which translates into $m_T = |y_{LA}f|$.

Using simple power counting considerations [77, 273] we can estimate the typical size of the y_{LA} and c_t parameters to be $y_{LA} \sim y_{Lt} \sim y_{top}$ and $c_t \sim 1$. Barring accidental suppressions in the complex CP-violating phase of c_t , we get that the present constraints from the electron EDM correspond to bounds on the top partner masses in the range 2 – 4 TeV. The ACME II experiment will extend the exclusion range to masses of order 10 – 20 TeV, whereas masses in the range 50 – 100 TeV will be tested by ACME III.

Another useful way to quantify the strength of the electron EDM bounds is to fix the mass of the top partners and derive the amount of suppression needed in the complex phase of c_t to pass the experimental bounds. Choosing masses of order 3 TeV, roughly of the order of the possible direct bounds from high-luminosity LHC, we can see that the present constraints still allow for order one complex phases. ACME II will lower the bound to $\sim 5\%$, while ACME III will be able to constrain CP-violating phases significantly below the 1% level.

It is important to stress that the bounds coming from the electron and light quark EDM's crucially depend on the assumption that the light fermion Yukawa couplings are not (strongly) modified with respect to the SM predictions. If the light fermion masses are generated through partial compositeness, this assumption is typically satisfied. One indeed expects all Yukawa couplings to deviate from their SM values only by corrections of order ξ . The current bounds $\xi \lesssim 0.1$ guarantee that the Yukawa couplings agree within $\sim 10\%$ with their SM values.

It is however conceivable that substantial modifications of the partial compositeness structure could exist for the light fermions. In such a case large deviations of the Yukawa couplings could be present. Strong suppression in some or all the light fermion Yukawa's would modify the relative importance of the constraints coming from the experimental measurements. As we discussed before, the contributions to the electron EDM are controlled by the electron Yukawa, whereas the light quark EDM and CEDM are proportional to the u and d Yukawa's. The experimental constraints on the electron and neutron EDM thus carry complementary information and can become more or less relevant in different contexts.

It is interesting to notice that the contributions to the Weinberg operator are independent of the light fermion Yukawa's and only depend on the top and top partners couplings to the Higgs. They can thus be used to extract bounds that are in principle more model independent than the ones coming from the electron and light quark EDM's. Using the approximation in Eq. (7.2.32), we find that the contribution to the Weinberg

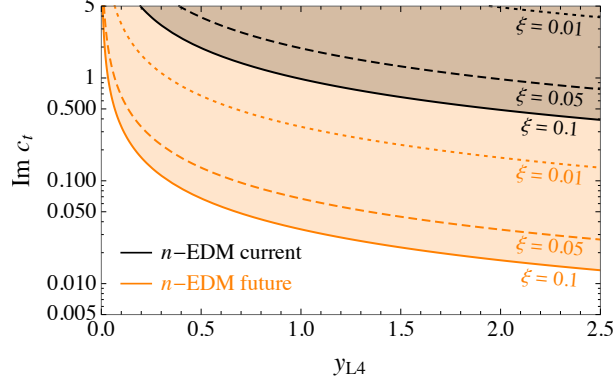


Figure 7.6: Bounds on the CP-violating part of the c_t coupling as a function of the y_{L4} mixing derived from the current and projected constraints on the neutron EDM. The results are derived by using the constraints on the Weinberg operator

operator in the $14 + 1$ model with a light fourplet is

$$w \simeq -\frac{g_s^3}{2(4\pi)^4 f} \text{Re Tr}[\Upsilon c_t M^{-1}] = \frac{2g_s^3}{(4\pi)^4} \frac{\sqrt{2} y_{L4}}{f^2 y_{Lt}} \text{Im } c_t \simeq \frac{2g_s^3}{(4\pi)^4} \frac{y_{L4} m_4}{\sqrt{m_4^2 + y_{L4}^2 f^2}} \frac{v}{f^2 m_{top}} \text{Im } c_t. \quad (7.2.47)$$

A noteworthy aspect of this formula is the fact that it depends on the top partners masses only indirectly. The dependence on m_4 only appears when we rewrite the y_{Lt} parameter as a function of the top mass. This feature indicates that the contributions to the Weinberg operator are not controlled by the lightest resonances, as was the case for the dipole operators, but instead can receive sizable contributions from the UV dynamics. Of course, since the IR and UV contributions are in general independent, we do not expect them to cancel each other. The result in Eq. (7.2.47) can thus be used as a lower estimate to obtain constraints on the parameter space of the model.

In Fig. 7.6 we show the bounds in the $(\text{Im } c_t, y_{L4})$ plane coming from the current (black lines) and projected (orange lines) neutron EDM measurements for various values of ξ ($\xi = 0.1, 0.05, 0.01$). These results are obtained by taking into account only the contributions from the Weinberg operator in Eq. (7.2.34) (we use the lower estimate of the effect to derive the numerical results), and neglecting the ones from the light-quark dipole operators. Notice that we also neglected additional contributions to the Weinberg operator that can be induced by the presence of a top CEDM [288]. These effects are of order

$$w_{t\text{-cedm}} = \frac{g_s^3}{32\pi^2} \frac{\tilde{d}_t}{m_t} \simeq \frac{g_s^3}{32\pi^2} \frac{1}{16\pi^2 f^2}. \quad (7.2.48)$$

and are subleading with respect to the contributions in eq. (7.2.47) if $y_{L4} \text{Im } c_t \gtrsim 0.2$. As can be seen from Fig. 7.6 these effects are irrelevant for the present constraints. They are instead expected to become comparable with the top partners contributions in part of the parameter space probed by future experiments. In this situation the constraint

given in Fig. 7.6 can still be considered as a lower bound, provided strong accidental cancellations do not occur.

We can see that, for $\xi = 0.1$, the current neutron EDM constraints typically forbid values of $\text{Im } c_t$ larger than ~ 1 . These bounds are competitive with the current ones from the electron EDM (see Fig. 7.5) if the top partner masses are $m_{X_{5/3}} \gtrsim 5 - 6$ TeV, whereas they are weaker for lighter resonances. Notice that the bound from the Weinberg operator roughly scales like f^{-2} , so it quickly degrades for smaller values of ξ . The bound from the electron EDM has instead a much milder dependence on ξ .

Future improvements on the neutron EDM measurements (orange lines in Fig. 7.6) could strengthen the bounds by more than one order of magnitude. The improved bounds, for $\xi = 0.1$, would be comparable to the present ones from the electron EDM for $m_{X_{5/3}} \simeq 1$ TeV. Notice however that the projected improvement in the electron EDM constraints (ACME III) would make the Weinberg operator bounds relevant only for very heavy top partners ($M_{X_{5/3}} \gtrsim 20$ TeV).

As we mentioned in the Introduction, the bounds we presented in this section apply directly to models in which the flavor structure is implemented through a “dynamical scale” mechanism (see ref. [280]). In these scenarios direct CP-violating effects involving the light SM fermions are strongly suppressed and the leading effects are generated only from two-loop contributions involving the top and its partners. In other flavor scenarios, for instance anarchic partial compositeness models, additional sizable CP-violating contributions can be present. We will briefly discuss these effects in the following.

In anarchic partial compositeness models, corrections to the light quark EDM’s and CEDM’s are typically generated at one loop [263] (see ref. [78] for a review). For a quark q these effects can be estimated as

$$\frac{d_q}{e} \sim \tilde{d}_q \sim \frac{m_q}{16\pi^2} \frac{1}{f^2}. \quad (7.2.49)$$

These contributions are roughly one inverse loop factor $16\pi^2/g_s^2 \simeq 10^2$ larger than the Barr-Zee effects, thus, barring accidental cancellations, are usually dominant. The current neutron EDM constraints lead to a lower bound $f \gtrsim 4.5$ TeV coming from the down-quark dipole operator. A slightly weaker constraint, $f \gtrsim 2$ TeV, is obtained from the up-quark dipole.

If the anarchic structure is naively extended to the lepton sector, large one-loop contributions to the electron EDM are present. The current bounds on the electron EDM imply a constraint $f \gtrsim 38$ TeV, which rules out top partners in the 50 – 100 TeV range. In these scenarios a similar bound also comes from the lepton flavor violating decay $\mu \rightarrow e\gamma$.

We finally consider models with flavor symmetries. In the case of U(3) symmetry [275], the one-loop contributions to the light-quark EDM’s are comparable to the ones in anarchic scenarios. A significant suppression of these effects can instead be present in U(2) models [276] if the partners of the light quarks are decoupled. In this

case the two-loop Barr-Zee contributions become dominant and the bounds derived in this section apply.

7.2.4 Comparison with direct top partner searches

It is also interesting to compare the bounds from CP-violating effects with the direct searches for top partners. We start the discussion by considering the constraints coming from the LHC. The strongest bounds on the mass of a light fourplet come from searches for the exotic charge-5/3 top partner, the $X_{5/3}$, which decays exclusively into Wt . So far the experimental searches focussed mainly on top partners pair production. The strongest bounds come from searches in the lepton plus jets final state, whose present constraints are $m_{X_{5/3}} > 1250$ GeV (ATLAS collaboration [257]) and $m_{X_{5/3}} > 1320$ GeV (CMS collaboration [258]).

Additional bounds come from searches in the same-sign dilepton final state, whose sensitivity is only slightly lower than the one in the lepton plus jets channel. The present bounds for pair-produced top partners are $m_{X_{5/3}} > 1160$ GeV from the CMS analysis in ref. [289] and $m_{X_{5/3}} > 990$ GeV from the ATLAS analysis in ref. [290].⁹ Interestingly, searches for charge-5/3 resonances in same-sign dileptons are sensitive not only to pair production but also to single production. This aspect was investigated in ref. [291] for the 8 TeV LHC searches. The same-sign dilepton search was found to be sensitive to single production with relatively high efficiencies, namely $\sim 50\%$ of the pair-production signal efficiency for the ATLAS search and $\sim 10\%$ for the CMS one. The 13 TeV searches are analogous to the 8 TeV ones, so one expects similar efficiencies to apply. The sensitivity to single production can significantly enhance the bounds for large values of c_t . Indeed this coupling controls the $WX_{5/3}t$ vertex [281],

$$g_{WX_{5/3}tR} = \frac{g}{\sqrt{2}} c_t \frac{v}{f}, \quad (7.2.50)$$

that mediates single production in association with a top quark.¹⁰

Interestingly, the searches in lepton plus jets and same-sign dilepton final states are sensitive not only to charge-5/3 resonances but also to states with charge $-1/3$ decaying into Wt . The bounds reported in the experimental analyses for resonances with charge 5/3 and $-1/3$ are quite close, thus signaling similar search efficiencies. A reasonable estimate of the bounds can thus be obtained by just adding the production cross sections for both types of partners. As we discussed before, the fourplet multiplet contains a state

⁹The ATLAS analysis is only available for 3.2/fb integrated luminosity at 13 TeV. This explains the significantly lower bound with respect to the CMS analysis, which instead exploits 35.9/fb integrated luminosity.

¹⁰Experimental searches for singly-produced heavy quarks decaying into Zt/b [292], ht/b [293] and Wb [294, 295] are also available in the literature. The bounds from these searches on fourplet top partners are however weaker than the ones we derived with the recast of the same-sign dilepton searches.

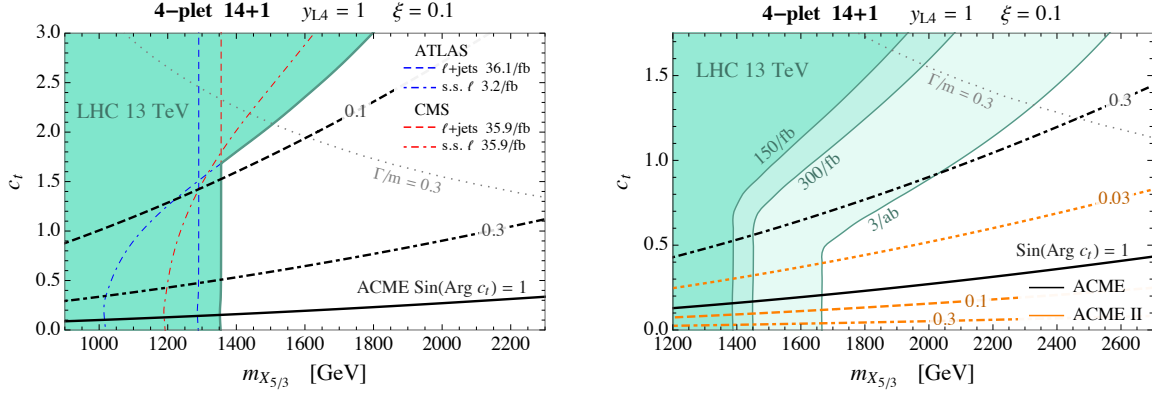


Figure 7.7: Bounds on the c_t coupling as a function of the mass of the $X_{5/3}$ resonance for the scenario with a light fourplet in the 14 + 1 model (for the choice $\xi = 0.1$ and $y_{L4} = 1$). The current bounds from the LHC data and from the constraints on the electron EDM are shown in the left panel, whereas the projections for the future LHC runs and the estimate of the future ACME II constraints are shown in the right panel. In the left panel we also show separately the direct bounds from the lepton plus jets (dashed lines) and for the same-sign dilepton analyses (dot-dashed lines) for ATLAS (blue) and CMS (red). The bound from the electron EDM current (black lines) and improved ACME II searches (orange lines) are shown for different choices of the complex phase of c_t ($\text{sin}(\text{Arg } c_t) = 1, 0.3, 0.1, 0.03$ for the solid, dashed, dot-dashed and dotted lines respectively). In the region above the dotted gray line the width of the $X_{5/3}$ resonance is above 30% of its mass.

with charge $-1/3$, the B , which decays into Wt with a branching ratio close to 100%. If the mass split between the $X_{5/3}$ and B states is below ~ 200 GeV, which requires relatively small value of y_{L4} ($y_{L4} \lesssim 1$ in the case $m_{X_{5/3}} \sim 1 - 2$ TeV and $\xi \simeq 0.1$), the same-sign dilepton signal is enhanced by almost a factor 2, with a significant impact on the exclusion bounds [281, 291].

The direct bounds on the mass of the $X_{5/3}$ resonance from the LHC searches are shown by the shaded green regions in Fig. 7.7. The current bounds are shown in the left panel, while the projections for the future LHC runs are in the right panel. For definiteness we set $\xi = 0.1$ (which roughly corresponds on the bound coming from precision electroweak tests [260] and from present Higgs couplings measurements [286]) and $y_{L4} = 1$. We also fix y_{R4} by requiring the top mass to have the correct value.

As we discussed before, the strongest indirect constraints from CP-violating effects come from the electron EDM measurements. The current bounds are shown in the figure by the black lines, while the ACME II projections are given by the orange lines. The bounds are presented for different values of the complex phase of c_t , namely $\text{sin}(\text{Arg } c_t) = 1, 0.3, 0.1, 0.03$. One can see that indirect bounds tend to be stronger than the ones from direct searches for larger values of the top partners masses. If the

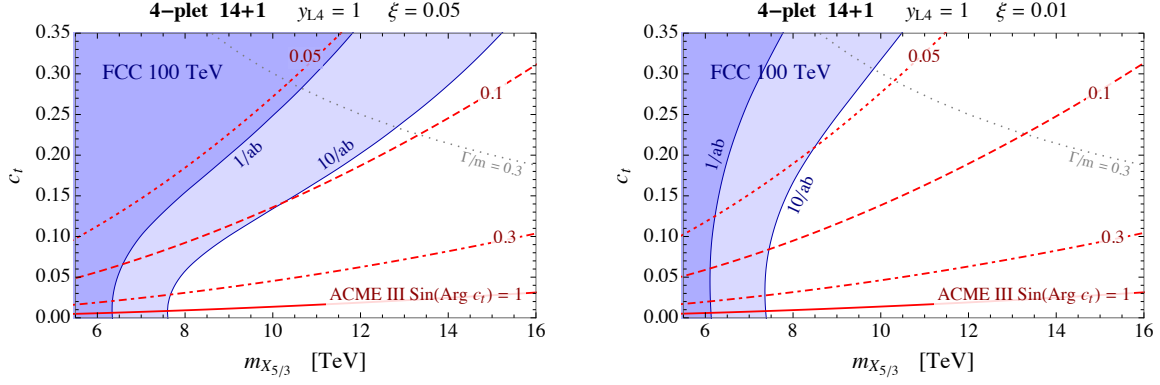


Figure 7.8: Future direct and indirect exclusion bounds on the c_t coupling as a function of the mass of the $X_{5/3}$ resonance for the scenario with a light fourplet in the $14 + 1$ model (for the choice $y_{L4} = 1$). The left and right panels correspond to $\xi = 0.05$ and $\xi = 0.01$ respectively. The direct bounds from top partners searches at FCC-hh are given by the blue shaded regions (for integrated luminosities $1/\text{ab}$ and $10/\text{ab}$). The red lines correspond to the indirect exclusions for the estimated ACME III sensitivity.

complex phase of c_t is not too small, $\sin(\text{Arg } c_t) \gtrsim 0.1$, the current ACME constraints can easily probe resonance masses ~ 2 TeV, which are not tested by the run-2 LHC data. Moreover it can be seen that the additional parameter space region probed by taking into account single production (corresponding to the improved LHC bounds at large c_t) can be also covered by the electron EDM constraints if $\sin(\text{Arg } c_t) \gtrsim 0.1$ for current searches and $\sin(\text{Arg } c_t) \gtrsim 0.05$ for the high-luminosity LHC and ACME II.

For different values of ξ the results in Fig. 7.7 change only mildly. The indirect bounds are nearly unaffected, while the direct searches are modified due to the rescaling of the single production coupling (see Eq. (7.2.50)). The dependence of the direct bounds on y_{L4} is also mild, since this parameter only controls the split between the $X_{5/3}$ and B masses. The bound on c_t coming from the electron EDM instead scales roughly linearly with y_{L4} as can be seen from Eq. (7.2.12) and Eq. (7.2.19).

Finally, in Fig. 7.8, we compare the estimate for the direct exclusion reach at a future 100 TeV hadron machine (FCC-hh) with the indirect bounds from the estimates of the ACME III sensitivity. In the left panel we set $\xi = 0.05$ which roughly corresponds to the high-luminosity LHC reach, while in the right panel we set $\xi = 0.01$ which is the projected sensitivity at a high-energy linear lepton collider (eg. ILC at 500 GeV center of mass energy with $\sim 500/\text{fb}$ integrated luminosity [287]). As one can see, in the absence of strong suppressions in the complex phase of c_t , the ACME III reach can easily surpass the FCC-hh ones in a large part of the parameter space of the $14 + 1$ model.

7.3 Non-minimal models

In order to highlight the main features of CP-violation due to the top partners, in the previous section we focussed on a simplified scenario with only one light multiplet. In generic realizations of the composite Higgs idea, however, it is not uncommon to find non-minimal set-ups with multiple light top partners. In the following we will discuss how the results we got in the simplified $14 + 1$ model are modified in the presence of additional light resonances. In addition we will consider an alternative scenario in which both the left-handed and right-handed top quark components are realized as elementary states. This set-up can be interpreted as an effective description of the MCHM₅ holographic scenario [251].

7.3.1 The $14 + 1$ model with a light singlet

As a first example we consider a more complete version of the $14 + 1$ model, including not only a light fourplet, but also a light singlet. The Lagrangian of the model is given by the terms in Eq. (7.2.1) plus the following additional operators involving the singlet ψ_1

$$\begin{aligned} \mathcal{L} = & i\bar{\psi}_1 \not{D}\psi_1 - (m_1\bar{\psi}_{1L}\psi_{1R} + \text{h.c.}) \\ & + \left(y_{L1}f(U^t\bar{q}_L^{14}U)_{55}\psi_{1R} - ic_L\bar{\psi}_{4L}^i\gamma^\mu d_\mu^i\psi_{1L} - ic_R\bar{\psi}_{4R}^i\gamma^\mu d_\mu^i\psi_{1R} + \text{h.c.} \right) \end{aligned} \quad (7.3.51)$$

The above Lagrangian contains four free parameters, that are in general complex. By field redefinitions two parameters can be made real, thus leaving two additional CP-violating sources corresponding to the complex phases of the combinations $c_L m_1 m_4^* y_{L1}^* y_{L4}$ and $c_R y_{L1}^* y_{L4}$. A convenient choice of phases is obtained by making the mass parameter m_1 and the elementary-composite mixing y_{L1} real. This choice makes manifest that CP-violating effects are necessarily related to the d_μ -symbol operators, and are controlled by the c_L and c_R parameters (on top of the c_t parameter we discussed in the previous section).

The mass of the singlet eigenstate \tilde{T} is

$$m_{\tilde{T}} \simeq |m_1| \left[1 + \frac{1}{4} \frac{y_{L1}^2 f^2 v^2}{m_1^2 f^2} + \dots \right]. \quad (7.3.52)$$

while the spectrum of the remaining states coincides with the one described in Section 7.2.1, apart from modifications arising at higher order in v/f .

The CP-violating Higgs couplings to the top partners are given by

$$-i c_{L,R} \bar{\psi}_{4L,R}^i \gamma^\mu d_\mu^i \psi_{1L,R} + \text{h.c.} \supset i \frac{c_{L,R}}{f} \partial_\mu h \left(\widehat{X}_{2/3L,R} \gamma^\mu \tilde{T}_{L,R} - \widetilde{\overline{T}}_{L,R} \gamma^\mu \tilde{T}_{L,R} \right) + \text{h.c.}, \quad (7.3.53)$$

where we only included the leading order terms in the v/f expansion. As in the simplified set-up we discussed in the previous section, also in the extended $14 + 1$ model the CP-violating effects arise only from charge $2/3$ fields.

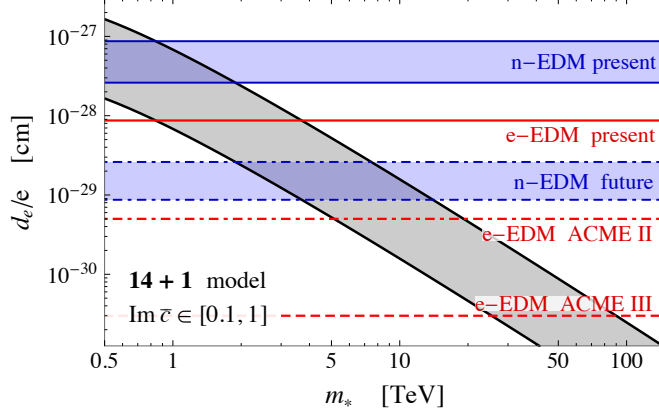


Figure 7.9: Estimate of the bound on the lightest top partner mass in the $14 + 1$ model with a fourplet and a singlet. The gray band shows the estimate of the corrections to the electron EDM given in Eq. (7.3.56) for $\text{Im } \bar{c} \in [0.1, 1]$. The solid red line shows the bound from the present electron EDM measurements, while the dot-dashed and dotted ones show the expected future limits. The blue bands show the constraints from the present and near-future neutron EDM measurements.

In the mass-eigenstate basis the coefficients of the CP-violating interactions that give rise to Barr-Zee-type contributions (see Eq. (7.2.14)) read

$$\begin{cases} c_{top,L} = \sqrt{2}v \frac{y_{L1}y_{L4}m_4f}{m_1(m_4^2 + y_{L4}^2f^2)} \text{Im } c_L \\ c_{T,L} = \sqrt{2}v \frac{y_{L1}y_{L4}m_1m_4f}{(m_4^2 + y_{L4}^2f^2)(m_4^2 + y_{L4}^2f^2 - m_1^2)} \text{Im } c_L \\ c_{\tilde{T},L} = -\sqrt{2}v \frac{y_{L1}y_{L4}m_4f}{m_1(m_4^2 + y_{L4}^2f^2 - m_1^2)} \text{Im } c_L \end{cases} \quad (7.3.54)$$

for the left-handed field interactions and

$$\begin{cases} c_{top,R} = -\sqrt{2}v \frac{y_{L4}y_{Lt}f}{m_4^2 + y_{L4}^2f^2} \text{Im } c_t \\ c_{T,R} = \sqrt{2}v \left[\frac{y_{L4}y_{Lt}f}{m_4^2 + y_{L4}^2f^2} \text{Im } c_t - \frac{y_{L4}y_{L1}f}{m_4^2 + y_{L4}^2f^2 - m_1^2} \text{Im } c_R \right] \\ c_{\tilde{T},R} = \sqrt{2}v \frac{y_{L4}y_{L1}f}{m_4^2 + y_{L4}^2f^2 - m_1^2} \text{Im } c_R \end{cases} \quad (7.3.55)$$

for the right-handed ones.

Interestingly, all CP-violating couplings show a similar power-counting scaling, independently of the fact that they originate from a d -symbol operator involving the t_R or involving only top partners. We generically expect $y_{L4} \sim y_{L1} \sim y_{Lt} \sim y_{top}$, $m_4 \sim m_1 \sim m_*$ and $c_L \sim c_R \sim c_t \sim 1$, so that all the couplings scale like $c \sim vfy_{top}^2/m_*^2$. As a consequence the contributions to the Barr-Zee effects coming from the various d -symbol

operators will be roughly of the same size. Using these estimates we can easily derive the typical size of the contributions to the electron EDM as a function of the top partners mass scale m_* ,

$$\frac{d_e}{e} \sim \frac{e^2}{48\pi^4} \frac{y_e}{\sqrt{2}} \text{Im} \bar{c} \frac{y_{top}^2 v}{m_*^2} \log \frac{m_*^2}{m_{top}^2}. \quad (7.3.56)$$

In the above formula we included a factor $\text{Im} \bar{c}$, which encodes the typical size of the CP-violating part of the d -symbol operator couplings. An analogous formula can be straightforwardly derived for the contributions to the quark dipole moments.

In Fig. 7.9 we compare the estimate in Eq. (7.3.56) with the present and projected future bounds from measurements of the electron and neutron EDM. To take into account possible accidental suppressions we vary the factor $\text{Im} \bar{c}$ in the range $[0.1, 1]$. One can see that the present bounds can roughly test top partner masses of order *few* TeV. The near-future improvements in the electron and neutron EDM's can push the bounds in the range 5 – 10 TeV, while ACME III could test partners with masses of order 40 – 100 TeV. We checked that the estimate in Eq. (7.3.56) is in good agreement with the results obtained through a numerical scan on the parameter space of the model.

7.3.2 The 5 + 5 2-site model

As a second scenario we consider the 2-site construction presented in refs. [254, 296] (see also ref. [297] for a similar set-up). This model is based on an extended set of global symmetries that ensure the calculability of the Higgs potential. For definiteness we will focus on the scenario in which the q_L and t_R fields are both elementary and are mixed with composite operators transforming in the fundamental representation of $\text{SO}(5)$ (we thus dub this set-up the ‘5 + 5’ model). This model can also be interpreted as a “deconstructed” version of the MCHM_5 holographic scenario [251].

The field content of the 5 + 5 2-site model contains one set of composite top partners that transform as a fourplet and as a singlet under the unbroken $\text{SO}(4)$ symmetry. The effective Lagrangian of the model can be written as

$$\begin{aligned} \mathcal{L} = & i\bar{q}_L \not{D} q_L + i\bar{t}_R \not{D} t_R + i\bar{\psi}_4 (\not{D} - i\phi) \psi_4 + i\bar{\psi}_1 \not{D} \psi_1 - (m_4 \bar{\psi}_{4L} \psi_{4R} + m_1 \bar{\psi}_{1L} \psi_{1R} + \text{h.c.}) \\ & + \left(y_L f \bar{q}_L^5 U \Psi + y_R f \bar{t}_R^5 U \Psi - i c_L \bar{\psi}_{4L}^i \gamma^\mu d_\mu^i \psi_{1L} - i c_R \bar{\psi}_{4R}^i \gamma^\mu d_\mu^i \psi_{1R} + \text{h.c.} \right), \end{aligned} \quad (7.3.57)$$

where $\Psi = (\psi_4, \psi_1)$ denotes the $\text{SO}(5)$ multiplet in the fundamental $\text{SO}(5)$ representation built from the ψ_4 and ψ_1 fields. Notice that the $\text{SO}(4)$ symmetry would allow for four independent mixing terms of the elementary q_L and t_R fields with the ψ_4 and ψ_1 multiplets. The structure in Eq. (7.3.57) is dictated by the requirement of calculability of the Higgs potential.

All the parameters in the effective Lagrangian can in general be complex. By field redefinitions, three parameters can be made real, leaving 3 physical complex phases. A convenient choice, which we will use in the following, is to remove the phases from

the elementary-composite mixings y_L and y_R and from one of the top partners mass parameters, either m_1 or m_4 . With this convention, the coefficients of the d_μ -symbol operators remain in general complex.

Two free parameters can be chosen by fixing the top and Higgs masses. The top mass, at leading order in the v/f expansion is given by

$$m_{top}^2 \simeq \frac{1}{2} \frac{y_L^2 y_R^2 f^2 |m_4 - m_1|^2}{(|m_4|^2 + y_L^2 f^2)(|m_1|^2 + y_R^2 f^2)} v^2. \quad (7.3.58)$$

The Higgs mass can be conveniently related to the masses of the top partners, namely [254] (see also ref. [255])

$$m_h \simeq m_{top} \frac{\sqrt{2N_c} m_T m_{\tilde{T}}}{\pi f} \sqrt{\frac{\log(m_T/m_{\tilde{T}})}{m_T^2 - m_{\tilde{T}}^2}}, \quad (7.3.59)$$

where $N_c = 3$ is the number of QCD colors, while m_T and $m_{\tilde{T}}$ denote the masses of the top partners with the quantum numbers of the top left and top right components respectively. The T and \tilde{T} masses are approximately given by

$$m_T \simeq \sqrt{|m_4|^2 + y_L^2 f^2}, \quad m_{\tilde{T}} \simeq \sqrt{|m_1|^2 + y_R^2 f^2}. \quad (7.3.60)$$

This relation in Eq. (7.3.59) is valid with fair accuracy, $\sim 20\%$, and is only mildly modified by the presence of additional heavier top partners.

Remarkably, Eq. (7.3.59) implies a tight relation between the mass of the lightest top partners and the Goldstone decay constant f , namely

$$m_{lightest} \lesssim \frac{\pi}{\sqrt{3}} \frac{m_h}{m_{top}} f \simeq 1.4 f. \quad (7.3.61)$$

Exclusion bounds on the top partner masses can thus be translated into lower bounds on the compositeness scale f . The relation in Eq. (7.3.61) is saturated only if $m_T \simeq m_{\tilde{T}} \simeq m_{lightest}$. If the T and \tilde{T} masses are significantly far apart, the lightest partner can be even a factor of ~ 2 lighter than the estimate in Eq. (7.3.61).

Let us now discuss the CP-violating effects. We start by considering the properties of the Yukawa couplings. We saw that in the $14 + 1$ model, all the mass parameters and elementary-composite mixings can be made real by field redefinitions, therefore the Yukawa couplings alone can not generate CP-violating effects. The situation is different in the $5 + 5$ set-up, in which one physical complex phase can not be removed from the $y_{L,R}$ and $m_{4,1}$ parameters. In principle this could allow for CP-violating Yukawa couplings. Noticeably, in the fermion mass eigenstate basis, only the off-diagonal Yukawa interactions can be complex, while the diagonal ones are necessarily real. We will now present a general proof of this result that will allow us to identify the structural properties from which it stems and the class of models for which it is valid.

The dynamics of the various resonances and their couplings with the Higgs can be encoded into a formal effective Lagrangian obtained by integrating out all the top

partner fields in the gauge interaction basis. The only fields remaining in this effective description are the elementary components q_L and t_R .¹¹ Notice that these fields have an overlap with the whole set of mass eigenstates, thus they can describe any of them by just imposing the appropriate mass-shell condition. The effective Lagrangian contains operators with the generic form

$$i\bar{q}_L^5 p^{2n} \not{D} q_L^5, \quad i\bar{t}_R^5 p^{2n} \not{D} t_R^5, \quad (7.3.62)$$

which correct the kinetic terms of the q_L and t_R fields. These operators, however, are necessarily real, so they do not give rise to CP-violating effects. The effective Lagrangian also contains a unique “mass” term, namely

$$\bar{m} \bar{q}_L^5 U t_R^5 + \text{h.c.}, \quad (7.3.63)$$

which is the only invariant allowed by the symmetry structure of the model that does not contain derivatives. This operator gives rise not only to the mass terms but also to the Yukawa couplings.

The \bar{m} coefficient is in general complex. Nevertheless, when we redefine the fields to make the masses real, we automatically remove all complex phases from \bar{m} . In such a way also the diagonal Yukawa couplings are automatically made real. Notice that this result is true only in models in which a single “mass” invariant is present. If multiple invariants are allowed, the Yukawa couplings are not “aligned” with the masses, thus making the masses real in general does not remove the complex phases from the diagonal Yukawa couplings. A scenario with multiple invariants can be obtained by embedding both the q_L and the t_R fields in the 14 representation of $\text{SO}(5)$.

Since the diagonal Yukawa couplings are real, the only interactions that can generate CP-violating contributions through Barr-Zee-type effects are the ones coming from the d -symbol operators. Their explicit form at leading order in the v/f expansion (using the convention in Eq. (7.2.14)) reads

$$\left\{ \begin{array}{l} c_{top,L} = -\sqrt{2}v f y_L^2 \frac{\text{Im}[c_L(m_1 m_4^* + y_R^2 f^2)]}{(|m_4|^2 + y_L^2 f^2)(|m_1|^2 + y_R^2 f^2)} \\ c_{X_{2/3},L} = -\sqrt{2}v f y_R^2 \frac{\text{Im} c_L}{|m_1|^2 + y_R^2 f^2 - |m_4|^2} \\ c_{T,L} = \frac{\sqrt{2}v f}{|m_4|^2 + y_L^2 f^2 - |m_1|^2 - y_R^2 f^2} \left[y_R^2 \text{Im} c_L - y_L^2 \frac{\text{Im}[c_L(m_1 m_4^* + y_R^2 f^2)]}{|m_4|^2 + y_L^2 f^2} \right] \\ c_{\tilde{T},L} = -(c_{top,L} + c_{X_{2/3},L} + c_{T,L}) \end{array} \right. \quad (7.3.64)$$

¹¹This effective description is analogous to the “holographic” effective Lagrangian in extra-dimensional models, which is a function of the UV boundary values of the extra-dimensional fields [298, 299].

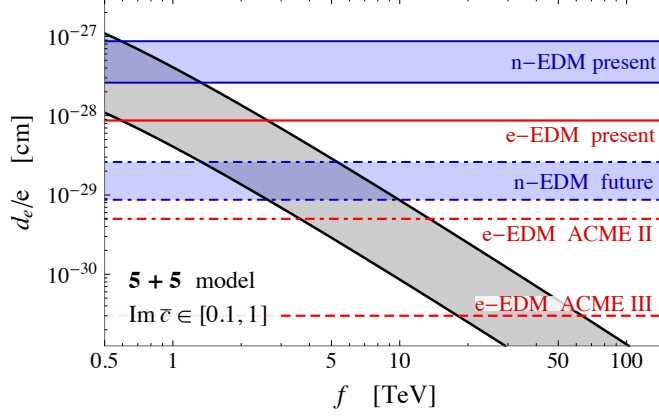


Figure 7.10: Estimate of the bound on the compositeness scale f in the $5 + 5$ model. The gray band shows the estimate of the corrections to the electron EDM given in Eq. (7.3.66) for $\text{Im } \bar{c} \in [0.1, 1]$. The solid red line shows the bound from the present electron EDM measurements, while the dot-dashed and dotted ones show the expected future limits. The blue bands show the constraints from the present and near-future neutron EDM measurements.

for the left-handed field interactions and

$$\left\{ \begin{array}{l} c_{top,R} = \frac{\sqrt{2}vf y_R^2}{|m_1|^2 + y_R^2 f^2} \left[\frac{\text{Im}[c_R(m_1^* m_4 + y_L^2 f^2)]}{|m_4|^2 + y_L^2 f^2} + \text{Im}[c_R m_1^*/m_4^*] \right] \\ c_{X_{2/3},R} = -\sqrt{2}vf y_R^2 \frac{\text{Im}[c_R m_1^*/m_4^*]}{|m_1|^2 + y_R^2 f^2 - |m_4|^2} \\ c_{T,R} = -\frac{\sqrt{2}vf}{|m_4|^2 + y_L^2 f^2 - |m_1|^2 - y_R^2 f^2} \left[y_L^2 \text{Im } c_R - y_R^2 \frac{\text{Im}[c_R(m_1^* m_4 + y_L^2 f^2)]}{|m_4|^2 + y_L^2 f^2} \right] \\ c_{\bar{T},R} = -(c_{top,R} + c_{X_{2/3},R} + c_{T,R}) \end{array} \right. \quad (7.3.65)$$

for the right-handed ones.

Interestingly, the dependence of the CP-violating coefficients on the elementary-composite mixings and on the masses of the top partners is analogous to the one we found in the $14 + 1$ set-up. This result confirms that the CP-violating effects in composite Higgs scenarios share some “universal” structure and are generically expected to be sizable independently of the details of the model.

Using the explicit expressions for the top mass in Eq. (7.3.58), one finds that the elementary-composite mixing parameters can be estimated as $y_L \sim y_R \sim y_{top} m_{lightest}/f$. Putting this result together with the estimate in Eq. (7.3.61), we can express the corrections to the electron EDM as a function of the compositeness scale f , namely

$$\frac{d_e}{e} \sim \frac{e^2}{48\pi^4} \frac{y_e}{\sqrt{2}} \text{Im } \bar{c} \frac{m_{top}}{1.4f^2} \log \frac{(1.4f)^2}{m_{top}^2}. \quad (7.3.66)$$

This is a quite remarkable result, since it allows us to convert directly the bounds on

dipole operators into constraints on f . The numerical value of the estimate in Eq. (7.3.66) is shown in Fig. 7.10, together with the experimental bounds. To allow for a certain amount of cancellation we varied the parameter $\text{Im } \bar{c}$ in the range $[0.1, 1]$. The present data give bounds $f \gtrsim 1$ TeV. Near-future improvements in the electron and neutron EDM's will test $f \sim 5$ TeV, while the ACME III expected reach could probe $f \sim 50$ TeV. Notice that these bounds are much stronger than the ones coming from direct searches. As shown in ref. [281], the LHC searches for top partners can now exclude the $5 + 5$ model for $f \simeq 780$ GeV, while the high-luminosity LHC program could only slightly increase the bound up to $f \simeq 1.1$ TeV.

It must be noticed that the estimate in Eq. (7.3.66) should be interpreted as a lower bound on the corrections to the electron EDM. To derive it we assumed that the relation in Eq. (7.3.61) is saturated. As we discussed before, this is true only if the T and \tilde{T} masses are comparable. In generic parameter space points the lightest partners can be even a factor ~ 2 lighter than the estimate, thus leading to EDM contributions larger by a factor ~ 4 . The presence of multiple CP-violating couplings can also give rise to, small, additional enhancements. We verified by a numerical scan that the bounds in Fig. 7.10 reproduce quite well the minimal constraints on f as a function of the typical size of the complex phases. They can thus be considered as robust constraints on the compositeness scale.

It is important to mention that the value of ξ can be directly connected to the amount of fine-tuning [256]. In CH scenarios the v/f ratio is not a free parameter, but rather a dynamical quantity fixed by the minimization of the radiatively-induced Higgs potential. In generic parameter space points ξ is expected to be of order one. Therefore, requiring a large separation between the Higgs vacuum expectation value and f implies a minimal amount of tuning of order $1/\xi$.¹² The constraints coming from the electron and neutron EDM's can thus be reinterpreted as bounds on the minimal amount of fine-tuning in the $5 + 5$ 2-site model. While $f \sim 1$ TeV allows for a relatively low tuning ($\xi \sim 0.1$), the future bounds are expected to test regions of the parameter space with a tuning significantly below 1%.

To conclude the discussion about the $5 + 5$ model, we consider the contributions to the Weinberg operator. Within the approximation in Eq. (7.2.32) we find

$$w \simeq \frac{g_s^3}{\sqrt{2}(4\pi)^4} \frac{\text{Im}(c_R - c_L) + \sqrt{2} \text{Im}(c_R c_L^*)}{f^2} \frac{|m_4|^2 - |m_1|^2}{|m_4 - m_1|^2}. \quad (7.3.67)$$

Analogously to what we found for the $14 + 1$ model (see Section 7.2.3), the top partners contributions to the Weinberg operator do not decouple in the limit of heavy resonances. The explicit result in Eq. (7.3.67) shows that, in addition to contributions linear in the $c_{L,R}$ parameters, quadratic pieces are present. The latter come from diagrams involving two Higgs interactions coming from the d -symbol operators. Notice that the above result

¹²Note that additional sources of tuning can be present due to peculiarities of the Higgs potential [256].

is reliable only if $m_4 - m_1$ is not too small. In the limit $m_4 = m_1$, the top mass vanishes (compare Eq. (7.3.58)) and the approximation in Eq. (7.2.32) is not valid.

To give an idea of the strength of the experimental bounds we fix the parameters by the relations $m_4 \sim m_1$ and $c_L \sim c_R$, moreover we set $\xi = 0.1$. The current bounds on the neutron EDM translate into a bound $c_{L,R} \lesssim 1$, whereas the expected improved measurements will allow to probe $c_{L,R} \sim 0.1$.

7.4 Summary

In this chapter we analyzed CP-violating effects induced by light top partners in composite Higgs scenarios. We found that the main effects arise at two-loop level through Barr-Zee-type diagrams and generate sizable contributions to the dipole moments of the electron and of the light SM quarks. Additional, although typically subleading, contributions are induced for the purely-gluonic Weinberg operator.

Noticeably, in a large class of models, Barr-Zee effects arise exclusively from top partner interactions involving the derivative of the Higgs field, namely $\partial_\mu h \bar{\chi}_i \gamma^\mu \chi_j$. The diagonal Yukawa couplings, instead, are necessarily CP-conserving, thus not contributing to the light SM fermions dipole operators. This result is valid in all models in which the effective Lagrangian contains only one invariant mass term for the top quark (see Section 7.3.2). Notice that this class of models is the most motivated one from a flavor perspective, since a suppression of flavor-violating effects mediated by the Higgs [300] is also present. Without such feature very strong bounds from Higgs-mediated flavor-changing neutral currents would be present.

We found that the overall structure of the CP-violating effects, and in particular the dependence on the masses of the top partners, is a rather universal feature and depends only mildly on the details of the model. The main contributions to the electron and light quark dipole moments can be interpreted as a running effect. At the one-loop level the top quark and its partners give rise to CP-odd contact interactions of the Higgs with the gauge fields (namely $H^2 F_{\mu\nu} \tilde{F}^{\mu\nu}$ with the photons and $H^2 G_{\mu\nu}^a \tilde{G}^{a\mu\nu}$ with the gluons). These operators, in turn, induce a running for the EDM's and CEDM's of the light SM fermions. We explicitly computed how the contributions due to the top and its partners can be matched onto the CP-violating Higgs contact interactions. In particular we found that running effects are always regulated at the top mass scale, since the top contribution to the Higgs contact operators exactly balances the ones coming from the top partners. Additional threshold contributions are found to be accidentally suppressed and numerically negligible.

In our analysis we focused exclusively on the role of the top and its partners and we did not take into account possible effects related to additional resonances. We also neglected the details of the flavor structure both in the quark and in the lepton sectors. These aspects are expected not to spoil the overall picture we described in this work.

They could however have some impact on the bounds, which is worth exploring. We leave this aspect for future investigation.

Although the CP-violating effects arise only at two-loop level, the present experimental bounds are tight enough to give non-trivial constraints on the top partners masses. The strongest bounds come from the measurement of the electron EDM, and can be used to probe top partners masses in the *few* TeV range (see Fig. 7.5 and Fig. 7.9). Upgraded experiments are expected to improve the bounds by one order of magnitude in the near future (ACME II) and by more than two orders of magnitude at a later stage (ACME III), hence pushing the indirect exclusions for top partners well above 10 – 20 TeV (Fig. 7.9). Bounds from neutron EDM measurements are slightly weaker than the ones from electron EDM, but could nevertheless test resonance masses in the 5 – 10 TeV range in the near future.

In a large part of the parameter space of explicit models, the indirect bounds coming from the electron EDM are competitive with the LHC direct searches for heavy vector-like quarks (see Fig. 7.7). In particular CP-violating effects are induced by the same operators that control the single-production vertices. In the absence of accidental cancellations or of accidentally small CP-violating phases, the indirect bounds from CP violation tend to surpass the ones from single production searches. The expected ACME II constraints will cover most of the LHC direct search reach even for complex phases as small as *few*%. ACME III could instead give constraints comparable with the direct ones achievable at future high-energy hadron colliders such as FCC-hh with 100 TeV center of mass energy (see Fig. 7.8).

Interestingly, in specific scenarios such as the $5 + 5$ 2-site model, the constraints from CP-violating effects can be translated into bounds on the Higgs compositeness scale f . While the present constraints are of order $f \gtrsim 1$ TeV, future improvements can push the bounds well above the 5 – 10 TeV range (see Fig. 7.10). In these scenarios the constraints on f can also be translated into lower bounds on the amount of fine tuning. For $f \sim 1$ TeV the minimal fine-tuning is of order 5 – 10%, whereas it becomes 0.1% for $f \sim 10$ TeV.

Appendix A

Higgs production and decay rates in the EFT framework

A.1 EFT cross section for hadron colliders

In this appendix we report the expressions for the production and decay rates of the Higgs boson as a function of the EFT parameters. The numerical results have been obtained at LO through Feynrules [152] and MadGraph [151] by using the model ‘‘Higgs effective Lagrangian’’ [301].

We start by listing the dependence on the single-Higgs couplings deformations (δc_z , c_{zz} , $c_{z\Box}$, $\hat{c}_{z\gamma}$, $\hat{c}_{\gamma\gamma}$, \hat{c}_{gg} , δy_t , δy_b , δy_τ). The modification of the total cross sections for associated production (ZH and WH) and VBF depend on the collider energy. The results at 7, 8, 13, 14, 33 and 100 TeV are given by

$$\frac{\sigma_{ZH}}{\sigma_{ZH}^{\text{SM}}} = 1 + \delta c_z \begin{pmatrix} 2.0 \\ 2.0 \\ 2.0 \\ 2.0 \\ 2.0 \\ 2.0 \end{pmatrix} + c_{z\Box} \begin{pmatrix} 7.6 \\ 7.8 \\ 8.3 \\ 8.4 \\ 9.1 \\ 10.0 \end{pmatrix} + c_{zz} \begin{pmatrix} 3.4 \\ 3.4 \\ 3.5 \\ 3.6 \\ 3.7 \\ 4.0 \end{pmatrix} - \hat{c}_{z\gamma} \begin{pmatrix} 0.060 \\ 0.061 \\ 0.067 \\ 0.068 \\ 0.077 \\ 0.086 \end{pmatrix} - \hat{c}_{\gamma\gamma} \begin{pmatrix} 0.028 \\ 0.028 \\ 0.030 \\ 0.032 \\ 0.034 \\ 0.037 \end{pmatrix}, \quad (\text{A.1.1})$$

$$\frac{\sigma_{WH}}{\sigma_{WH}^{\text{SM}}} = 1 + \delta c_z \begin{pmatrix} 2.0 \\ 2.0 \\ 2.0 \\ 2.0 \\ 2.0 \\ 2.0 \end{pmatrix} + c_{z\Box} \begin{pmatrix} 9.3 \\ 9.4 \\ 10.0 \\ 10.1 \\ 11.1 \\ 12.1 \end{pmatrix} + c_{zz} \begin{pmatrix} 4.4 \\ 4.4 \\ 4.6 \\ 4.6 \\ 5.0 \\ 5.3 \end{pmatrix} - \hat{c}_{z\gamma} \begin{pmatrix} 0.082 \\ 0.084 \\ 0.094 \\ 0.095 \\ 0.110 \\ 0.126 \end{pmatrix} - \hat{c}_{\gamma\gamma} \begin{pmatrix} 0.044 \\ 0.045 \\ 0.048 \\ 0.049 \\ 0.054 \\ 0.060 \end{pmatrix}, \quad (\text{A.1.2})$$

$$\frac{\sigma_{VBF}}{\sigma_{VBF}^{\text{SM}}} = 1 + \delta c_z \begin{pmatrix} 2.0 \\ 2.0 \\ 2.0 \\ 2.0 \\ 2.0 \\ 2.0 \end{pmatrix} - c_{z\Box} \begin{pmatrix} 2.2 \\ 2.2 \\ 2.5 \\ 2.5 \\ 3.0 \\ 3.7 \end{pmatrix} - c_{zz} \begin{pmatrix} 0.81 \\ 0.83 \\ 0.89 \\ 0.90 \\ 1.04 \\ 1.27 \end{pmatrix} + \hat{c}_{z\gamma} \begin{pmatrix} 0.029 \\ 0.030 \\ 0.033 \\ 0.034 \\ 0.041 \\ 0.051 \end{pmatrix} + \hat{c}_{\gamma\gamma} \begin{pmatrix} 0.0113 \\ 0.0117 \\ 0.0129 \\ 0.0131 \\ 0.0156 \\ 0.0193 \end{pmatrix}, \quad (\text{A.13})$$

where we employ the VBF cross section definition of ref. [66], namely we apply the following cuts on the two forward jets: $p_{T,j} > 20$ GeV, $|\eta_j| < 5$, and $m_{jj} > 250$ GeV.

The cross sections of the gluon fusion and $t\bar{t}H$ production modes are instead modified in an energy-independent way [66]. This is a consequence of the fact that at LO the gluon fusion energy scale is fixed by the Higgs bosons on-shell condition and is therefore \sqrt{s} independent, while the modification of $t\bar{t}H$ is simply due to a rescaling of the top Yukawa.

$$\frac{\sigma_{\text{ggF}}}{\sigma_{\text{ggF}}^{\text{SM}}} = 1 + 2\hat{c}_{gg} + 2.06\delta y_t - 0.06\delta y_b, \quad (\text{A.14})$$

$$\frac{\sigma_{\text{ttH}}}{\sigma_{\text{ttH}}^{\text{SM}}} = 1 + 2\delta y_t. \quad (\text{A.15})$$

The modifications of the decay widths are given by [66]

$$\frac{\Gamma_{\gamma\gamma}}{\Gamma_{\gamma\gamma}^{\text{SM}}} = 1 + 2.56\delta c_z + 2.13c_{z\Box} + 0.98c_{zz} - 0.066\hat{c}_{z\gamma} - 2.46\hat{c}_{\gamma\gamma} - 0.56\delta y_t, \quad (\text{A.16})$$

$$\frac{\Gamma_{Z\gamma}}{\Gamma_{Z\gamma}^{\text{SM}}} = 1 + 2.11\delta c_z - 3.4\hat{c}_{z\gamma} - 0.113\delta y_t, \quad (\text{A.17})$$

$$\frac{\Gamma_{\text{WW}}}{\Gamma_{\text{WW}}^{\text{SM}}} = 1 + 2.0\delta c_z + 0.67c_{z\Box} + 0.05c_{zz} - 0.0182\hat{c}_{z\gamma} - 0.0051\hat{c}_{\gamma\gamma}, \quad (\text{A.18})$$

$$\frac{\Gamma_{\text{ZZ}}}{\Gamma_{\text{ZZ}}^{\text{SM}}} = 1 + 2.0\delta c_z + 0.33c_{z\Box} + 0.19c_{zz} - 0.0081\hat{c}_{z\gamma} - 0.00111\hat{c}_{\gamma\gamma}, \quad (\text{A.19})$$

$$\frac{\Gamma_{\tau\tau}}{\Gamma_{\tau\tau}^{\text{SM}}} = 1 + 2.0\delta y_\tau, \quad (\text{A.110})$$

$$\frac{\Gamma_{bb}}{\Gamma_{bb}^{\text{SM}}} = 1 + 2.0\delta y_b, \quad (\text{A.111})$$

$$\frac{\Gamma_H}{\Gamma_H^{\text{SM}}} = 1 + 0.171\hat{c}_{gg} + 0.006c_{zz} - 0.0091\hat{c}_{z\gamma} + 0.15c_{z\Box} - 0.0061\hat{c}_{\gamma\gamma} + 0.48\delta c_z \quad (\text{A.112})$$

$$+ 1.15\delta y_b + 0.23\delta y_t + 0.13\delta y_\tau, \quad (\text{A.113})$$

where in the modification of the decay to two photons we made use of the one-loop

C^Γ [%]	$\gamma\gamma$	ZZ	WW	$f\bar{f}$	gg
H	0.49	0.83	0.73	0	0.66

Table A.1: Coefficients parametrizing the corrections to the Higgs partial widths due to loops involving the Higgs self-coupling (see eq. (A.1.15)) [62].

result¹ of ref. [302], suitably translated to the Higgs basis and evaluated at the renormalization scale $\mu = m_h$. The analog result for the decay to $Z\gamma$ is not yet available in the literature, and we only include the known terms. In any case, the corresponding branching ratio will be measured with a limited precision and the impact of the missing one-loop corrections is going to be negligible.

For completeness we also report the expressions for the dependence of the Higgs rates on the modification of the Higgs self-coupling κ_λ . These results were derived in ref. [62]. The modification to the Higgs production and decay rates can be parametrized as

$$\frac{\sigma}{\sigma_{\text{SM}}} = 1 + (\kappa_\lambda - 1)C^\sigma + \frac{(\kappa_\lambda^2 - 1)\delta Z_H}{1 - \kappa_\lambda^2\delta Z_H}, \quad (\text{A.1.14})$$

and

$$\frac{\Gamma}{\Gamma_{\text{SM}}} = 1 + (\kappa_\lambda - 1)C^\Gamma + \frac{(\kappa_\lambda^2 - 1)\delta Z_H}{1 - \kappa_\lambda^2\delta Z_H}. \quad (\text{A.1.15})$$

In the above expressions the term linear in κ_λ comes from diagrams that contribute directly to the production and decay processes. The corresponding coefficients C^σ and C^Γ for the inclusive cross sections are given in tables A.1 and A.2. The last terms in eqs. (A.1.14) and (A.1.15) comes from a rescaling of the Higgs kinetic term due to the self-energy diagram involving two insertions of the Higgs self-coupling. The corresponding quantity δZ_H is given by

$$\delta Z_H = -\frac{9}{16} \frac{G_\mu m_H^2}{\sqrt{2}\pi^2} \left(\frac{2\pi}{3\sqrt{3}} - 1 \right) \simeq -0.0015. \quad (\text{A.1.16})$$

We now report the expressions for the Higgs pair production differential cross section. This cross-section has been calculated in the EFT framework in ref. [76], as a function of the parameters δy_t , $\delta y_t^{(2)}$, \hat{c}_{gg} , $\hat{c}_{gg}^{(2)}$, and κ_λ . The ratio of the inclusive cross-section for Higgs-pair production to the corresponding SM prediction can be written

¹We observed that the NLO corrections in the $\gamma\gamma$ decay have no impact on the global fit once enough observables are included to remove the flat directions.

C^σ [%]	ggF	VBF	WH	ZH	$t\bar{t}H$
7 TeV	0.66	0.65	1.06	1.23	3.87
8 TeV	0.66	0.65	1.05	1.22	3.78
13 TeV	0.66	0.64	1.03	1.19	3.51
14 TeV	0.66	0.64	1.03	1.18	3.47

Table A.2: Coefficients parametrizing the corrections to the Higgs production cross sections due to loops involving the Higgs self-coupling (see eq. (A.1.14)) [62].

as

$$\frac{\sigma(pp \rightarrow hh)}{\sigma_{\text{sm}}(pp \rightarrow hh)} = A_1 (1 + \delta y_t)^4 + A_2 (\delta y_t^{(2)})^2 + A_3 \kappa_\lambda^2 (1 + \delta y_t)^2 + A_4 \kappa_\lambda^2 \hat{c}_{gg}^2 \quad (\text{A.1.17})$$

$$+ A_5 (\hat{c}_{gg}^{(2)})^2 + A_6 (1 + \delta y_t)^2 \delta y_t^{(2)} + A_7 \kappa_\lambda (1 + \delta y_t)^3 \quad (\text{A.1.18})$$

$$+ A_8 \kappa_\lambda (1 + \delta y_t) \delta y_t^{(2)} + A_9 \kappa_\lambda \hat{c}_{gg} \delta y_t^{(2)} + A_{10} \hat{c}_{gg}^{(2)} \delta y_t^{(2)} \quad (\text{A.1.19})$$

$$+ A_{11} \kappa_\lambda \hat{c}_{gg} (1 + \delta y_t)^2 + A_{12} \hat{c}_{gg}^{(2)} (1 + \delta y_t)^2 + A_{13} \kappa_\lambda^2 \hat{c}_{gg} (1 + \delta y_t) \quad (\text{A.1.20})$$

$$+ A_{14} \kappa_\lambda \hat{c}_{gg}^{(2)} (1 + \delta y_t) + A_{15} \kappa_\lambda \hat{c}_{gg} \hat{c}_{gg}^{(2)}, \quad (\text{A.1.21})$$

Notice that this parametrization can be used for the full uncut cross section and also for the cross section obtained after imposing cuts and acceptance factors. Moreover we can use the same expression to parametrize the differential cross section in each bin of the Higgs-pair invariant mass distribution. We report in table A.3 the inclusive and differential SM cross section at 14 TeV after imposing the cuts devised in ref. [76], as well as the values of the A_i .

Finally we consider the differential distributions for the Higgs associated production channels. In table A.4 we list the dependence of the differential cross section in ZH and WH on the single-Higgs EFT parameters. The results are presented for the binned invariant mass \hat{s} distribution. The cross sections have been computed by analyzing the events generated at LO by MadGraph through a custom made C++ code based on the MadAnalysis5 library [303, 304]. The coefficients that parametrize the dependence of the WH , ZH and $t\bar{t}H$ production channels on the Higgs self-coupling are listed in table A.5.

In tables A.6 and A.7 we list the estimates of the systematic uncertainties on the binned differential distributions. To estimate the expected errors on the inclusive cross sections, we compared the ATLAS projections for the 300/fb and 3/ab experimental uncertainties and assumed that they come from a sum in quadrature of systematic and statistical ones. In the ‘optimistic’ scenario in table A.6, we rescaled the statistical uncertainty by the square root of the ratio of SM number of events in each bin, whereas

m_{hh}^{reco} [GeV]	inclusive	250–400	400–550	550–700	700–850	850–1000	1000–
σ_{sm} [ab]	1.6	0.27	0.8	0.36	0.13	0.042	0.021
A_1	1.7	2.3	1.7	1.5	1.3	1.2	1.2
A_2	2.7	1.8	2.1	3.2	4.7	6.4	9.1
A_3	0.12	0.27	0.11	0.057	0.034	0.022	0.011
A_4	0.042	0.094	0.037	0.026	0.024	0.023	0.022
A_5	1.5	0.62	0.69	1.5	3.5	7.1	20.
A_6	-3.8	-4.0	-3.6	-3.8	-4.2	-4.5	-4.6
A_7	-0.82	-1.5	-0.84	-0.51	-0.36	-0.26	-0.17
A_8	0.98	1.4	0.96	0.83	0.78	0.73	0.67
A_9	0.45	0.81	0.46	0.33	0.23	0.14	0.003
A_{10}	2.2	2.1	2.0	2.4	2.8	2.5	-0.56
A_{11}	-0.32	-0.88	-0.33	-0.081	0.03	0.087	0.13
A_{12}	-1.0	-2.3	-1.3	-0.6	0.33	1.6	4.1
A_{13}	0.12	0.33	0.11	0.044	0.02	0.0092	0.0014
A_{14}	0.46	0.82	0.44	0.36	0.29	0.13	-0.27
A_{15}	0.41	0.48	0.31	0.39	0.57	0.81	1.3

Table A.3: Coefficients parametrizing the inclusive and differential cross section for double Higgs production via gluon fusion at $\sqrt{s} = 14$ TeV. By σ_{sm} we denote the SM cross section, while A_1 – A_{15} are the coefficients parametrizing the dependence of the cross on the EFT parameters as defined in eq. (A.1.21). The numerical results correspond to the ones derived in the analyses of ref. [76].

\sqrt{s}	$\sqrt{\hat{s}}/m_{\text{threshold}}$	WH						ZH					
		ϵ_{SM}	δc_z	$c_{z\Box}$	c_{zz}	$\hat{c}_{z\gamma}$	$\hat{c}_{\gamma\gamma}$	ϵ_{SM}	δc_z	$c_{z\Box}$	c_{zz}	$\hat{c}_{z\gamma}$	$\hat{c}_{\gamma\gamma}$
7 TeV	[1.0 – 1.1]	19 %	1.99	4.95	2.68	-0.0270	-0.0215	20 %	2.00	4.14	2.14	-0.0220	-0.0123
	[1.1 – 1.2]	20 %	2.00	5.84	3.10	-0.0349	-0.0258	21 %	2.00	4.81	2.42	-0.0290	-0.0154
	[1.2 – 1.5]	35 %	2.00	7.40	3.80	-0.0504	-0.0334	34 %	2.01	6.44	3.07	-0.0447	-0.0226
	[1.5 – 2.0]	18 %	2.01	12.4	5.71	-0.116	-0.0598	17 %	2.01	10.5	4.44	-0.0853	-0.0393
	[2.0 – 3.0]	7 %	2.01	23.	9.38	-0.271	-0.117	6 %	1.98	19.7	6.90	-0.192	-0.0780
8 TeV	[1.0 – 1.1]	19 %	2.01	4.93	2.66	-0.0275	-0.0215	20 %	2.00	4.10	2.12	-0.0231	-0.0126
	[1.1 – 1.2]	20 %	1.97	5.73	3.05	-0.0337	-0.0252	20 %	2.01	4.90	2.49	-0.0299	-0.0158
	[1.2 – 1.5]	34 %	2.01	7.51	3.81	-0.0533	-0.0342	35 %	2.01	6.40	3.05	-0.0453	-0.0226
	[1.5 – 2.0]	19 %	1.99	12.1	5.56	-0.113	-0.0582	18 %	2.00	10.6	4.51	-0.0872	-0.0400
	[2.0 – 3.0]	7 %	2.02	22.3	9.12	-0.264	-0.114	6 %	1.95	20.0	6.99	-0.202	-0.0804
13 TeV	[1.0 – 1.1]	18 %	2.02	4.96	2.70	-0.0265	-0.0216	19 %	2.02	4.06	2.09	-0.0226	-0.0121
	[1.1 – 1.2]	19 %	1.97	5.81	3.08	-0.0344	-0.0256	20 %	2.00	4.86	2.45	-0.0300	-0.0157
	[1.2 – 1.5]	34 %	2.00	7.44	3.76	-0.0532	-0.0339	34 %	1.98	6.37	3.04	-0.0445	-0.0222
	[1.5 – 2.0]	19 %	2.02	11.9	5.46	-0.111	-0.0572	18 %	2.01	10.6	4.53	-0.0887	-0.0406
	[2.0 – 3.0]	8 %	1.99	22.6	9.20	-0.269	-0.116	7 %	2.00	20.4	7.29	-0.196	-0.0808
14 TeV	[1.0 – 1.1]	18 %	2.00	5.01	2.72	-0.0267	-0.0217	19 %	2.01	4.14	2.12	-0.0237	-0.0126
	[1.1 – 1.2]	19 %	2.00	5.81	3.10	-0.0337	-0.0255	20 %	2.01	4.86	2.49	-0.0284	-0.0156
	[1.2 – 1.5]	34 %	2.01	7.44	3.76	-0.0535	-0.0340	34 %	2.00	6.35	3.02	-0.0448	-0.0221
	[1.5 – 2.0]	19 %	1.98	11.8	5.40	-0.112	-0.0572	18 %	1.98	10.5	4.44	-0.0873	-0.0396
	[2.0 – 3.0]	8 %	2.03	22.6	9.05	-0.276	-0.117	7 %	1.96	20.3	7.27	-0.193	-0.0800
33 TeV	[1.0 – 1.1]	17 %	1.98	4.96	2.68	-0.0274	-0.0216	18 %	2.02	4.16	2.16	-0.0228	-0.0124
	[1.1 – 1.2]	18 %	2.01	5.77	3.07	-0.0338	-0.0254	19 %	1.99	4.77	2.41	-0.0282	-0.0150
	[1.2 – 1.5]	33 %	1.99	7.43	3.73	-0.0544	-0.0340	34 %	1.99	6.45	3.08	-0.0453	-0.0225
	[1.5 – 2.0]	20 %	2.00	12.00	5.54	-0.110	-0.0574	19 %	2.02	10.4	4.37	-0.0862	-0.0390
	[2.0 – 3.0]	9 %	2.02	23.3	9.56	-0.274	-0.119	8 %	2.00	19.8	6.97	-0.190	-0.0777
100 TeV	[1.0 – 1.1]	16 %	2.01	4.92	2.66	-0.0271	-0.0215	17 %	2.02	3.98	2.05	-0.0238	-0.0118
	[1.1 – 1.2]	18 %	2.04	5.82	3.09	-0.0344	-0.0257	18 %	2.00	5.02	2.60	-0.0282	-0.0157
	[1.2 – 1.5]	33 %	1.97	7.48	3.77	-0.054	-0.0341	33 %	2.00	6.45	3.09	-0.0445	-0.0224
	[1.5 – 2.0]	20 %	2.02	11.9	5.47	-0.111	-0.0573	20 %	1.99	10.5	4.38	-0.0860	-0.0389
	[2.0 – 3.0]	10 %	1.99	23.1	9.40	-0.275	-0.118	9 %	2.00	20.0	6.90	-0.195	-0.0782

Table A.4: Effective field theory coefficient for each bin in the \hat{s} differential distribution. The bins extrema are expressed in units of $m_{\text{threshold}} \equiv m_V + m_h$. The ϵ_{sm} columns list the percentage of events that belong to each bin in the SM distribution.

C^σ [%]	[1.0 – 1.1]	[1.1 – 1.2]	[1.2 – 1.5]	[1.5 – 2.0]	[2.0 – 3.0]
WH	1.78 (0.18)	1.44 (0.19)	1.02 (0.34)	0.52 (0.19)	0.06 (0.08)
ZH	2.08 (0.19)	1.64 (0.20)	1.12 (0.34)	0.51 (0.18)	0.21 (0.07)
$t\bar{t}H$	8.57 (0.02)	6.63 (0.08)	4.53 (0.33)	2.83 (0.33)	1.61 (0.18)

Table A.5: Coefficients parametrizing the corrections to the differential Higgs production cross sections at 13 TeV in the WH , ZH and $t\bar{t}H$ channels due to loops involving the Higgs self-coupling (see eq. (A.1.14)). The bins extrema are expressed in units of $m_{\text{threshold}}$, defined as $m_{\text{threshold}} \equiv m_V + m_h$ for WH and ZH , and $m_{\text{threshold}} \equiv 2m_t + m_h$ for $t\bar{t}H$. In parentheses we give the fraction of events belonging to each bin in the SM distribution. The results are taken from ref. [62].

Process	Systematic	[1.0 – 1.1]	[1.1 – 1.2]	[1.2 – 1.5]	[1.5 – 2.0]	[2.0 – 3.0]
$H \rightarrow \gamma\gamma$ $t\bar{t}H$	0.04	0.74	0.41	0.23	0.23	0.3
$H \rightarrow \gamma\gamma$ WH	0.08	0.37	0.37	0.28	0.36	0.54
$H \rightarrow \gamma\gamma$ ZH	0.03	0.62	0.61	0.47	0.63	0.99
$H \rightarrow ZZ$ $t\bar{t}H$	0.05	0.98	0.53	0.29	0.29	0.39
$H \rightarrow ZZ$ WH	0.07	0.33	0.32	0.25	0.32	0.48
$H \rightarrow ZZ$ ZH	0.09	0.42	0.41	0.32	0.42	0.65
$H \rightarrow b\bar{b}$ WH	0.33	0.48	0.48	0.42	0.47	0.61
$H \rightarrow b\bar{b}$ ZH	0.10	0.23	0.22	0.18	0.23	0.34

Table A.6: Estimated relative uncertainties on the determination of the differential distributions in the associated Higgs production channels. These estimates correspond to the ‘optimistic’ scenario in which the systematic uncertainties are assumed to be the same for each bin and only the statistical uncertainty is rescaled according to the number of events in each bin.

we kept the systematic errors constant. In the ‘pessimistic’ scenario we rescaled the total (statistical plus systematic) uncertainty according to the number of events in each bin.

Process	[1.0 – 1.1]	[1.1 – 1.2]	[1.5 – 1.2]	[2.0 – 1.5]	[2.0 – 3.0]
$t\bar{t}H$	0.78	0.43	0.24	0.24	0.31
$H \rightarrow \gamma\gamma$	WH 0.41	0.4	0.3	0.4	0.6
	ZH 0.63	0.62	0.47	0.63	0.99
$t\bar{t}H$	1.04	0.56	0.3	0.3	0.4
$H \rightarrow ZZ$	WH 0.37	0.36	0.27	0.35	0.53
	ZH 0.46	0.45	0.35	0.47	0.72
$H \rightarrow b\bar{b}$	WH 0.86	0.84	0.62	0.82	1.26
	ZH 0.3	0.3	0.23	0.31	0.48

Table A.7: Estimated relative uncertainties on the determination of the differential distributions in the associated Higgs production channels. These estimates correspond to the ‘pessimistic’ scenario in which the total (statistical plus systematic) uncertainty is rescaled according to the number of events in each bin.

A.2 Trilinear dependence for e^+e^- colliders

C_1 (inclusive rates)	\sqrt{s} [GeV]						
	240	250	350	500	1000	1400	3000
$e^+e^- \rightarrow hZ$	0.017	0.015	0.0057	0.00099	-0.0012	-0.0011	-0.00054
$e^+e^- \rightarrow \nu\bar{\nu}h$ ★	0.0064	0.0064	0.0062	0.0061	0.0059	0.0058	0.0057
$e^+e^- \rightarrow e^+e^-h$ ★	0.0070	0.0070	0.0069	0.0067	0.0065	0.0065	0.0063
$e^+e^- \rightarrow t\bar{t}h$				0.086	0.017	0.0094	0.0037

Table A.8: Values of C_1 for the total cross-sections of Higgs production processes. ★ The numbers are for WW or ZZ fusion only.

In this appendix we collect the numerical values of the coefficients C_1 , defined in Eq.(4.2.2), which encode the corrections to single-Higgs processes due to a deformation of the Higgs trilinear coupling. In Table A.8 we report the C_1 coefficients for the total cross-section of the main single-Higgs production modes, namely Higgsstrahlung, vector-boson fusion and associated production with top quarks. Several values of the center-of-mass energy \sqrt{s} are reported in the table, corresponding to the benchmark runs of future lepton colliders considered in main text. The calculation has been performed with the help of the public tools FeynArts, FormCalc, LoopTools, and CUBA [305–307].

Notice that the values of C_1 for Higgsstrahlung, WW -boson fusion and ZZ -boson fusion are independent of the beam polarization if we restrict ourselves to diagrams up to one loop, as we did in our analysis. As for $e^+e^- \rightarrow t\bar{t}h$, the Higgs self-coupling gives rise to tiny beam polarization effects. Given the small impact of the latter production

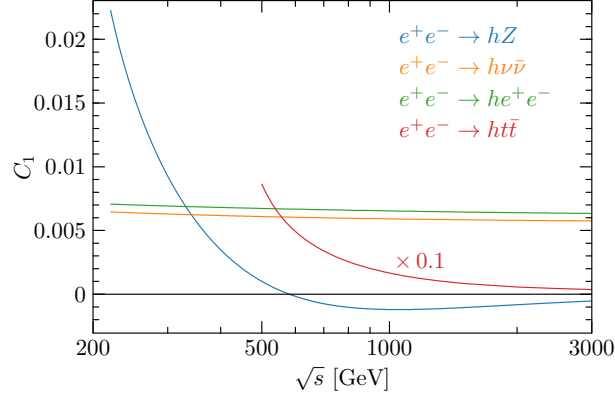


Figure A.1: Value of C_1 as a function of the center-of-mass energy \sqrt{s} for the $e^+e^- \rightarrow hZ$, $e^+e^- \rightarrow \nu\bar{\nu}h$, $e^+e^- \rightarrow he^+e^-$ and $e^+e^- \rightarrow ht\bar{t}$ single Higgs production processes. Notice that the result for Higgs production in association with a top-quark pair has been rescaled by a factor of 0.1.

mode in our analysis, we can safely neglect such effects. The dependence of the C_1 coefficients on the collider energy is also shown in Fig. A.1.

Besides the inclusive rates, we also checked the impact of a modified Higgs trilinear coupling on the angular asymmetries that can be built for the $e^+e^- \rightarrow hZ \rightarrow h\ell^+\ell^-$ case (see Refs. [146, 147]). We found that these effects are almost negligible and have no impact on our analysis.

Appendix B

Indirect constraints on the singlet model

In this Appendix we summarize the indirect constraints on the singlet model due to Higgs physics precision measurements and EWPO.

The singlet model gives a simple prediction for the signal strengths, since the branching ratios are not modified while the production cross sections are shifted globally by the Higgs mixing. Therefore, the Higgs production is reduced by a factor

$$\mu = 1 - \sin^2 \theta. \tag{B.0.1}$$

The ATLAS and CMS collaborations offered a combination of the LHC runs at 7 and 8 TeV in Ref. [35]. The global signal strength μ of the Higgs production rates, given by

$$\mu = 1.09_{-0.10}^{+0.11}, \tag{B.0.2}$$

is of particular importance since it can be directly applied to constrain the singlet model. The χ^2 analysis for the measured and expected signal is shown in the left panel of Fig. B.1. To assess the HL-LHC sensitivity, ATLAS estimates a 3.2% precision on a global coupling κ , and the precision can get down to 1.7% when the theory uncertainties are neglected [82]. In our case $\kappa = \sqrt{1 - \sin^2 \theta}$, and we translate those projections in the figure.

The EWPO from LEP also put constraints on the singlet extension of the SM. After integrating out the singlet field, one obtains the EFT operator

$$\mathcal{L} \supset \frac{c_H}{m_s^2} \mathcal{O}_H, \tag{B.0.3}$$

where the Wilson coefficient c_H can be matched to the original potential in Eq. (5.2.1) as $c_H = \lambda_{s\phi}^2 / (2\lambda_s)$, and the mass scale m_s is approximately the heavy scalar mass m_S in the small mixing angle limit.

The generated EFT operator \mathcal{O}_H induces the Higgs field redefinition that shifts the Higgs couplings by $\sim \sin^2 \theta$ and also induces other operators through RGE [134, 308]. In

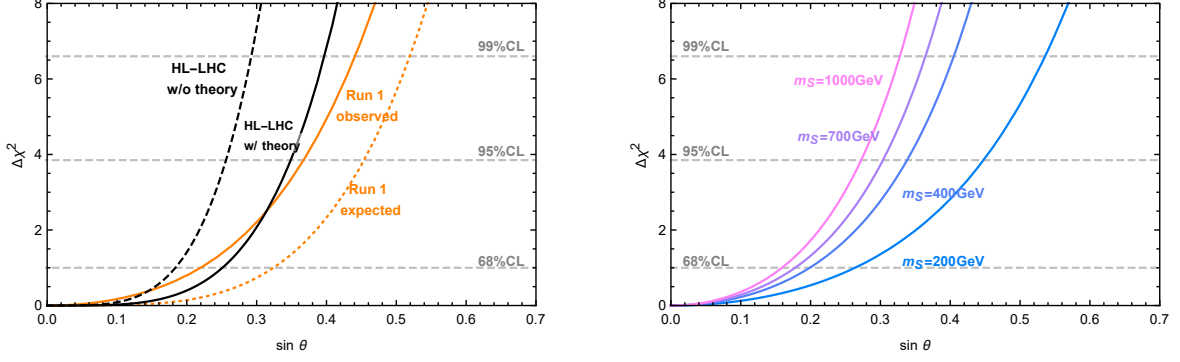


Figure B.1: $\Delta\chi^2$ as a function of the mixing angle $\sin\theta$ using different sets of data. **Left:** Using Higgs signal strengths, with the current LHC constraints and the projected ones at the HL-LHC. **Right:** Based on LEP constraints EWPO, for different values of the singlet mass.

particular, it generates the operator combinations $O_W + O_B$ and O_T , which shifts the S and T parameters

$$\Delta S = +\frac{1}{12\pi}c_H(m_S)\frac{v^2}{m_S^2}\log\left(\frac{m_S^2}{m_W^2}\right) \quad (\text{B.0.4})$$

$$\Delta T = -\frac{3}{16\pi c_W^2}c_H(m_S)\frac{v^2}{m_S^2}\log\left(\frac{m_S^2}{m_W^2}\right). \quad (\text{B.0.5})$$

Using the electroweak fit in Ref. [309, 310] one finds the constraints open

$$S = 0.06 \pm 0.09, \quad T = 0.10 \pm 0.07, \quad \rho = 0.91, \quad (\text{B.0.6})$$

where ρ is the correlation coefficient between the S and T parameters.

We show in the right panel of Fig. B.1 the $\Delta\chi^2$ on the mixing angle for different values of the singlet mass coming from the S and T constraints. We see that the constraints increase with the singlet mass, but a moderate mixing angle of $\sin\theta \sim 0.2$, is still allowed.

Appendix C

Summary of LEP-1 constraints on the light quark couplings

In this section we present the LEP-1 constraints obtained by profiling the χ^2 obtained from the bounds and correlation matrices derived in Ref. [69] from the LEP-1 data.

Minimal Flavour Violation

For the MFV case the vertex corrections have the following form:

$$[\delta g_{L,R}^{Zu,d}]_{ij} \simeq \left(A_{L,R}^{u,d} + B_{L,R}^{u,d} \frac{m_i}{m_3} \right) \delta_{ij}, \quad (\text{C.0.1})$$

where $i, j = 1, 2, 3$ stand for the family index. We are only interested on the constraints of the light quarks u, d , which are the only ones for which diboson production is sensitive. Using the results in Ref. [69] and after profiling over all other parameters related to the electron and neutrino couplings, we find

$$\begin{aligned} \begin{aligned} [\delta g_L^{Zu}]_{11} &= -0.002 \pm 0.003 \\ [\delta g_R^{Zu}]_{11} &= -0.003 \pm 0.005 \\ [\delta g_L^{Zd}]_{11} &= 0.002 \pm 0.005 \\ [\delta g_R^{Zd}]_{11} &= 0.016 \pm 0.027 \end{aligned} \quad , \quad \rho = \begin{pmatrix} 1 & 0.43 & 0.52 & 0.23 \\ & 1 & 0.19 & 0.36 \\ & & 1 & 0.90 \\ & & & 1 \end{pmatrix}, \end{aligned} \quad (\text{C.0.2})$$

In this case the vertex corrections are mostly sensitive to the A coefficient in Eq. (C.0.1), while the contribution from B is negligible since it is suppressed by $m_{u,d}/m_{t,b}$. Therefore, both LEP-1 and diboson production are only sensitive to the A coefficient when measuring the $Z\bar{q}q$ vertex corrections for u and d . Nonetheless, these bounds will also apply for the c and s quarks since in that case the B contribution is also negligible.

Flavour Universality

Under the assumption of Flavour Universality all the vertex corrections have the same value irrespective of their family index, i.e.

$$[\delta g_{L,R}^{Zu,d}]_{ij} = A_{L,R}^{u,d} \delta_{ij} \quad (\text{C.0.3})$$

in this case the bounds for the light quarks and heavy quarks coming from LEP-1 are the same. From [69] and after profiling over all other parameters the bounds from LEP-1 are given by,

$$\begin{aligned} \delta g_L^{Zu} &= -0.0017 \pm 0.002 \\ \delta g_R^{Zu} &= -0.0023 \pm 0.005 \\ \delta g_L^{Zd} &= 0.0028 \pm 0.001 \\ \delta g_R^{Zd} &= 0.019 \pm 0.008 \end{aligned}, \quad \rho = \begin{pmatrix} 1 & 0.83 & 0.04 & -0.11 \\ & 1 & -0.13 & -0.05 \\ & & 1 & 0.89 \\ & & & 1 \end{pmatrix}. \quad (\text{C.0.4})$$

In this case, diboson production will set bounds on all of $Z\bar{q}q$ from just measuring the vertices for u and d . Let us notice that for the up quarks, there is not a dramatic difference between the MFV and FU bounds coming from LEP-1, but for the down quarks the MFV assumption relaxes the bounds by about a factor four. This can be naively understood given that the b quark can be efficiently tagged and much better discriminated than the light quarks. On the other hand, for the case of MFV, the vertex correction to the $Z\bar{b}b$, i.e. $[\delta g_{L,R}^{Zd}]_{33}$ gives a good constrain to the parameters $A + B$ in Eq. (C.0.1), while $[\delta g_{L,R}^{Zd}]_{11}$ is only sensitive to A and has a much lower precision from the Z-pole observables.

Universal Theories

For the case of Universal theories the vertex corrections are related as follows ¹

$$\delta g_R^{Zu} = 2(\delta g_L^{Zu} + \delta g_L^{Zd}), \quad \delta g_R^{Zd} = -(\delta g_L^{Zu} + \delta g_L^{Zd}). \quad (\text{C.0.5})$$

We choose as the independent ones δg_L^{Zu} and δg_L^{Zd} . By using the χ^2 for FU theories, the constraints on the two independent parameters are

$$\begin{aligned} \delta g_L^{Zu} &= -0.00010 \pm 0.00019 \\ \delta g_L^{Zd} &= 0.00008 \pm 0.00018 \end{aligned}, \quad \rho = \begin{pmatrix} 1 & -0.93 \\ & 1 \end{pmatrix}. \quad (\text{C.0.6})$$

In this case, it seems that the current data from diboson searches may not be sensitive to Bosonic Theories, which we corroborate explicitly by performing a global fit, showing that with the current data we are an order of magnitude away from being sensitive to them. Nonetheless we may be sensitive to them at the HL-LHC as we show in Section 6.3.

¹This can be checked explicitly by for example writing the Higgs basis coefficients in terms of only bosonic operators in the SILH basis.

Appendix D

Summary of diboson constraints

All three aTGCs profiled

	Diboson	LEP (MFV)	LEP (FU)	Comb. MFV	Comb. FU
$[\delta g_L^{Zu}]_{11}$	-7.9 ± 10	-1.9 ± 3.1	-1.7 ± 2.1	-1.9 ± 2.8	-0.9 ± 2.0
$[\delta g_R^{Zu}]_{11}$	-40 ± 24	-2.6 ± 5	-2.3 ± 4.6	-1.3 ± 4.4	-0.9 ± 4.3
$[\delta g_L^{Zd}]_{11}$	-18 ± 7	2 ± 5.4	2.8 ± 1.5	-2 ± 2.5	0.8 ± 1.2
$[\delta g_R^{Zd}]_{11}$	20.3 ± 14.2	16 ± 27	20 ± 7.7	-1.8 ± 7.9	8.6 ± 5.6

Table D.1: Constraints ($\times 10^3$) on the vertex corrections in the case where the aTGC are non-negligible. In the first column, LHC diboson data. In the second and third, LEP with MFV and FU assumptions. Last two show the combination.

TGC without loop induced parameters ($\delta\kappa_\gamma = \lambda_\gamma = 0$)

	Diboson	LEP (MFV)	LEP (FU)	Comb MFV	Comb FU
$[\delta g_L^{Zu}]_{11}$	6.4 ± 6.4	-1.9 ± 3.1	-1.7 ± 2.1	-1.5 ± 2.7	-0.3 ± 1.8
$[\delta g_R^{Zu}]_{11}$	4.3 ± 6.4	-2.6 ± 5	-2.3 ± 4.6	-0.3 ± 3.9	0.6 ± 3.8
$[\delta g_L^{Zd}]_{11}$	-8.7 ± 5.2	2 ± 5.4	2.8 ± 1.5	-2 ± 2.5	0.6 ± 1.1
$[\delta g_R^{Zd}]_{11}$	-2.1 ± 8	16 ± 27	20 ± 7.7	-2.7 ± 7.7	7.7 ± 5.4

Table D.2: Constraints ($\times 10^3$) on the vertex corrections in the case where the loop induced aTGC are neglected, i.e. $\delta\kappa_\gamma = \lambda_\gamma = 0$. In the first column, LHC diboson data. In the second and third, LEP with MFV and FU assumptions. Last two show the combination.

No TGCs ($\delta g_{1z} = \delta \kappa_\gamma = \lambda_\gamma = 0$)

	Diboson	LEP (MFV)	LEP (FU)	Comb MFV	Comb FU
$[\delta g_L^{Zu}]_{11}$	0.6 ± 5.0	-1.9 ± 3.1	-1.7 ± 2.1	-0.7 ± 2.6	1.1 ± 1.6
$[\delta g_R^{Zu}]_{11}$	1.5 ± 6.1	-2.6 ± 5	-2.3 ± 4.6	1.5 ± 3.6	3.5 ± 3.4
$[\delta g_L^{Zd}]_{11}$	-5.3 ± 4.6	2 ± 5.4	2.8 ± 1.5	-2.8 ± 2.4	0.1 ± 1.1
$[\delta g_R^{Zd}]_{11}$	-0.71 ± 8	16 ± 27	20 ± 7.7	-6.2 ± 6.8	5.0 ± 5.4

Table D.3: Constraints ($\times 10^3$) on the vertex corrections in the case where the aTGC are neglected, i.e. $\delta g_{1z} = \delta \kappa_\gamma = \lambda_\gamma = 0$. In the first column, LHC diboson data. In the second and third, LEP with MFV and FU assumptions. Last two show the combination.

	$\delta g_{L,R}^{Zu,d} = 0$	$\delta g_{L,R}^{Zu,d} = \text{MFV}$	$\delta g_{L,R}^{Zu,d} = \text{FU}$
$\delta \kappa_\gamma$	12 ± 31	18 ± 35	24 ± 35
δg_{1z}	-7 ± 4	-7 ± 5	-9 ± 5
λ_γ	0 ± 6	0 ± 6	0 ± 6

Table D.4: Constraints ($\times 10^3$) on the anomalous triple gauge couplings. In the first column, the traditional analysis where the fermionic vertices are assumed to be SM-like. In the next two columns, where the fermion couplings are profiled using the LEP constraints for the MFV and FU assumptions, see Eqns. C.0.2 and C.0.4.

HL-LHC

	TGCs profiled	No Loop ($\delta \kappa_\gamma = \lambda_\gamma = 0$)	No TGCs	Exclusive fit
$[\delta g_L^{Zu}]_{11}$	0 ± 1.0	0 ± 0.9	± 0.8	± 0.2
$[\delta g_R^{Zu}]_{11}$	0 ± 2.0	0 ± 1.1	± 0.9	± 0.8
$[\delta g_L^{Zd}]_{11}$	0 ± 0.9	0 ± 0.8	± 0.7	± 0.2
$[\delta g_R^{Zd}]_{11}$	0 ± 1.7	0 ± 1.5	± 1.3	± 1.0

Table D.5: Constraints ($\times 10^3$) on the vertex corrections using the projections at HL-LHC of the $pp \rightarrow W^+W^- \rightarrow \ell\nu\ell\nu$ channel combined with the LEP-1 constraints for the MFV scenario. In the first column, we profile over the aTGCS as well as the other vertex corrections. In the second, we set to zero the *loop* parameters. In the third, we set to zero the aTGCs. In the last column we present an exclusive fit with only one parameter.

HL-LHC			
	$\delta g_{L,R}^{Zu,d} = 0$	$\delta g_{L,R}^{Zu,d} = \text{MFV}$	$\delta g_{L,R}^{Zu,d} = \text{FU}$
$\delta\kappa_\gamma$	± 4.0	± 5.1	± 4.9
δg_{1z}	± 0.8	± 1.2	± 1.1
λ_γ	± 1.3	± 1.5	± 1.3

Table D.6: Constraints ($\times 10^3$) on the aTGCs using the projections at HL-LHC of the $pp \rightarrow W^+W^- \rightarrow \ell\nu\ell\nu$ channel. In the first column, the traditional analysis where the fermionic vertices are assumed to be SM-like. In the next two columns, where the fermion couplings are profiled using the LEP constraints for the MFV and FU assumptions, see Eqns. C.0.2 and C.0.4.

	$\delta g_{L,R}^{Zu,d} = 0$	$\delta g_{L,R}^{Zu,d} = \text{Bosonic}$
δg_{1z}	± 0.4	± 0.7

Table D.7: Constraints ($\times 10^3$) on the δg_{1z} using the projections at HL-LHC of the $pp \rightarrow W^+W^- \rightarrow \ell\nu\ell\nu$ channel, and assuming that $\delta\kappa_\gamma = \lambda_\gamma = 0$. In the first column, the traditional analysis where the fermionic vertices are assumed to be SM-like. In the second column, the fermion couplings are profiled using the LEP constraints for Universal Theories, see Eqns. C.0.5 and C.0.6.

References

- [1] **ATLAS** Collaboration, G. Aad *et al.*, “Observation of a new particle in the search for the Standard Model Higgs boson with the ATLAS detector at the LHC,” *Phys. Lett.* **B716** (2012) 1–29, [arXiv:1207.7214 \[hep-ex\]](#).
- [2] **CMS** Collaboration, S. Chatrchyan *et al.*, “Observation of a new boson at a mass of 125 GeV with the CMS experiment at the LHC,” *Phys. Lett.* **B716** (2012) 30–61, [arXiv:1207.7235 \[hep-ex\]](#).
- [3] H. Georgi and S. L. Glashow, “Unity of All Elementary Particle Forces,” *Phys. Rev. Lett.* **32** (1974) 438–441.
- [4] L. Randall and C. Csaki, “The Doublet - triplet splitting problem and Higgses as pseudoGoldstone bosons,” in *Supersymmetry and unification of fundamental interactions. Proceedings, International Workshop, SUSY 95, Palaiseau, France, May 15-19, 1995*, pp. 99–109. 1995. [arXiv:hep-ph/9508208 \[hep-ph\]](#). [[235\(1995\)](#)].
- [5] E. Witten, “Deconstruction, $G(2)$ holonomy, and doublet triplet splitting,” in *Supersymmetry and unification of fundamental interactions. Proceedings, 10th International Conference, SUSY'02, Hamburg, Germany, June 17-23, 2002*, pp. 472–491. 2001. [arXiv:hep-ph/0201018 \[hep-ph\]](#).
http://www-library.desy.de/preparch/desy/proc/proc02-02/Proceedings/susy02/special/hertz_pr.ps.
- [6] S. Coleman and J. Mandula, “All possible symmetries of the s matrix,” *Phys. Rev.* **159** (Jul, 1967) 1251–1256.
<https://link.aps.org/doi/10.1103/PhysRev.159.1251>.
- [7] Yu. A. Golfand and E. P. Likhtman, “Extension of the Algebra of Poincare Group Generators and Violation of p Invariance,” *JETP Lett.* **13** (1971) 323–326. [*Pisma Zh. Eksp. Teor. Fiz.*13,452(1971)].
- [8] J. Wess and B. Zumino, “Supergauge Transformations in Four-Dimensions,” *Nucl. Phys.* **B70** (1974) 39–50. [[24\(1974\)](#)].
- [9] D. V. Volkov and V. P. Akulov, “Is the Neutrino a Goldstone Particle?,” *Phys. Lett.* **46B** (1973) 109–110.

- [10] E. Witten, “Dynamical Breaking of Supersymmetry,” *Nucl. Phys.* **B188** (1981) 513.
- [11] S. Dimopoulos and D. W. Sutter, “The Supersymmetric flavor problem,” *Nucl. Phys.* **B452** (1995) 496–512, [arXiv:hep-ph/9504415](https://arxiv.org/abs/hep-ph/9504415) [hep-ph].
- [12] D. J. H. Chung, L. L. Everett, G. L. Kane, S. F. King, J. D. Lykken, and L.-T. Wang, “The Soft supersymmetry breaking Lagrangian: Theory and applications,” *Phys. Rept.* **407** (2005) 1–203, [arXiv:hep-ph/0312378](https://arxiv.org/abs/hep-ph/0312378) [hep-ph].
- [13] G. F. Giudice and A. Masiero, “A Natural Solution to the mu Problem in Supergravity Theories,” *Phys. Lett.* **B206** (1988) 480–484.
- [14] N. Sakai and T. Yanagida, “Proton Decay in a Class of Supersymmetric Grand Unified Models,” *Nucl. Phys.* **B197** (1982) 533.
- [15] S. Weinberg, “Supersymmetry at Ordinary Energies. I. Masses and Conservation Laws,” *Phys. Rev.* **D26** (1982) 287.
- [16] C. A. et. al., “Events with large missing transverse energy at the cern collider: Iii. mass limits on supersymmetric particles,” *Physics Letters B* **198** no. 2, (1987) 261 – 270.
<http://www.sciencedirect.com/science/article/pii/0370269387915097>.
- [17] P. A. et. al., “Search for scalar leptons and scalar quarks at lep,” *Physics Letters B* **580** no. 1, (2004) 37 – 49. <http://www.sciencedirect.com/science/article/pii/S0370269303015545>.
- [18] R. Barbieri and G. F. Giudice, “Upper Bounds on Supersymmetric Particle Masses,” *Nucl. Phys.* **B306** (1988) 63–76.
- [19] R. Barbieri and A. Strumia, “The ’LEP paradox’,” in *4th Rencontres du Vietnam: Physics at Extreme Energies (Particle Physics and Astrophysics) Hanoi, Vietnam, July 19-25, 2000*. 2000. [arXiv:hep-ph/0007265](https://arxiv.org/abs/hep-ph/0007265) [hep-ph].
- [20] M. E. Peskin and T. Takeuchi, “Estimation of oblique electroweak corrections,” *Phys. Rev.* **D46** (1992) 381–409.
- [21] R. Barbieri, A. Pomarol, R. Rattazzi, and A. Strumia, “Electroweak symmetry breaking after LEP-1 and LEP-2,” *Nucl. Phys.* **B703** (2004) 127–146, [arXiv:hep-ph/0405040](https://arxiv.org/abs/hep-ph/0405040) [hep-ph].
- [22] S. Weinberg, “Implications of dynamical symmetry breaking,” *Phys. Rev. D* **13** (Feb, 1976) 974–996. <https://link.aps.org/doi/10.1103/PhysRevD.13.974>.
- [23] L. Susskind, “Dynamics of spontaneous symmetry breaking in the weinberg-salam theory,” *Phys. Rev. D* **20** (Nov, 1979) 2619–2625.
<https://link.aps.org/doi/10.1103/PhysRevD.20.2619>.

- [24] D. B. Kaplan and H. Georgi, “SU(2) x U(1) Breaking by Vacuum Misalignment,” *Phys. Lett.* **136B** (1984) 183–186.
- [25] R. Contino, Y. Nomura, and A. Pomarol, “Higgs as a holographic pseudoGoldstone boson,” *Nucl. Phys.* **B671** (2003) 148–174, [arXiv:hep-ph/0306259](#) [hep-ph].
- [26] S. Weinberg, “The Cosmological Constant Problem,” *Rev. Mod. Phys.* **61** (1989) 1–23. [,569(1988)].
- [27] **Supernova Search Team** Collaboration, A. G. Riess *et al.*, “Observational evidence from supernovae for an accelerating universe and a cosmological constant,” *Astron. J.* **116** (1998) 1009–1038, [arXiv:astro-ph/9805201](#) [astro-ph].
- [28] **Supernova Cosmology Project** Collaboration, S. Perlmutter *et al.*, “Measurements of Omega and Lambda from 42 high redshift supernovae,” *Astrophys. J.* **517** (1999) 565–586, [arXiv:astro-ph/9812133](#) [astro-ph].
- [29] H. Martel, P. R. Shapiro, and S. Weinberg, “Likely values of the cosmological constant,” *Astrophys. J.* **492** (1998) 29, [arXiv:astro-ph/9701099](#) [astro-ph].
- [30] R. Bousso and J. Polchinski, “Quantization of four form fluxes and dynamical neutralization of the cosmological constant,” *JHEP* **06** (2000) 006, [arXiv:hep-th/0004134](#) [hep-th].
- [31] T. Damour and J. F. Donoghue, “Constraints on the variability of quark masses from nuclear binding,” *Phys. Rev.* **D78** (2008) 014014, [arXiv:0712.2968](#) [hep-ph].
- [32] L. J. Hall, D. Pinner, and J. T. Ruderman, “The Weak Scale from BBN,” *JHEP* **12** (2014) 134, [arXiv:1409.0551](#) [hep-ph].
- [33] R. Harnik, G. D. Kribs, and G. Perez, “A Universe without weak interactions,” *Phys. Rev.* **D74** (2006) 035006, [arXiv:hep-ph/0604027](#) [hep-ph].
- [34] Y. Cui, “Natural Baryogenesis from Unnatural Supersymmetry,” *JHEP* **12** (2013) 067, [arXiv:1309.2952](#) [hep-ph].
- [35] **ATLAS, CMS** Collaboration, G. Aad *et al.*, “Measurements of the Higgs boson production and decay rates and constraints on its couplings from a combined ATLAS and CMS analysis of the LHC pp collision data at $\sqrt{s} = 7$ and 8 TeV,” *JHEP* **08** (2016) 045, [arXiv:1606.02266](#) [hep-ex].
- [36] S. Di Vita, C. Grojean, G. Panico, M. Riembau, and T. Vantalón, “A global view on the Higgs self-coupling,” *JHEP* **09** (2017) 069, [arXiv:1704.01953](#) [hep-ph].

- [37] S. Di Vita, G. Durieux, C. Grojean, J. Gu, Z. Liu, G. Panico, M. Riembau, and T. Vantalon, “A global view on the Higgs self-coupling at lepton colliders,” *JHEP* **02** (2018) 178, [arXiv:1711.03978 \[hep-ph\]](#).
- [38] M. Carena, Z. Liu, and M. Riembau, “Probing Electroweak Phase Transition via Enhanced Di-Higgs Production,” [arXiv:1801.00794 \[hep-ph\]](#).
- [39] G. Panico, M. Riembau, and T. Vantalon, “Probing light top partners with CP violation,” [arXiv:1712.06337 \[hep-ph\]](#).
- [40] N. Arkani-Hamed, T. Han, M. Mangano, and L.-T. Wang, “Physics opportunities of a 100 TeV proton-proton collider,” *Phys. Rept.* **652** (2016) 1–49, [arXiv:1511.06495 \[hep-ph\]](#).
- [41] T. Golling *et al.*, “Physics at a 100 TeV pp collider: beyond the Standard Model phenomena,” *CERN Yellow Report no. 3*, (2017) 441–634, [arXiv:1606.00947 \[hep-ph\]](#).
- [42] R. Contino *et al.*, “Physics at a 100 TeV pp collider: Higgs and EW symmetry breaking studies,” *CERN Yellow Report no. 3*, (2017) 255–440, [arXiv:1606.09408 \[hep-ph\]](#).
- [43] H. Abramowicz *et al.*, “Higgs physics at the CLIC electron-positron linear collider,” *Eur. Phys. J.* **C77** no. 7, (2017) 475, [arXiv:1608.07538 \[hep-ex\]](#).
- [44] “HL/HE LHC Meeting. 4-6 April 2018, Fermilab.” <https://indico.fnal.gov/event/16151/>.
- [45] M. Benedikt and F. Zimmermann, “Proton Colliders at the Energy Frontier,” *Nucl. Instrum. Meth.* (2018), [arXiv:1803.09723 \[physics.acc-ph\]](#).
- [46] M. Ruan, “Status & Updates from CEPC Simulation -Detector optimization.. Presentation at IAS (14th Jan. 2017).”.
- [47] A. Blondel, “Summary FCC-ee experiments. Presentation at the FCC Week (Berlin, 2 Jun 2017).”.
- [48] G. Durieux, C. Grojean, J. Gu, and K. Wang, “The leptonic future of the Higgs,” *JHEP* **09** (2017) 014, [arXiv:1704.02333 \[hep-ph\]](#).
- [49] J. F. Kamenik, S. Monteil, A. Semkiv, and L. V. Silva, “Lepton polarization asymmetries in rare semi-tauonic $b \rightarrow s$ exclusive decays at FCC-ee,” *Eur. Phys. J.* **C77** no. 10, (2017) 701, [arXiv:1705.11106 \[hep-ph\]](#).
- [50] V. Shiltsev, “A Phenomenological Cost Model for High Energy Particle Accelerators,” *JINST* **9** (2014) T07002, [arXiv:1404.4097 \[physics.acc-ph\]](#).

- [51] K. Fujii *et al.*, “The role of positron polarization for the initial 250 GeV stage of the International Linear Collider,” [arXiv:1801.02840 \[hep-ph\]](#).
- [52] **Linear Collide** Collaboration, L. Evans and S. Michizono, “The International Linear Collider Machine Staging Report 2017,” [arXiv:1711.00568 \[physics.acc-ph\]](#).
- [53] K. Fujii *et al.*, “Physics Case for the International Linear Collider,” [arXiv:1506.05992 \[hep-ex\]](#).
- [54] T. Barklow, J. Brau, K. Fujii, J. Gao, J. List, N. Walker, and K. Yokoya, “ILC Operating Scenarios,” [arXiv:1506.07830 \[hep-ex\]](#).
- [55] M. Aicheler, P. Burrows, M. Draper, T. Garvey, P. Lebrun, K. Peach, N. Phinney, H. Schmickler, D. Schulte, and N. Toge, “A Multi-TeV Linear Collider Based on CLIC Technology: CLIC Conceptual Design Report,” Tech. Rep. CERN-2012-007. SLAC-R-985. KEK-Report-2012-1. PSI-12-01. JAI-2012-001, Geneva, 2012. <http://cds.cern.ch/record/1500095>.
- [56] “ALEGRO Workshop. [Oxford, 26-29 March 2018.](#)”.
- [57] E. Houssecker and A. Chao *Phys. Perspect.* **13**: 146 (2011) . <https://doi.org/10.1007/s00016-010-0049-y>.
- [58] **Particle Data Group** Collaboration, C. Patrignani *et al.*, “Review of Particle Physics,” *Chin. Phys.* **C40** no. 10, (2016) 100001.
- [59] **LHC Higgs Cross Section Working Group** Collaboration, D. de Florian *et al.*, “Handbook of LHC Higgs Cross Sections: 4. Deciphering the Nature of the Higgs Sector,” [arXiv:1610.07922 \[hep-ph\]](#).
- [60] M. McCullough, “An Indirect Model-Dependent Probe of the Higgs Self-Coupling,” *Phys. Rev.* **D90** no. 1, (2014) 015001, [arXiv:1312.3322 \[hep-ph\]](#). [Erratum: *Phys. Rev.* **D92**, no. 3, 039903 (2015)].
- [61] M. Gorbahn and U. Haisch, “Indirect probes of the trilinear Higgs coupling: $gg \rightarrow h$ and $h \rightarrow \gamma\gamma$,” *JHEP* **10** (2016) 094, [arXiv:1607.03773 \[hep-ph\]](#).
- [62] G. Degrandi, P. P. Giardino, F. Maltoni, and D. Pagani, “Probing the Higgs self coupling via single Higgs production at the LHC,” *JHEP* **12** (2016) 080, [arXiv:1607.04251 \[hep-ph\]](#).
- [63] W. Bizon, M. Gorbahn, U. Haisch, and G. Zanderighi, “Constraints on the trilinear Higgs coupling from vector boson fusion and associated Higgs production at the LHC,” *JHEP* **07** (2017) 083, [arXiv:1610.05771 \[hep-ph\]](#).

- [64] G. Degrandi, M. Fedele, and P. P. Giardino, “Constraints on the trilinear Higgs self coupling from precision observables,” *JHEP* **04** (2017) 155, [arXiv:1702.01737 \[hep-ph\]](#).
- [65] G. D. Kribs, A. Maier, H. Rzehak, M. Spannowsky, and P. Waite, “Electroweak oblique parameters as a probe of the trilinear Higgs boson self-interaction,” *Phys. Rev.* **D95** no. 9, (2017) 093004, [arXiv:1702.07678 \[hep-ph\]](#).
- [66] A. Falkowski, “Effective field theory approach to LHC Higgs data,” *Pramana* **87** no. 3, (2016) 39, [arXiv:1505.00046 \[hep-ph\]](#).
- [67] A. Falkowski and A. Falkowski, “Higgs Basis: Proposal for an EFT basis choice for LHC HXSWG,”. <https://cds.cern.ch/record/2001958>.
- [68] A. Pomarol and F. Riva, “Towards the Ultimate SM Fit to Close in on Higgs Physics,” *JHEP* **01** (2014) 151, [arXiv:1308.2803 \[hep-ph\]](#).
- [69] A. Efrati, A. Falkowski, and Y. Soreq, “Electroweak constraints on flavorful effective theories,” *JHEP* **07** (2015) 018, [arXiv:1503.07872 \[hep-ph\]](#).
- [70] O. Bessidskaia Bylund, F. Maltoni, I. Tsirikos, E. Vryonidou, and C. Zhang, “Probing top quark neutral couplings in the Standard Model Effective Field Theory at NLO in QCD,” *JHEP* **05** (2016) 052, [arXiv:1601.08193 \[hep-ph\]](#).
- [71] D. Buarque Franzosi and C. Zhang, “Probing the top-quark chromomagnetic dipole moment at next-to-leading order in QCD,” *Phys. Rev.* **D91** no. 11, (2015) 114010, [arXiv:1503.08841 \[hep-ph\]](#).
- [72] F. Maltoni, E. Vryonidou, and C. Zhang, “Higgs production in association with a top-antitop pair in the Standard Model Effective Field Theory at NLO in QCD,” *JHEP* **10** (2016) 123, [arXiv:1607.05330 \[hep-ph\]](#).
- [73] J. Elias-Miro, J. R. Espinosa, E. Masso, and A. Pomarol, “Higgs windows to new physics through d=6 operators: constraints and one-loop anomalous dimensions,” *JHEP* **11** (2013) 066, [arXiv:1308.1879 \[hep-ph\]](#).
- [74] **ATLAS** Collaboration, T. A. collaboration, “Search for new phenomena in $t\bar{t}$ final states with additional heavy-flavour jets in pp collisions at $\sqrt{s} = 13$ TeV with the ATLAS detector,” 2016.
- [75] R. Contino, A. Falkowski, F. Goertz, C. Grojean, and F. Riva, “On the Validity of the Effective Field Theory Approach to SM Precision Tests,” *JHEP* **07** (2016) 144, [arXiv:1604.06444 \[hep-ph\]](#).

- [76] A. Azatov, R. Contino, G. Panico, and M. Son, “Effective field theory analysis of double Higgs boson production via gluon fusion,” *Phys. Rev.* **D92** no. 3, (2015) 035001, [arXiv:1502.00539 \[hep-ph\]](#).
- [77] G. F. Giudice, C. Grojean, A. Pomarol, and R. Rattazzi, “The Strongly-Interacting Light Higgs,” *JHEP* **06** (2007) 045, [arXiv:hep-ph/0703164 \[hep-ph\]](#).
- [78] G. Panico and A. Wulzer, “The Composite Nambu-Goldstone Higgs,” *Lect. Notes Phys.* **913** (2016) pp.1-316, [arXiv:1506.01961 \[hep-ph\]](#).
- [79] J. de Blas, M. Chala, M. Perez-Victoria, and J. Santiago, “Observable Effects of General New Scalar Particles,” *JHEP* **04** (2015) 078, [arXiv:1412.8480 \[hep-ph\]](#).
- [80] **CMS Collaboration**, “Projected Performance of an Upgraded CMS Detector at the LHC and HL-LHC: Contribution to the Snowmass Process,” in *Proceedings, 2013 Community Summer Study on the Future of U.S. Particle Physics: Snowmass on the Mississippi (CSS2013): Minneapolis, MN, USA, July 29-August 6, 2013*. 2013. [arXiv:1307.7135 \[hep-ex\]](#).
<https://inspirehep.net/record/1244669/files/arXiv:1307.7135.pdf>.
- [81] M. E. Peskin, “Estimation of LHC and ILC Capabilities for Precision Higgs Boson Coupling Measurements,” in *Proceedings, 2013 Community Summer Study on the Future of U.S. Particle Physics: Snowmass on the Mississippi (CSS2013): Minneapolis, MN, USA, July 29-August 6, 2013*. 2013. [arXiv:1312.4974 \[hep-ph\]](#).
<http://www.slac.stanford.edu/econf/C1307292/docs/submittedArxivFiles/1312.4974.pdf>.
- [82] “Projections for measurements of Higgs boson signal strengths and coupling parameters with the ATLAS detector at a HL-LHC,” Tech. Rep. ATL-PHYS-PUB-2014-016, CERN, Geneva, Oct, 2014.
<http://cds.cern.ch/record/1956710>.
- [83] C. Anastasiou, C. Duhr, F. Dulat, E. Furlan, T. Gehrmann, F. Herzog, A. Lazopoulos, and B. Mistlberger, “High precision determination of the gluon fusion Higgs boson cross-section at the LHC,” *JHEP* **05** (2016) 058, [arXiv:1602.00695 \[hep-ph\]](#).
- [84] “Prospective results for vector-boson fusion-mediated Higgs-boson searches in the four lepton final state at the High Luminosity Large Hadron Collider,” Tech. Rep. ATL-PHYS-PUB-2016-008, CERN, Geneva, Apr, 2016.
<http://cds.cern.ch/record/2145377>.
- [85] **ATLAS Collaboration** Collaboration, “Measurement prospects for VBF $H \rightarrow WW^{(*)} \rightarrow e\nu\mu\nu$ production with 3 ab^{-1} of HL-LHC pp -collisions,” Tech.

- Rep. ATL-PHYS-PUB-2016-018, CERN, Geneva, Aug, 2016.
<https://cds.cern.ch/record/2209092>.
- [86] “Projections for measurements of Higgs boson cross sections, branching ratios and coupling parameters with the ATLAS detector at a HL-LHC,” Tech. Rep. ATL-PHYS-PUB-2013-014, CERN, Geneva, Oct, 2013.
<http://cds.cern.ch/record/1611186>.
- [87] C. Grojean, E. Salvioni, M. Schlaffer, and A. Weiler, “Very boosted Higgs in gluon fusion,” *JHEP* **05** (2014) 022, [arXiv:1312.3317](https://arxiv.org/abs/1312.3317) [hep-ph].
- [88] A. Azatov, C. Grojean, A. Paul, and E. Salvioni, “Taming the off-shell Higgs boson,” *Zh. Eksp. Teor. Fiz.* **147** (2015) 410–425, [arXiv:1406.6338](https://arxiv.org/abs/1406.6338) [hep-ph]. [*J. Exp. Theor. Phys.*120,354(2015)].
- [89] A. Azatov, C. Grojean, A. Paul, and E. Salvioni, “Resolving gluon fusion loops at current and future hadron colliders,” *JHEP* **09** (2016) 123, [arXiv:1608.00977](https://arxiv.org/abs/1608.00977) [hep-ph].
- [90] A. Butter, O. J. P. Éboli, J. Gonzalez-Fraile, M. C. Gonzalez-Garcia, T. Plehn, and M. Rauch, “The Gauge-Higgs Legacy of the LHC Run I,” *JHEP* **07** (2016) 152, [arXiv:1604.03105](https://arxiv.org/abs/1604.03105) [hep-ph].
- [91] A. Falkowski, M. Gonzalez-Alonso, A. Greljo, D. Marzocca, and M. Son, “Anomalous Triple Gauge Couplings in the Effective Field Theory Approach at the LHC,” *JHEP* **02** (2017) 115, [arXiv:1609.06312](https://arxiv.org/abs/1609.06312) [hep-ph].
- [92] “Update of the prospects for the $H \rightarrow Z\gamma$ search at the High-Luminosity LHC,” Tech. Rep. ATL-PHYS-PUB-2014-006, CERN, Geneva, May, 2014.
<http://cds.cern.ch/record/1703276>.
- [93] N. Kauer and G. Passarino, “Inadequacy of zero-width approximation for a light Higgs boson signal,” *JHEP* **08** (2012) 116, [arXiv:1206.4803](https://arxiv.org/abs/1206.4803) [hep-ph].
- [94] F. Caola and K. Melnikov, “Constraining the Higgs boson width with ZZ production at the LHC,” *Phys. Rev.* **D88** (2013) 054024, [arXiv:1307.4935](https://arxiv.org/abs/1307.4935) [hep-ph].
- [95] J. M. Campbell, R. K. Ellis, and C. Williams, “Bounding the Higgs width at the LHC using full analytic results for $gg \rightarrow e^-e^+\mu^-\mu^+$,” *JHEP* **04** (2014) 060, [arXiv:1311.3589](https://arxiv.org/abs/1311.3589) [hep-ph].
- [96] **CMS** Collaboration, V. Khachatryan *et al.*, “Constraints on the Higgs boson width from off-shell production and decay to Z-boson pairs,” *Phys. Lett.* **B736** (2014) 64–85, [arXiv:1405.3455](https://arxiv.org/abs/1405.3455) [hep-ex].

- [97] **ATLAS** Collaboration, G. Aad *et al.*, “Constraints on the off-shell Higgs boson signal strength in the high-mass ZZ and WW final states with the ATLAS detector,” *Eur. Phys. J.* **C75** no. 7, (2015) 335, [arXiv:1503.01060 \[hep-ex\]](#).
- [98] C. Englert and M. Spannowsky, “Limitations and Opportunities of Off-Shell Coupling Measurements,” *Phys. Rev.* **D90** (2014) 053003, [arXiv:1405.0285 \[hep-ph\]](#).
- [99] G. Cacciapaglia, A. Deandrea, G. Drieu La Rochelle, and J.-B. Flament, “Higgs couplings: disentangling New Physics with off-shell measurements,” *Phys. Rev. Lett.* **113** no. 20, (2014) 201802, [arXiv:1406.1757 \[hep-ph\]](#).
- [100] “Off-shell Higgs signal strength measurement using high-mass $H \rightarrow ZZ \rightarrow 4l$ events at High Luminosity LHC,” Tech. Rep. ATL-PHYS-PUB-2015-024, CERN, Geneva, Jul, 2015. <http://cds.cern.ch/record/2037715>.
- [101] S. Biswas, E. Gabrielli, and B. Mele, “Single top and Higgs associated production as a probe of the Htt coupling sign at the LHC,” *JHEP* **01** (2013) 088, [arXiv:1211.0499 \[hep-ph\]](#).
- [102] M. Farina, C. Grojean, F. Maltoni, E. Salvioni, and A. Thamm, “Lifting degeneracies in Higgs couplings using single top production in association with a Higgs boson,” *JHEP* **05** (2013) 022, [arXiv:1211.3736 \[hep-ph\]](#).
- [103] F. Demartin, F. Maltoni, K. Mawatari, and M. Zaro, “Higgs production in association with a single top quark at the LHC,” *Eur. Phys. J.* **C75** no. 6, (2015) 267, [arXiv:1504.00611 \[hep-ph\]](#).
- [104] F. Bishara, U. Haisch, P. F. Monni, and E. Re, “Constraining Light-Quark Yukawa Couplings from Higgs Distributions,” *Phys. Rev. Lett.* **118** no. 12, (2017) 121801, [arXiv:1606.09253 \[hep-ph\]](#).
- [105] G. Bonner and H. E. Logan, “Constraining the Higgs couplings to up and down quarks using production kinematics at the CERN Large Hadron Collider,” [arXiv:1608.04376 \[hep-ph\]](#).
- [106] H. Khanpour, S. Khatibi, and M. Mohammadi Najafabadi, “Probing Higgs boson couplings in $H+\gamma$ production at the LHC,” *Phys. Lett.* **B773** (2017) 462–469, [arXiv:1702.05753 \[hep-ph\]](#).
- [107] M. Farina, C. Grojean, and E. Salvioni, “(Dys)Zphilia or a custodial breaking Higgs at the LHC,” *JHEP* **07** (2012) 012, [arXiv:1205.0011 \[hep-ph\]](#).
- [108] Q.-H. Cao, Y. Liu, and B. Yan, “Measuring trilinear Higgs coupling in WHH and ZHH productions at the high-luminosity LHC,” *Phys. Rev.* **D95** no. 7, (2017) 073006, [arXiv:1511.03311 \[hep-ph\]](#).

- [109] V. D. Barger, T. Han, and R. J. N. Phillips, “Double Higgs Boson Bremsstrahlung From W and Z Bosons at Supercolliders,” *Phys. Rev.* **D38** (1988) 2766.
- [110] M. Moretti, S. Moretti, F. Piccinini, R. Pittau, and A. D. Polosa, “Higgs boson self-couplings at the LHC as a probe of extended Higgs sectors,” *JHEP* **02** (2005) 024, [arXiv:hep-ph/0410334](#) [hep-ph].
- [111] J. Baglio, A. Djouadi, R. Gröber, M. M. Mühlleitner, J. Quevillon, and M. Spira, “The measurement of the Higgs self-coupling at the LHC: theoretical status,” *JHEP* **04** (2013) 151, [arXiv:1212.5581](#) [hep-ph].
- [112] R. Contino, C. Grojean, M. Moretti, F. Piccinini, and R. Rattazzi, “Strong Double Higgs Production at the LHC,” *JHEP* **05** (2010) 089, [arXiv:1002.1011](#) [hep-ph].
- [113] M. J. Dolan, C. Englert, N. Greiner, and M. Spannowsky, “Further on up the road: $hhjj$ production at the LHC,” *Phys. Rev. Lett.* **112** (2014) 101802, [arXiv:1310.1084](#) [hep-ph].
- [114] M. J. Dolan, C. Englert, N. Greiner, K. Nordstrom, and M. Spannowsky, “ $hhjj$ production at the LHC,” *Eur. Phys. J.* **C75** no. 8, (2015) 387, [arXiv:1506.08008](#) [hep-ph].
- [115] F. Bishara, R. Contino, and J. Rojo, “Higgs pair production in vector-boson fusion at the LHC and beyond,” *Eur. Phys. J.* **C77** no. 7, (2017) 481, [arXiv:1611.03860](#) [hep-ph].
- [116] U. Baur, T. Plehn, and D. L. Rainwater, “Probing the Higgs selfcoupling at hadron colliders using rare decays,” *Phys. Rev.* **D69** (2004) 053004, [arXiv:hep-ph/0310056](#) [hep-ph].
- [117] R. Grober and M. Muhlleitner, “Composite Higgs Boson Pair Production at the LHC,” *JHEP* **06** (2011) 020, [arXiv:1012.1562](#) [hep-ph].
- [118] R. Contino, M. Ghezzi, M. Moretti, G. Panico, F. Piccinini, and A. Wulzer, “Anomalous Couplings in Double Higgs Production,” *JHEP* **08** (2012) 154, [arXiv:1205.5444](#) [hep-ph].
- [119] V. Barger, L. L. Everett, C. B. Jackson, and G. Shaughnessy, “Higgs-Pair Production and Measurement of the Triscalar Coupling at LHC(8,14),” *Phys. Lett.* **B728** (2014) 433–436, [arXiv:1311.2931](#) [hep-ph].
- [120] H.-J. He, J. Ren, and W. Yao, “Probing new physics of cubic Higgs boson interaction via Higgs pair production at hadron colliders,” *Phys. Rev.* **D93** no. 1, (2016) 015003, [arXiv:1506.03302](#) [hep-ph].

- [121] “Prospects for measuring Higgs pair production in the channel $H(\rightarrow \gamma\gamma)H(\rightarrow b\bar{b})$ using the ATLAS detector at the HL-LHC,” Tech. Rep. ATL-PHYS-PUB-2014-019, CERN, Geneva, Oct, 2014. <http://cds.cern.ch/record/1956733>.
- [122] **ATLAS Collaboration** Collaboration, “Study of the double Higgs production channel $H(\rightarrow b\bar{b})H(\rightarrow \gamma\gamma)$ with the ATLAS experiment at the HL-LHC,” Tech. Rep. ATL-PHYS-PUB-2017-001, CERN, Geneva, Jan, 2017. <https://cds.cern.ch/record/2243387>.
- [123] U. Baur, T. Plehn, and D. L. Rainwater, “Examining the Higgs boson potential at lepton and hadron colliders: A Comparative analysis,” *Phys. Rev.* **D68** (2003) 033001, [arXiv:hep-ph/0304015](https://arxiv.org/abs/hep-ph/0304015) [hep-ph].
- [124] M. J. Dolan, C. Englert, and M. Spannowsky, “Higgs self-coupling measurements at the LHC,” *JHEP* **10** (2012) 112, [arXiv:1206.5001](https://arxiv.org/abs/1206.5001) [hep-ph].
- [125] D. E. Ferreira de Lima, A. Papaefstathiou, and M. Spannowsky, “Standard model Higgs boson pair production in the $(b\bar{b})(b\bar{b})$ final state,” *JHEP* **08** (2014) 030, [arXiv:1404.7139](https://arxiv.org/abs/1404.7139) [hep-ph].
- [126] **ATLAS Collaboration** Collaboration, “Projected sensitivity to non-resonant Higgs boson pair production in the $b\bar{b}b\bar{b}$ final state using proton–proton collisions at HL-LHC with the ATLAS detector,” Tech. Rep. ATL-PHYS-PUB-2016-024, CERN, Geneva, Oct, 2016. <https://cds.cern.ch/record/2221658>.
- [127] A. Papaefstathiou, L. L. Yang, and J. Zurita, “Higgs boson pair production at the LHC in the $b\bar{b}W^+W^-$ channel,” *Phys. Rev.* **D87** no. 1, (2013) 011301, [arXiv:1209.1489](https://arxiv.org/abs/1209.1489) [hep-ph].
- [128] A. J. Barr, M. J. Dolan, C. Englert, and M. Spannowsky, “Di-Higgs final states augMT2ed – selecting hh events at the high luminosity LHC,” *Phys. Lett.* **B728** (2014) 308–313, [arXiv:1309.6318](https://arxiv.org/abs/1309.6318) [hep-ph].
- [129] F. Goertz, A. Papaefstathiou, L. L. Yang, and J. Zurita, “Higgs boson pair production in the D=6 extension of the SM,” *JHEP* **04** (2015) 167, [arXiv:1410.3471](https://arxiv.org/abs/1410.3471) [hep-ph].
- [130] Q.-H. Cao, B. Yan, D.-M. Zhang, and H. Zhang, “Resolving the Degeneracy in Single Higgs Production with Higgs Pair Production,” *Phys. Lett.* **B752** (2016) 285–290, [arXiv:1508.06512](https://arxiv.org/abs/1508.06512) [hep-ph].
- [131] Q.-H. Cao, G. Li, B. Yan, D.-M. Zhang, and H. Zhang, “Double Higgs production at the 14 TeV LHC and a 100 TeV pp collider,” *Phys. Rev.* **D96** no. 9, (2017) 095031, [arXiv:1611.09336](https://arxiv.org/abs/1611.09336) [hep-ph].

- [132] S. Boselli, C. M. Carloni Calame, G. Montagna, O. Nicrosini, F. Piccinini, and A. Shivaji, “Higgs decay into four charged leptons in the presence of dimension-six operators,” *JHEP* **01** (2018) 096, [arXiv:1703.06667 \[hep-ph\]](#).
- [133] N. Craig, M. Farina, M. McCullough, and M. Perelstein, “Precision Higgsstrahlung as a Probe of New Physics,” *JHEP* **03** (2015) 146, [arXiv:1411.0676 \[hep-ph\]](#).
- [134] B. Henning, X. Lu, and H. Murayama, “What do precision Higgs measurements buy us?,” [arXiv:1404.1058 \[hep-ph\]](#).
- [135] J. Ellis and T. You, “Sensitivities of Prospective Future e^+e^- Colliders to Decoupled New Physics,” *JHEP* **03** (2016) 089, [arXiv:1510.04561 \[hep-ph\]](#).
- [136] S.-F. Ge, H.-J. He, and R.-Q. Xiao, “Probing new physics scales from Higgs and electroweak observables at e^+e^- Higgs factory,” *JHEP* **10** (2016) 007, [arXiv:1603.03385 \[hep-ph\]](#).
- [137] J. de Blas, M. Ciuchini, E. Franco, S. Mishima, M. Pierini, L. Reina, and L. Silvestrini, “Electroweak precision observables and Higgs-boson signal strengths in the Standard Model and beyond: present and future,” *JHEP* **12** (2016) 135, [arXiv:1608.01509 \[hep-ph\]](#).
- [138] J. Ellis, P. Roloff, V. Sanz, and T. You, “Dimension-6 Operator Analysis of the CLIC Sensitivity to New Physics,” *JHEP* **05** (2017) 096, [arXiv:1701.04804 \[hep-ph\]](#).
- [139] H. Khanpour and M. Mohammadi Najafabadi, “Constraining Higgs boson effective couplings at electron-positron colliders,” *Phys. Rev.* **D95** no. 5, (2017) 055026, [arXiv:1702.00951 \[hep-ph\]](#).
- [140] T. Barklow, K. Fujii, S. Jung, R. Karl, J. List, T. Ogawa, M. E. Peskin, and J. Tian, “Improved Formalism for Precision Higgs Coupling Fits,” *Phys. Rev.* **D97** no. 5, (2018) 053003, [arXiv:1708.08912 \[hep-ph\]](#).
- [141] T. Barklow, K. Fujii, S. Jung, M. E. Peskin, and J. Tian, “Model-Independent Determination of the Triple Higgs Coupling at e^+e^- Colliders,” *Phys. Rev.* **D97** no. 5, (2018) 053004, [arXiv:1708.09079 \[hep-ph\]](#).
- [142] R. Contino, C. Grojean, D. Pappadopulo, R. Rattazzi, and A. Thamm, “Strong Higgs Interactions at a Linear Collider,” *JHEP* **02** (2014) 006, [arXiv:1309.7038 \[hep-ph\]](#).
- [143] J. J. van der Bij, “Does Low-energy Physics Depend on the Potential of a Heavy Higgs Particle?,” *Nucl. Phys.* **B267** (1986) 557–565.

- [144] C. Shen and S.-h. Zhu, “Anomalous Higgs-top coupling pollution of the triple Higgs coupling extraction at a future high-luminosity electron-positron collider,” *Phys. Rev.* **D92** no. 9, (2015) 094001, [arXiv:1504.05626 \[hep-ph\]](#).
- [145] F. Maltoni, D. Pagani, A. Shivaji, and X. Zhao, “Trilinear Higgs coupling determination via single-Higgs differential measurements at the LHC,” *Eur. Phys. J.* **C77** no. 12, (2017) 887, [arXiv:1709.08649 \[hep-ph\]](#).
- [146] M. Beneke, D. Boito, and Y.-M. Wang, “Anomalous Higgs couplings in angular asymmetries of $H \rightarrow Z\ell^+\ell^-$ and $e^+e^- \rightarrow HZ$,” *JHEP* **11** (2014) 028, [arXiv:1406.1361 \[hep-ph\]](#).
- [147] N. Craig, J. Gu, Z. Liu, and K. Wang, “Beyond Higgs Couplings: Probing the Higgs with Angular Observables at Future e^+e^- Colliders,” *JHEP* **03** (2016) 050, [arXiv:1512.06877 \[hep-ph\]](#).
- [148] C. F. Dürig, *Measuring the Higgs Self-coupling at the International Linear Collider*. PhD thesis, Hamburg U., Hamburg, 2016. <http://bib-pubdb1.desy.de/search?cc=Publication+Database&of=hd&p=reportnumber:DESY-THESIS-2016-027>.
- [149] **ILD** Collaboration, J. Tian and K. Fujii, “Measurement of Higgs couplings and self-coupling at the ILC,” *PoS EPS-HEP2013* (2013) 316, [arXiv:1311.6528 \[hep-ph\]](#).
- [150] C. F. Durig, J. Tian, J. List, K. Fujii, and M. Kurata, “Update on higgs self-coupling analyses for ild. .”.
- [151] J. Alwall, R. Frederix, S. Frixione, V. Hirschi, F. Maltoni, O. Mattelaer, H. S. Shao, T. Stelzer, P. Torrielli, and M. Zaro, “The automated computation of tree-level and next-to-leading order differential cross sections, and their matching to parton shower simulations,” *JHEP* **07** (2014) 079, [arXiv:1405.0301 \[hep-ph\]](#).
- [152] A. Alloul, N. D. Christensen, C. Degrande, C. Duhr, and B. Fuks, “FeynRules 2.0 - A complete toolbox for tree-level phenomenology,” *Comput. Phys. Commun.* **185** (2014) 2250–2300, [arXiv:1310.1921 \[hep-ph\]](#).
- [153] B. Fuks and K. Mawatari, “Bsmc characterisation. ..”.
- [154] F. R. Klinkhamer and N. S. Manton, “A Saddle Point Solution in the Weinberg-Salam Theory,” *Phys. Rev.* **D30** (1984) 2212.
- [155] V. A. Kuzmin, V. A. Rubakov, and M. E. Shaposhnikov, “On the Anomalous Electroweak Baryon Number Nonconservation in the Early Universe,” *Phys. Lett.* **155B** (1985) 36.

- [156] P. B. Arnold and L. D. McLerran, “Sphalerons, Small Fluctuations and Baryon Number Violation in Electroweak Theory,” *Phys. Rev.* **D36** (1987) 581.
- [157] P. B. Arnold and L. D. McLerran, “The Sphaleron Strikes Back,” *Phys. Rev.* **D37** (1988) 1020.
- [158] S. Yu. Khlebnikov and M. E. Shaposhnikov, “The Statistical Theory of Anomalous Fermion Number Nonconservation,” *Nucl. Phys.* **B308** (1988) 885–912.
- [159] A. D. Sakharov, “Violation of CP Invariance, c Asymmetry, and Baryon Asymmetry of the Universe,” *Pisma Zh. Eksp. Teor. Fiz.* **5** (1967) 32–35. [Usp. Fiz. Nauk161,61(1991)].
- [160] P. Huet and A. E. Nelson, “Electroweak baryogenesis in supersymmetric models,” *Phys. Rev.* **D53** (1996) 4578–4597, [arXiv:hep-ph/9506477](https://arxiv.org/abs/hep-ph/9506477) [hep-ph].
- [161] M. Carena, M. Quiros, and C. E. M. Wagner, “Opening the window for electroweak baryogenesis,” *Phys. Lett.* **B380** (1996) 81–91, [arXiv:hep-ph/9603420](https://arxiv.org/abs/hep-ph/9603420) [hep-ph].
- [162] M. Laine and K. Rummukainen, “The MSSM electroweak phase transition on the lattice,” *Nucl. Phys.* **B535** (1998) 423–457, [arXiv:hep-lat/9804019](https://arxiv.org/abs/hep-lat/9804019) [hep-lat].
- [163] M. Laine, “Electroweak phase transition beyond the standard model,” in *Strong and electroweak matter. Proceedings, Meeting, SEWM 2000, Marseille, France, June 13-17, 2000*, pp. 58–69. 2000. [arXiv:hep-ph/0010275](https://arxiv.org/abs/hep-ph/0010275) [hep-ph]. http://inspirehep.net/record/535577/files/arXiv:hep-ph_0010275.pdf.
- [164] J. R. Espinosa, “Dominant two loop corrections to the MSSM finite temperature effective potential,” *Nucl. Phys.* **B475** (1996) 273–292, [arXiv:hep-ph/9604320](https://arxiv.org/abs/hep-ph/9604320) [hep-ph].
- [165] M. Carena, M. Quiros, and C. E. M. Wagner, “Electroweak baryogenesis and Higgs and stop searches at LEP and the Tevatron,” *Nucl. Phys.* **B524** (1998) 3–22, [arXiv:hep-ph/9710401](https://arxiv.org/abs/hep-ph/9710401) [hep-ph].
- [166] S. J. Huber, P. John, and M. G. Schmidt, “Bubble walls, CP violation and electroweak baryogenesis in the MSSM,” *Eur. Phys. J.* **C20** (2001) 695–711, [arXiv:hep-ph/0101249](https://arxiv.org/abs/hep-ph/0101249) [hep-ph].
- [167] J. M. Cline and K. Kainulainen, “A New source for electroweak baryogenesis in the MSSM,” *Phys. Rev. Lett.* **85** (2000) 5519–5522, [arXiv:hep-ph/0002272](https://arxiv.org/abs/hep-ph/0002272) [hep-ph].

- [168] M. Carena, M. Quiros, M. Seco, and C. E. M. Wagner, “Improved results in supersymmetric electroweak baryogenesis,” *Nucl. Phys.* **B650** (2003) 24–42, [arXiv:hep-ph/0208043](#) [hep-ph].
- [169] C. Lee, V. Cirigliano, and M. J. Ramsey-Musolf, “Resonant relaxation in electroweak baryogenesis,” *Phys. Rev.* **D71** (2005) 075010, [arXiv:hep-ph/0412354](#) [hep-ph].
- [170] V. Cirigliano, Y. Li, S. Profumo, and M. J. Ramsey-Musolf, “MSSM Baryogenesis and Electric Dipole Moments: An Update on the Phenomenology,” *JHEP* **01** (2010) 002, [arXiv:0910.4589](#) [hep-ph].
- [171] M. Carena, G. Nardini, M. Quiros, and C. E. M. Wagner, “The Effective Theory of the Light Stop Scenario,” *JHEP* **10** (2008) 062, [arXiv:0806.4297](#) [hep-ph].
- [172] M. Quiros and M. Seco, “Electroweak baryogenesis in the MSSM,” *Nucl. Phys. Proc. Suppl.* **81** (2000) 63–70, [arXiv:hep-ph/9903274](#) [hep-ph].
- [173] D. Delepine, J. M. Gerard, R. Gonzalez Felipe, and J. Weyers, “A Light stop and electroweak baryogenesis,” *Phys. Lett.* **B386** (1996) 183–188, [arXiv:hep-ph/9604440](#) [hep-ph].
- [174] C. L. Wainwright, S. Profumo, and M. J. Ramsey-Musolf, “Phase Transitions and Gauge Artifacts in an Abelian Higgs Plus Singlet Model,” *Phys. Rev.* **D86** (2012) 083537, [arXiv:1204.5464](#) [hep-ph].
- [175] M. Quiros, “Finite temperature field theory and phase transitions,” in *Proceedings, Summer School in High-energy physics and cosmology: Trieste, Italy, June 29-July 17, 1998*, pp. 187–259. 1999. [arXiv:hep-ph/9901312](#) [hep-ph].
- [176] A. V. Kotwal, M. J. Ramsey-Musolf, J. M. No, and P. Winslow, “Singlet-catalyzed electroweak phase transitions in the 100 TeV frontier,” *Phys. Rev.* **D94** no. 3, (2016) 035022, [arXiv:1605.06123](#) [hep-ph].
- [177] D. Curtin, P. Meade, and C.-T. Yu, “Testing Electroweak Baryogenesis with Future Colliders,” *JHEP* **11** (2014) 127, [arXiv:1409.0005](#) [hep-ph].
- [178] P. Huang, A. Joglekar, B. Li, and C. E. M. Wagner, “Probing the Electroweak Phase Transition at the LHC,” *Phys. Rev.* **D93** no. 5, (2016) 055049, [arXiv:1512.00068](#) [hep-ph].
- [179] T. Huang, J. M. No, L. Pernié, M. Ramsey-Musolf, A. Safonov, M. Spannowsky, and P. Winslow, “Resonant di-Higgs boson production in the $b\bar{b}WW$ channel: Probing the electroweak phase transition at the LHC,” *Phys. Rev.* **D96** no. 3, (2017) 035007, [arXiv:1701.04442](#) [hep-ph].

- [180] C.-Y. Chen, J. Kozaczuk, and I. M. Lewis, “Non-resonant Collider Signatures of a Singlet-Driven Electroweak Phase Transition,” *JHEP* **08** (2017) 096, [arXiv:1704.05844 \[hep-ph\]](#).
- [181] D. Goncalves, T. Han, and S. Mukhopadhyay, “Off-shell Higgs Probe to Naturalness,” [arXiv:1710.02149 \[hep-ph\]](#).
- [182] P. Huang, A. J. Long, and L.-T. Wang, “Probing the Electroweak Phase Transition with Higgs Factories and Gravitational Waves,” *Phys. Rev.* **D94** no. 7, (2016) 075008, [arXiv:1608.06619 \[hep-ph\]](#).
- [183] D. Curtin, P. Meade, and H. Ramani, “Thermal Resummation and Phase Transitions,” [arXiv:1612.00466 \[hep-ph\]](#).
- [184] M. Jiang, L. Bian, W. Huang, and J. Shu, “Impact of a complex singlet: Electroweak baryogenesis and dark matter,” *Phys. Rev.* **D93** no. 6, (2016) 065032, [arXiv:1502.07574 \[hep-ph\]](#).
- [185] W. Cheng and L. Bian, “From inflation to cosmological electroweak phase transition with a complex scalar singlet,” [arXiv:1801.00662 \[hep-ph\]](#).
- [186] K. Fuyuto and E. Senaha, “Improved sphaleron decoupling condition and the Higgs coupling constants in the real singlet-extended standard model,” *Phys. Rev.* **D90** no. 1, (2014) 015015, [arXiv:1406.0433 \[hep-ph\]](#).
- [187] P. Basler, M. Krause, M. Muhlleitner, J. Wittbrodt, and A. Wlotzka, “Strong First Order Electroweak Phase Transition in the CP-Conserving 2HDM Revisited,” *JHEP* **02** (2017) 121, [arXiv:1612.04086 \[hep-ph\]](#).
- [188] P. Basler, M. Muhlleitner, and J. Wittbrodt, “The CP-Violating 2HDM in Light of a Strong First Order Electroweak Phase Transition and Implications for Higgs Pair Production,” [arXiv:1711.04097 \[hep-ph\]](#).
- [189] F. Goertz, A. Papaefstathiou, L. L. Yang, and J. Zurita, “Higgs Boson self-coupling measurements using ratios of cross sections,” *JHEP* **06** (2013) 016, [arXiv:1301.3492 \[hep-ph\]](#).
- [190] F. P. Huang, P.-H. Gu, P.-F. Yin, Z.-H. Yu, and X. Zhang, “Testing the electroweak phase transition and electroweak baryogenesis at the LHC and a circular electron-positron collider,” *Phys. Rev.* **D93** no. 10, (2016) 103515, [arXiv:1511.03969 \[hep-ph\]](#).
- [191] F. Goertz, “Electroweak Symmetry Breaking without the μ^2 Term,” *Phys. Rev.* **D94** no. 1, (2016) 015013, [arXiv:1504.00355 \[hep-ph\]](#).

- [192] L. Di Luzio, R. Gröber, and M. Spannowsky, “Maxi-sizing the trilinear Higgs self-coupling: how large could it be?,” *Eur. Phys. J.* **C77** no. 11, (2017) 788, [arXiv:1704.02311 \[hep-ph\]](#).
- [193] A. Katz and M. Perelstein, “Higgs Couplings and Electroweak Phase Transition,” *JHEP* **07** (2014) 108, [arXiv:1401.1827 \[hep-ph\]](#).
- [194] C.-Y. Chen, S. Dawson, and I. M. Lewis, “Exploring resonant di-Higgs boson production in the Higgs singlet model,” *Phys. Rev.* **D91** no. 3, (2015) 035015, [arXiv:1410.5488 \[hep-ph\]](#).
- [195] S. Dawson and I. M. Lewis, “NLO corrections to double Higgs boson production in the Higgs singlet model,” *Phys. Rev.* **D92** no. 9, (2015) 094023, [arXiv:1508.05397 \[hep-ph\]](#).
- [196] T. Robens and T. Stefaniak, “LHC Benchmark Scenarios for the Real Higgs Singlet Extension of the Standard Model,” *Eur. Phys. J.* **C76** no. 5, (2016) 268, [arXiv:1601.07880 \[hep-ph\]](#).
- [197] I. M. Lewis and M. Sullivan, “Benchmarks for Double Higgs Production in the Singlet Extended Standard Model at the LHC,” *Phys. Rev.* **D96** no. 3, (2017) 035037, [arXiv:1701.08774 \[hep-ph\]](#).
- [198] S. Dawson and I. M. Lewis, “Singlet Model Interference Effects with High Scale UV Physics,” *Phys. Rev.* **D95** no. 1, (2017) 015004, [arXiv:1605.04944 \[hep-ph\]](#).
- [199] P. Huang, A. Joglekar, M. Li, and C. E. M. Wagner, “Corrections to Di-Higgs Production with Light Stops and Modified Higgs Couplings,” [arXiv:1711.05743 \[hep-ph\]](#).
- [200] **ATLAS** Collaboration, M. Aaboud *et al.*, “Search for pair production of Higgs bosons in the $b\bar{b}b\bar{b}$ final state using proton–proton collisions at $\sqrt{s} = 13$ TeV with the ATLAS detector,” *Phys. Rev.* **D94** no. 5, (2016) 052002, [arXiv:1606.04782 \[hep-ex\]](#).
- [201] **ATLAS** Collaboration, G. Aad *et al.*, “Searches for Higgs boson pair production in the $hh \rightarrow bb\tau\tau, \gamma\gamma WW^*, \gamma\gamma bb, bbbb$ channels with the ATLAS detector,” *Phys. Rev.* **D92** (2015) 092004, [arXiv:1509.04670 \[hep-ex\]](#).
- [202] **CMS** Collaboration, A. M. Sirunyan *et al.*, “Search for Higgs boson pair production in events with two bottom quarks and two tau leptons in proton-proton collisions at $\sqrt{s} = 13$ TeV,” [arXiv:1707.02909 \[hep-ex\]](#).
- [203] **CMS Collaboration** Collaboration, “Search for resonant and non-resonant Higgs boson pair production in the $b\bar{b}l\nu l\nu$ final state at $\sqrt{s} = 13$ TeV,” Tech.

Rep. CMS-PAS-HIG-17-006, CERN, Geneva, 2017.
<https://cds.cern.ch/record/2257068>.

- [204] **CMS Collaboration** Collaboration, “Search for Higgs boson pair production in the final state containing two photons and two bottom quarks in proton-proton collisions at $\sqrt{s} = 13$ TeV,” Tech. Rep. CMS-PAS-HIG-17-008, CERN, Geneva, 2017. <https://cds.cern.ch/record/2273383>.
- [205] **CMS Collaboration** Collaboration, “Search for resonant pair production of Higgs bosons decaying to bottom quark-antiquark pairs in proton-proton collisions at 13 TeV,” Tech. Rep. CMS-PAS-HIG-17-009, CERN, Geneva, 2017. <https://cds.cern.ch/record/2292044>.
- [206] R. N. Lerner and J. McDonald, “Gauge singlet scalar as inflaton and thermal relic dark matter,” *Phys. Rev.* **D80** (2009) 123507, [arXiv:0909.0520](https://arxiv.org/abs/0909.0520) [hep-ph].
- [207] G. Degrandi, S. Di Vita, J. Elias-Miro, J. R. Espinosa, G. F. Giudice, G. Isidori, and A. Strumia, “Higgs mass and vacuum stability in the Standard Model at NNLO,” *JHEP* **08** (2012) 098, [arXiv:1205.6497](https://arxiv.org/abs/1205.6497) [hep-ph].
- [208] J. Campbell, M. Carena, R. Harnik, and Z. Liu, “Interference in the $gg \rightarrow h \rightarrow \gamma\gamma$ On-Shell Rate and the Higgs Boson Total Width,” [arXiv:1704.08259](https://arxiv.org/abs/1704.08259) [hep-ph].
- [209] M. Carena and Z. Liu, “Challenges and opportunities for heavy scalar searches in the $t\bar{t}$ channel at the LHC,” *JHEP* **11** (2016) 159, [arXiv:1608.07282](https://arxiv.org/abs/1608.07282) [hep-ph].
- [210] E. W. N. Glover and J. J. van der Bij, “HIGGS BOSON PAIR PRODUCTION VIA GLUON FUSION,” *Nucl. Phys.* **B309** (1988) 282–294.
- [211] G. Cowan, K. Cranmer, E. Gross, and O. Vitells, “Asymptotic formulae for likelihood-based tests of new physics,” *Eur. Phys. J.* **C71** (2011) 1554, [arXiv:1007.1727](https://arxiv.org/abs/1007.1727) [physics.data-an]. [Erratum: *Eur. Phys. J.*C73,2501(2013)].
- [212] J. R. Espinosa, T. Konstandin, and F. Riva, “Strong Electroweak Phase Transitions in the Standard Model with a Singlet,” *Nucl. Phys.* **B854** (2012) 592–630, [arXiv:1107.5441](https://arxiv.org/abs/1107.5441) [hep-ph].
- [213] J. M. No and M. Ramsey-Musolf, “Probing the Higgs Portal at the LHC Through Resonant di-Higgs Production,” *Phys. Rev.* **D89** no. 9, (2014) 095031, [arXiv:1310.6035](https://arxiv.org/abs/1310.6035) [hep-ph].
- [214] C. Grojean, G. Servant, and J. D. Wells, “First-order electroweak phase transition in the standard model with a low cutoff,” *Phys. Rev.* **D71** (2005) 036001, [arXiv:hep-ph/0407019](https://arxiv.org/abs/hep-ph/0407019) [hep-ph].

- [215] C. Delaunay, C. Grojean, and J. D. Wells, “Dynamics of Non-renormalizable Electroweak Symmetry Breaking,” *JHEP* **04** (2008) 029, [arXiv:0711.2511 \[hep-ph\]](#).
- [216] B. Henning, X. Lu, and H. Murayama, “How to use the Standard Model effective field theory,” *JHEP* **01** (2016) 023, [arXiv:1412.1837 \[hep-ph\]](#).
- [217] A. Falkowski and F. Riva, “Model-independent precision constraints on dimension-6 operators,” *JHEP* **02** (2015) 039, [arXiv:1411.0669 \[hep-ph\]](#).
- [218] Z. Zhang, “Time to Go Beyond Triple-Gauge-Boson-Coupling Interpretation of W Pair Production,” *Phys. Rev. Lett.* **118** no. 1, (2017) 011803, [arXiv:1610.01618 \[hep-ph\]](#).
- [219] J. Baglio, S. Dawson, and I. M. Lewis, “An NLO QCD effective field theory analysis of W^+W^- production at the LHC including fermionic operators,” *Phys. Rev.* **D96** no. 7, (2017) 073003, [arXiv:1708.03332 \[hep-ph\]](#).
- [220] G. D’Ambrosio, G. F. Giudice, G. Isidori, and A. Strumia, “Minimal flavor violation: An Effective field theory approach,” *Nucl. Phys.* **B645** (2002) 155–187, [arXiv:hep-ph/0207036 \[hep-ph\]](#).
- [221] A. Biekötter, A. Knochel, M. Krämer, D. Liu, and F. Riva, “Vices and virtues of Higgs effective field theories at large energy,” *Phys. Rev.* **D91** (2015) 055029, [arXiv:1406.7320 \[hep-ph\]](#).
- [222] M. Farina, G. Panico, D. Pappadopulo, J. T. Ruderman, R. Torre, and A. Wulzer, “Energy helps accuracy: electroweak precision tests at hadron colliders,” *Phys. Lett.* **B772** (2017) 210–215, [arXiv:1609.08157 \[hep-ph\]](#).
- [223] S. Alioli, M. Farina, D. Pappadopulo, and J. T. Ruderman, “Precision Probes of QCD at High Energies,” *JHEP* **07** (2017) 097, [arXiv:1706.03068 \[hep-ph\]](#).
- [224] R. Franceschini, G. Panico, A. Pomarol, F. Riva, and A. Wulzer, “Electroweak Precision Tests in High-Energy Diboson Processes,” *JHEP* **02** (2018) 111, [arXiv:1712.01310 \[hep-ph\]](#).
- [225] G. Panico, F. Riva, and A. Wulzer, “Diboson Interference Resurrection,” *Phys. Lett.* **B776** (2018) 473–480, [arXiv:1708.07823 \[hep-ph\]](#).
- [226] A. Azatov, J. Elias-Miro, Y. Reyimuaji, and E. Venturini, “Novel measurements of anomalous triple gauge couplings for the LHC,” *JHEP* **10** (2017) 027, [arXiv:1707.08060 \[hep-ph\]](#).
- [227] R. S. Gupta, A. Pomarol, and F. Riva, “BSM Primary Effects,” *Phys. Rev.* **D91** no. 3, (2015) 035001, [arXiv:1405.0181 \[hep-ph\]](#).

- [228] V. Shtabovenko, R. Mertig, and F. Orellana, “New Developments in FeynCalc 9.0,” *Comput. Phys. Commun.* **207** (2016) 432–444, [arXiv:1601.01167 \[hep-ph\]](#).
- [229] A. Falkowski, B. Fuks, K. Mawatari, K. Mimasu, F. Riva, and V. Sanz, “Rosetta: an operator basis translator for Standard Model effective field theory,” *Eur. Phys. J.* **C75** no. 12, (2015) 583, [arXiv:1508.05895 \[hep-ph\]](#).
- [230] “A summary of the atlas and cms constraints on anomalous trigple gauge couplings is found in.” <https://twiki.cern.ch/twiki/bin/view/CMSPublic/PhysicsResultsSMPaTGC>.
- [231] **CMS** Collaboration, A. M. Sirunyan *et al.*, “Search for anomalous couplings in boosted $WW/WZ \rightarrow \ell\nu q\bar{q}$ production in proton-proton collisions at $\sqrt{s} = 8$ TeV,” *Phys. Lett.* **B772** (2017) 21–42, [arXiv:1703.06095 \[hep-ex\]](#).
- [232] **ATLAS** Collaboration, G. Aad *et al.*, “Measurement of W^+W^- production in pp collisions at $\sqrt{s}=7$ TeV with the ATLAS detector and limits on anomalous WWZ and $WW\gamma$ couplings,” *Phys. Rev.* **D87** no. 11, (2013) 112001, [arXiv:1210.2979 \[hep-ex\]](#). [Erratum: Phys. Rev.D88,no.7,079906(2013)].
- [233] **ATLAS** Collaboration, G. Aad *et al.*, “Measurement of total and differential W^+W^- production cross sections in proton-proton collisions at $\sqrt{s} = 8$ TeV with the ATLAS detector and limits on anomalous triple-gauge-boson couplings,” *JHEP* **09** (2016) 029, [arXiv:1603.01702 \[hep-ex\]](#).
- [234] **CMS** Collaboration, V. Khachatryan *et al.*, “Measurement of the W^+W^- cross section in pp collisions at $\sqrt{s} = 8$ TeV and limits on anomalous gauge couplings,” *Eur. Phys. J.* **C76** no. 7, (2016) 401, [arXiv:1507.03268 \[hep-ex\]](#).
- [235] **ATLAS** Collaboration, G. Aad *et al.*, “Measurements of $W^\pm Z$ production cross sections in pp collisions at $\sqrt{s} = 8$ TeV with the ATLAS detector and limits on anomalous gauge boson self-couplings,” *Phys. Rev.* **D93** no. 9, (2016) 092004, [arXiv:1603.02151 \[hep-ex\]](#).
- [236] **CMS** Collaboration, V. Khachatryan *et al.*, “Measurement of the WZ production cross section in pp collisions at $\sqrt{s} = 7$ and 8 TeV and search for anomalous triple gauge couplings at $\sqrt{s} = 8$ TeV,” *Eur. Phys. J.* **C77** no. 4, (2017) 236, [arXiv:1609.05721 \[hep-ex\]](#).
- [237] **ATLAS** Collaboration, T. A. collaboration, “Measurement of $W^\pm Z$ boson pair-production in pp collisions at $\sqrt{s} = 13$ TeV with the ATLAS Detector and confidence intervals for anomalous triple gauge boson couplings,”.
- [238] F. Gianotti *et al.*, “Physics potential and experimental challenges of the LHC luminosity upgrade,” *Eur. Phys. J.* **C39** (2005) 293–333, [arXiv:hep-ph/0204087 \[hep-ph\]](#).

- [239] A. Falkowski, M. Gonzalez-Alonso, A. Greljo, and D. Marzocca, “Global constraints on anomalous triple gauge couplings in effective field theory approach,” *Phys. Rev. Lett.* **116** no. 1, (2016) 011801, [arXiv:1508.00581 \[hep-ph\]](#).
- [240] J. A. Dror, M. Farina, E. Salvioni, and J. Serra, “Strong tW Scattering at the LHC,” *JHEP* **01** (2016) 071, [arXiv:1511.03674 \[hep-ph\]](#).
- [241] S. Alioli, M. Farina, D. Pappadopulo, and J. T. Ruderman, “Catching a New Force by the Tail,” *Phys. Rev. Lett.* **120** no. 10, (2018) 101801, [arXiv:1712.02347 \[hep-ph\]](#).
- [242] A. Azatov, R. Contino, C. S. Machado, and F. Riva, “Helicity selection rules and noninterference for BSM amplitudes,” *Phys. Rev.* **D95** no. 6, (2017) 065014, [arXiv:1607.05236 \[hep-ph\]](#).
- [243] D. Liu, A. Pomarol, R. Rattazzi, and F. Riva, “Patterns of Strong Coupling for LHC Searches,” *JHEP* **11** (2016) 141, [arXiv:1603.03064 \[hep-ph\]](#).
- [244] R. Contino, D. Marzocca, D. Pappadopulo, and R. Rattazzi, “On the effect of resonances in composite Higgs phenomenology,” *JHEP* **10** (2011) 081, [arXiv:1109.1570 \[hep-ph\]](#).
- [245] D. Pappadopulo, A. Thamm, R. Torre, and A. Wulzer, “Heavy Vector Triplets: Bridging Theory and Data,” *JHEP* **09** (2014) 060, [arXiv:1402.4431 \[hep-ph\]](#).
- [246] A. Thamm, R. Torre, and A. Wulzer, “Future tests of Higgs compositeness: direct vs indirect,” *JHEP* **07** (2015) 100, [arXiv:1502.01701 \[hep-ph\]](#).
- [247] S. V. Chekanov, J. T. Childers, D. Frizzell, J. Proudfoot, and R. Wang, “Precision searches in dijets at the HL-LHC and HE-LHC,” [arXiv:1710.09484 \[hep-ex\]](#).
- [248] **CMS Collaboration** Collaboration, “CMS at the High-Energy Frontier. Contribution to the Update of the European Strategy for Particle Physics,” Tech. Rep. CMS-NOTE-2012-006. CERN-CMS-NOTE-2012-006, CERN, Geneva, Oct, 2012. <https://cds.cern.ch/record/1494600>.
- [249] R. Contino, “The Higgs as a Composite Nambu-Goldstone Boson,” in *Physics of the large and the small, TASI 09, proceedings of the Theoretical Advanced Study Institute in Elementary Particle Physics, Boulder, Colorado, USA, 1-26 June 2009*, pp. 235–306. 2011. [arXiv:1005.4269 \[hep-ph\]](#). <https://inspirehep.net/record/856065/files/arXiv:1005.4269.pdf>.
- [250] B. Bellazzini, C. Csáki, and J. Serra, “Composite Higgses,” *Eur. Phys. J.* **C74** no. 5, (2014) 2766, [arXiv:1401.2457 \[hep-ph\]](#).

- [251] K. Agashe, R. Contino, and A. Pomarol, “The Minimal composite Higgs model,” *Nucl. Phys.* **B719** (2005) 165–187, [arXiv:hep-ph/0412089](#) [hep-ph].
- [252] D. B. Kaplan, “Flavor at SSC energies: A New mechanism for dynamically generated fermion masses,” *Nucl. Phys.* **B365** (1991) 259–278.
- [253] R. Contino, L. Da Rold, and A. Pomarol, “Light custodians in natural composite Higgs models,” *Phys. Rev.* **D75** (2007) 055014, [arXiv:hep-ph/0612048](#) [hep-ph].
- [254] O. Matsedonskyi, G. Panico, and A. Wulzer, “Light Top Partners for a Light Composite Higgs,” *JHEP* **01** (2013) 164, [arXiv:1204.6333](#) [hep-ph].
- [255] D. Marzocca, M. Serone, and J. Shu, “General Composite Higgs Models,” *JHEP* **08** (2012) 013, [arXiv:1205.0770](#) [hep-ph].
- [256] G. Panico, M. Redi, A. Tesi, and A. Wulzer, “On the Tuning and the Mass of the Composite Higgs,” *JHEP* **03** (2013) 051, [arXiv:1210.7114](#) [hep-ph].
- [257] **ATLAS** Collaboration, M. Aaboud *et al.*, “Search for pair production of heavy vector-like quarks decaying to high- p_T W bosons and b quarks in the lepton-plus-jets final state in pp collisions at $\sqrt{s} = 13$ TeV with the ATLAS detector,” *JHEP* **10** (2017) 141, [arXiv:1707.03347](#) [hep-ex].
- [258] **CMS** Collaboration, C. Collaboration, “Search for top quark partners with charge $5/3$ in the single-lepton final state at $\sqrt{s} = 13$ TeV,”.
- [259] C. Anastasiou, E. Furlan, and J. Santiago, “Realistic Composite Higgs Models,” *Phys. Rev.* **D79** (2009) 075003, [arXiv:0901.2117](#) [hep-ph].
- [260] C. Grojean, O. Matsedonskyi, and G. Panico, “Light top partners and precision physics,” *JHEP* **10** (2013) 160, [arXiv:1306.4655](#) [hep-ph].
- [261] M. Carena, L. Da Rold, and E. Pontón, “Minimal Composite Higgs Models at the LHC,” *JHEP* **06** (2014) 159, [arXiv:1402.2987](#) [hep-ph].
- [262] S. M. Barr and A. Zee, “Electric Dipole Moment of the Electron and of the Neutron,” *Phys. Rev. Lett.* **65** (1990) 21–24. [Erratum: *Phys. Rev. Lett.* 65,2920(1990)].
- [263] M. König, M. Neubert, and D. M. Straub, “Dipole operator constraints on composite Higgs models,” *Eur. Phys. J.* **C74** no. 7, (2014) 2945, [arXiv:1403.2756](#) [hep-ph].
- [264] S. Weinberg, “Larger Higgs Exchange Terms in the Neutron Electric Dipole Moment,” *Phys. Rev. Lett.* **63** (1989) 2333.

- [265] J. Brod, U. Haisch, and J. Zupan, “Constraints on CP-violating Higgs couplings to the third generation,” *JHEP* **11** (2013) 180, [arXiv:1310.1385 \[hep-ph\]](#).
- [266] J. Kopp and M. Nardecchia, “Flavor and CP violation in Higgs decays,” *JHEP* **10** (2014) 156, [arXiv:1406.5303 \[hep-ph\]](#).
- [267] **ACME** Collaboration, J. Baron *et al.*, “Order of Magnitude Smaller Limit on the Electric Dipole Moment of the Electron,” *Science* **343** (2014) 269–272, [arXiv:1310.7534 \[physics.atom-ph\]](#).
- [268] W. B. Cairncross, D. N. Gresh, M. Grau, K. C. Cossel, T. S. Roussy, Y. Ni, Y. Zhou, J. Ye, and E. A. Cornell, “Precision Measurement of the Electron’s Electric Dipole Moment Using Trapped Molecular Ions,” *Phys. Rev. Lett.* **119** no. 15, (2017) 153001, [arXiv:1704.07928 \[physics.atom-ph\]](#).
- [269] C. A. Baker *et al.*, “An Improved experimental limit on the electric dipole moment of the neutron,” *Phys. Rev. Lett.* **97** (2006) 131801, [arXiv:hep-ex/0602020 \[hep-ex\]](#).
- [270] B. Graner, Y. Chen, E. G. Lindahl, and B. R. Heckel, “Reduced Limit on the Permanent Electric Dipole Moment of Hg199,” *Phys. Rev. Lett.* **116** no. 16, (2016) 161601, [arXiv:1601.04339 \[physics.atom-ph\]](#). [Erratum: *Phys. Rev. Lett.* **119**, no. 11, 119901 (2017)].
- [271] R. Picker, “How the minuscule can contribute to the big picture: the neutron electric dipole moment project at TRIUMF,” *JPS Conf. Proc.* **13** (2017) 010005, [arXiv:1612.00875 \[physics.ins-det\]](#).
- [272] J. Doyle, “Search for the electric dipole moment of the electron with thorium monoxide – the acme experiment.
http://online.kitp.ucsb.edu/online/nuclear_c16/doyle/. talk at the kitp conference: Symmetry tests in nuclei and atoms,” 2016.
- [273] A. De Simone, O. Matsedonskyi, R. Rattazzi, and A. Wulzer, “A First Top Partner Hunter’s Guide,” *JHEP* **04** (2013) 004, [arXiv:1211.5663 \[hep-ph\]](#).
- [274] B. Keren-Zur, P. Lodone, M. Nardecchia, D. Pappadopulo, R. Rattazzi, and L. Vecchi, “On Partial Compositeness and the CP asymmetry in charm decays,” *Nucl. Phys.* **B867** (2013) 394–428, [arXiv:1205.5803 \[hep-ph\]](#).
- [275] M. Redi and A. Weiler, “Flavor and CP Invariant Composite Higgs Models,” *JHEP* **11** (2011) 108, [arXiv:1106.6357 \[hep-ph\]](#).
- [276] R. Barbieri, D. Buttazzo, F. Sala, and D. M. Straub, “Flavour physics from an approximate $U(2)^3$ symmetry,” *JHEP* **07** (2012) 181, [arXiv:1203.4218 \[hep-ph\]](#).

- [277] M. Redi, “Leptons in Composite MFV,” *JHEP* **09** (2013) 060, [arXiv:1306.1525 \[hep-ph\]](#).
- [278] C. Delaunay, O. Gedalia, S. J. Lee, G. Perez, and E. Ponton, “Ultra Visible Warped Model from Flavor Triviality and Improved Naturalness,” *Phys. Rev.* **D83** (2011) 115003, [arXiv:1007.0243 \[hep-ph\]](#).
- [279] L. Vecchi, “A Flavor Sector for the Composite Higgs,” *Phys. Lett.* **B727** (2013) 130–135, [arXiv:1206.4701 \[hep-ph\]](#).
- [280] G. Panico and A. Pomarol, “Flavor hierarchies from dynamical scales,” *JHEP* **07** (2016) 097, [arXiv:1603.06609 \[hep-ph\]](#).
- [281] O. Matsedonskyi, G. Panico, and A. Wulzer, “Top Partners Searches and Composite Higgs Models,” *JHEP* **04** (2016) 003, [arXiv:1512.04356 \[hep-ph\]](#).
- [282] S. R. Coleman, J. Wess, and B. Zumino, “Structure of phenomenological Lagrangians. 1,” *Phys. Rev.* **177** (1969) 2239–2247.
- [283] C. G. Callan, Jr., S. R. Coleman, J. Wess, and B. Zumino, “Structure of phenomenological Lagrangians. 2.,” *Phys. Rev.* **177** (1969) 2247–2250.
- [284] D. Stockinger, “The Muon Magnetic Moment and Supersymmetry,” *J. Phys.* **G34** (2007) R45–R92, [arXiv:hep-ph/0609168 \[hep-ph\]](#).
- [285] D. A. Dicus, “Neutron Electric Dipole Moment From Charged Higgs Exchange,” *Phys. Rev.* **D41** (1990) 999.
- [286] **ATLAS** Collaboration, G. Aad *et al.*, “Constraints on new phenomena via Higgs boson couplings and invisible decays with the ATLAS detector,” *JHEP* **11** (2015) 206, [arXiv:1509.00672 \[hep-ex\]](#).
- [287] S. Dawson *et al.*, “Working Group Report: Higgs Boson,” in *Proceedings, 2013 Community Summer Study on the Future of U.S. Particle Physics: Snowmass on the Mississippi (CSS2013): Minneapolis, MN, USA, July 29-August 6, 2013*. 2013. [arXiv:1310.8361 \[hep-ex\]](#).
<https://inspirehep.net/record/1262795/files/arXiv:1310.8361.pdf>.
- [288] J. F. Kamenik, M. Papucci, and A. Weiler, “Constraining the dipole moments of the top quark,” *Phys. Rev.* **D85** (2012) 071501, [arXiv:1107.3143 \[hep-ph\]](#).
[Erratum: *Phys. Rev.* D88, no.3, 039903 (2013)].
- [289] **CMS** Collaboration, C. Collaboration, “Search for heavy vector-like quarks decaying to same-sign dileptons.”

- [290] **ATLAS** Collaboration, T. A. collaboration, “Search for new physics using events with b -jets and a pair of same charge leptons in 3.2 fb^{-1} of pp collisions at $\sqrt{s} = 13 \text{ TeV}$ with the ATLAS detector,”
- [291] O. Matsedonskyi, G. Panico, and A. Wulzer, “On the Interpretation of Top Partners Searches,” *JHEP* **12** (2014) 097, [arXiv:1409.0100 \[hep-ph\]](#).
- [292] **CMS** Collaboration, A. M. Sirunyan *et al.*, “Search for single production of a vector-like T quark decaying to a Z boson and a top quark in proton-proton collisions at $\sqrt{s} = 13 \text{ TeV}$,” [arXiv:1708.01062 \[hep-ex\]](#).
- [293] **CMS** Collaboration, V. Khachatryan *et al.*, “Search for single production of a heavy vector-like T quark decaying to a Higgs boson and a top quark with a lepton and jets in the final state,” *Phys. Lett.* **B771** (2017) 80–105, [arXiv:1612.00999 \[hep-ex\]](#).
- [294] **ATLAS** Collaboration, T. A. collaboration, “Search for single production of vector-like quarks decaying into Wb in pp collisions at $\sqrt{s} = 13 \text{ TeV}$ with the ATLAS detector,”
- [295] **CMS** Collaboration, A. M. Sirunyan *et al.*, “Search for single production of vector-like quarks decaying into a b quark and a W boson in proton-proton collisions at $\sqrt{s} = 13 \text{ TeV}$,” *Phys. Lett.* **B772** (2017) 634–656, [arXiv:1701.08328 \[hep-ex\]](#).
- [296] G. Panico and A. Wulzer, “The Discrete Composite Higgs Model,” *JHEP* **09** (2011) 135, [arXiv:1106.2719 \[hep-ph\]](#).
- [297] S. De Curtis, M. Redi, and A. Tesi, “The 4D Composite Higgs,” *JHEP* **04** (2012) 042, [arXiv:1110.1613 \[hep-ph\]](#).
- [298] R. Contino and A. Pomarol, “Holography for fermions,” *JHEP* **11** (2004) 058, [arXiv:hep-th/0406257 \[hep-th\]](#).
- [299] G. Panico and A. Wulzer, “Effective action and holography in 5D gauge theories,” *JHEP* **05** (2007) 060, [arXiv:hep-th/0703287 \[hep-th\]](#).
- [300] K. Agashe and R. Contino, “Composite Higgs-Mediated FCNC,” *Phys. Rev.* **D80** (2009) 075016, [arXiv:0906.1542 \[hep-ph\]](#).
- [301] A. Alloul, B. Fuks, and V. Sanz, “Phenomenology of the Higgs Effective Lagrangian via FEYNRULES,” *JHEP* **04** (2014) 110, [arXiv:1310.5150 \[hep-ph\]](#).
- [302] C. Hartmann and M. Trott, “Higgs Decay to Two Photons at One Loop in the Standard Model Effective Field Theory,” *Phys. Rev. Lett.* **115** no. 19, (2015) 191801, [arXiv:1507.03568 \[hep-ph\]](#).

- [303] E. Conte, B. Dumont, B. Fuks, and C. Wymant, “Designing and recasting LHC analyses with MadAnalysis 5,” *Eur. Phys. J.* **C74** no. 10, (2014) 3103, [arXiv:1405.3982 \[hep-ph\]](#).
- [304] E. Conte, B. Fuks, and G. Serret, “MadAnalysis 5, A User-Friendly Framework for Collider Phenomenology,” *Comput. Phys. Commun.* **184** (2013) 222–256, [arXiv:1206.1599 \[hep-ph\]](#).
- [305] T. Hahn, “Generating Feynman diagrams and amplitudes with FeynArts 3,” *Comput. Phys. Commun.* **140** (2001) 418–431, [arXiv:hep-ph/0012260 \[hep-ph\]](#).
- [306] T. Hahn and M. Perez-Victoria, “Automatized one loop calculations in four-dimensions and D-dimensions,” *Comput. Phys. Commun.* **118** (1999) 153–165, [arXiv:hep-ph/9807565 \[hep-ph\]](#).
- [307] T. Hahn, “CUBA: A Library for multidimensional numerical integration,” *Comput. Phys. Commun.* **168** (2005) 78–95, [arXiv:hep-ph/0404043 \[hep-ph\]](#).
- [308] N. Craig, C. Englert, and M. McCullough, “New Probe of Naturalness,” *Phys. Rev. Lett.* **111** no. 12, (2013) 121803, [arXiv:1305.5251 \[hep-ph\]](#).
- [309] M. Baak, M. Goebel, J. Haller, A. Hoecker, D. Kennedy, R. Kogler, K. Moenig, M. Schott, and J. Stelzer, “The Electroweak Fit of the Standard Model after the Discovery of a New Boson at the LHC,” *Eur. Phys. J.* **C72** (2012) 2205, [arXiv:1209.2716 \[hep-ph\]](#).
- [310] **Gfitter Group** Collaboration, M. Baak, J. Cúth, J. Haller, A. Hoecker, R. Kogler, K. Mönig, M. Schott, and J. Stelzer, “The global electroweak fit at NNLO and prospects for the LHC and ILC,” *Eur. Phys. J.* **C74** (2014) 3046, [arXiv:1407.3792 \[hep-ph\]](#).